Diamond-based quantum networks with multi-qubit nodes

Kalb, Norbert

DOI
10.4233/uuid:249753ae-9000-446a-9375-63c1e1165cc1

Publication date
2018

Document Version
Final published version

Citation (APA)
Kalb, N. (2018). Diamond-based quantum networks with multi-qubit nodes.
https://doi.org/10.4233/uuid:249753ae-9000-446a-9375-63c1e1165cc1

DIAMOND-BASED QUANTUM NETWORKS WITH MULTI-QUBIT NODES

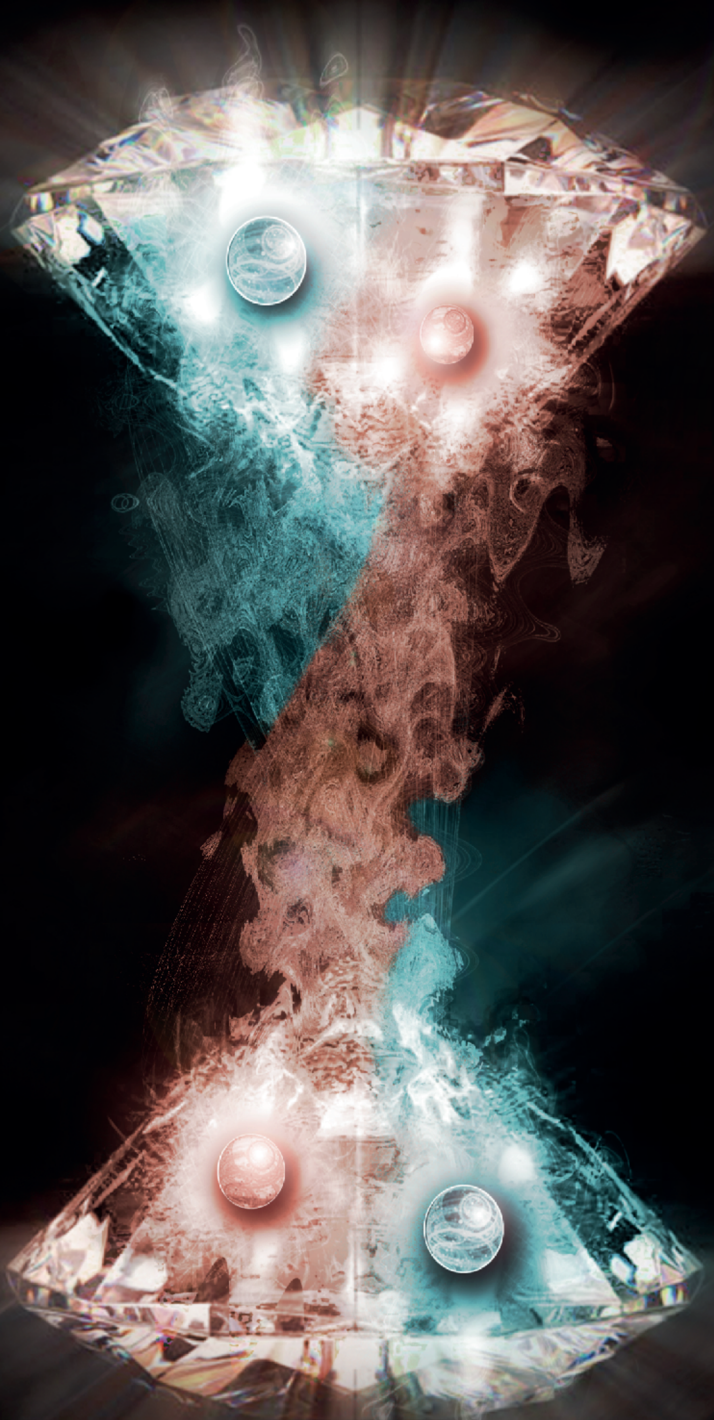

NORBERT KALB

DIAMOND-BASED QUANTUM NETWORKS WITH MULTI-QUBIT NODES

DIAMOND-BASED QUANTUM NETWORKS WITH MULTI-QUBIT NODES

Dissertation

for the purpose of obtaining the degree of doctor
at Delft University of Technology,
by the authority of the Rector Magnificus prof. dr. ir. T.H.J.J. van der Hagen,
Chair of the Board for Doctorates,
to be defended publicly on
Thursday 5 April 2018 at 12:30 o' clock

by

Norbert KALB

Master of Science in Physics,
Technische Universität München, Germany,
born in Nuremberg, Germany.

This dissertation has been approved by the promotor.

Composition of the doctoral committee:

Rector Magnificus,	chairperson
Prof. dr. ir. R. Hanson	Delft University of Technology, promotor

Independent members:

Prof. dr. C. W. J. Beenakker	Leiden University
Prof. dr. D. P. DiVincenzo	RWTH Aachen University, Germany
Prof. dr. T. E. Northup	University of Innsbruck, Austria
Prof. dr. W. Tittel	Delft University of Technology
Prof. dr. ir. L. M. K. Vandersypen	Delft University of Technology

Other members:

Prof. dr. S. D. C. Wehner	Delft University of Technology

ISBN 978-90-8593-338-0

Casimir PhD series, Delft-Leiden 2018-06

Cover design by Cheyenne Hensgens

Printed by Gildeprint – www.gildeprint.nl

An electronic copy of this dissertation is available at http://repository.tudelft.nl/.

CONTENTS

Summary **ix**

Samenvatting **xi**

Kurzdarstellung **xiii**

1 Introduction **1**
References 5

2 Theoretical description and experimental control of single NV centres **7**
2.1 The NV centre in diamond 8
2.2 Device capabilities 9
2.3 Addressing and controlling ^{13}C nuclear spins 18
2.4 Generating remote entanglement 22
References 27

3 Quantum Zeno subspaces by repeated multi-spin projections **31**
3.1 The quantum Zeno effect 32
3.2 Experimental system and sequence 32
3.3 Quantum Zeno effect for a single spin. 34
3.4 Zeno subspaces: preserving a logical qubit 34
3.5 Zeno subspaces: two logical qubits 37
3.6 Scaling law for the suppression of dephasing 37
3.7 Discussion 39
3.8 Supplementary Information 40
References 46

4 Analysis of a quantum memory with an optical interface in diamond **49**
4.1 NV centres as quantum network nodes 50
4.2 Control and characterization of nuclear spins in diamond 50
4.3 A model for carbon spin dephasing during entanglement generation 53
4.4 ^{13}C spins are promising quantum memories 56
4.5 Methods 57
References 58

5 Robust Quantum-Network Memory Using Nuclear Spins **61**
5.1 NVs as node for layered quantum networks 62
5.2 Experimental setting 62
5.3 Electronic spin reset 65
5.4 Single-nuclear-spin quantum memory 66
5.5 Decoherence-protected subspace quantum memory 69

5.6 Scaling of the dephasing rate with hyperfine coupling strength and repump duration . . . 70
5.7 Conclusion and outlook. . . . 71
5.8 Supplementary Information . . . 72
References . . . 78

6 **Dephasing mechanisms of memories for quantum networks** **81**
6.1 Introduction . . . 82
6.2 Experimental system . . . 83
6.3 Performance of a strongly-coupled nuclear spin memory . . . 85
6.4 Microwave control errors . . . 86
6.5 Spin-flip mechanisms of the NV electron spin . . . 88
6.6 Current limits to memory robustness . . . 89
6.7 Electron spin initialization errors . . . 92
6.8 Discussion and outlook . . . 94
References . . . 97

7 **A loophole-free Bell test** **101**
7.1 Bell tests and loopholes in experimental demonstrations . . . 102
7.2 Experimental realization . . . 105
7.3 Set-up characterization . . . 107
7.4 First experimental trial . . . 109
7.5 Second experimental trial . . . 109
7.6 Combined P-value for the two tests . . . 111
7.7 Conclusion . . . 112
7.8 Supplementary Information . . . 113
7.9 Supplementary Information - Second experimental trial . . . 118
References . . . 120

8 **Deterministic delivery of remote entanglement** **123**
8.1 The quantum link efficiency . . . 124
8.2 Single-photon entangling protocol . . . 126
8.3 NV-state protection by dynamical decoupling . . . 129
8.4 Deterministic entanglement generation . . . 131
8.5 Outlook . . . 133
8.6 Supplementary information . . . 133
References . . . 148

9 **Distillation of remote entanglement** **151**
9.1 Introduction . . . 152
9.2 Distillation of remote entangled states . . . 152
9.3 Quantum network nodes . . . 154
9.4 Robust storage of quantum information . . . 155
9.5 Experimental entanglement distillation . . . 156
9.6 Distillation results. . . . 158
9.7 Ebit rate . . . 161
9.8 Towards multi-node quantum networks . . . 162

9.9 Supplementary Information . . . 162
References . . . 181

10 Conclusions and outlook 185
10.1 Summary . . . 186
10.2 Experimental platforms for quantum networks . . . 186
10.3 NV-based three-node networks . . . 188
10.4 Future directions . . . 191
10.5 Conclusion . . . 194
References . . . 195

Acknowledgements 201

List of Publications 205

Curriculum Vitæ 207

SUMMARY

Quantum networks promise to be the future architecture for secure communication and distributed quantum computation. This thesis describes experiments on nitrogen-vacancy (NV) centres that lead towards a versatile multi-node quantum network consisting of multi-qubit nodes.

The NV centre in diamond is a spinful optically-active crystal defect. NVs are a prime network-node candidate due to demonstrated coherence times beyond 100 ms and longitudinal relaxation times exceeding 1 s and their spin-selective optical interface which facilitates the generation of spin-photon entanglement. Entangling links between nodes are therefore readily created by overlapping the emission of two NVs on a beam splitter. Besides NVs, we further address individual ^{13}C nuclear spins in the vicinity and use these spins as a quantum resource. Our goal is to propel these nuclear spins to constitute robust quantum memories which store and manipulate quantum information in an NV-based quantum network. The experiments described in this thesis are thematically separated into three groups.

First, we explore the NV-nuclear interplay. We demonstrate nuclear-spin control by observing the Zeno effect on up to two logical qubits within the state space of three nuclear spins (Chapter 3). We further realize that the always-on magnetic hyperfine interaction between NV and nuclear spins will limit the nuclear spin coherence when entangling distant NV centres (Chapter 4). A systematic experimental study probes our theoretical prediction and we additionally demonstrate improved robustness for logical states within decoherence-protected state spaces (Chapter 5) and finally for individual nuclear spins (Chapter 6).

Second, we use remote NV-NV entangled states to demonstrate experimental milestones in quantum networks. The realization of a high-fidelity entangled link over a distance of 1.3 km permits the loophole-free violation of Bell's inequality (Chapter 7). We further increase the entangling rate by three orders of magnitude such that it exceeds the decoherence rate of an entangled state on our network. This allows us to convert our probabilistic entanglement generation into a deterministic process which delivers entangled states at prespecified moments in time (Chapter 8).

Third, we finally combine the concepts of nuclear-spin quantum memories and remote entanglement generation to demonstrate entanglement distillation in a network setting (Chapter 9). We subsequently generate two raw entangled input states between two remote NV centres. The first state is stored on nuclear spins to liberate both NVs for the second round of state generation. Finally, a higher-fidelity entangled state is distilled via local operations. This constitutes the first quantum-network demonstration that relies on the control of multiple fully-coherent quantum systems per network node.

SAMENVATTING

Kwantumnetwerken zijn een veelbelovend toekomstige architectuur voor veilige communicatie en gedistribueerde kwantumberekeningen. Dit proefschrift beschrijft experimenten aan stikstof-gat roosterdefecten (NV centrum) die naar een veelzijdig kwantumnetwerk met vele knooppunten leiden, waarbij ieder knooppunt meerdere qubits omvat.

Het NV centrum in diamant is een optisch actief roosterdefect met een elektronische spin. Het NV is een uitstekende kandidaat knooppunten omdat coherentietijden groter dan 100 ms en relaxatietijden groter dan 1 s zijn al aangetoond. Een NV kan spin-selectief aangestuurd worden, waardoor spin-fotonverstrengeling kan worden gerealiseerd. Als de niet-onderscheidbare emissie van twee NVs op een stralingsdeler overlappen wordt de “welke-weg“ informatie gewist en verstrengeling tussen de spins van de twee NVs over een lange afstand gegenereerd. Verder kunnen door een NV enkele ^{13}C kernspins in de omgeving aangestuurd en gebruikt worden als qubits. Ons doel is deze kernspins te ontwikkelen tot een robuust kwantumgeheugen waardoor kwantuminformatie bewaard en verwerkt kan worden in een op NV’s gebaseerd kwantumnetwerk. De experimenten in dit proefschrift zijn daarom opgedeeld in drie groepen.

Ten eerste worden interacties tussen NV en kernspin verkend. We demonstreren de kwaliteit van de kernspincontrole door het initialiseren en sturen van twee logische qubits binnen de toestandsruimte van drie kernspins (Hoofdstuk 3). Daarna stellen wij vast dat tijdens het verstrengelen van twee NVs de altijd-aan magnetische hyperfijne koppeling tussen NV en kernspin de kernspin coherentie beperkt (Hoofdstuk 4). Een systematisch onderzoek bevestigt deze theoretische voorspelling en bovendien laten we zien dat logische toestanden in decoherentie-beschermde toestandsruimtes een betere kwantumgeheugen kunnen zijn (Hoofdstuk 5). Uiteindelijk bereiken wij dezelfde kwantumgeheugen stabiliteit met een enkele kernspin (Hoofdstuk 6).

Ten tweede gebruiken wij verstrengeling van twee NVs over een lange afstand om experimentele mijlpaalen in het veld van kwantumnetwerken te laten zien. Een verstrengelde NV-NV toestand van hoge kwaliteit over een afstand van 1.3 km staat de overtreding van Bell’s ongelijkheid toe waarbij alle achterdeurtjes dicht blijven (Hoofdstuk 7). Verder wordt het proces van NV-NV verstrengeling drie ordes van grootte versneld waardoor een verstrengelde toestand op ons netwerk sneller kan worden gemaakt dan dat hij gaat verloren. Hierdoor veranderen wij de probabilistische generatie van verstrengeling in een deterministisch proces dat verstrengelde toestanden op vooraf bepaalde tijden aflevert (Hoofdstuk 8).

Ten slotte worden de principes van kernspin kwantumgeheugen en lange-afstand verstrengeling gecombineerd om verstrengelingsdestillatie op een kwantumnetwerk te laten zien (Hoofdstuk 9). Twee ruwe verstrengelde toestanden tussen twee NVs worden achtereenvolgens gemaakt. De eerste toestand wordt in een kernspin opgeslagen om de NVs voor de tweede verstrengelingsronde beschikbaar te maken. Nadat beide toestanden succesvol gemaakt zijn gebruiken wij uiteindelijk lokale controle om een enkele verstrengelde toestand van hogere kwaliteit te distilleren. Dit destillatie experiment is de eerste demonstratie van een kwantumnetwerk dat is gebouwd op controle over meerdere coherente kwantumsystemen per knooppunt.

KURZDARSTELLUNG

Quantennetzwerke sind eine vielversprechende Zukunftstechnologie mit Aussicht auf unknackbare Verschlüsselungsmethoden und dezentralisierte Quantenberechnungen. Diese Arbeit beschreibt Experimente auf dem Weg zu einem komplexen Quantennetzwerk, wobei jeder Netzwerkknoten mehrere Quantenzustände befassen kann.

Das Stickstoff-Fehlstellen-Zentrum (NV) ist ein magnetisches Farbzentrum in Diamant. Da NV-Zentren Kohärenzzeiten über 100 ms und Relaxationszeiten über 1 s besitzen agieren sie als hervorragende Netzwerkknoten. Die spinselektiven optischen Übergänge des NVs ermöglichen die quantenmechanische Verschränkung des NV spins mit emittierten Photonen. Wird die Emission zweier NVs auf einem Strahlteiler überlappt so wird die “welcher-wegïnformation gelöscht und dadurch zwei Netzwerkknoten mittels Verschränkung verbunden. Neben einzelnen NVs können ^{13}C Kernspins im Kristallgitter des Diamanten als zusätzliche Quantenresource genutzt werden. Techniken um diese Kernspins als robuste Quantenspeicher in einem NV-basierten Netwerk zu nutzen wurden noch nicht erforscht. Der Inhalt dieser Arbeit gliedert sich deshalb in drei Teile.

Zuerst wird das Zusammenspiel von NV und Kernspin erkundet. Kontrolle über mehrere Kernspins wird demonstriert indem zwei logische Qubits im Zustandsraum dreier Kernspins initialisiert und wiederholt projiziert werden (Kapitel 3). Theoretische Analysen zeigen, dass die magnetische Wechselwirkung zwischen NV und Kernspin die nukleare Kohärenz unter voller Netzwerkaktivität limitieren wird (Kapitel 4). Diese Überlegungen werden anhand einer experimentellen Studie bestätigt, wobei logische Zustände genutzt werden um verbesserte Quantenspeicher zu demonstrieren (Kapitel 5). Schließlich werden vergleichbare Ergebnisse mit einzelnen Kernspins erzielt (Kapitel 6).

Als zweites wird NV-NV Verschränkung genutzt um Meilensteine auf dem Weg zum Quantennetzwerk zu demonstrieren. Ein hochqualitativer verschränkter NV-NV Zustand über eine Distanz von 1.3 km erlaubt die schlupflochfreie Verletzung der Bellschen Ungleichung (Kapitel 7). Ausserdem wird die Verschränkungsrate um drei Größenordnungen angehoben und ist damit Größer als die gemessenen Dekohäherenzraten. Dies erlaubt die Wandlung der probabilistischen Verschränkungserzeugung hin zu einem deterministischen Prozess der Verschränkung auf Knopfdruck generiert (Kapitel 8).

Letztendlich werden kernspinbasierte Quantenspeicher mit der Verschränkungserzeugung kombiniert um Verschränkungsdistillation zu demonstrieren (Kapitel 9). Hierzu werden zwei verschränkte Eingangszustände zwischen zwei entfernten NVs erzeugt. Der erste Zustand wird in Kernspinspeichern abgelegt um beide NVs für die zweite Verschränkungsrunde zu befreien. Schlussendlich wird ein verschränkter Zustand von höherer Qualität aus den Eingangszuständen mittels lokaler Operationen distilliert. Dieses Experiment dient als erste Demonstration eines Quantennetzwerks unter Nutzung mehrerer quantenmechanischer Freiheitsgrade per Netzwerkknoten.

1

INTRODUCTION

The theory of Quantum Mechanics (QM) is one of the most accurate and successful frameworks for the description of our world. QM and the more extensive flavours of it, such as quantum field theory, have given us the widely-successful standard model of particle physics. The predictions of these theories are corroborated by measurements of the fine structure constant below the parts per billion level[1,2].

Besides its fundamental relevance, QM has been instrumental for the inception of breakthrough technologies that rely on the QM description of effectively non-interacting particles and have made their way into modern households. For instance QM accurately describes the electronic band structure of semiconductors by simply considering single electrons in periodic potentials thus enabling our modern information age. Non-invasive magnetic resonance imaging techniques (MRI) are likewise key when making diagnoses and grant longevity on a daily basis. The invention of MRI would be improbable without a rigorous understanding of magnetic atomic nuclei and their interaction with radiation in isolation.

In contrast to the successful phenomenological description of our reality, we do not grasp the origin of key aspects, that lie at the heart of QM. Quantum entanglement[3,4] arises from the framework of QM and its experimental observation led in part to the 2012 Nobel Prize in Phyiscs *"for ground-breaking experimental methods that enable measuring and manipulation of individual quantum systems"*. The surge in control over QM systems fostered the ongoing debate on interpretations of QM[5,6].

The success of non-interacting QM systems for applications and the prospect of a deeper fundamental understanding have sparked a plethora of proposals that are purposely designed to show strong interactions with applications and potential fundamental implications in mind. Akin to binary logic in contemporary processing units these systems comprise a number of well-isolated, yet fully controllable, QM systems with a binary level structure – so-called qubits.

The envisioned quantum technologies group naturally into three sectors: computation, simulation and communication; each promising vast advantages over their classical counterpart for certain applications. Early on Deutsch, Shor, Grover and others realized that certain algorithms on QM computers may require far fewer resources (in terms of memory and/or time) than an analogous classical computation[7]. Realizing such a quantum computer would significantly improve our computational power for tasks such as prime factorization and the search in unsorted databases.The simulation of quantum systems with classical means poses exponential challenges since the complex coefficients required to describe a general superposition grows exponentially with the quantum mechanical state space. Therefore using a well-designed quantum system to emulate the behaviour of another QM system of interest is a promising path towards the efficient simulation of quantum systems[8]. Finally, sending quantum states between two communicating parties may allow for the creation of certifiably secure communication channels[9,10]. Depending on the exact implementation these communication channels are either enabled by the Heisenberg uncertainty principle or the monogamy of entanglement[11].

Despite their differing goals, these three technologies can have considerable overlap when it comes to their realization. In particular, an extended quantum network is a promising means of achieving all three[12] while enabling the distribution of many-body quantum states over macroscopic distances to test the limits of QM. A quantum network is a distributed architecture that consists of stationary nodes containing multiple well-controlled qubits. Nodes establish entangling links between each other by using photons as mediators. Photons are a convenient choice since they are easy to transport over large distances, suffer little decoherence and therefore constitute the ideal flying qubit for communication purposes.

Currently quantum networks are still in a proof-of-concept phase. Only point-to-point connections in elementary two-node networks have been realized with various experimental platforms[13–18]. Moreover each node only contained a single qubit for communication purposes and potentially one other degree of freedom in a phase-insensitive eigenstate[19,20]. Quantum memories that sustain their coherence while generating entanglement have so far remained elusive.

We use optically active Nitrogen-vacancy (NV) centres in diamond to push the envelope on state-of-the-art quantum networks by demonstrating network protocols that require the storage of multiple entangled states. The NV centre is an atomic point defect in diamond consisting of a substitutional Nitrogen atom and an adjacent empty lattice site. The NV shows tremendous promise for quantum technologies due to its optical interface, an easily addressable ground-state spin that is paired with long coherence times and in particular the ability to address individual nuclear spins in the vicinity as a quantum resource.

In recent years, many key advancements have propelled NVs to the forefront of experimental quantum network platforms. After the first isolation of single NVs[21], ground-state spin control[22] was demonstrated and has meanwhile been brought into strong-driving regime[23]. Magnetic coupling between the NV electron spin and surrounding ^{13}C nuclear spins[24] was shown to result in an effective multi-qubit register. Advanced register control led to the execution of simple quantum computation protocols such as Grover's algorithm[25] and demonstrations of quantum error correction[26–28]. At cryogenic temperatures spin-photon entanglement was observed[29] and subsequently remote entanglement of two NV electron spins was shown[15]. This culminated in the unconditional teleportation of a state that was initialized after the entangling link was generated[19]. This rapid sequence of breakthrough results underpins the fruitfulness of the NV-based approach to quantum networking.

This thesis demonstrates the marriage of all core concepts for general-purpose quantum networks with NV centres. In particular we provide a deep investigation of surrounding nuclear spins as quantum memories and demonstrate record-high entangling rates between two NVs in spatially-separated diamonds. We further combine these two key concepts to create, store and manipulate two entangled states. From these two states we distill a single entangled state of higher fidelity via local operations[30,31].

Chapter 2 lays out the properties of the NV centre at cryogenic temperatures and provides an overview of our standard control techniques. **Chapter 3** explores the coupling of a single NV centre to the surrounding spin bath. We show initialization and control over three individual nuclear spins, culminating in three-partite parity measurements that invoke the quantum Zeno effect thereby elongating the lifetime of two logical qubits. **Chapter 4** provides a theoretical description of ^{13}C nuclear spins as quantum memories in a diamond-based quantum network. **Chapter 5** subsequently experimentally examines the robustness of five nuclear spins while performing entangling attempts on a close-by NV centre. **Chapter 6** revisits the concept of nuclear spin memories for quantum networks and explores dephasing mechanisms due to experimental control errors. **Chapter 7** validates the notion that quantum networks may result in fundamental insights by generating entanglement between two electron spins at a distance of 1.3 km to demonstrate the loophole-free violation of Bell's inequality. **Chapter 8** demonstrates a single-photon entangling scheme which dramatically increases the entangling rate by three orders of magnitude. We use this improved rate in conjunction with long NV coherence times for the deterministic generation of entanglement at prespecified moments in time. The nuclear spin memories are finally utilized in **Chapter 9** to store remote entangled states and to realize the distillation of entanglement between NV-based multiqubit registers at a distance of 2 meters. **Chapter 10** summarizes the current state of experimental quantum networks in more detail and outlines future challenges as well as experiments in NV-based quantum networks. We further provide clear avenues for experimental improvement.

REFERENCES

[1] D. Hanneke, S. Fogwell and G. Gabrielse, *New Measurement of the Electron Magnetic Moment and the Fine Structure Constant,* Physical Review Letters **100**, 120801 (2008).

[2] T. Aoyama, M. Hayakawa, T. Kinoshita and M. Nio, *Tenth-Order QED Contribution to the Electron g - 2 and an Improved Value of the Fine Structure Constant,* Physical Review Letters **109**, 111807 (2012).

[3] J. S. Bell, *On the Einstein Podolsky Rosen paradox,* Physics **1**, 195 (1964).

[4] S. J. Freedman and J. F. Clauser, *Experimental Test of Local Hidden-Variable Theories,* Physical Review Letters **28**, 938 (1972).

[5] F. Laloë, *Do We Really Understand Quantum Mechanics?* (Cambridge University Press, 2012).

[6] M. Schlosshauer, J. Kofler and A. Zeilinger, *A Snapshot of Foundational Attitudes Toward Quantum Mechanics,* Studies in History and Philosophy of Science Part B: Studies in History and Philosophy of Modern Physics **44**, 222 (2013).

[7] T. D. Ladd *et al.*, *Quantum computers,* Nature **464**, 45 (2010).

[8] R. P. Feynman, *Simulating physics with computers,* International Journal of Theoretical Physics **21**, 467 (1982).

[9] C. H. Bennett and G. Brassard, *Quantum cryptography: Public key distribution and coin tossing,* Proceedings of IEEE International Conference on Computers, Systems and Signal Processing **175**, 8 (1984).

[10] A. K. Ekert, *Quantum cryptography based on Bell's theorem,* Physical Review Letters **67**, 661 (1991).

[11] A. Ekert and R. Renner, *The ultimate physical limits of privacy,* Nature **507**, 443 (2014).

[12] H. J. Kimble, *The quantum internet,* Nature **453**, 1023 (2008).

[13] D. L. Moehring *et al.*, *Entanglement of single-atom quantum bits at a distance,* Nature **449**, 68 (2007).

[14] S. Ritter *et al.*, *An elementary quantum network of single atoms in optical cavities,* Nature **484**, 195 (2012).

[15] H. Bernien *et al.*, *Heralded entanglement between solid-state qubits separated by three metres,* Nature **497**, 86 (2013).

[16] A. Delteil *et al.*, *Generation of heralded entanglement between distant hole spins,* Nature Physics **12**, 218 (2016).

[17] A. Narla *et al.*, *Robust Concurrent Remote Entanglement Between Two Superconducting Qubits,* Physical Review X **6**, 031036 (2016).

[18] R. Stockill *et al.*, *Phase-Tuned Entangled State Generation between Distant Spin Qubits,* Physical Review Letters **119**, 010503 (2017).

[19] W. Pfaff *et al.*, *Unconditional quantum teleportation between distant solid-state quantum bits,* Science **345**, 532 (2014).

[20] D. Hucul *et al.*, *Modular entanglement of atomic qubits using photons and phonons,* Nature Physics **11**, 37 (2015).

[21] A. Gruber *et al.*, *Scanning Confocal Optical Microscopy and Magnetic Resonance on Single Defect Centers,* Science **276**, 2012 (1997).

[22] F. Jelezko, T. Gaebel, I. Popa, A. Gruber and J. Wrachtrup, *Observation of Coherent Oscillations in a Single Electron Spin,* Physical Review Letters **92**, 076401 (2004).

[23] G. D. Fuchs, V. V. Dobrovitski, D. M. Toyli, F. J. Heremans and D. D. Awschalom, *Gigahertz Dynamics of a Strongly Driven Single Quantum Spin,* Science **326**, 1520 (2009).

[24] L. Childress *et al.*, *Coherent Dynamics of Coupled Electron and Nuclear Spin Qubits in Diamond,* Science **314**, 281 (2006).

[25] L. Robledo *et al.*, *High-fidelity projective read-out of a solid-state spin quantum register,* Nature **477**, 574 (2011).

[26] T. H. Taminiau, J. Cramer, T. van der Sar, V. V. Dobrovitski and R. Hanson, *Universal control and error correction in multi-qubit spin registers in diamond,* Nature Nanotechnology **9**, 171 (2014).

[27] G. Waldherr *et al.*, *Quantum error correction in a solid-state hybrid spin register,* Nature **506**, 204 (2014).

[28] J. Cramer *et al.*, *Repeated quantum error correction on a continuously encoded qubit by real-time feedback,* Nature Communications **7**, 11526 (2016).

[29] E. Togan *et al.*, *Quantum entanglement between an optical photon and a solid-state spin qubit,* Nature **466**, 730 (2010).

[30] C. H. Bennett *et al.*, *Purification of Noisy Entanglement and Faithful Teleportation via Noisy Channels,* Physical Review Letters **76**, 722 (1996).

[31] D. Deutsch *et al.*, *Quantum Privacy Amplification and the Security of Quantum Cryptography over Noisy Channels,* Physical Review Letters **77**, 2818 (1996).

2

THEORETICAL DESCRIPTION AND EXPERIMENTAL CONTROL OF SINGLE NV CENTRES

This chapter summarizes the relevant concepts and experimental methods which recurr throughout this thesis. Section 2.1 discusses the level structure of the NV. Typical diamond devices and methods to manipulate NVs are described in Sec. 2.2. Section 2.3 provides experiments to characterize and benchmark the control over ^{13}C nuclear spins in the vicinity of a single NV. Finally, we elaborate on photon-mediated entanglement generation between remote NVs in Sec. 2.4.

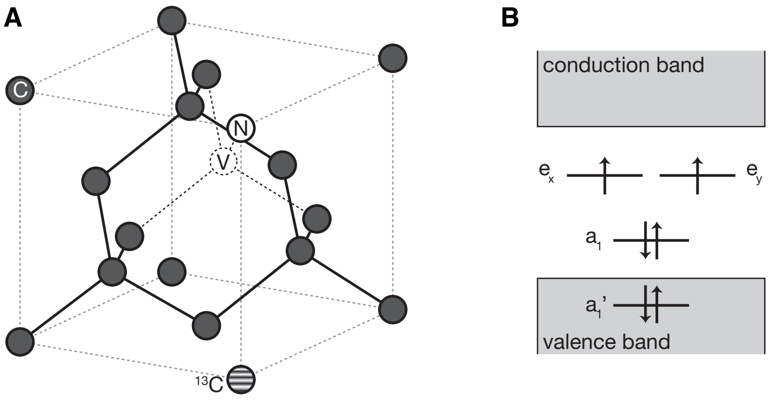

Figure 2.1 | The NV centre in diamond. Adapted from Pfaff, Bernien[3,4]. (**A**) A NV centre in the unit cell of the diamond crystal lattice. NVs are formed by combining a substitutional nitrogen atom (N) with an adjacent vacant lattice site (V). The naturally occuring carbon isotopes are ^{12}C (grey, natural abundance of 98.9%, $I = 0$) and ^{13}C (hatched, natural abundance of 1.1%, $I = \frac{1}{2}$). (**B**) Molecular orbitals of NV^{-}. The electronic ground-state occupancy of the molecular orbitals (labels give their symmetry) follows from Pauli's exclusion principle.

2.1. THE NV CENTRE IN DIAMOND

The diamond carbon lattice is host to a wide range of optically active defects. To date more than 100 colour centres have been observed and a significant fraction of these centres has been studied[1,2]. Throughout this thesis we focus solely on the nitrogen-vacancy (NV) centre, an atomic defect comprised of a substitutional nitrogen atom and an adjacent vacant lattice site (Fig. 2.1A). An optically-active electron spin is associated with the NV. In the neutral charge state NV^0, the electronic wave function is composed of five electrons, two from the nitrogen atom and the other three from the unpaired electrons of the vacancy-neighbouring carbon atoms. In this thesis we focus on the negative charge state NV^{-}, where another electron from the environment, e.g. nearby charge traps, is captured.

The level structure of NV^{-} and NV^0 can be described in terms of molecular orbitals (Fig. 2.1B)[5]. These states are constructed from linear combinations of the dangling sp^3 orbitals associated with the vacancy-neighbouring atoms by considering the $C_{3\mathrm{v}}$ symmetry of the defect[6–8]. Both the ground state and the first optically excited state solely have unoccupied energy levels within the band gap of diamond. This hinders electron loss to the conduction band as well as electron accumulation from the valence band and therefore grants NV^{-} optical properties akin to an individual trapped ion[9]. Considering a combination of spin-spin, spin-orbit interaction and Coulomb repulsion between the six electrons within the centre results in a orbital-singlet spin-triplet ground state that couples optically to a orbital-doublet spin-triplet state (see Fig. 2.2). The excited state can decay to intermediate spin-singlet states. Decay from the singlet states back into the ground-state tripled favours the state with $m_s = 0$ spin projection.

Ground-state spin qubit The ground state spin state $m_s = 0$ is separated from $m_s = \pm 1$ by $D \approx 2.88\,\mathrm{GHz}$ predominantly due to spin-spin interactions[13]. The spin states $m_s = \pm 1$ are susceptible to magnetic fields via the Zeeman effect with a gyromagnetic ratio of $\gamma_e = 2.802\,\mathrm{MHz/G}$ (see Fig. 2.2 bottom right). Resulting in the ground-state spin Hamiltonian

$$H_{\mathrm{GS}}/\hbar = DS_z^2 + \gamma_e(S_x B_x + S_y B_y + S_z B_z) \tag{2.1}$$

with the spin-1-matrices S_i. Experiments in all chapters use the ground-state spin states as a qubit ($|0\rangle \equiv m_s = 0$ and $|1\rangle \equiv m_s = -1$ or $m_s = +1$). The required individual addressability is obtained by applying a magnetic field of $\approx 415\,\mathrm{G}$ (Chapter 7 uses $\approx 36\,\mathrm{G}$) aligned with the NV crystal axis (z-axis of the chosen coordinate system).

2.2. DEVICE CAPABILITIES

This section describes the diamond chips we use and gives benchmark numbers for the NV centre control in such devices, such as optical read-out fidelities and typical coherence times.

2.2.1. DEVICE FABRICATION AND SETUP

All experiments in this thesis are performed on single NV centres that occur naturally in CVD-grown ultra-pure type IIa diamonds, which are grown along the ⟨100⟩ crystal orientation. Post-growth, samples are cut along the ⟨111⟩ crystal direction. New samples are grown and shipped by Element Six Innovation and run through a standardized in-house fabrication procedure.

After an initial boiling triacid (equal parts of perchloric, sulfuric and nitric acid) clean, we use electron-beam lithography to define a gold microwave stripline and a coordinate grid on the diamond surface. This grid allows us to uniquely identify and reproducibly find NV centres in the sample via confocal excitation with green light and collection of the NV-emission into the PSB (Fig. 2.2). Upon finding an NV we perform a characterization routine at room temperature as follows. We select NVs with a ⟨111⟩ crystal orientation by polarization extinction measurements of their luminescence. We further investigate the direct nuclear spin environment via optically detected magnetic resonance[14]. We exclude NV centres that couple to one or multiple ^{13}C nuclear spins with a coupling strength exceeding $\sim 1\,\mathrm{MHz}$.

We next define a hemispherical solid immersion lens (SIL) around the position of each characterized NV by diamond milling with a focused gallium ion beam[15,16]. All rays emitted from the centroid of an etched hemisphere have a normal angle of incidence with respect to the surface such that no refraction and total internal reflection occurs. SILs therefore dramatically improve the collection efficiency and enhance the signal to

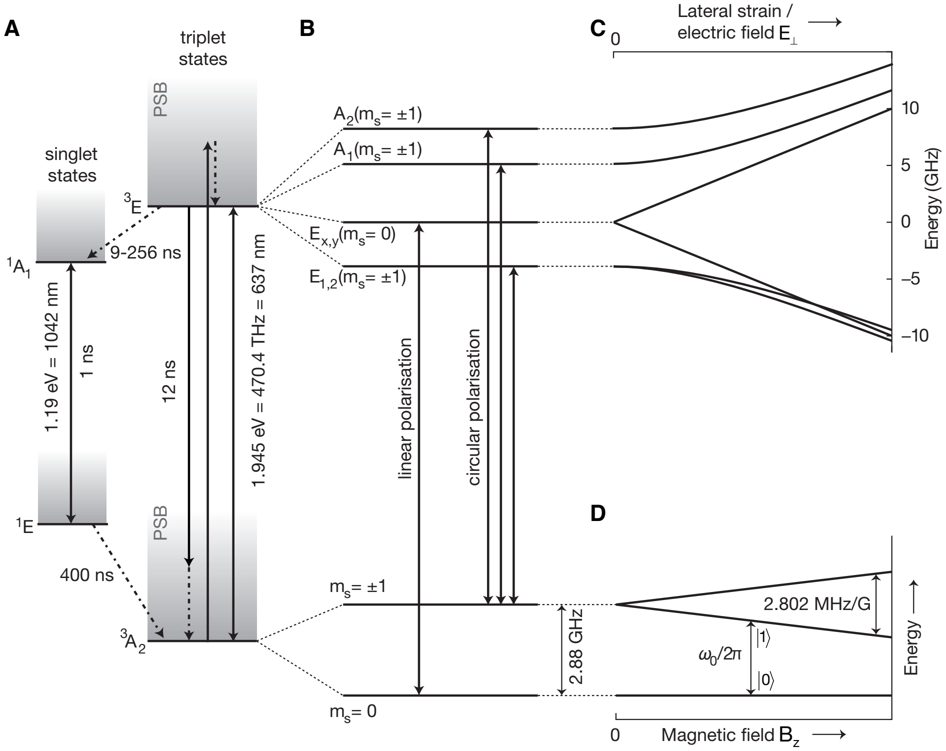

Figure 2.2 | Electronic structure of the negatively-charged NV centre. Adapted from Pfaff, Bernien[3,4]. **(A)**: Excitation and emission within the spin-triplet manifold $^3A_2 \leftrightarrow ^3E$ can occur resonantly, i.e. without emission of additional phonons (Zero-phonon-line; ZPL), and off-resonantly via the respective phonon sideband (PSB; dotted-dashed arrows). Durations indicate decay times in the low-temperature-low-strain regime ($T \approx 4\,\mathrm{K}$ and $E_\perp < 3\,\mathrm{GHz}$). ^3E also has state-dependent decay channels to the spin-singlet level $^1A_1$ and therefore varying decay rates ($9 - 256\,\mathrm{ns}$; Ref.[10]). **(B)**: The ground state spin states of $^3A_2$ are split into two levels, one with double degeneracy ($m_s = \pm 1$). The excited state ^3E is split into four energy levels by spin-spin and spin-orbit interactions. The two lower lying levels are doubly degenerate ($E_{x,y}$ and $E_{1,2}$). The fine structure of ^3E is only observed at cryogenic temperatures. Optical transitions from the ground to the excited state are spin selective (spin state in brackets) and obey selection rules. The excitation dipole lies in the orthogonal plane w.r.t. the NV crystal axis. **(C)** The energy eigenvalues within ^3E depend on the applied lateral strain and/or electric field. Both have the same effect up to first order[11,12]. In comparison the ground state experiences weak shifts with strain and electric field[6]. **(D)**: A magnetic field along the NV crystal axis can be applied to lift the degeneracy of $m_s = +1$ and $m_s = -1$. This guarantees individual addressability and allows for the definition of a qubit within the ground state triplet $^3A_2$ ($|0\rangle/|1\rangle$).

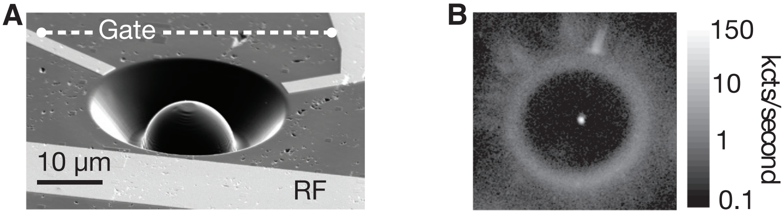

Figure 2.3 | Diamond device characteristics. Figure adapted from Pfaff, Bernien[3,4]. (**A**) Scanning-electron micrograph of the sample surface. A NV centre is located in a hemispherical SIL (centre). We additionally fabricate a gold stripline (RF) to deliver radio-frequency pulses and gold electrodes (Gate) for DC Stark tuning of optical transition frequencies. (**B**) Confocal microscope scan of a SIL with green excitation ($\lambda = 532\,\mathrm{nm}$). Detected fluorescence is frequency-filtered to collect the PSB of the NV ($\lambda > 637\,\mathrm{nm}$). We observe the contour of the milled hemisphere and the strong fluorescence signal from the NV at the central position. The unit kcts/second gives the detected photons (in thousands) per second.

noise ratio. Note that the milled volume increases with NV depth which in turn lengthens the duration of the milling process. We only consider NVs up to a limited depth ($\sim 21\,\mu$m) to ensure a reasonable milling duration on the order of hours to mitigate undesired drifts during milling.

Marker grid, stripline and material, which was redeposited during the milling, is removed with another boiling triacid clean. Afterwards a short oxygen plasma is applied to perform a reactive-ion etch of the top layer ($\sim 30\,\mathrm{nm}$) and cleanse the diamond from residual Gallium contamination. A gold stripline for radio-frequency signals and gold electrodes for DC Stark-tuning[11,12] of the NV excited state are defined in another lithography step (thickness 200 nm; see Fig. 2.3A). We finally grow a Al_2O_3 anti-reflection coating (ideal thickness for $\lambda = 637\,\mathrm{nm}$: $\sim 90\,\mathrm{nm}$) via atomic layer deposition[17]. This coating provides improved photon collection efficiencies and significantly enhances the signal-to-noise ratio when resonantly exciting with 637 nm light.

The surface conductors are connected to a PCB by standard wire bonding to facilitate the delivery of on-chip signals. The PCB including sample is then mounted in a home-built confocal microscope that allows for cryogenic sample temperatures. A detailed description of our microscope configuration is given in Refs. 4, 18. Figure 2.4 depicts an overview of all major signal generators and control units that allow us to perform the experiments of the following sections and chapters. Detection of ZPL photons requires the filtering of excitation light at the same frequency. We use a cross-polarized light configuration which rejects any resonant excitation via a polarizer (Semrock PBP01-639/21). We additionally insert a tunable bandpass filter (Semrock TBP01-700/13) to suppress the detection of PSB photons that were sent into the ZPL path.

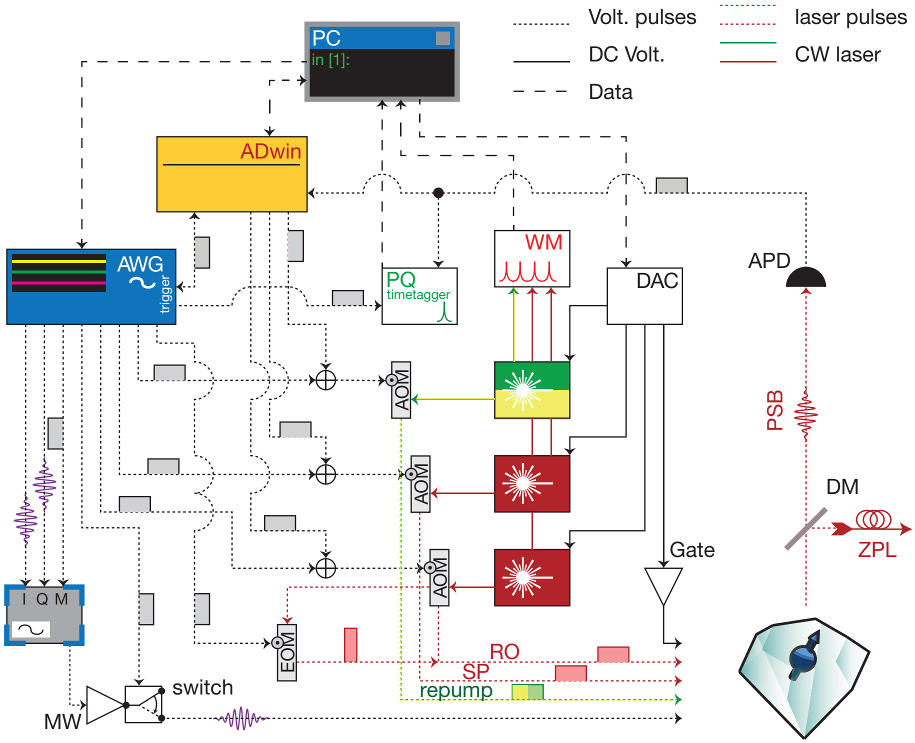

Figure 2.4 | **Schematic of the control logic for our NV experiments**. Figure adapted from Hensen[18]. A PC programs the overarching control loop on a microcontroller (Jaeger ADwin Pro II) and pulse sequences with nanosecond resolution onto an arbitrary waveform generator (Tektronix AWG5014C). The AWG is triggered by the ADwin to start the pulse sequences. The AWG sends trigger (M) and modulated voltage pulses (I and Q) to the inputs of a microwave source (Rhode and Schwarz SMBV100A or SGS100) to synthesize AC current signals with arbitrary phase. These pulses are subsequently amplified (Amplifier Research 40S1G4) with a downstream AWG-controlled switch on a home-built PCB (Triquint TGS2355-SM or Hittite HMC544) to isolate the NV from amplifier noise while idling (used in Chapters 3,8). ADwin DAC voltages and AWG voltage pulses are combined on a home-built voltage combiner and sent to acousto-optic modulators (AOM, Gooch and Housego) to synthesize laser pulses with rise times of ~ 20ns. The AWG additionally controls an electro-optic amplitude modulator (EOM, Jenoptik) to generate short (~ 2 ns) optical pulses. We typically use three light sources (Toptica for 637 nm and 575 nm, Newfocus for 637 nm and Coherent for 532 nm) for different tasks (repump, RO, SP, see following sections). The laser frequency is monitored via a wavemeter (WM, HighFinesse WS6 or WSU) and long-term stabilized via a PC controlled feedback loop that accesses DAC channels (ADwin or Labjack) which are fed into the laser control. One DAC channel is fed into a home-built DC amplifier and delivered to the gate electrodes on the sample to shift the NV emission frequency (Fig. 2.3). The NV emission is spectrally split into phonon-sideband (PSB) and zero-phonon line (ZPL) by a dichroic mirror (DM; Semrock L2NL-0016; custom made razor edge at 637 nm). Avalanche photo diodes (APD; Laser Components Count or Picoquant τ-spad) detect NV fluorescence which is subsequently recorded by the ADwin for counting purposes and a time-to-digital converter (PicoQuant TimeHarp 260N or HydraHarp 400) which is synchronized with the AWG sequence for time resolved measurements.

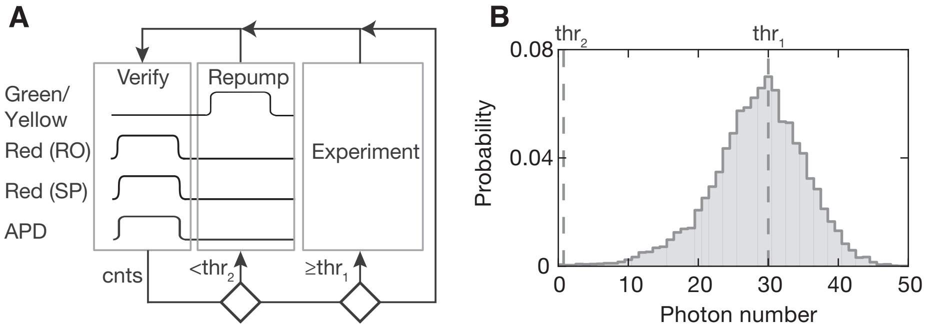

Figure 2.5 | Verification of optimal charge and resonance conditions. Figure adapted from Hensen[18]. (**A**) Logical sequence. We count the number of photons while resonantly exciting the NV centre in a dark-state-free laser configuration (RO and SP). The charge state is reinitialized if the detected number of photons is below thr_2 (Repump). The experimental sequence is started if the number of detected photons surpasses thr_1. The verification step is repeated if none of these two conditions apply and after completion of any other logical step. (**B**) Typical probability distribution of detected photons during the verification period in case all lasers are on resonance. We additionally indicate the thresholds for the start of the experimental sequence ($\mathrm{thr}_1 = 30$) and for charge-state initialization with a yellow laser ($\mathrm{thr}_2 = 1$). Note that in this case we only apply the yellow repumping pulse if no photons were detected to initiate the charge reinitialization only if necessary.

2.2.2. OPTICAL ADDRESSING

In the following, we describe optical control techniques. Most of these techniques were originally developed for the state manipulation of trapped ions[9] and have been adapted to suit the specifics of the NV system.

CHARGE AND RESONANCE VERIFICATION

In order to repeatedly and reliably address individual NV centres with resonant laser light one has to overcome two hurdles. First verification that the defect is in the desired charge-state: NV^-. NV^- is converted to NV^0 by a two-photon absorption process that occasionally occurs during experimental trials[19]. Methods to reset the charge state are essential to increase the experimental repetition rate. Second, the local charge environment of the defect fluctuates and in turn modifies the optical transition frequencies of the defect (see Fig. 2.2 top-right). This may lead to fluctuating resonance conditions which is particularly detrimental for the generation of remote NV-NV entanglement as it requires indistinguishable emission from both emitters[20].

A signature that satisfies both requirements can be obtained by exciting the NV with a combination of laser fields tuned to the expected resonance frequencies and counting the amount of detected fluorescence photons in the PSB (Fig. 2.5). Importantly the laser linewidths are far below the lifetime-limited linewidth of the NV centre and intensities far below saturation power have to be used. This ensures maximum sensitivity with respect to spectral diffusion. Collecting a sufficient amount of photons for verification is short (~ 50 μs) when compared to typical timescales of slow spectral diffusion for unilluminated samples (minutes or larger[21]). Choosing the laser frequencies such that no dark state occurs (each state of the ground state triplet is independently coupled to an optically excited state) gives a strongly elevated fluorescence signal (Fig. 2.6A). We proceed to the experimental sequence if the number of detected photons surpasses a predefined threshold that is chosen according to the calibrated photon distribution if all light fields are resonant (Fig. 2.5B).

Two strategies are used throughout this thesis to ensure that the NV remains in NV^- and spectral diffusion is counteracted efficiently. The use of intense (tens of μW in front of the microscope objective) and short (tens of μs) green laser pulses — $\lambda = 532$ nm — accomplishes two things. First, the probability of finding the defect afterwards in NV^- is about 75 %[19]. Second, intense green illumination reconfigures the charge environment of the NV and therefore broadens the optical transitions of the NV inhomogeneously[22]. The verification procedure then selects optical configurations that are close to optimal. This technique is simple to implement since no feedback on the emission frequency is required.

While this technique is simple to implement, there are indications that the excessive use of green light also induces slowly-decaying dynamics in the charge environment which spectrally broaden the NV emission and therefore hamper the fidelity of remote entangled states[4]. Furthermore, DC stark tuning of optical transition frequencies is less effective in this configuration due to screening effects which in turn requires fast switching of the applied DC voltages[18,20].

Alternatively, we use a weak (tens of nW) and long (300 μs) yellow ($\lambda \approx 575$ nm) laser pulse that accomplishes the charge reinitialization by resonant excitation of NV^0. This technique allows for deterministic charge state initialization and improved spectral properties of the emission[23]. While this technique largely eliminates inhomogenoeus broadening of the NV emission, the required experimental control to keep the system on resonance is increased. In particular we use PID feedback loops to tune the frequencies of the applied lasers as well as the applied DC voltage for stark-shifting which allows us to mitigate small-amplitude spectral diffusion[18].

Occasionally the optical transitions of the NV undergo a rapid change such that all resonant fluorescence signal is lost, we then employ wide-frequency-range (~ 200 MHz) automated search algorithms to bring the system back on resonance[24]. The frequency and magnitude of these disruptions appear to vary for each NV centre. We hypothesize that these jumps in frequency stem from the discrete population dynamics of nearby charge traps that alter the electric field at the position of the NV dramatically due to their vicinity.

INITIALIZATION

We use the spin selective optical interface of NV^- for high-fidelity initialization (infidelity below 0.3 %[25]) and QND read-out. Both tasks are implemented by using light at two different frequencies that individually addresses optical transitions with the most favourable properties for the desired task (Fig. 2.6A).

For initialization we use a resonant beam that couples the two $|m_s| = 1$ ground states to the optically excited states $E_{1,2}$ (used throughout all experimental chapters) or alternatively to the individual states - or combinations of - $A_{1,2}$ (see Ch. 5). The poor cyclicity of these optically excited states allows for rapid pumping of the spin state into $m_s = 0$ with a high-fidelity. Using the transitions to $E_{1,2}$ is favourable as only a single light field is required: irrespective of the applied magnetic field, both ground and excited states are subject to the same Zeeman shift. The states $A_{1,2}$ experience a lower Zeeman shift which requires multiple independent light fields for electron spin reinitialization in moderate magnetic. Such laser configurations can be obtained by either using two independent light-sources or by using a frequency-modulated individual laser beam. Note that in the latter case coherent dark states in the ground-state may form which requires fast phase scrambling of the frequency modulation to achieve rapid spin pumping.

OPTICAL READ-OUT

In contrast to initialization, single-shot read-out (SSRO) relies on closed-cycle spin-dependent optical transitions. In the low-strain regime ($E_\perp < 3\,\mathrm{GHz}$) the two excited states $E_{x,y}$ provide a low spin-flip probability per excitation of $\sim 0.5\,\%$ and therefore excellent cycling behaviour to obtain high-fidelity SSRO (average fidelity $F \approx 90\,\% - 97\,\%$)[18]. In this regime spin-flips occur in the optical cycle due to finite coupling to the singlet states and therefore limit the maximum readout fidelity. At larger strain-induced shifts E_y becomes non-cycling due to a level anti-crossing with the states $E_{1,2}$ and we therefore solely rely on resonantly exciting E_x in this regime. The readout fidelity of the chosen dark qubit state $|1\rangle$ is limited by detector dark counts and off-resonant excitation.

Note that choosing E_x as optical readout transition can become unsuitable at elevated lateral strain and low magnetic fields since the excitation frequency becomes degenerate with the transition of the $|m_s| = 1$ ground states to A_1. Figure 2.6B shows the calculated transition frequencies for $\omega_0 : m_s = 0 \rightarrow E_x$ and $\omega_\pm : m_s = \pm 1 \rightarrow A_1$ at a magnetic field of 400 G along the NV crystal axis. Since the ground-state spin states and A_1 experience different Zeeman shifts, we are able to choose the qubit encoding such that non-degenerate excitation frequencies are obtained. This enables the use of NVs in the high-strain regime for our quantum network protocols (see Chapters 9,8).

The frequency overlap of E_x and A_1 is probed by initializing the electron spin into all combinations of ground-state spin levels and recording the detected fluorescence during readout. Figure 2.6C shows a characteristic example for the obtained readout fidelities. The data for 0 (± 1) are obtained by optically pumping the NV on the $E_{1,2}$ (E_x) transition into the state $m_s = 0$ (a mixture of $m_s = \pm 1$). We additionally probe the ± 1 states individually by pumping into $m_s = 0$ and applying a microwave π-pulse (estimated infidelity $< 1\%$; see Sec. 2.2.3). For the lateral strain configuration of this particular NV centre, initialization into $m_s = -1$ yields a significantly better average read-out fidelity

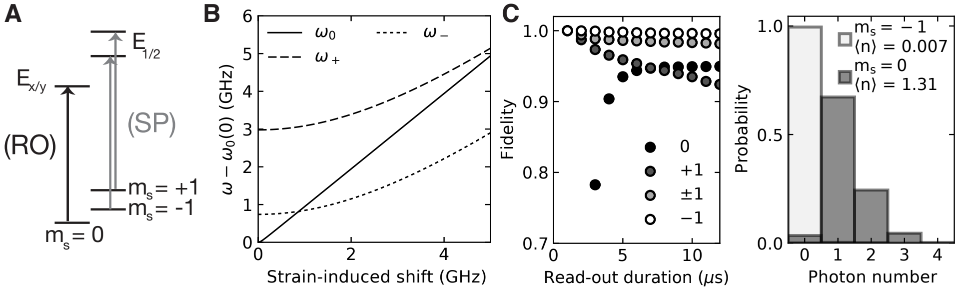

Figure 2.6 | Ground-state qubit selection via single-shot read-out. (**A**) Relevant level scheme of the NV centre including optical transitions for read-out (RO), transitions for optical spin pumping (SP). (**B**) Excitation frequencies ω_0 and $\omega_\pm$ in a magnetic field of 400 G calculated as a function of the strain-induced frequency shift of ω_0[6]. The magnetic-field-induced splitting of the excitation frequencies $\omega_\pm$ allows us to find a suitable ground-state qubit definition in a wide strain regime. (**C**) Left: Calibrating optical single-shot readout of the NV for four different types of state initialization allows for the identification of the current strain regime and the desired qubit definition. Typical values for the average readout fidelity, i.e. the probability to detect at least one photon for $m_s = 0$ and no photons for the best dark-state configuration, are sample dependent and range from 0.9 to 0.97. We typically observe optimal fidelities for read-out durations of $\sim 10\,\mu$s. Right: Photon number histogram for the best state configuration. We turn the excitation light off as soon as one photon has been detected during one individual readout run.

than $m_s = +1$ and we therefore choose $|1\rangle \equiv m_s = -1$. This configuration guarantees a large spectral separation of the optical excitation frequencies. A crucial requirement when using short optical pulses to generate spin-photon entanglement (see Sec. 2.4). Besides finding the optimal qubit definition of the ground-state, an accurate determination of the readout fidelities is also key when renormalizing the measured statistics to obtain the underlying spin state of any subsequently shown measurement[3].

2.2.3. Ground-state spin manipulation and coherence

Electron spin manipulation

We realize arbitrary single-qubit rotations of the electron spin via AC current pulses. The frequency of the AC signal is tuned on resonance with the energy splitting of the chosen ground state qubit transition. These pulses are delivered to the NV via the on-chip stripline (see Sec. 2.2.1) and generate an oscillating magnetic field that induces transitions between the ground-state spin states. Specific rotation angles such as $\pi/2$ and π are calibrated by variation of pulse duration and amplitude.

The electronic spin interacts with surrounding nuclear spins via the magnetic hyperfine interaction. The surrounding ^{13}C nuclear spin bath creates a slowly fluctuating magnetic field at the position of the NV spin with a typical spectral width of $\sim$ 100 kHz in samples of natural isotopic abundance. Apart from the surrounding spin bath, the NV most prominently interacts with the nuclear spin of the host nitrogen atom, which has been used as a quantum resource in many pioneering experiments[23,26–29].

In this thesis, experiments are not carried out on the nitrogen spin. The large interaction strength with the electron spin ($\approx 2\,\mathrm{MHz}$ for $^{14}\mathrm{N}$ with $I = 1$) makes the nitrogen spin an unsuitable quantum memory under optical excitation of the NV (Chapters 4,5). The nitrogen spin is typically seen as a hinderance to high-fidelity addressing of the NV since the NV ground-state transitions experience a nitrogen-state-dependent frequency shift. We realize high control fidelities of the electron spin by measurement-based initialization of the nitrogen spin state (Ch. 3, see also Ref. 3) or by applying strong driving fields[30] with Rabi frequencies $\gtrsim 10\,\mathrm{MHz}$. In the latter case, we additionally use amplitude-shaped Hermite pulses[31] (see Chapters 5,9,8) to decrease the frequency selectivity and therefore improve the robustness of our operations with respect to the spectral broadening of the nitrogen nuclear spin. A detailed description of methods to utilize the nitrogen nuclear spin as additional quantum resource can be found in Refs. 3,32.

LONGITUDINAL RELAXATION TIME

We now turn to the description of coherence times of the NV spin state. Longitudinal relaxation (T_1) mainly occurs due to two reasons. First, extrinsic control fields do not exert the required extinction ratio such that there is a finite probabilistic interaction with the control field at all times. Second, sample-intrinsic relaxation occurs due to two-phonon Orbach processes (scaling with $\propto T^5$ and therefore negligible at 4 K) or energy-conserving cross-relaxation with other NVs in the vicinity[33]. Both sample-intrinsic relaxation mechanisms impose no verified hard limit on T_1 for single NV centres in CVD-grown low-NV-density diamonds at cryogenic temperatures. In principle, this allows for hour long relaxation times, given that extrinsic control fields can be switched off with a high extinction ratio[21].

We use an additional microwave switch that rejects incident current noise injected by the radio-frequency amplifier during idling in Chapters 3,8. In combination with a double-pass AOM configuration that provides high on/off ratios for the switching of our laser fields, we achieve longitudinal relaxation times of several seconds. Without a microwave switch we obtain typical relaxation times of 300 ms which suffice for the experiments in Chapters 7,5,9.

NV ELECTRON SPIN COHERENCE TIME

Superpositions of NV spin states experience a free-induction decay (T_2^*) of $\sim 1-10\,\mu\mathrm{s}$, induced by the interaction with the surrounding nuclear spin bath. Dynamical decoupling, i.e. repetitive application of regularly-spaced inversion pulses, provides an avenue to extend the coherence time (T_2) by orders of magnitude as it mitigates quasi-static magnetic field fluctuations[34].

Figure 2.7 shows the fidelity of an NV superposition state as a function of evolution time and a varying number of inversion pulses. For the shown data we choose the inter-pulse

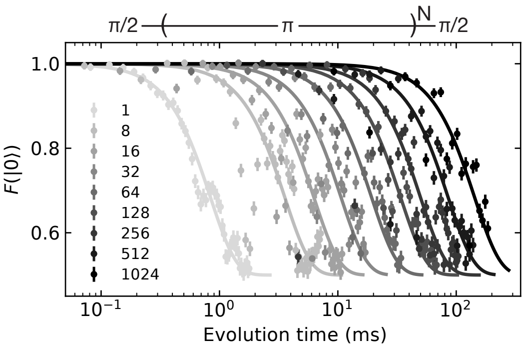

Figure 2.7 | Ground-state coherence time T_2. Top: We apply N inversion pulses in total while the NV is in a superposition state. The phase of the decoupling sequence follows the XY8 scheme to mitigate pulse infidelities[34]. A final $\pi/2$-pulse brings the NV ideally into the state $|0\rangle$. Bottom: T_2 increases with the number of applied inversion pulses (see legend). In the shown example, up to 1024 inversion pulses are applied resulting in a maximum coherence time of 142(9) ms when fitting Gaussian decay curves. Note that this could be extended even further by using more inversion pulses[21].

delay such that it corresponds to an integer multiple of the bare Larmor period associated with the ^{13}C spin bath (for $\gamma_{13C} = 1.0705\,\text{kHz/G}$ and $B \sim 400\,\text{G}$ we obtain typical Larmor periods of $\sim 2.3\,\mu$s). Narrow collapses of the state fidelity suggest that the NV is resonantly decoupled with the dynamics of other magnetic impurities or clusters of ^{13}C spins and therefore shows strong interaction with these entities[35]. Such interactions and therefore coherence collapses are NV specific and have to be characterized for each individual NV centre when trying to obtain long phase coherence times (see also Chapter 8).

Note that alternatively isotopically purified samples can be used to obtain long coherence times (up to 0.5 s measured in ensembles) for a smaller number of inversion pulses[36,37]. Samples with a natural carbon composition have however the advantage of providing several accessible nuclear spins as additional quantum resources for multi-qubit experiments.

2.3. ADDRESSING AND CONTROLLING ^{13}C NUCLEAR SPINS

Throughout the previous section, surrounding nuclear spins have been considered a nuisance that inhibits long NV coherence times. Tailored dynamical decoupling sequences however allow for individual addressing of the unique nuclear spin configuration of each NV centre. Here we focus on a practical description of the employed techniques to characterize and control nuclear spins around an NV centre. These methods have been pioneered in 2012 (Refs. 38–40) and have been fully developed into universal control methods by Taminiau et al.[41]. An extensive description is also found in Ref. 42.

CHARACTERIZING THE NUCLEAR SPIN BATH

The resonance frequencies of ^{13}C spins and the NV spin differ vastly in a magnetic field of $B \sim 400\,\mathrm{G}$ such that we describe the Hamiltonian of the dipolar coupling in secular approximation (here for a single ^{13}C spin) and a frame that rotates with the energy splitting of the NV qubit states

$$H/\hbar = |0\rangle\langle 0|H_0 + |1\rangle\langle 1|H_1 \quad \text{with} \quad H_0 = \omega_L I_z \quad H_1 = (\omega_L \pm A_\parallel) I_z + A_\perp I_x. \tag{2.2}$$

The Hamiltonian effectively results in an NV-state-dependent shift ($|0\rangle$ or $|1\rangle$) of the nuclear precession frequency and tilt of the nuclear quantization axis according to the position-dependent hyperfine parameters $A_\parallel, A_\perp$. The relative sign of $A_\parallel$ depends on the chosen definition of the NV qubit state $|1\rangle$ ($m_s = \pm 1$). I_i are the Pauli spin matrices of the nuclear spin and $\omega_L = \gamma_{13\mathrm{C}} B$ is the nuclear Larmor frequency.

Our decoupling sequences are composed of the primitive unit $(\tau - \pi - 2\tau - \pi - \tau)$ which gives nuclear spin evolution operators V_0 (V_1) for the NV being initially in $|0\rangle$ ($|1\rangle$)

$$V_0 = e^{-iH_0\tau} e^{-iH_1 2\tau} e^{-iH_0\tau} \quad V_1 = e^{-iH_1\tau} e^{-iH_0 2\tau} e^{-iH_1\tau}. \tag{2.3}$$

These two operators constitute antiparallel rotations of the nuclear spin if τ is chosen to be resonant with the electron-nuclear dynamics: $\tau_k \approx \frac{(2k-1)\pi}{2\omega_L + A_\parallel}$ for the large field regime $\omega_L \gg A_\perp, A_\parallel$ and the resonance order $k \in \mathbb{N}_{>0}$. The nuclear environment is probed by sweeping the inter-pulse delay 2τ. To this end, we initialize the NV in a balanced superposition, perform $N/2$ decoupling primitives and read the NV out after a final $\pi/2$ pulse. The electron-state dependent rotation of the nuclear spin entangles both particles on resonance. These resonances are observed as τ-periodic collapses of NV coherence (Fig. 2.8).

Considering a single nuclear spin j, the probability to recover the initial NV superposition state after the decoupling sequence is given by[39]

$$(M_j + 1)/2 = \left(\mathrm{Re}\left[\mathrm{Tr}\left[V_{0,j}^{N/2} (V_{1,j}^{N/2})^\dagger\right]\right] + 1\right)/2. \tag{2.4}$$

Under the assumption that nuclear-nuclear interactions are slow the response M of the entire spin bath is obtained by multiplying the individual response functions of all nuclear spins M_j. These functions are then used to identify individual nuclear spins in the measured dynamical decoupling spectroscopy by choosing hyperfine parameters that reproduce the measured signal. In the data of Fig. 2.8 we find seven ^{13}C spins that are addressable (i.e. have well resolved resonances) in either qubit configuration of the NV.

CONTROLLING NUCLEAR SPINS

Control over a nuclear spin is exerted by decoupling the electron at a resonant inter-pulse delay to synthesize arbitrary rotations in the equatorial plane of the nuclear Bloch sphere $R_\phi(\pm\theta) = \exp[\mp i(\cos\phi I_x + \sin\phi I_y)\cdot\theta]$. Note that the sign of the rotation angle θ is given by the initial electron spin state. Phase control, i.e. rotations around I_z and

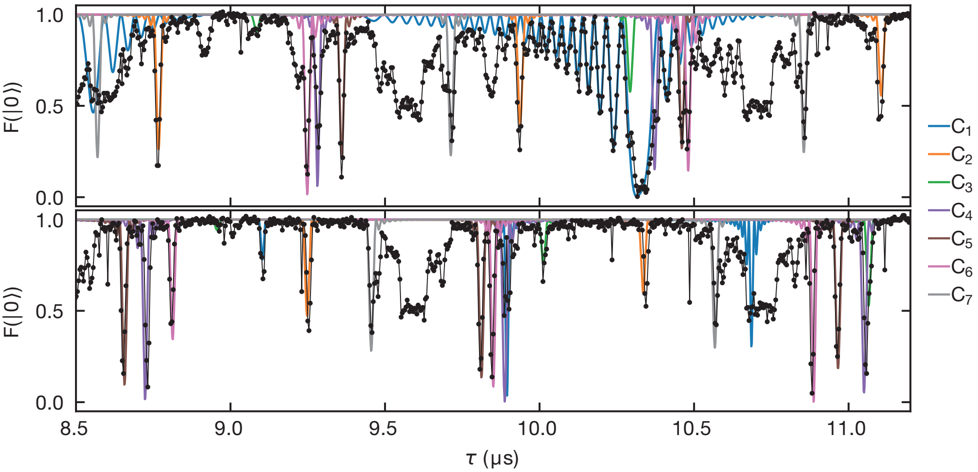

Figure 2.8 | Characterizing the nuclear-spin environment. Top (bottom) panel depicts the measured electron coherence on the transition $m_s = 0 \rightarrow m_s = +1$ ($m_s = -1$) as a function of the inter-pulse delay τ for a total of 64 inversion pulses. Seven nuclear spins (coloured lines derived from Eq. (2.4)) were identified and subsequently controlled for this particular NV. We only consider the interaction with individual nuclear spins such that the electron spins response may differ from the simulation where resonances overlap.

therefore control over ϕ, is realized by idling the electron spin in a known state such that the nuclear spin experiences a precession according to H_0 or H_1. We determine these electron-state-dependent precession frequencies in calibration measurements with relative accuracies of 10^{-6}.

Phase-control is alternatively obtained by decoupling of the electro with short ($\tau < \pi/\omega_L$) inter-pulse delays that are off-resonant to all ^{13}C nuclear spins. This evolves the target nuclear spin independently of the electron spin state. This type of phase control is critical for sequential multi-partite nuclear spin measurements (Ch. 3) and the preservation of NV coherence because idle electron spins decohere rapidly. Optionally the inter-pulse delay is extended to be commensurate with the Larmor period ($\tau_m = m \cdot 2\pi/\omega_L$, $m \in \mathbb{N}_{>0}$) which might be beneficial if critical feedback operations are being computed by the ADwin microcontroller (Chapter 9).

Nuclear spin states are initialized and readout by generating electron-nuclear spin entanglement and subsequent readout of the electron spin state which is now correlated with the nuclear spin. Ideally the entangling gate fulfills the following conditions for optimal performance:

1. The electron spin solely interacts with the addressed nuclear spin and leaves other nuclear spins unperturbed.

2. The electron-state dependent nuclear rotation creates a maximally entangled state,

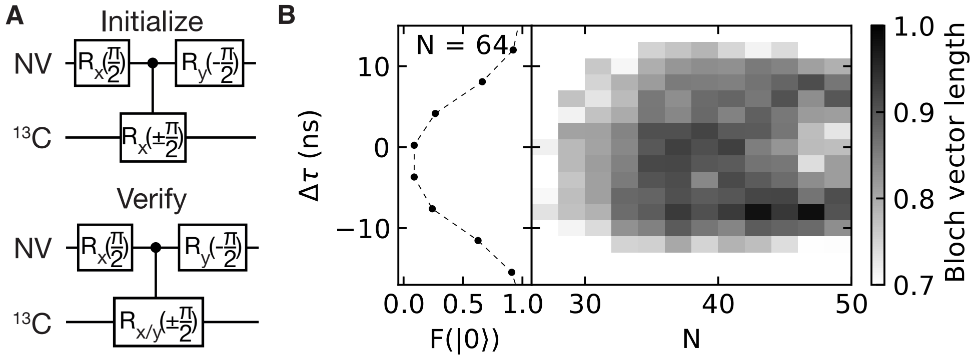

Figure 2.9 | **Nuclear-spin-gate optimization**. (**A**) Quantum gate sequence performed to initialize (top) and verify (bottom) the equatorial Bloch vector length $\sqrt{\langle\sigma_x\rangle^2+\langle\sigma_y\rangle^2}$ of the nuclear spin state with the Pauli spin matrices σ_i. Each sequence block is followed by optical readout of the NV. (**B**) Experimental results. Left panel: Shape of the nuclear spin resonance. Detected by dynamical decoupling spectroscopy with 64 inversion pulses (see Fig. 2.8). Dashed line serves as guide to the eye. Right panel: Measured equatorial Bloch vector length (gray scale) as a function of inversion pulses N and detuning from resonance $\Delta\tau$. We find optimal measurement-based initialization and read-out for a slight detuning $\Delta\tau \approx -8$ns and 42 or 48 inversion pulses (measured Bloch vector lengths ~ 0.97). All data with a measured Bloch vector length below 0.7 are represented as blank space.

i.e. $\pm\theta = \pm\frac{\pi}{2}$ and the electron spin is initialized into $(|0\rangle+|1\rangle)/\sqrt{2}$ with negligible error.

3. The gate duration is as short as possible to mitigate unwanted interaction with the remote spin bath and minimize the duration of multi-qubit algorithms.

Figure 2.9A depicts our symmetric two-step protocol to optimize the gate parameters for entanglement based readout and initialization. The NV is initially prepared in state $|0\rangle$ and the nuclear spin is assumed to be in a mixed state of $|\pm X\rangle \equiv (|\uparrow\rangle \pm |\downarrow\rangle)/\sqrt{2}$. After the initial gate sequence we ideally obtain a combined electron-nuclear state of

$$(|0\rangle\langle 0| \otimes |+X\rangle\langle +X| + |1\rangle\langle 1| \otimes |-X\rangle\langle -X|)/2.$$

Measuring the electron in $|0\rangle$ therefore initializes the nuclear spin in $|+X\rangle$. This sequence is then executed a second time to confirm the successful initialization of the nuclear spin. Unknown systematic offsets in the expected nuclear spin phase after such a gate sequence are overcome by measuring the Bloch vector length in the equatorial plane of the Bloch sphere $\sqrt{\langle I_x\rangle^2+\langle I_y\rangle^2}$.

We optimize the nuclear spin control for a resonance by sweeping the number of inversion pulses and the inter-pulse delay around the resonance (Fig. 2.9B). Performing the optimization protocol on several decoupling resonances allows for an ideal state initialization fidelity. For the discussed NV with seven nuclear spins, all initialization fidelities were measured within $0.9 < F < 0.98$. Residual errors on the order of 1 % may arise during the NV measurement from dark counts, spin flips during the last optical cycle and off-resonant excitation. The remaining infidelity arises from unwanted electron-nuclear interactions for the chosen inter-pulse delay, microwave pulse infidelities and nuclear dephasing due to nuclear-nuclear hyperfine interaction.

Note that this protocol specifically addresses a combination of the first two requirements of the prior list. Faster nuclear spin gates are obtained by selecting resonances with short inter-pulse delay under the condition that they perform well in this optimization protocol. Finally, the ideal choice of gate parameters should take the targeted experiment and therefore the gate sequence as well as coherence times of all utilized quantum systems into account.

2.4. GENERATING REMOTE ENTANGLEMENT

The spin-selective optical interface of NV$^-$ can be used to establish remote NV-NV entanglement in a heralded fashion. Remote NV-NV entangling schemes rely on photonic qubits as entanglement mediators. We use photon number states in our entangling protocols, where $|0\rangle_{\mathrm{ph}}$ ($|1\rangle_{\mathrm{ph}}$) represents the absence (presence) of a photon in the desired radiative mode. In order to avoid confusion we relabel the NV qubit states in this section such that $|\uparrow\rangle \equiv |0\rangle$ and $|\downarrow\rangle \equiv |1\rangle$.

In this section, we describe the basic protocol for remote NV-NV entanglement generation and then supply further implementation-specific details subsequently. Both NV centres are initialized into a generalized superposition state $\sqrt{\alpha}|\uparrow\rangle + \sqrt{1-\alpha}|\downarrow\rangle$ with the bright-state probability α. A spin-selective optical π pulse excites the NV centre state $|\uparrow\rangle$ to the optically excited state from where it decays spontaneously emitting a photon in the process. The NV-photon states of NV A and NV B are

$$(\sqrt{\alpha}|\uparrow\rangle_{\mathrm{A}}|1\rangle_{\mathrm{ph,A}} + \sqrt{1-\alpha}|\downarrow\rangle_{\mathrm{A}}|0\rangle_{\mathrm{ph,A}}) \otimes (\sqrt{\alpha}|\uparrow\rangle_{\mathrm{B}}|1\rangle_{\mathrm{ph,B}} + \sqrt{1-\alpha}|\downarrow\rangle_{\mathrm{B}}|0\rangle_{\mathrm{ph,B}}). \tag{2.5}$$

The radiative modes are guided towards a beam splitter with input ports a and b and output ports c and d. The beam splitter realizes the following operation[43]:

$$|1\rangle_{\mathrm{ph,A,a}} \rightarrow \frac{|1\rangle_{\mathrm{ph,A,c}} + |1\rangle_{\mathrm{ph,A,d}}}{\sqrt{2}} \quad |1\rangle_{\mathrm{ph,B,b}} \rightarrow \frac{|1\rangle_{\mathrm{ph,B,c}} - |1\rangle_{\mathrm{ph,B,d}}}{\sqrt{2}}. \tag{2.6}$$

Using the standard definitions for bosonic creation and annihilation operators $a_i^\dagger|n\rangle_i = \sqrt{n+1}|n\rangle_i$, $a_i|n\rangle_i = \sqrt{n}|n-1\rangle_i$ and the assumption that both photonic excitations are indistinguishable in all degrees of freedom, i.e. $|1\rangle_{\mathrm{ph,A,(c,d)}} = |1\rangle_{\mathrm{ph,B,(c,d)}}$, then the resulting state of the total system becomes

$$\begin{aligned}
&\frac{\alpha}{\sqrt{2}}|\uparrow\rangle_{\mathrm{A}}|\uparrow\rangle_{\mathrm{B}}(|2\rangle_{\mathrm{ph,c}}|0\rangle_{\mathrm{ph,d}}-|0\rangle_{\mathrm{ph,c}}|2\rangle_{\mathrm{ph,d}})\\
&+\sqrt{(\alpha-\alpha^2)/2}(|\uparrow\rangle_{\mathrm{A}}|\downarrow\rangle_{\mathrm{B}}+|\downarrow\rangle_{\mathrm{A}}|\uparrow\rangle_{\mathrm{B}})|1\rangle_{\mathrm{ph,c}}|0\rangle_{\mathrm{ph,d}}\\
&+\sqrt{(\alpha-\alpha^2)/2}(|\uparrow\rangle_{\mathrm{A}}|\downarrow\rangle_{\mathrm{B}}-|\downarrow\rangle_{\mathrm{A}}|\uparrow\rangle_{\mathrm{B}})|0\rangle_{\mathrm{ph,c}}|1\rangle_{\mathrm{ph,d}}\\
&+(1-\alpha)|\downarrow\rangle_{\mathrm{A}}|\downarrow\rangle_{\mathrm{B}}|0\rangle_{\mathrm{ph,c}}|0\rangle_{\mathrm{ph,d}}.
\end{aligned} \tag{2.7}$$

In our experiments we use non-number resolving detectors such that the states $|2\rangle_{\mathrm{ph}}$ and $|1\rangle_{\mathrm{ph}}$ are not discriminated. Moreover we operate in a regime of high photon loss caused by imperfections in the collection optics and the fact that only $\sim 3\,\%$ of all NV fluorescence is emitted into the ZPL. It is crucial to solely rely on ZPL photons since the emission of an additional phonon in the PSB would constitute an uncontrolled degree of freedom that washes out all coherences of the entangled state.

In this high photon-loss regime and under the assumption of symmetric detection efficiencies, we find that the probability for two-photon-emission events out of which only one was detected is then given by the initial bright state population α. The NV-NV density matrix after detecting a photon is therefore given by

$$(1-\alpha)|\psi_\phi^\pm\rangle\langle\psi_\phi^\pm|+\alpha|\uparrow\rangle_{\mathrm{A}}|\uparrow\rangle_{\mathrm{B}}\langle\uparrow|_{\mathrm{A}}\langle\uparrow|_{\mathrm{B}}, \tag{2.8}$$

with the odd-parity entangled states $|\psi_\phi^\pm\rangle=(|\uparrow_{\mathrm{A}}\downarrow_{\mathrm{B}}\rangle\pm e^{-i\phi}|\downarrow_{\mathrm{A}}\uparrow_{\mathrm{B}}\rangle)/\sqrt{2}$. The relative sign of the internal phase ϕ of the entangled state depends on the detector that observed the photon. The internal phase ϕ is composed from several individual phase accumulation processes such as the phase of the excitation pulse at the position of the NV, a difference in emission frequency for both NVs and fluctuations of the optical path length[20,44].

This thesis encompasses three different methods for remote entanglement generation. We require access to the internal phase ϕ to harness the power of quantum mechanics for our networking tasks. In the following we examine how each protocol achieves this individually.

Single-photon scheme (Chapter 8)[44] Following the original proposal by Cabrillo et al.[44], we directly make use of the states generated in Eq. (2.8). By varying α one realizes a trade-off between entanglement generation rate and maximal state fidelity. Note that extreme asymmetric optical losses for both NV centres may lead to the generation of skewed states. Practically these asymmetries cause only slight losses in state fidelity (0.1 % for $p_{\mathrm{det,A}}/p_{\mathrm{det,B}}\sim 2$) and can be easily resolved by introducing more losses into the channel with higher transmission. This scheme is particularly attractive for entanglement generation with high rates as only a single photon detection event is required for which the probability scales as αp_{det} with the bare single-photon detection probability p_{det}.

However, the single-photon scheme is not robust with respect to optical path length fluctuations. The optical phase therefore has to be stabilized or tracked over the course of the entire experiment. In Chapter 8 this is achieved by an interferometric set-up with a piezo actuator for path length stabilization. In addition we use a single light source for the interferometric phase stabilization and excitation of both NV centres such that all frequency fluctuations and therefore changes in the excitation phase are common mode.

Two-photon scheme (Chapter 7) [45] This protocol was devised by Barrett and Kok[45]. Following their method we generate the state of Eq. (2.8) with $\alpha = 0.5$, flip the NV states $|\uparrow\rangle \leftrightarrow |\downarrow\rangle$ to obtain

$$\left(|\psi^{\pm}_{-\phi}\rangle\langle\psi^{\pm}_{-\phi}| + |\downarrow\rangle_{\mathrm{A}}|\downarrow\rangle_{\mathrm{B}}\langle\downarrow|_{\mathrm{A}}\langle\downarrow|_{\mathrm{B}}\right)/2. \tag{2.9}$$

Another round of optical excitation and subsequent photon detection then projects the state into one of the pure states $|\psi^{\pm}_{0}\rangle$. We obtain the relative sign + (−) if the same detector clicked twice (different detectors clicked). The additional excitation round therefore accomplishes two things. First, the unwanted separable admixture $|\uparrow\rangle_{\mathrm{A}}|\uparrow\rangle_{\mathrm{B}}$ is excluded by converting the bright state $|\uparrow\rangle$ to the dark state $|\downarrow\rangle$ which is incompatible with a second photon-detection event. The entangled state acquires a newly imprinted phase ϕ' which is ideally equal to ϕ and therefore cancels. This is a reasonable assumption given that the NV emission frequencies and optical path lengths are not expected to change during the $\sim 250\,\mathrm{ns}$ window between excitation rounds.

Using two independent light fields for excitation will lead to dephasing due to fluctuations in the relative excitation phase between the two excitation rounds. Chapter 7 therefore employs a phase-locking scheme that distributes one light field to the other network node, references both laser frequencies to each other and creates a feedback loop via commercially available locking electronics (Menlo systems DXD200). This ensures that the relative laser phase remains stable during each round of the protocol.

In summary, two-photon schemes require negligible overhead in terms of path stabilization and produce high-fidelity states without a fundamental limit. In turn they only provide a low success probability that scales with $0.5p^2_{\mathrm{det}}$. These schemes have therefore been the workhorse for experiments that require the generation of a single entangled state[20,46–48] and were used to demonstrate the loophole-free violation of Bell's inequality (Ch. 7; Ref. 49 uses a two photon-protocol base don a single excitation round).

Memory-assisted scheme (Chapter 9) [50] Proposed by Campbell and Benjamin[50], this scheme makes use of an additional qubit per network node for state storage. After successfully generating the first entangled state (Eq. (2.8)), we swap the state onto a memory qubit (with states $|\uparrow\rangle_{\mathrm{m}}$ and $|\downarrow\rangle_{\mathrm{m}}$) in each network node. Next we continue with more state generation rounds until another success is detected and a state with internal phase

ϕ' is generated.

$$\begin{aligned}&\Big((1-\alpha)|\psi^{\pm}_{\phi'}\rangle\langle\psi^{\pm}_{\phi'}|+\alpha|\uparrow\rangle_{\mathrm{A,nv}}|\uparrow\rangle_{\mathrm{B,nv}}\langle\uparrow|_{\mathrm{A,nv}}\langle\uparrow|_{\mathrm{B,nv}}\Big)\otimes\\&\Big((1-\alpha)|\psi^{\pm}_{\phi}\rangle\langle\psi^{\pm}_{\phi}|+\alpha|\uparrow\rangle_{\mathrm{A,m}}|\uparrow\rangle_{\mathrm{B,m}}\langle\uparrow|_{\mathrm{A,m}}\langle\uparrow|_{\mathrm{B,m}}\Big).\end{aligned}\tag{2.10}$$

We finally perform a memory-controlled NOT operation within each network node. The action of the controlled NOT is as follows:

$$\begin{aligned}|\uparrow\rangle_{\mathrm{nv}}|\uparrow\rangle_{\mathrm{m}}&\rightarrow|\downarrow\rangle_{\mathrm{nv}}|\uparrow\rangle_{\mathrm{m}}\\|\downarrow\rangle_{\mathrm{nv}}|\uparrow\rangle_{\mathrm{m}}&\rightarrow|\uparrow\rangle_{\mathrm{nv}}|\uparrow\rangle_{\mathrm{m}}\\|\uparrow\rangle_{\mathrm{nv}}|\downarrow\rangle_{\mathrm{m}}&\rightarrow|\uparrow\rangle_{\mathrm{nv}}|\downarrow\rangle_{\mathrm{m}}\\|\downarrow\rangle_{\mathrm{nv}}|\downarrow\rangle_{\mathrm{m}}&\rightarrow|\downarrow\rangle_{\mathrm{nv}}|\downarrow\rangle_{\mathrm{m}}.\end{aligned}\tag{2.11}$$

This results in the following output states for each of the four possible state combinations in the input density matrix. For clarity we assume that the generated entangled states have a positive internal phase corresponding to a certain detection signature in the experiment. We further provide the probability of occurrence on the left side.

$$\begin{aligned}(1-\alpha)^2:&\,|\uparrow_{\mathrm{A}}\downarrow_{\mathrm{B}}\rangle_{\mathrm{m}}\cdot(|\downarrow_{\mathrm{A}}\downarrow_{\mathrm{B}}\rangle_{\mathrm{nv}}+e^{-i\phi'}|\uparrow_{\mathrm{A}}\uparrow_{\mathrm{B}}\rangle_{\mathrm{nv}})/2+e^{-i\phi}|\downarrow_{\mathrm{A}}\uparrow_{\mathrm{B}}\rangle_{\mathrm{m}}\cdot(|\uparrow_{\mathrm{A}}\uparrow_{\mathrm{B}}\rangle_{\mathrm{nv}}+e^{-i\phi'}|\downarrow_{\mathrm{A}}\downarrow_{\mathrm{B}}\rangle_{\mathrm{nv}})/2\\\alpha(1-\alpha):&\,(|\uparrow_{\mathrm{A}}\downarrow_{\mathrm{B}}\rangle_{\mathrm{m}}|\downarrow_{\mathrm{A}}\uparrow_{\mathrm{B}}\rangle_{\mathrm{nv}}+e^{-i\phi}|\downarrow_{\mathrm{A}}\uparrow_{\mathrm{B}}\rangle_{\mathrm{m}}|\uparrow_{\mathrm{A}}\downarrow_{\mathrm{B}}\rangle_{\mathrm{nv}})/\sqrt{2}\\(1-\alpha)\alpha:&\,|\uparrow_{\mathrm{A}}\uparrow_{\mathrm{B}}\rangle_{\mathrm{m}}(|\uparrow_{\mathrm{A}}\downarrow_{\mathrm{B}}\rangle_{\mathrm{nv}}+e^{-i\phi'}|\downarrow_{\mathrm{A}}\uparrow_{\mathrm{B}}\rangle_{\mathrm{nv}})/\sqrt{2}\\\alpha^2:&\,|\uparrow_{\mathrm{A}}\uparrow_{\mathrm{B}}\rangle_{\mathrm{m}}|\downarrow_{\mathrm{A}}\downarrow_{\mathrm{B}}\rangle_{\mathrm{nv}}\end{aligned}\tag{2.12}$$

After regrouping of all terms it turns out that measuring both NVs in the bright state $|\uparrow_{\mathrm{A}}\uparrow_{\mathrm{B}}\rangle_{\mathrm{nv}}$ occurs with a probability of $(1-\alpha)^2/2$ and projects the two memory qubits into the pure state $(e^{-i\phi}|\uparrow_{\mathrm{A}}\downarrow_{\mathrm{B}}\rangle_{\mathrm{m}}+e^{-i\phi'}|\downarrow_{\mathrm{A}}\uparrow_{\mathrm{B}}\rangle_{\mathrm{m}})/\sqrt{2}$ which is a phase-independent maximally entangled state as long as $\phi\approx\phi'$. This can be guaranteed by adhering to the same procedures as for the two-photon scheme but here with the added complexity that the two rounds of successful state generation are more than one electron-nuclear gate (i.e. $\sim 1\,\mathrm{ms}$) apart.

The memory-assisted scheme combines properties of both, the single- and two-photon schemes. Assuming that the memories do not dephase during entangling attempts one obtains a quasi-linear scaling of the success rate $\sim p_{det}$. One can additionally steer the initial state fidelity and the raw state generation rate by changing α. Besides, absolute phase stability of the optical set-up is not required, although the optical path has to be stable during the execution of the protocol. These advantages come with the need for additional qubits within the network nodes which increases the complexity of the experimental setup and sequence. Ultimately, networks with sophisticated multi-qubit nodes might rely on this type of state generation[51]. We use this scheme in Chapter 9 to demonstrate entanglement distillation in a quantum network setting.

The entangling schemes demonstrated in this thesis use feedback loops and DC Stark tuning to keep the NV excitation frequency on resonance with the local excitation light (see Sec. 2.2.2). Naturally the stabilization procedure is imperfect such that residual frequency detuning of the NV emission profiles and other causes of distinguishability (such as differing polarization) lead to imperfect interference when estimating the photonic wave function overlap and give rise to state-imperfections on the percent level[52]. A more detailed summary of the sources of error is given in Chapter 10.

REFERENCES

[1] G. Davies, *Properties and Growth of Diamond*, EMIS Data Review Series (INSPEC, the Institution of Electrical Engineers, 1994).

[2] F. Jelezko and J. Wrachtrup, *Single defect centres in diamond: A review,* physica status solidi (a) **203**, 3207 (2006).

[3] W. Pfaff, *Quantum Measurement and Entanglement of Spin Quantum Bits in Diamond*, Ph.d. thesis, Delft University of Technology (2013).

[4] H. Bernien, *Control, Measurement and Entanglement of Remote Quantum Spin Registers in Diamond*, Ph.d. thesis, Delft University of Technology (2014).

[5] J. H. N. Loubser and J. A. Van Wyk, *Optical spin-polarisation in a triplet state in irradiated and annealed type 1b diamonds,* Diamond Research , 11 (1977).

[6] M. W. Doherty *et al.*, *The nitrogen-vacancy colour centre in diamond,* Physics Reports **528**, 1 (2013).

[7] J. R. Maze *et al.*, *Properties of nitrogen-vacancy centers in diamond: The group theoretic approach,* New Journal of Physics **13**, 025025 (2011).

[8] M. W. Doherty, N. B. Manson, P. Delaney and L. C. L. Hollenberg, *The negatively charged nitrogen-vacancy centre in diamond: The electronic solution,* New Journal of Physics **13**, 025019 (2011).

[9] D. Leibfried, R. Blatt, C. Monroe and D. Wineland, *Quantum dynamics of single trapped ions,* Reviews of Modern Physics **75**, 281 (2003).

[10] M. L. Goldman *et al.*, *Phonon-Induced Population Dynamics and Intersystem Crossing in Nitrogen-Vacancy Centers,* Physical Review Letters **114**, 145502 (2015).

[11] P. Tamarat *et al.*, *Stark Shift Control of Single Optical Centers in Diamond,* Physical Review Letters **97**, 083002 (2006).

[12] L. C. Bassett, F. J. Heremans, C. G. Yale, B. B. Buckley and D. D. Awschalom, *Electrical Tuning of Single Nitrogen-Vacancy Center Optical Transitions Enhanced by Photoinduced Fields,* Physical Review Letters **107**, 266403 (2011).

[13] A. Lenef and S. C. Rand, *Electronic structure of the N-V center in diamond: Theory,* Physical Review B **53**, 13441 (1996).

[14] A. Gruber *et al.*, *Scanning Confocal Optical Microscopy and Magnetic Resonance on Single Defect Centers,* Science **276**, 2012 (1997).

[15] J. P. Hadden *et al.*, *Strongly enhanced photon collection from diamond defect centers under microfabricated integrated solid immersion lenses,* Applied Physics Letters **97**, 241901 (2010).

[16] M. Jamali *et al.*, *Microscopic diamond solid-immersion-lenses fabricated around single defect centers by focused ion beam milling,* Review of Scientific Instruments **85**, 123703 (2014).

[17] T. K. Yeung, D. Le Sage, L. M. Pham, P. L. Stanwix and R. L. Walsworth, *Anti-reflection coating for nitrogen-vacancy optical measurements in diamond,* Applied Physics Letters **100**, 251111 (2012).

[18] B. Hensen, *Quantum Nonlocality with Spins in Diamond*, Ph.d. thesis, Delft University of Technology (2016).

[19] N. Aslam, G. Waldherr, P. Neumann, F. Jelezko and J. Wrachtrup, *Photo-induced ionization dynamics of the nitrogen vacancy defect in diamond investigated by single-shot charge state detection,* New Journal of Physics **15**, 013064 (2013).

[20] H. Bernien *et al.*, *Heralded entanglement between solid-state qubits separated by three metres,* Nature **497**, 86 (2013).

[21] M. H. Abobeih *et al.*, *One-second coherence for a single electron spin coupled to a multi-qubit nuclear-spin environment,* arXiv , 1801.01196 (2018).

[22] L. Robledo, H. Bernien, I. van Weperen and R. Hanson, *Control and Coherence of the Optical Transition of Single Nitrogen Vacancy Centers in Diamond,* Physical Review Letters **105**, 177403 (2010).

[23] W. Pfaff *et al.*, *Unconditional quantum teleportation between distant solid-state quantum bits,* Science **345**, 532 (2014).

[24] J. Bakermans, *Stable Emission and Excitation of the Nitrogen-Vacancy Centre for Quantum Communication*, Master's thesis, Leiden University (2016).

[25] L. Robledo *et al.*, *High-fidelity projective read-out of a solid-state spin quantum register,* Nature **477**, 574 (2011).

[26] P. Neumann *et al.*, *Single-Shot Readout of a Single Nuclear Spin,* Science **329**, 542 (2010).

[27] G. D. Fuchs, G. Burkard, P. V. Klimov and D. D. Awschalom, *A quantum memory intrinsic to single nitrogen-vacancy centres in diamond,* Nature Physics **7**, 789 (2011).

[28] W. Pfaff *et al.*, *Demonstration of entanglement-by-measurement of solid-state qubits,* Nature Physics **9**, 29 (2013).

[29] G. Waldherr *et al.*, *Quantum error correction in a solid-state hybrid spin register,* Nature **506**, 204 (2014).

[30] B. Hensen *et al.*, *Loophole-free Bell inequality violation using electron spins separated by 1.3 kilometres,* Nature **526**, 682 (2015).

[31] L. M. K. Vandersypen and I. L. Chuang, *NMR techniques for quantum control and computation,* Reviews of Modern Physics **76**, 1037 (2005).

[32] M. S. Blok, *Quantum Measurement and Real-Time Feedback with a Spin-Register in Diamond*, Ph.d. thesis, Delft University of Technology (2015).

[33] A. Jarmola, V. M. Acosta, K. Jensen, S. Chemerisov and D. Budker, *Temperature- and Magnetic-Field-Dependent Longitudinal Spin Relaxation in Nitrogen-Vacancy Ensembles in Diamond,* Physical Review Letters **108**, 197601 (2012).

[34] G. de Lange, Z. H. Wang, D. Ristè, V. V. Dobrovitski and R. Hanson, *Universal Dynamical Decoupling of a Single Solid-State Spin from a Spin Bath,* Science **330**, 60 (2010).

[35] F. Shi *et al.*, *Sensing and atomic-scale structure analysis of single nuclear-spin clusters in diamond,* Nature Physics **10**, 21 (2014).

[36] G. Balasubramanian *et al.*, *Ultralong spin coherence time in isotopically engineered diamond,* Nature Materials **8**, 383 (2009).

[37] N. Bar-Gill, L. M. Pham, A. Jarmola, D. Budker and R. L. Walsworth, *Solid-state electronic spin coherence time approaching one second,* Nature Communications **4**, 1743 (2013).

[38] S. Kolkowitz, Q. P. Unterreithmeier, S. D. Bennett and M. D. Lukin, *Sensing Distant Nuclear Spins with a Single Electron Spin,* Physical Review Letters **109**, 137601 (2012).

[39] T. H. Taminiau *et al.*, *Detection and Control of Individual Nuclear Spins Using a Weakly Coupled Electron Spin,* Physical Review Letters **109**, 137602 (2012).

[40] N. Zhao *et al.*, *Sensing single remote nuclear spins,* Nature Nanotechnology **7**, 657 (2012).

[41] T. H. Taminiau, J. Cramer, T. van der Sar, V. V. Dobrovitski and R. Hanson, *Universal control and error correction in multi-qubit spin registers in diamond,* Nature Nanotechnology **9**, 171 (2014).

[42] J. Cramer, *Quantum Error Correction with Spins in Diamond*, Ph.d. thesis, Delft University of Technology (2016).

[43] T. Legero, T. Wilk, A. Kuhn and G. Rempe, *Time-resolved two-photon quantum interference,* Applied Physics B **77**, 797 (2003).

[44] C. Cabrillo, J. I. Cirac, P. García-Fernández and P. Zoller, *Creation of entangled states of distant atoms by interference,* Physical Review A **59**, 1025 (1999).

[45] S. D. Barrett and P. Kok, *Efficient high-fidelity quantum computation using matter qubits and linear optics,* Physical Review A **71**, 060310 (2005).

[46] D. L. Moehring *et al.*, *Entanglement of single-atom quantum bits at a distance,* Nature **449**, 68 (2007).

[47] J. Hofmann *et al.*, *Heralded Entanglement Between Widely Separated Atoms,* Science **337**, 72 (2012).

[48] A. Narla *et al.*, *Robust Concurrent Remote Entanglement Between Two Superconducting Qubits,* Physical Review X **6**, 031036 (2016).

[49] W. Rosenfeld *et al.*, *Event-Ready Bell Test Using Entangled Atoms Simultaneously Closing Detection and Locality Loopholes,* Physical Review Letters **119**, 010402 (2017).

[50] E. T. Campbell and S. C. Benjamin, *Measurement-Based Entanglement under Conditions of Extreme Photon Loss,* Physical Review Letters **101**, 130502 (2008).

[51] N. H. Nickerson, J. F. Fitzsimons and S. C. Benjamin, *Freely Scalable Quantum Technologies Using Cells of 5-to-50 Qubits with Very Lossy and Noisy Photonic Links,* Physical Review X **4**, 041041 (2014).

[52] H. Bernien *et al.*, *Two-Photon Quantum Interference from Separate Nitrogen Vacancy Centers in Diamond,* Physical Review Letters **108**, 043604 (2012).

3

EXPERIMENTAL CREATION OF QUANTUM ZENO SUBSPACES BY REPEATED MULTI-SPIN PROJECTIONS IN DIAMOND

N. Kalb, J. Cramer, M. Markham, D.J. Twitchen, R. Hanson and T.H. Taminiau

Repeated observations inhibit the coherent evolution of quantum states through the quantum Zeno effect. In multi-qubit systems this effect provides new opportunities to control complex quantum states. Here, we experimentally demonstrate that repeatedly projecting joint observables of multiple spins creates quantum Zeno subspaces and simultaneously suppresses dephasing caused by a quasi-static environment. We encode up to two logical qubits in these subspaces and show that the enhancement of the dephasing time with increasing number of projections follows a scaling law that is independent of the number of spins involved. These results provide new experimental insight into the interplay between frequent multi-spin measurements and slowly varying noise and pave the way for tailoring the dynamics of multi-qubit systems through repeated projections.

The results in this chapter have been published in Nature Communications **7**, 13111 (2016).

3.1. THE QUANTUM ZENO EFFECT

The quantum Zeno effect restricts the evolution of repeatedly observed quantum systems. For a two-dimensional system the state simply is frozen in one of two eigenstates of the measurement operator [1–10]. In multi-dimensional systems, however, Zeno subspaces are formed that can contain complex quantum states and dynamics: repeated observations create a barrier that blocks coherent evolution between subspaces, but leaves coherences and dynamics within those subspaces intact [11]. Analogous effects can also be realized through coherent control pulses or strong driving fields that decouple transitions between the subspaces [12–19]. Pioneering experiments have highlighted that the non-trivial dynamics in Zeno subspaces can be used to prepare exotic quantum states [20–24]. However, the opportunities to tailor the dynamics of multi-qubit systems by restricting coherent evolution have remained unexplored.

Here we show that repeated multi-spin projections on individually controlled spins create quantum Zeno subspaces that can encode multiple logical qubits while suppressing dephasing caused by the environment. We realize these repeated projections for up to three nuclear spins in diamond using the optical transition of a nearby electron spin. We then encode up to two logical qubits — including entangled states of logical qubits — and show that increasing the frequency of the projections supresses the dephasing of quantum states. Finally, we theoretically derive and experimentally verify a scaling law that shows that the increase in dephasing time is independent of the number of spins involved.

3.2. EXPERIMENTAL SYSTEM AND SEQUENCE

Our system consists of three ^{13}C spins ($I = \frac{1}{2}$) surrounding a single nitrogen vacancy (NV) centre ($|0\rangle_{\mathrm{NV}}$: $m_s = 0$ and $|1\rangle_{\mathrm{NV}}$: $m_s = -1$) in diamond (see Sec. 3.8.1). The natural evolution of the ^{13}C spins is dominated by dephasing due to the slowly fluctuating surrounding bath of ^{13}C spins (dephasing times $T_2^* = 12.4(9)$, $8.2(7)$ and $21(1)$ ms for spin 1, 2, and 3 respectively) [25]. Because the fluctuations are quasi-static, the Hamiltonian in a given experiment is $H = \sum_{i=1}^{k} \Delta_i \hat{\sigma}_{z,i}/2$, with k the number of spins and the detuning Δ_i for spin i drawn from a Gaussian distribution with $\sigma = \sqrt{2}/T_2^*$. We denote the Pauli operators as $\hat{\sigma}_{\mathrm{x}}$, $\hat{\sigma}_{\mathrm{y}}$, $\hat{\sigma}_{\mathrm{z}}$ and the identity as $\hat{I}$.

The quantum Zeno effect arises when an observable $\hat{O}$ is projected (superoperator $M(\hat{O})$). Here we consider dichotomic observables with eigenvalues ±1. A projection leaves the system's density matrix (ρ_{s}) in block-diagonal form with respect to the projectors $P_\pm = (\hat{I} \pm \hat{O})/2$, see Ref. 11:

$$M(\hat{O})\rho_s = P_+ \rho_{\mathrm{s}} P_+^\dagger + P_- \rho_{\mathrm{s}} P_-^\dagger = \frac{\rho_{\mathrm{s}} + \hat{O}\rho_{\mathrm{s}}\hat{O}^\dagger}{2}. \tag{3.1}$$

Repeatedly projecting observable $\hat{O}$ thus inhibits coherent evolution between the two eigenspaces of $\hat{O}$. We choose joint multi-spin observables of the form $\hat{O} = \hat{\sigma}_{\mathrm{x}}^{\otimes k}$, which anti-commute with all terms in the Hamiltonian H, so that rapid projections ideally re-

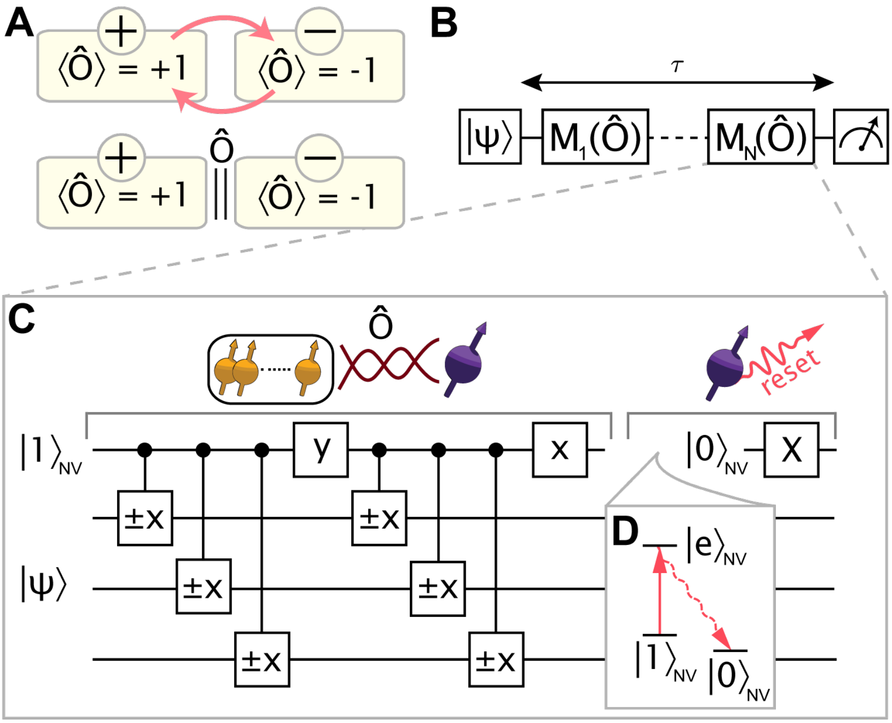

Figure 3.1 | **Concept and experimental sequence**. (**A**) Quantum Zeno subspaces. The state space of a quantum system is divided into two subspaces (yellow boxes) of an observable Ô. Plus and minus signs indicate eigenvalues of the associated operator. Coherent transitions between the two subspaces occur while the system is unperturbed (top, red arrows) but are strongly inhibited if Ô is repeatedly projected (bottom). (**B**) Experimental sequence. After initialization in $|\psi\rangle$, N equidistantly distributed projections M(Ô) (see Eq. (3.1)) are applied during a total evolution time τ and the state of the system is read out. (**C**) Realization of $\mathrm{M}(\hat{\mathrm{O}} = \hat{\sigma}_\mathrm{x}\hat{\sigma}_\mathrm{x}\hat{\sigma}_\mathrm{x})$ for three nuclear spins. First, the state of the nuclear spins (yellow) is entangled with the ancilla electron-spin state (purple). Second, the electron spin is projected and reinitialized in $|1\rangle_\mathrm{NV}$ (see also panel D) through a long $30\,\mu$s optical pumping pulse to $|0\rangle_\mathrm{NV}$ and a subsequent microwave π-pulse (X). Such a long laser excitation pulse ensures that the NV is projected. The x and y gates are $\pi/2$ rotations around the X- and Y-axis respectively. Controlled gates indicate that the direction is determined by the electron spin[26]. See Fig. 3.10 for pulse sequences for projections on one and two spins. (**D**) Relevant electron spin levels for optical repumping through selective resonant excitation of $|1\rangle_\mathrm{NV}$ to $|e\rangle_\mathrm{NV}$. We prepare the nuclear spin states in the $\langle\hat{\mathrm{O}}\rangle = +1$ subspace and associate this subspace to the electron state $|0\rangle_\mathrm{NV}$ in the entangling sequence so that the optical projection ideally never excites the NV center.

sult in the effective Zeno Hamiltonian $H_\mathrm{Zeno} = P_\pm H P_\pm^\dagger = 0$, see Ref. 11. Applying these projections therefore suppresses dephasing for each nuclear spin, but leaves quantum states and driven dynamics inside the two subspaces untouched (Fig. 3.1A).

To investigate quantum Zeno subspaces we use the following experimental sequence (Fig. 3.1B). We first initialize the nuclear spins in the desired state and prepare the electron spin in $|1\rangle_{\mathrm{NV}}$. Crucially, leaving the electron in $|1\rangle_{\mathrm{NV}}$ creates a different frequency shift for each of the three ^{13}C spins that suppresses resonant flip-flop interactions among the ^{13}C spins during idle time[27]. We then apply a total of N projections that are equally distributed in time. Finally, the nuclear spin state is read out using the electron spin as an ancilla[26,28–32]. Here we consider the case of an even number of projections. The results for an odd number of projections N give rise to additional effects at long evolution times due to the time-correlations in the noise and are discussed in Fig. 3.8. The total evolution time τ is defined from the end of the initialization to the start of the read-out. We subtract the time that control operations are applied to the nuclear spins (averaged over all spins), as dephasing might be suppressed during driving (for a comparison see Fig. 3.9).

We experimentally realize repeated multi-spin projections on the ^{13}C spins by using the NV electron spin as an ancilla spin (Fig. 3.1C). First, we entangle the NV electron spin state with the projections on the eigenspaces of $\hat{O}$ ($\langle\hat{O}\rangle = +1$ or -1), so that the combined state is $\alpha|\langle\hat{O}\rangle = +1\rangle|0\rangle_{\mathrm{NV}} + \beta||\langle\hat{O}\rangle = -1\rangle|1\rangle_{\mathrm{NV}}$[25,33]. Second, we apply an optical excitation that is resonant only if the electron-spin state is $|1\rangle_{\mathrm{NV}}$ ("reset")[25], which projects the quantum state and re-initializes the NV electron spin in $|0\rangle_{\mathrm{NV}}$ through optical pumping (Fig. 3.1D). Note that it is not required to extract or record the outcome of the optical measurement. To mitigate extra dephasing caused by the stochastic nature of the optical re-initialization (time constant of $\sim 1\,\mu$s), we use ^{13}C spins with a NV-^{13}C hyperfine coupling that is small compared to the inverse of the time constant for re-initialization (all couplings are below $2\pi\cdot 50\,$kHz)[34,35]. In addition, we design the gate sequence so that $|0\rangle_{\mathrm{NV}}$ is associated with the subspace of the initial nuclear state: ideally the electron spin is never optically excited and the projection constitutes a null measurement.

3.3. QUANTUM ZENO EFFECT FOR A SINGLE SPIN

To illustrate the quantum Zeno effect and to benchmark our system, we first consider a single ^{13}C spin and study the dephasing of the superposition state $|X\rangle \equiv (|0\rangle + |1\rangle)/\sqrt{2}$ for $\hat{O} = \hat{\sigma}_{\mathrm{x}}$ (Fig. 3.2A). We initialize the ^{13}C spin in $|X\rangle$ with an initial state fidelity of 0.95(2) and apply up to $N = 16$ projections. For a fixed total evolution time of 40 ms , we observe a significant increase of the state fidelity with an increasing number of projections (Fig. 3.2B). The complete time traces show that the dephasing time increases as more projections are applied (Fig. 3.2C); the superposition state is protected by the quantum Zeno effect. In this example, however, the Zeno subspaces contain just a single state and therefore cannot encode general quantum states.

3.4. ZENO SUBSPACES: PRESERVING A LOGICAL QUBIT

We next investigate Zeno subspaces that can contain an arbitrary two-dimensional quantum state, i.e. a complete logical quantum bit, by performing joint projections on two ^{13}C spins. We set the joint observable $\hat{O} = \hat{\sigma}_{\mathrm{x}}\hat{\sigma}_{\mathrm{x}}$, so that the four-dimensional state space

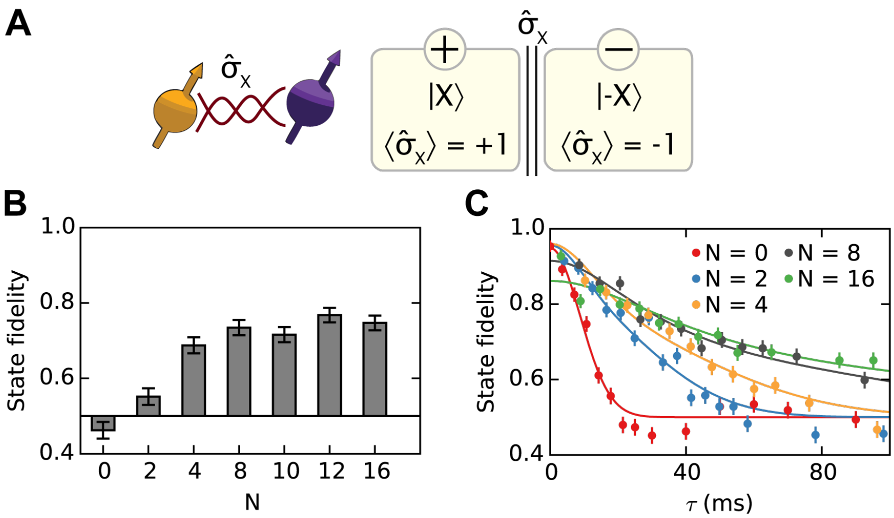

Figure 3.2 | Quantum Zeno effect for a single spin superposition state. (**A**) Quantum Zeno subspaces for a single nuclear spin (spin 1) and $\hat{O} = \hat{\sigma}_X$. Each eigenspace of $\hat{\sigma}_X$ consists of one state ($|X\rangle$ or $|-X\rangle$) with the respective eigenvalue indicated by the circled +/- signs. (**B**) State fidelity for $|X\rangle$ after $\tau = 40\,\text{ms}$. The fidelity initially increases with the number of projections N. (**C**) The complete time traces for the storage of $|X\rangle$ show that the dephasing time increases with the number of projections. The curves are fits to the theoretically expected fidelity (see Eq. (3.3)). All data are corrected for the final read-out fidelity (Fig. 3.7 and Sec. 3.8.3). All error bars are 1 s.d.

is divided into two coherent two-level subspaces (Fig. 3.3A). In these subspaces a logical qubit, which can hold an arbitrary quantum state, can be defined as $|\psi\rangle_L = \alpha|0\rangle_L + \beta|1\rangle_L$, with $|0\rangle_L = |X,X\rangle$ and $|1\rangle_L = |-X,-X\rangle$, and with logical operators $\hat{Z}_L = \hat{\sigma}_X\hat{I}$ and $\hat{X}_L = \hat{\sigma}_Z\hat{\sigma}_Z$. Note that logical-qubit superposition states are generally entangled states of the two ^{13}C spins.

We characterize the storage of arbitrary quantum states by preparing all six logical basis states $\{|0\rangle_L, |1\rangle_L, (|0\rangle_L \pm |1\rangle_L)/\sqrt{2}, (|0\rangle_L \pm i|1\rangle_L)/\sqrt{2}\}$ and averaging the final logical state fidelities[36] (Fig. 3.3B). The logical qubit without projections shows the same decay as a single ^{13}C spin, but with a slightly reduced initial fidelity ($F = 0.89(1)$) due to the overhead of creating the entangled states $|\psi\rangle_L$. Applying projections of the joint-observable $\hat{\sigma}_X\hat{\sigma}_X$ strongly suppresses the dephasing by the environment, while preserving the logical qubit states. As a result, the average state fidelity for the logical qubit surpasses the best ^{13}C nuclear spin used, while still remaining above the threshold of 2/3 for the storage of quantum states[37]. This result demonstrates the suppression of the dephasing of a complete logical qubit through the quantum Zeno effect.

Interestingly, preserving the logical qubit does not actually require the coherence of the

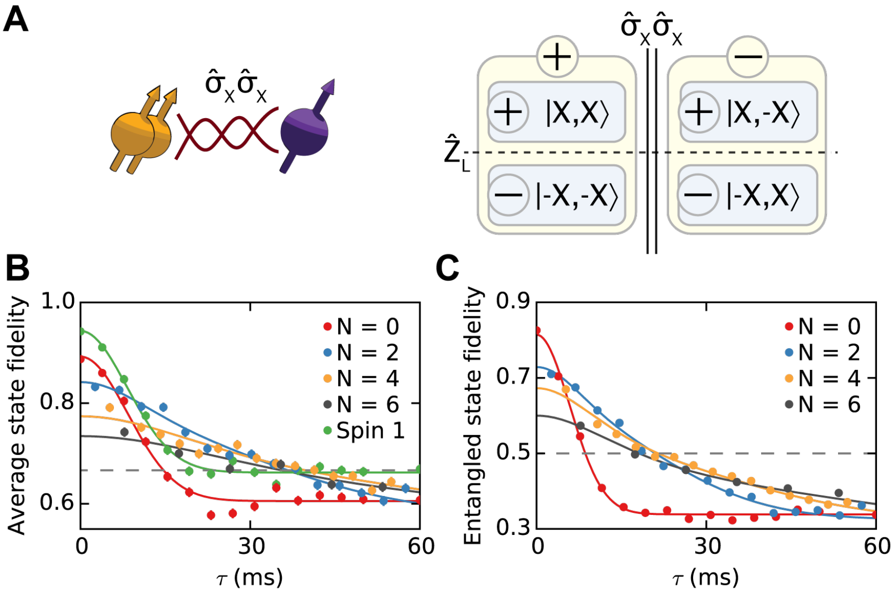

Figure 3.3 | **Storing a logical quantum bit by repeated two-spin projections**. (**A**) Schematic: the four-dimensional state-space of two ^{13}C spins (spin 1 and 2) is divided into two subspaces by repetitively projecting $\hat{O} = \hat{\sigma}_x\hat{\sigma}_x$ through entanglement with the ancilla spin. We define a logical quantum bit with logical operator $\hat{Z}_L = \hat{\sigma}_x\hat{I}$ (dashed line) and associate $\hat{\sigma}_x$ in $\hat{Z}_L$ with the spin with the longest coherence time (spin 1). (**B**) Storing a logical quantum bit. The average logical state fidelity for the six logical input states, e.g. $(1 + \langle\hat{Z}_L\rangle)/2$ for $|0\rangle_L$, as a function of time and for a varying number of projections N. To compare the results to the best possible decay for a single nuclear spin, we compare to the individual decay of spin 1 and eliminate potential systematic detunings by measuring $\sqrt{\langle\hat{\sigma}_x\rangle^2 + \langle\hat{\sigma}_y\rangle^2}$ (instead of $\langle\hat{\sigma}_x\rangle$ or $\langle\hat{\sigma}_y\rangle$). The dashed horizontal line is the classical limit of 2/3[37]. (**C**) Preserving two-spin entangled states. The two-spin state fidelity, averaged over the four entangled input states, indicates that general two-spin states in the subspace are preserved. Above the dashed horizontal line ($F = 0.5$) the state is entangled. For $N = 2$, 4 and 6 projections, entanglement is preserved longer than without projections. Solid lines are fits to Eq. (3.3) with the initial amplitude A, an offset and the effective dephasing time $T^*_{2,\mathrm{eff}}$ as free parameters. Error bars are 1 s.d. and are smaller than the symbols.

second spin to be maintained, as follows from the logical operator $\hat{Z}_L = \hat{\sigma}_x\hat{I}$. To show that the complete two-spin state is preserved, including entanglement between the two nuclear spins, we measure the average state fidelity with the ideal two-spin state for the four entangled initial states as a function of time (Fig. 3.3C). The duration for which genuine entanglement persists (two-spin state fidelity > 0.5) is extended for $N = 2$, 4 and 6 projections compared to the case without any projections, indicating that the barrier introduced by the projections inhibits dephasing for any two-spin state within the Zeno subspace.

3.5. ZENO SUBSPACES: TWO LOGICAL QUBITS

Realizing Zeno subspaces with even more dimensions enables the exploration of complex states of multiple logical qubits within the subspaces. We include a third nuclear spin and set $\hat{O} = \hat{\sigma}_\text{x}\hat{\sigma}_\text{x}\hat{\sigma}_\text{x}$ to create a protected four-dimensional subspace, which can host two logical qubits defined by the logical operators $\hat{Z}_\text{L1} = \hat{\sigma}_\text{x}\hat{I}\hat{\sigma}_\text{x}$, $\hat{X}_\text{L1} = \hat{I}\hat{\sigma}_\text{z}\hat{\sigma}_\text{z}$ and $\hat{Z}_\text{L2} = \hat{I}\hat{\sigma}_\text{x}\hat{\sigma}_\text{x}$, $\hat{X}_\text{L2} = \hat{\sigma}_\text{z}\hat{I}\hat{\sigma}_\text{z}$ (Fig. 3.4A). Each pure state within the $\langle\hat{O}\rangle = +1$ subspace can be expressed in terms of the logical two-qubit states:

$$\alpha|X,X,X\rangle + \beta|-X,X,-X\rangle + \gamma|X,-X,-X\rangle + \delta|-X,-X,X\rangle \\ = \alpha|0,0\rangle_\text{L} + \beta|0,1\rangle_\text{L} + \gamma|1,0\rangle_\text{L} + \delta|1,1\rangle_\text{L} \quad (3.2)$$

To investigate the inhibition of dephasing of the two logical qubits by repeated projections we prepare three different logical states: the logical eigenstate $|0,0\rangle_\text{L}$, the logical superposition state $|X,0\rangle_\text{L} = |0,0\rangle_\text{L} + |1,0\rangle_\text{L})/\sqrt{2}$ and the entangled logical state $|\Phi^+\rangle_\text{L} = (|0,0\rangle_\text{L} + |1,1\rangle_\text{L})/\sqrt{2}$. Preserving this set of states requires repeated projections of the three-spin operator $\hat{\sigma}_\text{x}\hat{\sigma}_\text{x}\hat{\sigma}_\text{x}$ since they are not eigenstates of a single two-spin operator.

The logical state fidelities for all three states show a clear prolongation of the decay times for $N = 2$ and $N = 4$ three-spin projections (Fig. 3.4B and C). Moreover, for a range of evolution times, the absolute logical state fidelities are increased despite the initial loss of fidelity due to the complexity of the experimental sequence (33 two-qubit gates for $N = 4$, which in total require 1276 refocusing pulses on the electron spin). These results confirm that the introduced three-spin projections inhibit dephasing of the individual spins while preserving the two logical qubits in a quantum Zeno subspace.

3.6. SCALING LAW FOR THE SUPPRESSION OF DEPHASING

To gain a detailed quantitative understanding of the quantum-Zeno effect for multi-spin projections, we derive a complete analytical description for the evolution. We model the projections as instantaneous and the noise as a quasi-static Gaussian frequency detuning, independent for each nuclear spin. We find an analytic solution for the decay of the expectation value of observables that are sensitive to dephasing (for N projections and total evolution time τ):

$$\frac{A}{2^{N+1}} \sum_{l=0}^{N+1} \binom{N+1}{l} e^{-\left(\frac{t_{Nl}}{T^*_{2,\text{eff}}}\right)^2} \text{ with } t_{Nl} = \tau - \frac{2l}{N+1}\tau. \quad (3.3)$$

Here $A \leq 1$ is the initial amplitude determined by experimental fidelities and $1/T^*_{2,\text{eff}} = \sqrt{\sum_{i=1}^{k}(1/T^*_{2,i})^2}$ is an effective joint decay rate of all involved spins. This result is valid for

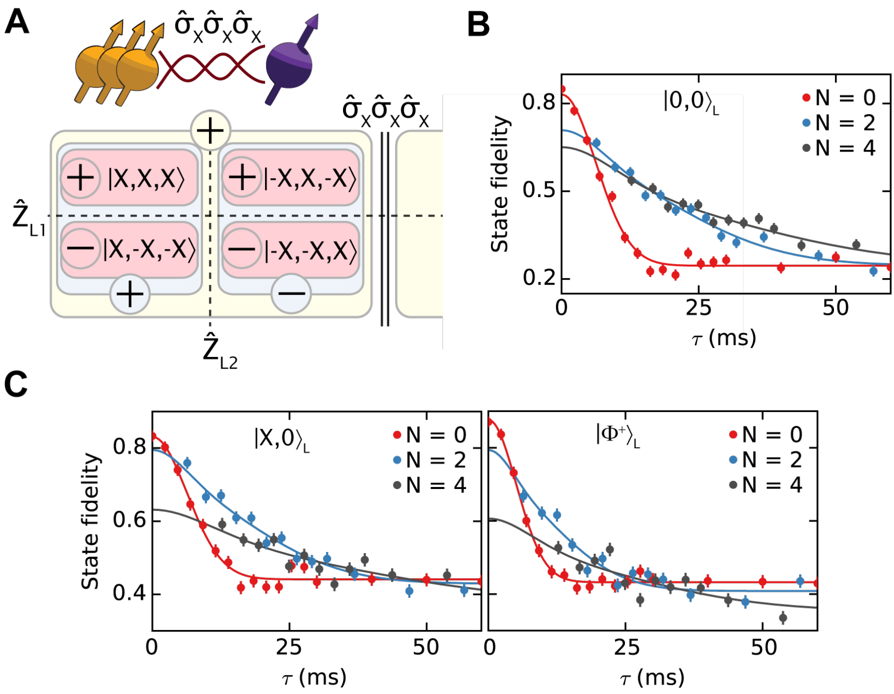

Figure 3.4 | Two logical qubits in a quantum Zeno subspace. (**A**) Schematic for three nuclear spins (spins 1,2 and 3) and $\hat{O} = \hat{\sigma}_x\hat{\sigma}_x\hat{\sigma}_x$. Two four-dimensional subspaces are created (yellow box). For simplicity we only show the positive subspace, which contains states of the form $\alpha|X,X,X\rangle + \beta|-X,X,-X\rangle + \gamma|X,-X,-X\rangle + \delta|-X,-X,X\rangle$. Within this subspace two logical qubits are defined by the logical operators $\hat{Z}_{L1} = \hat{\sigma}_x\hat{I}\hat{\sigma}_x$, $\hat{X}_{L1} = \hat{I}\hat{\sigma}_z\hat{\sigma}_z$ and $\hat{Z}_{L2} = \hat{I}\hat{\sigma}_x\hat{\sigma}_x$, $\hat{X}_{L2} = \hat{\sigma}_z\hat{I}\hat{\sigma}_z$ (blue and red boxes). (**B**,**C**) Logical state fidelities for three logical states: eigenstate $|0,0\rangle_L$, superposition state $|X,0\rangle_L$, and the entangled state $|\Phi^+\rangle_L = (|0,0\rangle_L + |1,1\rangle_L)/\sqrt{2}$. The results show that repeated projections of the three-spin operator $\hat{O} = \hat{\sigma}_x\hat{\sigma}_x\hat{\sigma}_x$ preserve the two logical qubits while inhibiting dephasing. Solid lines are fits to Eq. (3). The fidelities decay to different values for large τ because $|\Phi^+\rangle_L$ and $|X,0\rangle_L$ are eigenstates of operators of the form $\hat{I}\hat{\sigma}_z\hat{\sigma}_z$ or one of its permutations, whose expectation values are unaffected by dephasing. Error bars are 1 s.d.

any system size, i.e. number of spins, and number of projections N (both even and odd). A detailed derivation of Eq. (3.3) is given in Sec. 3.8.2.

We fit all experimental data in Figs. 3.2-3.4 with A, $T^*_{2,\text{eff}}$ and an offset, to account for the fact that two out of six cardinal states are insensitive to dephasing, as free parameters. We find good agreement with the experimentally obtained dephasing curves (see Tab. 3.1 for all fit values). To analyze the increase of the decay time with increasing number of projections we compile the extracted values from all experiments with an even number of projections and with 1, 2 and 3 nuclear spins in Fig. 3.5. The results reveal a scaling

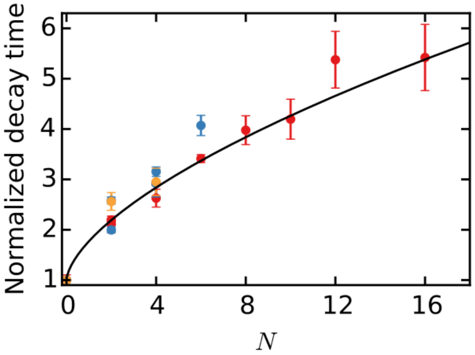

Figure 3.5 | Scaling of the decay time with increasing number of projections. The fitted decay times for all measurements in this article (Figs. 3.2-3.4) are compared to the theoretical decay time enhancement (solid line). All values are taken relative to the value without projections ($N = 0$). The data are averaged according to the number of operators in the expectation values that are subject to dephasing (i.e. the number of $\hat{\sigma}_X$ and/or $\hat{\sigma}_Y$). Red: One operator. Blue: Two operators. Orange: Three operators (see Fig. 3.11 for raw data). To show that the normalized decay time is independent of the number of nuclear spins, we distinguish data with a differing total number of nuclear spins. For instance, measurements of $\langle\hat{\sigma}_X\rangle$ (with $\hat{O} = \hat{\sigma}_X$) or $\langle\hat{\sigma}_X\hat{I}\rangle$ (with $\hat{O} = \hat{\sigma}_X\hat{\sigma}_X$) are represented by separate data points. The theory curve is obtained by evaluating Eq. (3.3) up to $N = 16$ (see Fig. 3.6). The obtained curve depends only on the functional shape of the underlying quasi-static noise spectrum. Error bars are 1 s.d.

law that is independent of the number of spins involved, in good quantitative agreement with our theoretical model.

3.7. DISCUSSION

In conclusion, we have observed that repeatedly projecting joint-observables of multi-spin systems creates quantum Zeno subspaces that can hold complex quantum states, and that these Zeno subspaces are resilient to environmental dephasing. While suppression of dephasing may also be achieved through alternative techniques such as coherent refocusing[17–19], our results provide direct experimental insight into the physics of repeated multi-spin measurements and Zeno subspaces in low-frequency noise environments. The results are also of practical relevance in the context of quantum error correction and detection codes, in which errors are detected through repeated measurements of joint obsservables[25,38,39]. Moreover, the demonstrated methods pave the way for investigating the effect of repeated measurements in various noise environments, e.g. non-Markovian noise, and for exploring and engineering complex dynamics of multi-qubit systems under tailored decoherence[40–43].

CONTRIBUTIONS

N.K. and T.H.T. devised the experiment. N.K., J.C. and T.H.T. prepared and characterized the experimental apparatus. D.J.T. and M.M. grew the diamond substrate. N.K. collected and analysed the data with the help of R.H. and T.H.T. N.K. and T.H.T. wrote the original form of this chapter with input from all authors which was then adapted by N.K. for this thesis.

3.8. SUPPLEMENTARY INFORMATION

3.8.1. DEVICE CHARACTERISTICS

The experiments were conducted in a confocal microscope at cryogenic temperatures (4 K). The investigated sample is a chemical-vapour-deposition homoepitaxially grown diamond of type IIa with a natural composition of carbon isotopes. The diamond has been cut along the $< 111 >$ crystal axis and was grown by Element Six.

3.8.2. ANALYTICAL MODEL AND DATA PROCESSING

DERIVATION OF THE ANALYTICAL MODEL

This section outlines the derivation of Eq. (3.3). We consider k two-level systems with random, uncorrelated and constant detuning Δ_i for each two-level system. Without loss of generality, the initial ($t = 0$) state is chosen to be the balanced superposition state $|X_1 \cdots X_k\rangle$. This state is an eigenstate of the projected operator $\hat{\sigma}_{\mathrm{x},1} \cdots \hat{\sigma}_{\mathrm{x,k}}$. After the first projection at time t and evolution of the system for another time t an analytic expression for the expectation value $\langle \hat{\sigma}_{\mathrm{x},1} \cdots \hat{\sigma}_{\mathrm{x,k}} \rangle_{N=1} = \mathrm{Tr}\left[\rho \hat{\sigma}_{\mathrm{x},1} \cdots \hat{\sigma}_{\mathrm{x,k}}\right]$, with the density matrix ρ, can be derived.

$$\begin{aligned} \langle \hat{\sigma}_{\mathrm{x},1} \cdots \hat{\sigma}_{\mathrm{x,k}} \rangle_{N=1} &= \frac{1}{2^k} \sum_{\alpha_1 \in \{-1,+1\}} \cdots \sum_{\alpha_N \in \{-1,+1\}} \cos^2[(\sum_{i=1}^{k} \alpha_i \Delta_i) t] \\ &= \frac{1}{2^{k-1}} \sum_{\alpha_2 \ldots \alpha_k} \cos^2[(\Delta_1 + \sum_{i=2}^{k} \alpha_i \Delta_i) t]\,. \end{aligned} \tag{3.4}$$

With the sum over all possible combinations of relative detunings by choosing the binary values of $\alpha_i = \pm 1 \; \forall \; i \in \{1, 2, ..., k\}$. Note that the notation for the sum over all configurations of α_i has been simplified for the last equality. This sum of cosine terms originates from static terms in the relevant entries of the density matrix after projection. The formula for a single projection ($N = 1$) is then readily extended to N projections

$$\langle \hat{\sigma}_{\mathrm{x},1} \cdots \hat{\sigma}_{\mathrm{x,k}} \rangle_N = \frac{1}{2^{k-1}} \sum_{\alpha_2 \ldots \alpha_k} \cos^{N+1}[(\Delta_1 + \sum_{i=2}^{k} \alpha_i \Delta_i) t]. \tag{3.5}$$

We obtain the ensemble average $\overline{\langle \hat{\sigma}_{x,1} \cdots \hat{\sigma}_{x,k} \rangle_N}$ by integration over a normal distribution $G_i[\Delta_i]$ of width $\sigma_i = \sqrt{2}/T^*_{2,i}$ for each Δ_i

$$\overline{\langle \hat{\sigma}_{\mathrm{x},1} \cdots \hat{\sigma}_{\mathrm{x,k}} \rangle_N} = \int \cdots \int \langle \hat{\sigma}_{\mathrm{x},1} \cdots \hat{\sigma}_{\mathrm{x,k}} \rangle_N \prod_{i=1}^{k} G_i[\Delta_i] d\Delta_i. \tag{3.6}$$

We single out one summand of $\langle\hat{\sigma}_{\mathrm{x},1}\cdots\hat{\sigma}_{\mathrm{x,k}}\rangle_N$ with general α_i and perform the integration. The $\cos^{N+1}$ term is rewritten by using Euler's formula and the Binomial theorem

$$\cos^{N+1}[(\Delta_1+\sum_{i=2}^{k}\alpha_i\Delta_i)t]=\frac{1}{2^{N+1}}\sum_{l=0}^{N+1}\binom{N+1}{l}\exp\left[i(\Delta_1+\sum\alpha_i\Delta_i))t\right]^{N+1-2l}. \tag{3.7}$$

After inserting this rewritten cosine term into Eq. (3.6) we obtain a product of Fourier transformations for each summand in Eq. (3.7). It becomes clear that the precise assignment of the α_i coefficients does not play a role for the evaluation of the integral since the Fourier transformation and inverse Fourier transformation of a Gaussian give the same result: i.e. the precise assignment of $\alpha_i=\pm1$ does not play a role for the evaluated integral. The normalization factor of $\frac{1}{2^{k-1}}$ therefore drops out when summing over all possible configurations of α_i. Evaluating Eq. (3.6) results in an analytic expression for the ensemble average $\overline{\langle\hat{\sigma}_{\mathrm{x},1}\cdots\hat{\sigma}_{\mathrm{x,k}}\rangle}_N$

$$\overline{\langle\hat{\sigma}_{\mathrm{x},1}\cdots\hat{\sigma}_{\mathrm{x,k}}\rangle}_N=\frac{1}{2^{N+1}}\sum_{l=0}^{N+1}\binom{N+1}{l}\exp\left[-((N+1-2l)t)^2\sum_{i=1}^{k}(1/T^*_{2,i})^2\right]. \tag{3.8}$$

Eq. (3.8) describes the expected decay curve for a joint k-partite observable after N joint projections. All operations are separated by the same duration t. Involving multiple nuclear spins results in an effective decay time $(1/T^*_{2,\mathrm{eff}})^2=\sum_i(1/T^*_{2,i})^2$ (as expected from the convolution of two Normal distributions). Correlations which are only partially subject to dephasing, e.g. $\langle\hat{\sigma}_{\mathrm{z},1}\hat{\sigma}_{\mathrm{y},2}\rangle$, only incorporate the relevant decoherence times (for the given example: $T^*_{2,\mathrm{eff}}=T^*_{2,2}$). In the main text, t is replaced by the total evolution time $\tau=(N+1)t$.

FITTING ROUTINE

The fits to the data are performed in the following way. First, the decay without projections ($N=0$) is fit with a Gaussian function. The initial amplitude, offset and width are extracted. Second, in order to fit data sets with multiple projections Eq. (3.8) is multiplied with the extracted amplitude and the offset is added (the offset originates from constant $\langle\hat{\sigma}_{\mathrm{z},1}\cdots\hat{\sigma}_{\mathrm{z,k}}\rangle$ correlations that are not subject to dephasing and play a role when determining average state fidelities). The data set is then fitted with three free parameters: $T^*_{2,\mathrm{eff}}$, a global amplitude damping that parametrizes errors due to the added complexity of the experiment and the aforementioned constant offset.

SCALING LAW

In order to obtain the theory curve in Fig. 3.5, we compute the theoretical enhancement of the dephasing time for a given number of projections. We calculate the normalized $\frac{1}{\sqrt{e}}$-time of Eq. (3.8) for N being even and smaller than 17. A modified scaling law, $1+\mu N^{\nu}$, is fit to the extracted characteristic dephasing times and the parameters $\mu=0.77(1)$ and $\nu=0.63(1)$ (see Fig. 3.6) are found.

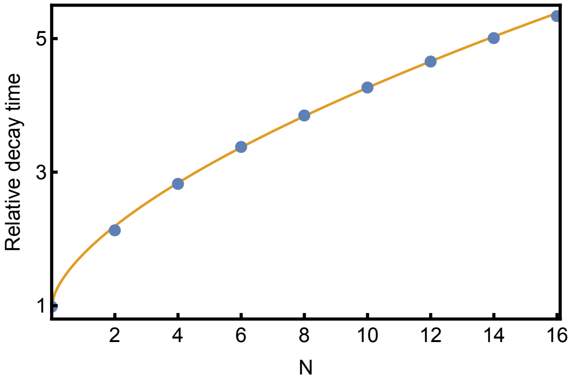

Figure 3.6 |Blue data: extracted $\frac{1}{\sqrt{e}}$-time from the analytical solutions to Eq. (3.8). Orange line: Fitting the extracted times to the power law $1+\mu M^{\nu}$ yields $\mu = 0.77(1)$ and $\nu = 0.63(1)$ and gives a good approximation for the experimentally investigated number of projections N.

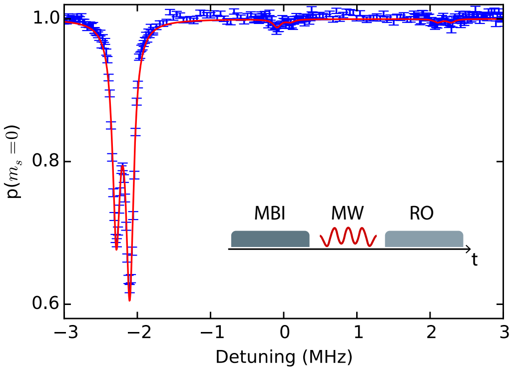

Figure 3.7 | Electron spin resonance to determine the initialization fidelity of the ^{14}N nuclear spin ($\mathrm{I} = 1$) in $\mathrm{m_I} = -1$. Inset: Schematic of the experimental sequence. After measurement-based initialization of the nucleus (MBI) a weak microwave pulse (MW)[33] with a duration of $8\,\mu$s is applied and followed by optical read out (RO) of the electron spin. The detuning is relative to the central microwave frequency (1.74667(1) GHz) of the $\mathrm{m_s} = 0$ to $\mathrm{m_s} = -1$ transition of the electron spin. The transition is split into six lines due to strong hyperfine coupling to the ^{14}N nuclear spin (with a coupling strength of $2\pi \cdot 2.195(1)$ MHz) and a ^{13}C nuclear spin ($\mathrm{I} = 1/2$, with a coupling strength of $2\pi \cdot 182(1)$ kHz) in the vicinity of the NV centre. The data is therefore fit to six Lorentzian functions with variable width, spacing and amplitude. From the fitted amplitudes we extract the population of the ^{14}N nuclear spin after MBI: $\mathrm{p}_{-1} = 0.96(1)$ $\quad \mathrm{p}_0 = 0.022(8)$ $\quad \mathrm{p}_{+1} = 0.014(8)$. All error bars are 1 s.d.

3.8.3. ^{13}C SPIN READ-OUT CORRECTION

We correct the read-out results for errors introduced by the final conditional gates on the ^{13}C spins to obtain the actual state fidelity. We employ a characterization technique de-

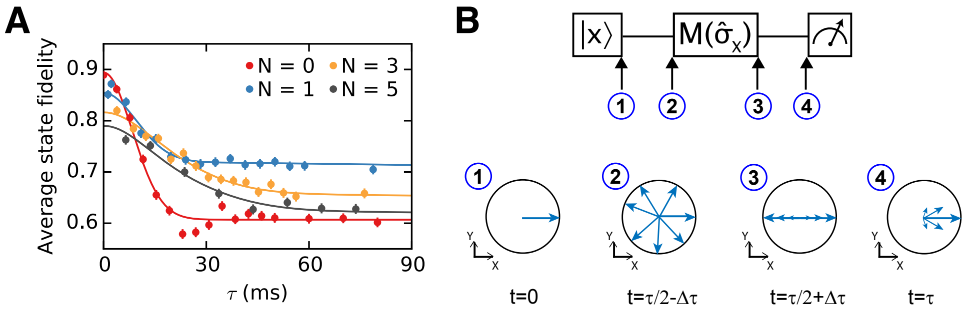

Figure 3.8 | **Analysis for an odd number of projections**. (**A**) Experimental results for the logical qubit in the two-spin case (Fig. 3.3B). We observe a clear elevation of the average state fidelity for times much longer than T_2^* for 1 (blue) and 3 (orange) projections. This was also observed in J. Cramer et al.[25] for $N = 1$. The behavior for times much longer than the decoherence time is fully explained by our model and can be accurately fit with Eq. (3.8). (**B**) Schematic explanation of the elevated signal for large evolution times $\tau \gg T_2^*$. Top panel: A spin-1/2 particle is initialized in a superposition state $|X\rangle$, evolves freely for a time $\tau/2$ until it is projected ($M(\hat{\sigma}_X)$) onto $|\pm X\rangle$ and is finally read out after a total evolution time of τ. Bottom panel: Sketch of an ensemble of states in the XY plane of the Bloch sphere. The state of the particle is well defined after initialization ①. The state is however completely mixed due to a random frequency detuning before projection ② if the free evolution $\tau/2$ is much longer than the dephasing time T_2^*. Projection into $|\pm X\rangle$ effectively projects the Bloch vector onto the x-axis ③. The frequency detuning of the particle remains constant after projection such that the ensemble average partly rephases (similarly to a spin echo) after another evolution time of $\tau/2$ ④. We call this effect a filter since a single projection of $\hat{\sigma}_X$ completely mixes the state if the particle is in $|\pm Y\rangle = (|X\rangle \pm i|-X\rangle)/\sqrt{2}$, effectively filtering those cases out. In contrast states which are affected by a detuning but got rotated to $|\pm X\rangle$ at the time of the projection are unaffected. All error bars are 1 s.d.

veloped in reference 25 and determine correction factors (C_{C_i}) for one-, two- and three-spin expectation values. The applied correction assumes a symmetric initialization and read-out process as well as a constant loss of fidelity due to imperfect initialization of the ^{14}N spin of the NV centre. The probability to find the ^{14}N spin in $m_I = -1$ after initialization is found to be 0.96(1) (see Fig. 3.7). We obtain the following correction factors

$$C_{C_1} = 0.94(1) \qquad C_{C_2} = 0.94(1) \qquad C_{C_1C_2} = 0.93(2)$$
$$C_{C_1C_2C_3} = 0.90(2) \qquad C_{C_1C_3} = 0.93(2) \qquad C_{C_2C_3} = 0.95(2). \tag{3.9}$$

SUPPLEMENTARY FIGURES AND TABLES

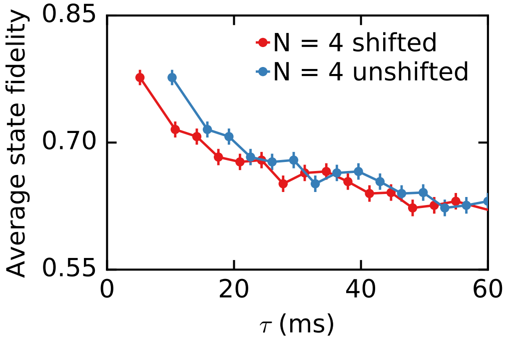

Figure 3.9 | As stated in the main text, the average driving time is subtracted from the evolution time since dephasing might be largely suppressed during driving. Here we provide a comparison of data with subtracted average driving time (red) and an unshifted data set (blue). The applied shift is 5.06 ms. The shown data corresponds to the data in Fig. 3.3B with $N = 4$. All error bars are 1 s.d.

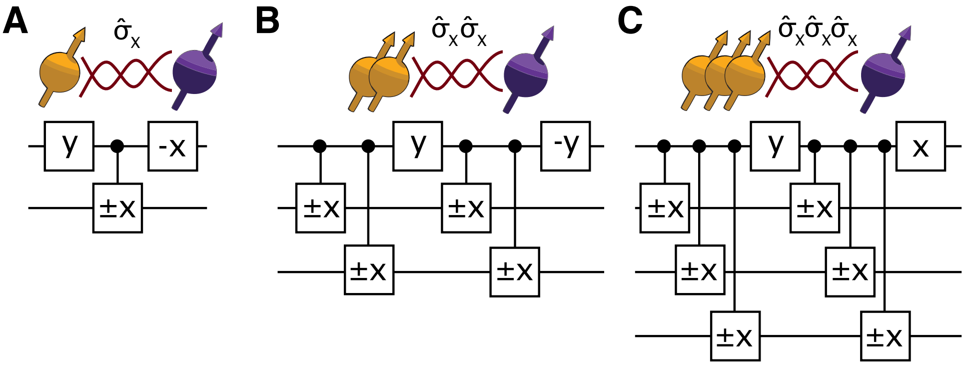

Figure 3.10 | Gate sequences to project the observables $\hat{\sigma}_x$ (**A**), $\hat{\sigma}_x\hat{\sigma}_x$ (**B**) and $\hat{\sigma}_x\hat{\sigma}_x\hat{\sigma}_x$ (**C**). x and y are $\pi/2$ rotations around the X and Y axis with the orientation given by the sign. We use a combination of dynamical decoupling sequences that act as rotations on the ^{13}C nuclear spins with the sign controlled by the electron spin[26] (controlled gates in all panels). Compared to a standard CNOT these gates cause an extra unconditional $\pi/2$ rotation. We pre-compensate this extra rotation with the gates before the first gate on the electron spin. Note that for a single spin (panel a) all eigenstates ($|\pm X\rangle$) of the projected observable are unaffected by the extra operation and one can therefore omit the compensation.

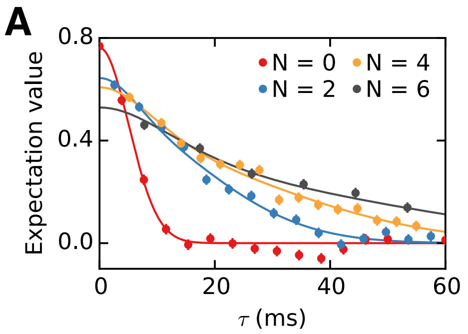

Figure 3.11 |(**A**) Decay of $\langle\hat{\sigma}_X\hat{\sigma}_X\rangle$ for a varying number of projections. The data are averaged over six input states that correspond to the states used for Fig. 3.3B. The number of projections N is given in the legend. (**B**) Decay of $\langle\hat{\sigma}_X\hat{\sigma}_X\hat{\sigma}_X\rangle$. The data are averaged over the three states of Fig. 3.4B and C. The fitted $1/\sqrt{e}$-time for $N = 0$ is 4.6(2) ms. The amount of projections for each data trace is given in the legend. The fitted, relative, decay constants for these data are included in Fig. 3.5. All error bars are 1 s.d.

	fitted T_2^* (ms)	expected $T_{2,eff}^*$ (ms)
C_1	12.4(9)	/
C_2	8.2(7)	/
C_3	21(1)	/
C_1C_2	7.1(3)	6.8(3)
$C_1C_2C_3$	6.5(2)	6.5(4)

Table 3.1 |Comparison of fitted and expected decay time T_2^* for multi-qubit observables. The expected T_2^* value is calculated by assuming uncorrelated noise and using $\left(1/T_{2,\mathrm{eff}}^*\right)^2 = \sum_i \left(1/T_{2,i}^*\right)^2$. We find agreement between expected and measured decay times.

REFERENCES

[1] B. Misra and E. C. G. Sudarshan, *The Zeno's paradox in quantum theory,* Journal of Mathematical Physics **18**, 756 (1977).

[2] W. M. Itano, D. J. Heinzen, J. J. Bollinger and D. J. Wineland, *Quantum Zeno effect,* Physical Review A **41**, 2295 (1990).

[3] J. Wolters, M. Strauß, R. S. Schoenfeld and O. Benson, *Quantum Zeno phenomenon on a single solid-state spin,* Physical Review A **88**, 020101 (2013).

[4] K. Kakuyanagi *et al.*, *Observation of quantum Zeno effect in a superconducting flux qubit,* New Journal of Physics **17**, 063035 (2015).

[5] J. Peise *et al.*, *Interaction-free measurements by quantum Zeno stabilization of ultracold atoms,* Nature Communications **6**, 6811 (2015).

[6] D. H. Slichter *et al.*, *Quantum Zeno effect in the strong measurement regime of circuit quantum electrodynamics,* New Journal of Physics **18**, 053031 (2016).

[7] Y. S. Patil, S. Chakram and M. Vengalattore, *Measurement-Induced Localization of an Ultracold Lattice Gas,* Physical Review Letters **115**, 140402 (2015).

[8] S. R. Wilkinson *et al.*, *Experimental evidence for non-exponential decay in quantum tunnelling,* Nature **387**, 575 (1997).

[9] M. C. Fischer, B. Gutiérrez-Medina and M. G. Raizen, *Observation of the Quantum Zeno and Anti-Zeno Effects in an Unstable System,* Physical Review Letters **87**, 040402 (2001).

[10] Y. Kondo, Y. Matsuzaki, K. Matsushima and J. G. Filgueiras, *Using the quantum Zeno effect for suppression of decoherence,* New Journal of Physics **18**, 013033 (2016).

[11] P. Facchi and S. Pascazio, *Quantum Zeno Subspaces,* Physical Review Letters **89**, 080401 (2002).

[12] P. Facchi, D. A. Lidar and S. Pascazio, *Unification of dynamical decoupling and the quantum Zeno effect,* Physical Review A **69**, 032314 (2004).

[13] L. Viola and S. Lloyd, *Dynamical suppression of decoherence in two-state quantum systems,* Physical Review A **58**, 2733 (1998).

[14] D. Dhar, L. K. Grover and S. M. Roy, *Preserving Quantum States using Inverting Pulses: A Super-Zeno Effect,* Physical Review Letters **96**, 100405 (2006).

[15] W. Zheng *et al.*, *Experimental demonstration of the quantum Zeno effect in NMR with entanglement-based measurements,* Physical Review A **87**, 032112 (2013).

[16] H. Singh, Arvind and K. Dorai, *Experimental protection against evolution of states in a subspace via a super-Zeno scheme on an NMR quantum information processor,* Physical Review A **90**, 052329 (2014).

[17] M. Zhong *et al.*, *Optically addressable nuclear spins in a solid with a six-hour coherence time,* Nature **517**, 177 (2015).

[18] P. C. Maurer *et al.*, *Room-Temperature Quantum Bit Memory Exceeding One Second,* Science **336**, 1283 (2012).

[19] G. de Lange, Z. H. Wang, D. Ristè, V. V. Dobrovitski and R. Hanson, *Universal Dynamical Decoupling of a Single Solid-State Spin from a Spin Bath,* Science **330**, 60 (2010).

[20] Z. Leghtas *et al.*, *Confining the state of light to a quantum manifold by engineered two-photon loss,* Science **347**, 853 (2015).

[21] L. Bretheau, P. Campagne-Ibarcq, E. Flurin, F. Mallet and B. Huard, *Quantum dynamics of an electromagnetic mode that cannot contain N photons,* Science **348**, 776 (2015).

[22] A. Signoles *et al.*, *Confined quantum Zeno dynamics of a watched atomic arrow,* Nature Physics **10**, 715 (2014).

[23] G. Barontini, L. Hohmann, F. Haas, J. Estève and J. Reichel, *Deterministic generation of multiparticle entanglement by quantum Zeno dynamics,* Science **349**, 1317 (2015).

[24] F. Schäfer *et al.*, *Experimental realization of quantum zeno dynamics,* Nature Communications **5** (2014).

[25] J. Cramer *et al.*, *Repeated quantum error correction on a continuously encoded qubit by real-time feedback,* Nature Communications **7**, 11526 (2016).

[26] T. H. Taminiau, J. Cramer, T. van der Sar, V. V. Dobrovitski and R. Hanson, *Universal control and error correction in multi-qubit spin registers in diamond,* Nature Nanotechnology **9**, 171 (2014).

[27] N. Bloembergen, *On the interaction of nuclear spins in a crystalline lattice,* Physica **15**, 386 (1949).

[28] L. Robledo *et al.*, *High-fidelity projective read-out of a solid-state spin quantum register,* Nature **477**, 574 (2011).

[29] G. Waldherr *et al.*, *Quantum error correction in a solid-state hybrid spin register,* Nature **506**, 204 (2014).

[30] A. Dréau, P. Spinicelli, J. R. Maze, J.-F. Roch and V. Jacques, *Single-Shot Readout of Multiple Nuclear Spin Qubits in Diamond under Ambient Conditions,* Physical Review Letters **110**, 060502 (2013).

[31] L. Jiang *et al.*, *Repetitive Readout of a Single Electronic Spin via Quantum Logic with Nuclear Spin Ancillae,* Science **326**, 267 (2009).

[32] P. Neumann *et al.*, *Single-Shot Readout of a Single Nuclear Spin,* Science **329**, 542 (2010).

[33] W. Pfaff *et al.*, *Unconditional quantum teleportation between distant solid-state quantum bits,* Science **345**, 532 (2014).

[34] M. S. Blok, N. Kalb, A. Reiserer, T. H. Taminiau and R. Hanson, *Towards quantum networks of single spins: Analysis of a quantum memory with an optical interface in diamond,* Faraday Discussions **184**, 173 (2015).

[35] A. Reiserer *et al.*, *Robust Quantum-Network Memory Using Decoherence-Protected Subspaces of Nuclear Spins,* Physical Review X **6**, 021040 (2016).

[36] S. J. van Enk, N. Lütkenhaus and H. J. Kimble, *Experimental procedures for entanglement verification,* Physical Review A **75**, 052318 (2007).

[37] S. Massar and S. Popescu, *Optimal Extraction of Information from Finite Quantum Ensembles,* Physical Review Letters **74**, 1259 (1995).

[38] B. M. Terhal, *Quantum error correction for quantum memories,* Reviews of Modern Physics **87**, 307 (2015).

[39] G. A. Paz-Silva, A. T. Rezakhani, J. M. Dominy and D. A. Lidar, *Zeno Effect for Quantum Computation and Control,* Physical Review Letters **108**, 080501 (2012).

[40] J. T. Barreiro *et al.*, *An open-system quantum simulator with trapped ions,* Nature **470**, 486 (2011).

[41] P. Zanardi and L. Campos Venuti, *Coherent Quantum Dynamics in Steady-State Manifolds of Strongly Dissipative Systems,* Physical Review Letters **113**, 240406 (2014).

[42] D. K. Burgarth *et al.*, *Exponential rise of dynamical complexity in quantum computing through projections,* Nature Communications **5**, 5173 (2014).

[43] G. A. Álvarez, D. D. B. Rao, L. Frydman and G. Kurizki, *Zeno and Anti-Zeno Polarization Control of Spin Ensembles by Induced Dephasing,* Physical Review Letters **105**, 160401 (2010).

4

ANALYSIS OF A QUANTUM MEMORY WITH AN OPTICAL INTERFACE IN DIAMOND

M.S. Blok*, N. Kalb*, A. Reiserer, T.H. Taminiau and R. Hanson

Single defect centers in diamond have emerged as a powerful platform for quantum optics experiments and quantum information processing tasks[1]. Connecting spatially separated nodes via optical photons[2] to form a quantum network will enable distributed quantum computing and long-range quantum communication. Initial experiments on trapped atoms and ions as well as defects in diamond have demonstrated entanglement between two nodes over several meters[3–6]. To realize multi-node networks, additional quantum bit systems that store quantum states while new entanglement links are established are highly desirable. Such memories allow for distillation, purification and repeater protocols that extend the size, speed and distance of the network[7–10]. However, to be effective the memory must be robust against the entanglement generation protocol, which typically must be repeated many times. Here we evaluate the prospect of using carbon nuclear spins in diamond as quantum memories that are compatible with quantum networks based on single nitrogen vacancy (NV) defects in diamond. We present a theoretical framework to describe the dephasing of the nuclear spins under repeated generation of NV spin-photon entanglement and show that quantum states can be stored for hundreds of repetitions using realistic experimental coupling parameters. This result demonstrates that nuclear spins with weak hyperfine couplings are promising quantum memories for quantum networks.

The results in this chapter have been published in Faraday discussions **184**, 173 (2015).

*Equally contributing authors

4.1. NV CENTRES AS QUANTUM NETWORK NODES

Spins associated with the nitrogen-vacancy (NV) center, an atomic defect in diamond, have recently emerged as a promising platform for quantum networks[1,11]. The NV-center's long-lived electron spin state ($S = 1$) can be controlled by magnetic resonance and can be initialized and read out optically. At cryogenic temperatures (< 10K), coherent optical transitions allow for the generation of spin-photon entanglement[12] and of entanglement between spatially separated NV center electron spins[6,13].

In addition, the electron spin couples to nuclear spins in the environment through the hyperfine interaction. Control over the host nitrogen spin and over multiple nearby ^{13}C spins has been demonstrated[14–20]. As these nuclear spins can be well isolated from their environments, coherence times of more than one second have been demonstrated[21], making them interesting candidates for quantum network memories.

A major challenge for realizing quantum memories based on nuclear spins is to overcome the dephasing that is introduced while using the electron spin as an optical interface to generate spin-photon entanglement. Consider the general case of an entanglement protocol that is inherently probabilistic due to lossy optical channels. The protocol therefore must be repeated many times in order to establish an entanglement link between adjacent network nodes. Whenever the entanglement attempt fails, the electron spin is projected in a random state, and therefore it has to be re-initialized by optical pumping after each repetition. Because the exact time at which the electron spin is reset is uncertain (optical pumping is a stochastic process) and the electron-nuclear interaction is always present, the electron reset can cause nuclear spin dephasing (Fig. 4.1). A promising route to overcome this dephasing of the quantum memory is to use relatively distant ^{13}C spins with weak hyperfine couplings, which are less sensitive to fluctuations of the electron spin.

In this manuscript we explore the storage of quantum states in ^{13}C spins during the repeated generation of NV spin-photon entanglement. We first discuss the experimental techniques to control nuclear spins and demonstrate a method to directly measure the frequency difference $\mathrm{d}f$ that governs the nuclear dephasing[22] (see Fig. 4.1). We then analyze the spin-photon entanglement protocol, develop a model to describe the dephasing of nuclear spins, and calculate the fidelity of nuclear spin quantum memories with realistic coupling parameters under many repetitions of the entanglement protocol.

4.2. CONTROL AND CHARACTERIZATION OF NUCLEAR SPINS IN DIAMOND

We begin by discussing the experimental methods to control the NV center and nearby ^{13}C nuclear spins. We then introduce a Ramsey-spectroscopy method to directly determine the frequency df, which governs the dephasing process, and characterize four candidate ^{13}C spins near a single NV-center. These experimental results highlight the universal presence of controllable nuclear spin memories and provide a realistic set of

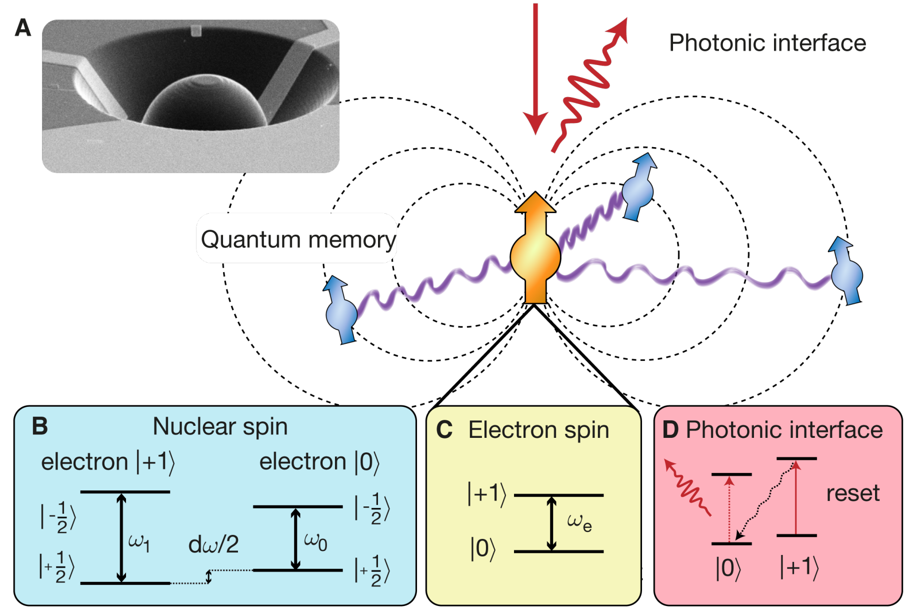

Figure 4.1 | **The NV-center as a network node including a quantum memory**. A single electron spin (orange) is coupled (purple curly lines) to individual carbon spins (blue) via the magnetic dipole field (black dashed lines) associated with the electron spin. A laser beam (red straight arrow) is used to prepare and read-out the spin state by collecting the florescence (red curly arrow). (**A**) Scanning electron microscope image of the sample. A solid-immersion lens is fabricated with a focused ion beam in single-crystalline diamond for high collection efficiency. An on-chip gold stripline (bottom) enables microwave-control. (**B**) Level scheme for the quantum memory (^{13}C-spin, $I = 1/2$). The hyperfine coupling introduces energy level splittings (ω_0 and ω_1) that depend on the state of the electron spin, where $\omega_0 = (2\pi)\gamma_c B$ with γ_c the gyromagnetic ratio of the carbon spin and B the magnetic field and ω_1 depends on the hyperfine coupling, which is set by the distance to the electron spin. (**C**) Relevant ground-state energy levels of the electron spin ($S = 1$). The degeneracy of the $m_s = \pm 1$ states is lifted by applying a magnetic field along the quantization axis of the NV-center. We define the electron spin qubit in the $|0\rangle \equiv |m_s = 0\rangle$, $|1\rangle \equiv |m_s = +1\rangle$ manifold. Here $B_z = (303 \pm 1)\,\mathrm{G}$ leading to an energy level splitting $\omega_e \approx (2\pi)\,3.73\,\mathrm{GHz}$. (**D**) Diagram of the electron spin including the relevant ground-, and excited-state levels. At low temperature the zero phonon line ($\approx 637\,\mathrm{nm}$) exhibits spin-preserving optical transitions that can be addressed selectively. In the experiment, two lasers with different frequency are used to address the E' transition for electron spin initialization (solid red) and the E_y transition for readout (fidelity $= 0.93(5)$) and generating spin-photon entanglement (dashed red).

input parameters for the theoretical calculations.

At the heart of the experiment is a single Nitrogen-Vacancy (NV) center in high purity (Type IIa) single-crystal diamond grown by chemical-vapor-deposition. The diamond is mounted in a bath cryostat at a temperature of $T = 4.2\,\mathrm{K}$. It has a natural abundance (1.1%) of ^{13}C spins in an otherwise spin-free lattice. The NV electronic spin is polarized and measured optically by spin-selective resonant excitation[12,23,24]. To obtain high single-shot readout fidelities, a solid-immersion lens was fabricated on top of the NV center and a single-layer aluminum-oxide anti-reflective coating was deposited[13] (Fig. 4.1). The electronic spin is controlled by microwaves applied through an on-chip line (Rabi frequency: 3.3 MHz).

We detect and control multiple ^{13}C nuclear spins in the spin bath surrounding the NV center using recently developed methods that coherently exploit the electron-nuclear interaction by periodically switching the electron state at well-defined times[20,25–27]. We apply sequences of the form $(\tau - \pi - 2\tau - \pi - \tau)^{(M/2)}$, where π denotes a microwave pulse that rotates the electron by 180 degrees, 2τ is the interpulse delay and M the total number of π-pulses. For τ precisely resonant with the electron-nuclear dynamics, this sequence imprints a phase on the electron spin conditional on the nuclear spin state.

Because the hyperfine interaction is determined by the specific position of each nuclear spin relative to the NV center, the resonance condition for τ is different for each nuclear spin. We can thus characterize the nuclear spin environment[20] by preparing the electron in a superposition state and measuring the phase that is acquired when sweeping τ. Here we select four individual ^{13}C spins to study in more detail, and design controlled gates following Taminiau et al.[27].

The nuclear spin dynamics are characterized by the nuclear spin precession frequencies ω_0 and ω_1, corresponding to the electron spin being in $m_s = 0$ and $m_s = 1$, respectively (see Sec. 4.5). To directly determine the frequencies ω_0, ω_1 and $\mathrm{d}f = (\omega_1 - \omega_0)/2\pi$ for each of the four nuclear spins we perform the experimental sequence[22] shown in Fig. 4.2A. The electron is prepared in state $\rho_{0,e} = |0\rangle\langle 0|$, whereas the nuclear spin state is un-polarized (mixed state $\rho_{m,C} = (|0\rangle\langle 0| + |1\rangle\langle 1|)/2$). The first set of gates correlates the electron state with the X-projection of the nuclear spin state, so that the state is $\rho_{0,e} \otimes \rho_{X,C} + \rho_{1,e} \otimes \rho_{-X,C}$, with $\rho_{\pm X,C} = |\pm X\rangle\langle \pm X|$ and $|\pm X\rangle = (|0\rangle_C \pm |1\rangle_C)/\sqrt{2}$. The controlled nuclear spin rotations are realized by the pulse sequences described above, with τ resonant for that specific spin. Second, the nuclear spin evolves freely, either with ω_0 or with ω_1, depending on the electron state. Finally the phase accumulation of the nuclear spin is measured by correlating it to the electron spin before reading out the electron spin.

The beating observed in the signal directly yields the frequency difference $\mathrm{d}f$ and therefore the additional phase picked up due to the time the electron spent in $m_s = +1$. For the four spins we find $\mathrm{d}f = (29.6 \pm 0.6), (-32.2 \pm 0.3), (38.6 \pm 0.2)$ and $(45.6 \pm 0.6)\,\mathrm{kHz}$ respectively. These values show that several nuclear spins with coupling strengths between $20 - 50\,\mathrm{kHz}$ are readily available in diamond samples with a natural abundance of ^{13}C.

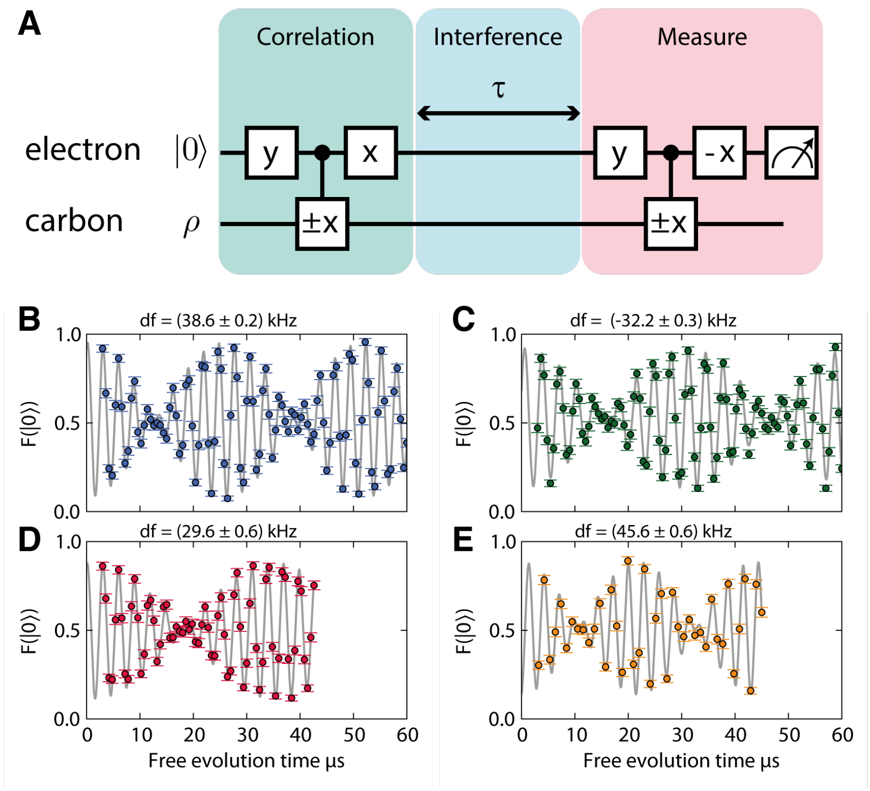

4

Figure 4.2 | Characterization of single ^{13}C spins. (**A**) Circuit diagram to determine ω_0 and ω_1 of individual ^{13}C spins via the electron spin. The conditional gates on the carbon spin are implemented using resonant dynamical decoupling techniques as explained in the main text. Because the evolution of the carbon spin is correlated with an eigenstate of the electron spin during the interference, a coherent signal can be observed even for $\tau \gg T^{*}_{2,\mathrm{electron}} = (4.18 \pm 0.01)\,\mu$s. (**B**)-(**E**) The resulting interference signal measured for four individual ^{13}C spins near a single NV-center. Grey lines are fits to the data with function $F = \frac{A}{2}\cos(\omega_0\tau + \phi_0) + \frac{B}{2}\cos(\omega_1\tau + \phi_1) + c$. We find $\omega_0/2\pi = (326.0 \pm 0.2), (325.9 \pm 0.2), (325.1 \pm 0.5), (325.9 \pm 0.4)$ kHz (B-E), consistent with the gyromagnetic ratio of a ^{13}C spin in a field of (303 ± 1) G. For the second frequency component we find $\omega_1/2\pi = (364.6 \pm 0.1), (293.7 \pm 0.2), (354.7 \pm 0.5), (371.5 \pm 0.4)$ kHz. The data are taken with 500 repetitions per data point and the error bars correspond to one standard deviation.

4.3. A MODEL FOR CARBON SPIN DEPHASING DURING ENTANGLEMENT GENERATION

We analyze the performance of ^{13}C spins as quantum memory in the context of the heralded entanglement protocol proposed by Barrett and Kok[28], which was implemented by Bernien et al.[6]. The protocol is based on the creation of spin-photon entanglement at both nodes, followed by two-photon interference and measurement of these photons. The protocol is probabilistic since it is susceptible to photon loss. Importantly, successful generation of entanglement is heralded by the detection of the two photons and thus the sequence can be repeated until successful.

Spin-photon entanglement is created using the following sequence. The electron spin is prepared in state $|0\rangle_e$ by optical pumping (Fig. 4.3). Using microwaves the electron spin is then brought in a coherent superposition. Next, the NV center is optically excited with a short laser pulse that is only resonant if the spin is in state $|0\rangle_e$. Spontaneous emission generates a photon that is entangled with the state of the spin: $|\Psi\rangle = \frac{1}{\sqrt{2}}(|0\rangle_e|1\rangle_P + |1\rangle_e|0\rangle_P)$ where $|1\rangle_P$ ($|0\rangle_P$) denotes the presence (absence) of a photon. The goal is that the nuclear spin memory reliably stores quantum states during many repetitions of this sequence.

The performance of a quantum memory can be characterized by its ability to store an unknown quantum state $|\psi\rangle = \alpha|0\rangle_c + \beta e^{i\varphi}|1\rangle_c$. During the spin-photon entanglement sequences the phase of the nuclear spin state is affected in two ways. First, when the emitted photon is lost (heralding fails), the electron spin state is randomly projected into either $|0\rangle_e$ or $|1\rangle_e$ resulting in nuclear spin evolutions with ω_0 or ω_1, respectively. Second, before the next repetition, the electron spin is reset by optical pumping, a stochastic process that introduces a distribution of spin flip times. These two effects are now analyzed separately.

After a single round of optical excitation that generates spin-photon entanglement, the electron spin is projected into an unknown eigenstate if the photon is lost. The carbon spin acquires a phase $d\omega t$ if the electron is projected in $|1\rangle_e$, where $d\omega = (2\pi)\, df$ and t the time at which the reset is applied. When this process is repeated N times, the number of times k that the electron is projected in $|1\rangle_e$ is given by a binomial distribution and the final state fidelity F of the carbon spin state is given by:

$$F = \frac{1}{2} + \frac{1}{2^{N+1}} \sum_{k=0}^{N} \binom{N}{k} \cos\left(k\, d\omega t\right) \tag{4.1}$$

where the electron spin reset is taken to be instantaneous and we only consider that the initial memory state is $|\psi\rangle = \frac{1}{\sqrt{2}}(|0\rangle_c + |1\rangle_c)$. Figure 4.3B shows the calculated fidelity as a function of the time t, for two carbon spins that were identified in Fig. 4.2. For each carbon spin there is a unique condition at $t = 2\pi/d\omega$, for which the phase is independent on the electron state resulting in $F = 1$. Note that in the full entanglement protocol[6,28] an electron π-pulse is applied between rounds of excitation, so that this phase difference can be cancelled for all t.

In reality the reset of the electron spin by spin pumping is a stochastic process because it involves multiple transitions to the optically excited state, as well as mixing between multiple excited states. Here we model the dynamics of this process an exponential distribution $e^{-t'/\tau_{\mathrm{reset}}}$ with a characteristic time τ_{reset}. In Fig. 4.3C we compare the results of a Monte-Carlo simulation that includes the probabilistic reset time t' with the curve

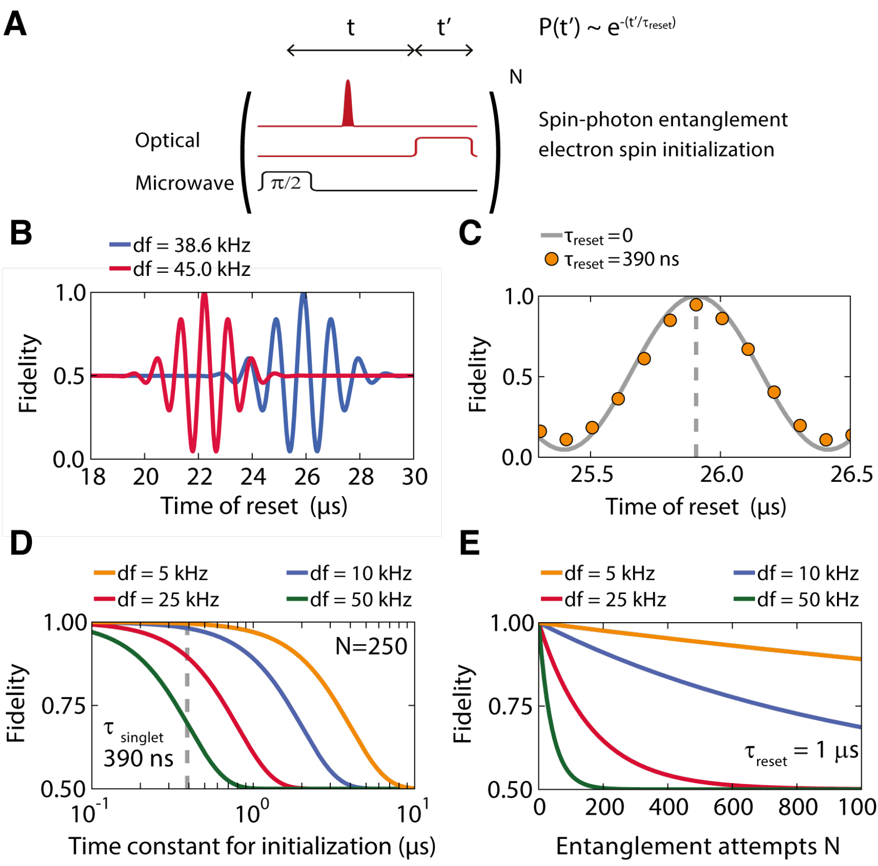

Figure 4.3 | Simulations of the dephasing of a ^{13}C spin quantum memory while generating entanglement. (**A**) Diagram for the single-photon heralding protocol to create entanglement. (**B**) Simulations of the fidelity for different ^{13}C spins after $\mathrm{N} = 50$ repetitions of the protocol, assuming that the reset is instantaneous ($t' = 0$, Eq. (4.1)). The initial state of a carbon spin can be perfectly preserved by choosing the time between the $\pi/2$-pulse and the reset to $t = 2\pi/d\omega$. (**C**) The effect of the spin pumping process on the fidelity of the memory after $\mathrm{N} = 50$ repetitions. Orange dots are a Monte-Carlo simulation where for every electron spin reset, a time t' is drawn from an exponential probability distribution with $\tau_{\text{reset}} = 390\,\text{ns}$. Grey line is a comparison with an ideal reset. $d\omega = (2\pi)\,38.6\,\text{kHz}$ (**D**) Dependence of the memory fidelity on the characteristic reset time τ_{reset} using Eq. (4.2). (**E**) Dephasing of the memory as a function of entanglement attempts for different coupling strengths, fixing $\tau_{\text{reset}} = 1\,\mu\text{s}$.

of Eq. (4.1). As expected the same behavior is observed, but the maximum fidelity is reduced since the stochastic reset leads to dephasing of the carbon spin.

To analyze the effect of the electron spin reset on the nuclear spin in detail we now assume that $t = 2\pi/d\omega$ which allows us to derive an analytical expression for the fidelity of the carbon spin (see Sec. 4.5 for the derivation of this result):

$$F = \frac{1}{2} + \frac{1}{2^{N+1}}\left(1 + e^{-\frac{1}{2}\tau_{\mathrm{reset}}^2 d\omega^2}\right)^N \tag{4.2}$$

In Fig. 4.3D we plot the resulting memory fidelity after 250 entanglement repetitions versus the reset constant τ_{reset}, for different values of $\mathrm{d}f$. Although for an instantaneous reset ($\tau_{\mathrm{reset}} \rightarrow 0$) the state can be perfectly preserved, a finite uncertainty in the reset time constant reduces the fidelity, with the effect being stronger for higher coupling strengths $\mathrm{d}f$. A natural lower limit to the reset time τ_{reset} is the slowest decay rate involved in the spin pumping process. For the NV center this is expected to be the singlet lifetime $\tau_{\mathrm{singlet}} \approx 390\,\mathrm{ns}$[29]. For this value, Fig. 4.3D predicts that for coupling strengths of $df < 10\,\mathrm{kHz}$ the state can be preserved with a fidelity of $> 98\,\%$ even after 250 entanglement attempts.

The reset constants currently reported in the literature are approximately $1\,\mu\mathrm{s}$[6]. In Fig. 4.3E we plot the fidelity as a function of number of entanglement attempts for $\tau_{\mathrm{reset}} = 1\,\mu\mathrm{s}$. These calculations predict that 25 repetitions of the entanglement protocol will yield a fidelity of 90.3 % for the lowest coupling strength found in Fig. 4.2, which would already provide significant speed advantages in establishing entanglement links[8]. For coupling strengths $df < 10\,\mathrm{kHz}$, hundreds of repetitions become feasible. Such lower coupling strengths are available in isotopically purified diamonds[21].

We emphasize that the model presented here does not include the detailed excited state dynamics of the spin pumping process. We expect that averaging over rapid spin flips and time spent in states with zero spin projection during these dynamics will further reduce actual dephasing. We therefore expect that our analysis sets a lower bound for the number of possible repetitions.

4.4. ^{13}C SPINS ARE PROMISING QUANTUM MEMORIES

We have modelled the dephasing of nuclear spins quantum memories coupled to an electron spin that is repeatedly used to establish spin-photon entanglement. We find that nuclear spins with weak hyperfine couplings (20 – 50 kHz) are readily available and can be used to store quantum states during 25 entanglement attempts with a fidelity of 90.3 %, while nuclear spins in isotopically purified samples with coupling strengths below 10 kHz can enable hundreds of repetitions. These results demonstrate that nuclear spins with weak hyperfine coupling strengths are promising quantum memories for quantum networks and provide a route towards entanglement distillation and quantum repeaters.

CONTRIBUTIONS

N.K. developed and analysed the theoretical model. T.H.T. devised and performed the shown experiments. M.S.B. wrote the original manuscript with input from all authors.

N.K. adapted the original manuscript for this thesis.

4.5. METHODS

We take the limit of $\gamma_c B \gg A_\perp$ (with $A_\perp$ the hyperfine component perpendicular to the static magnetic field) such that the eigenstates of the ^{13}C-spin are independent of the electron and the only net effect of the electron-carbon coupling is that the carbon acquires a phase depending on the state of the electron. Choosing the rotating frame of the carbon resonant with the energy splitting for the electron in $|0\rangle_e$, the carbon state will acquire a phase $e^{id\omega t}$ for the electron in $|1\rangle_e$ (with $d\omega = (2\pi)\,df$) and does not evolve otherwise.

We derive an expression for the maximally achievable memory. The scheme of Fig. 4.3A is repeated N times. Phase errors occur if the electron spin has to be reinitialized by pumping it to another spin state. During every execution of the protocol, the electron spin is projected into $|0\rangle_e$ or $|1\rangle_e$ with equal probability. The probability for k repumping events is then given by a binomial distribution

$$P_{ek} = \frac{1}{2^N}\binom{N}{k} \tag{4.3}$$

Every time the electron is reset from $|1\rangle_e$ into $|0\rangle_e$ the memory spin will pick up a random phase $\delta\theta = d\omega(t' - \tau_{\text{reset}})$ which is given by the difference between energy levels of the carbon spin conditional on the electron spin $d\omega$ and the deviation $(t' - \tau_{\text{reset}})$ from the mean repumping time. The overall acquired phase for k repumping events is then the sum of the individual random phases. The fidelity with the initial memory state after N repetitions is thus given by

$$F_k = \frac{1}{2}(1 + \cos(\sum_{k=0}^{N} \delta\theta)) \tag{4.4}$$

Under the assumption that the distributions for all repumping events are independent the problem can be seen as a random walk in accumulated repumping time. Each step of this random walk is then exponentially distributed around the mean repumping time τ_{reset}. The probability distribution of the summed repumping time is given by[30]

$$P(t') = \frac{t'^{k-1}}{\tau_{\text{reset}}^{k}(k-1)!} e^{-t'/\tau_{\text{reset}}} \approx \frac{1}{\sigma\sqrt{2\pi}} e^{-\frac{(t'-\mu)^2}{2\sigma^2}} \tag{4.5}$$

where we use the central limit theorem to approximate this distribution by a normal distribution with width $\sigma = \tau_{\text{reset}}\sqrt{k}$ and mean $\mu = \tau_{\text{reset}} k$, as we are interested in solutions for a large number of repumping events. The expected fidelity after N experimental runs is calculated by summing over the probability distributions for the electronic state and the corresponding accumulated repumping time

$$\begin{aligned} F_N = {} & \sum_{k=0}^{N} P_{ek}\int F_k P(t')\,dt' \\ = {} & \frac{1}{2}+\frac{1}{2}\sum_{k=0}^{N} P_{ek}\, e^{-\frac{1}{2}k\tau_{\text{reset}}^2 d\omega^2} \\ = {} & \frac{1}{2}+\frac{1}{2^{N+1}}\left(1+e^{-\frac{1}{2}\tau_{\text{reset}}^2 d\omega^2}\right) \end{aligned} \tag{4.6}$$

REFERENCES

[1] W. B. Gao, A. Imamoglu, H. Bernien and R. Hanson, *Coherent manipulation, measurement and entanglement of individual solid-state spins using optical fields,* Nature Photonics **9**, 363 (2015).

[2] H. J. Kimble, *The quantum internet,* Nature **453**, 1023 (2008).

[3] D. L. Moehring *et al.*, *Entanglement of single-atom quantum bits at a distance,* Nature **449**, 68 (2007).

[4] S. Ritter *et al.*, *An elementary quantum network of single atoms in optical cavities,* Nature **484**, 195 (2012).

[5] J. Hofmann *et al.*, *Heralded Entanglement Between Widely Separated Atoms,* Science **337**, 72 (2012).

[6] H. Bernien *et al.*, *Heralded entanglement between solid-state qubits separated by three metres,* Nature **497**, 86 (2013).

[7] C. H. Bennett *et al.*, *Purification of Noisy Entanglement and Faithful Teleportation via Noisy Channels,* Physical Review Letters **76**, 722 (1996).

[8] E. T. Campbell and S. C. Benjamin, *Measurement-Based Entanglement under Conditions of Extreme Photon Loss,* Physical Review Letters **101**, 130502 (2008).

[9] H.-J. Briegel, W. Dür, J. I. Cirac and P. Zoller, *Quantum Repeaters: The Role of Imperfect Local Operations in Quantum Communication,* Physical Review Letters **81**, 5932 (1998).

[10] L. Childress, J. M. Taylor, A. S. Sørensen and M. D. Lukin, *Fault-Tolerant Quantum Communication Based on Solid-State Photon Emitters,* Physical Review Letters **96**, 070504 (2006).

[11] L. Childress and R. Hanson, *Diamond NV centers for quantum computing and quantum networks,* MRS Bulletin **38**, 134 (2013).

[12] E. Togan *et al.*, *Quantum entanglement between an optical photon and a solid-state spin qubit,* Nature **466**, 730 (2010).

[13] W. Pfaff *et al.*, *Unconditional quantum teleportation between distant solid-state quantum bits,* Science **345**, 532 (2014).

[14] F. Jelezko, T. Gaebel, I. Popa, A. Gruber and J. Wrachtrup, *Observation of Coherent Oscillations in a Single Electron Spin,* Physical Review Letters **92**, 076401 (2004).

[15] M. V. G. Dutt *et al.*, *Quantum Register Based on Individual Electronic and Nuclear Spin Qubits in Diamond,* Science **316**, 1312 (2007).

[16] P. Neumann *et al.*, *Multipartite Entanglement Among Single Spins in Diamond,* Science **320**, 1326 (2008).

[17] B. Smeltzer, J. McIntyre and L. Childress, *Robust control of individual nuclear spins in diamond,* Physical Review A **80**, 050302 (2009).

[18] G. D. Fuchs, G. Burkard, P. V. Klimov and D. D. Awschalom, *A quantum memory intrinsic to single nitrogen-vacancy centres in diamond,* Nature Physics **7**, 789 (2011).

[19] T. van der Sar *et al.*, *Decoherence-protected quantum gates for a hybrid solid-state spin register,* Nature **484**, 82 (2012).

[20] T. H. Taminiau *et al.*, *Detection and Control of Individual Nuclear Spins Using a Weakly Coupled Electron Spin,* Physical Review Letters **109**, 137602 (2012).

[21] P. C. Maurer *et al.*, *Room-Temperature Quantum Bit Memory Exceeding One Second,* Science **336**, 1283 (2012).

[22] A. Laraoui *et al.*, *High-resolution correlation spectroscopy of ^{13}C spins near a nitrogen-vacancy centre in diamond,* Nature Communications **4**, 1651 (2013).

[23] P. Tamarat *et al.*, *Spin-flip and spin-conserving optical transitions of the nitrogen-vacancy centre in diamond,* New Journal of Physics **10**, 045004 (2008).

[24] L. Robledo *et al.*, *High-fidelity projective read-out of a solid-state spin quantum register,* Nature **477**, 574 (2011).

[25] S. Kolkowitz, Q. P. Unterreithmeier, S. D. Bennett and M. D. Lukin, *Sensing Distant Nuclear Spins with a Single Electron Spin,* Physical Review Letters **109**, 137601 (2012).

[26] N. Zhao *et al.*, *Sensing single remote nuclear spins,* Nature Nanotechnology **7**, 657 (2012).

[27] T. H. Taminiau, J. Cramer, T. van der Sar, V. V. Dobrovitski and R. Hanson, *Universal control and error correction in multi-qubit spin registers in diamond,* Nature Nanotechnology **9**, 171 (2014).

[28] S. D. Barrett and P. Kok, *Efficient high-fidelity quantum computation using matter qubits and linear optics,* Physical Review A **71**, 060310 (2005).

[29] M. W. Doherty *et al.*, *The nitrogen-vacancy colour centre in diamond,* Physics Reports **528**, 1 (2013).

[30] Mohamed Akkouchi, *On the convolution of exponential distributions,* Journal of the Chungcheong Mathematical Society **21** (2008).

5

ROBUST QUANTUM-NETWORK MEMORY USING DECOHERENCE-PROTECTED SUBSPACES OF NUCLEAR SPINS

A. Reiserer*, N. Kalb*, M.S. Blok, K.J.M. van Bemmelen, T.H. Taminiau,
R. Hanson, M. Markham and D.J. Twitchen

The realization of a network of quantum registers is an outstanding challenge in quantum science and technology. We experimentally investigate a network node that consists of a single nitrogen-vacancy (NV) center electronic spin hyperfine-coupled to nearby nuclear spins. We demonstrate individual control and readout of five nuclear spin qubits within one node. We then characterize the storage of quantum superpositions in individual nuclear spins under repeated application of a probabilistic optical inter-node entangling protocol. We find that the storage fidelity is limited by dephasing during the electronic spin reset after failed attempts. By encoding quantum states into a decoherence-protected subspace of two nuclear spins we show that quantum coherence can be maintained for over 1000 repetitions of the remote entangling protocol. These results and insights pave the way towards remote entanglement purification and the realisation of a quantum repeater using NV center quantum network nodes.

The results in this chapter have been published in Physical Review X **6**, 021040 (2016).

*Equally contributing authors

5.1. NVS AS NODE FOR LAYERED QUANTUM NETWORKS

Linking multi-qubit nodes into a large-scale quantum network[1–4] will open up exciting opportunities ranging from fundamental tests[5] and enhanced time-keeping[6] to applications in quantum computing and cryptography[1,7–9]. Pioneering experiments with atomic ensembles[3], single atoms trapped in vacuum[2,4,10,11] and spins in solids[12–14] have demonstrated entanglement between two optically connected nodes. Directly extending these schemes to quantum networks involving many nodes and spanning large distances is hindered by unavoidable imperfections, including photon loss and local control errors, which cause the success probability and entanglement fidelity to decay rapidly both with number of nodes and with distance.

These challenges can be overcome via entanglement purification[15] in a repeater-type[16] setting that exploits quantum memories within each node[7,17,18]. Crucially, one needs to control and readout individual qubits within the node as well as create entanglement with remote qubits without inducing decoherence on the other qubits in the node. In principle, each of these tasks can be accomplished probabilistically using detectors and quantum memories for single optical photons[19], but the resulting inefficiency poses a severe challenge for practical quantum network realizations[2,3]. Instead, many efforts are geared towards a layered architecture, as depicted in Fig. 5.1A. Here, remote quantum nodes are *probabilistically* coupled via optical photons, while each node has several *deterministically* addressable memory qubits that do not interact with and are therefore not disturbed by the optical channel.

A promising candidate for implementing such a quantum network architecture is the nitrogen-vacancy (NV) center in diamond. The NV electronic spin provides an optical interface that can be used to establish entanglement between distant nodes[13,20,21], while nearby nuclear spins can serve as multi-qubit registers[22–25] with second-long coherence times demonstrated in isolation[26]. Here, we address the open challenge of robust simultaneous execution of these two processes — remote entanglement generation and local qubit storage — which is a key prerequisite for entanglement purification and quantum repeaters and therefore a critical task in quantum networks. We implement individual control over five nuclear spin qubits, in which we store quantum states while repeatedly using the electronic spin in a sequence which has previously been used to generate inter-node entanglement[13,20,21]. We study in detail how the fidelity of storage depends on the coupling between electronic and nuclear spins and on the average time the electronic spin is in an unknown quantum state. We then use decoherence-protected subspaces (DPSs) to enhance the robustness of quantum state storage, which enables us to increase the exponential decay constant of the qubit fidelity above 1000 repetitions of the inter-node entangling sequence.

5.2. EXPERIMENTAL SETTING

The experiments are performed on a diamond device with a natural abundance of ^{13}C nuclear spins ($I = 1/2$, $m_I = 1/2 \equiv |\uparrow\rangle$, $m_I = -1/2 \equiv |\downarrow\rangle$). We cool the device to a tem-

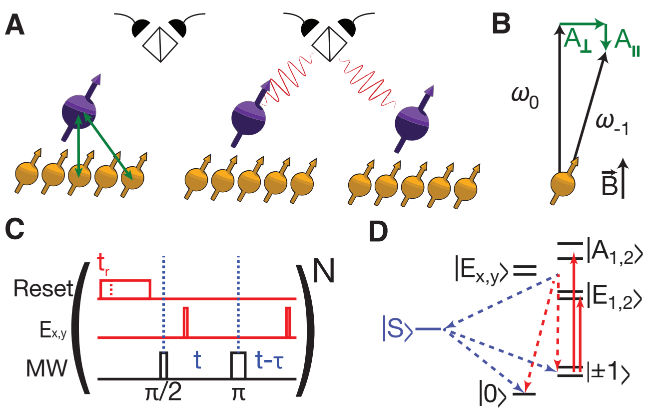

Figure 5.1 | (**A**) Layered quantum network architecture. Individual electronic spins (purple spin symbols) are entangled probabilistically over large distances using photons (red curly lines). Each electronic spin is hyperfine coupled to a quantum register of surrounding nuclear spins (yellow) that can be deterministically controlled (green arrows). (**B**) Electron-nuclear coupling. The nuclear spins precess in an external magnetic field $\vec{B}$. The precession axis and frequency, ω_0 or ω_{-1}, (black vectors) depend on the state of the electronic spin, $|0\rangle$ or $|-1\rangle$, via the hyperfine interaction with parallel component $A_\parallel$ and perpendicular component $A_\perp$ (green vectors). (**C**) Experimental sequence to generate entanglement between remote NV electronic spins[27]. By optical pumping on the "Reset" transition, the spin is initialized in $|0\rangle$ at time t_r. Subsequently, a spin superposition state is created via a microwave $\pi/2$ pulse. Spin-photon entanglement is then generated via two optical excitations, separated by a microwave π-pulse that inverts the spin state $|0\rangle \leftrightarrow |-1\rangle$. (**D**) NV electronic orbital and spin level scheme at cryogenic temperature. The ground states $|0\rangle$ ($|\pm1\rangle$) are optically coupled to the excited states $|E_{x,y}\rangle$ ($|E_{1,2}\rangle$ and $|A_{1,2}\rangle$, red arrows), respectively. These states decay either directly (red dashed arrows) or via the metastable spin singlet states $|S\rangle$ (blue dashed arrows) to one of the ground states.

perature of 4 K in a Helium bath cryostat and apply a magnetic field of 40 mT along the NV symmetry axis. Before each experimental run we prepare the NV center in the negative charge state and ensure resonance with the lasers[23]. By using spin-selective optical transitions the electronic spin ($S = 1$, $m_s = 0 \equiv |0\rangle$, $m_s = \pm1 \equiv |\pm1\rangle$) is initialized with a fidelity above 0.99 and readout in a single shot with an average fidelity of about 0.94. We employ tailored pulse sequences on the electronic spin[28,29] that yield high-fidelity individual control of five ^{13}C spin qubits surrounding the NV center studied here (the same as in Ref. 29). In Table 5.1 we list for each nuclear spin qubit the measured hyperfine coupling parameters, the dephasing time T_2^* and the combined fidelity of spin initialization and readout $F_{i,r}$.

We now focus on nuclear spin coherence during application of the Barrett-Kok internode entangling sequence[27] (see Fig. 5.1C) that was used in recent experiments[13,20,21]. This protocol has two steps. First, entanglement between the electronic spin and the emission time of a single photon is created at both nodes. Subsequently the two pho-

^{13}C number	$\frac{\Delta\omega}{2\pi}$ (kHz)	$A_\parallel$ (kHz)	$A_\perp$ (kHz)	T_2^* (ms)	$F_{i,r}$
1	-15.4	-11.0	55	6(1)	0.89(2)
2	18.4	21.2	43	13(1)	0.96(2)
3	23.7	24.7	26	19(2)	0.97(2)
4	-37.0	-36.0	25	10(1)	0.92(2)
5	-48.6	-48.7	12	4(1)	0.90(2)

Table 5.1 |Experimentally determined parameters of the five ^{13}C nuclear spin qubits used in this work: hyperfine couplings $\mathrm{A}_\parallel$ and $\mathrm{A}_\perp$, precession frequency difference $\Delta\omega$, and combined initialization and readout fidelity $\mathrm{F}_{\mathrm{i,r}}$. The hyperfine parameters are measured via dynamical decoupling spectroscopy[30] and have an uncertainty in the last digit.

tons are measured after interfering on a beamsplitter, probabilistically projecting the electronic spins into a maximally entangled state. Because of unavoidable inefficiencies including photon loss, this sequence has to be repeated many times to generate remote entanglement with a high probability.

Each time an entanglement attempt fails the electronic spin of the NV center is projected into an unknown state and has to be reset. This can lead to decoherence of the surrounding nuclear spin quantum memories via the (always-on) hyperfine interaction. The interaction Hamiltonian is in secular approximation:

$$H_{hf}/2\pi = A_\parallel S_z I_z + A_\perp S_z I_x. \tag{5.1}$$

Here, S and I denote the electronic and nuclear spin operators, respectively, and $A_\parallel$ ($A_\perp$) denote the parallel (perpendicular) hyperfine coupling strength. If the electronic spin state is $|0\rangle$, the nuclear spin will precess at the Larmor frequency $\omega_0 = 2\pi \times \gamma|\vec{B}|$ around the applied magnetic field $\vec{B}$ (see Fig. 5.1B), where $\gamma = 11$ kHz/mT is the nuclear gyromagnetic ratio. If the electronic spin state is $|-1\rangle$, however, the nuclear spin will precess around a slightly tilted axis and at a different frequency $\omega_{-1} = 2\pi \times \sqrt{(\gamma|\vec{B}| + A_\parallel)^2 + A_\perp^2}$. In a sufficiently strong magnetic field, $\gamma|\vec{B}| \gg \sqrt{A_\perp^2 + A_\parallel^2}$, the change in precession axis is quadratically suppressed and nuclear spin decoherence is mainly caused by dephasing due to the linear change in the precession frequency

$$\Delta\omega = \omega_0 - \omega_{-1} \simeq 2\pi \times A_\parallel. \tag{5.2}$$

Thus, randomisation of the electronic spin state is expected to lead to dephasing of a nuclear spin on a timescale that is inversely proportional to the parallel hyperfine coupling strength[31,32].

This dephasing can be mitigated by a suited dynamical decoupling sequence[32], which is inherent in the Barrett-Kok entangling sequence (Fig. 5.1C): for $\tau = 0$, the time interval between the microwave (MW) $\pi/2$ pulse and the MW π pulse has the same duration as the time interval between the MW π pulse and the start of the electronic spin reset.

Thus, the electronic spin will be in $|0\rangle$ and $|-1\rangle$ for an equal amount of time, irrespective of the random optical projection. Thus, under the condition that the spin reset is instantaneous and happens at a precisely known time, the dephasing is exactly nullified. However, electronic spin reset by optical pumping is a stochastic process of finite time duration. As the spin state is not known during this process, it induces irreversible dephasing of the nuclear spins. Therefore, it is desirable to use nuclear spins with weak coupling strength and to make the electronic spin reset as short as possible.

5.3. ELECTRONIC SPIN RESET

We first investigate the spin reset process and optimize the reset time. We initialize the electronic spin in $|0\rangle$ by applying laser fields that are on resonance either with the transitions $|-1\rangle \leftrightarrow |E_1\rangle$ and $|+1\rangle \leftrightarrow |E_2\rangle$ or, for comparison, with the transitions $|-1\rangle \leftrightarrow |A_1\rangle$ and $|+1\rangle \leftrightarrow |A_2\rangle$; see Fig. 5.1D. Compared to our previous remote entanglement experiments[13,20,21], the use of higher magnetic fields requires a second laser beam because of the comparably large ground state Zeeman splitting between $|-1\rangle$ and $|+1\rangle$ of about 2 GHz. The lasers address different excited states to avoid pumping to a coherent dark state. Both repump laser beams have approximately circular polarization and equal power. The excited states have a lifetime on the order of 10 ns[33]. From the excited states, the NV can decay either back to $|\pm 1\rangle$, or to the metastable spin singlet states $|S\rangle$. In addition, spin mixing in the excited states also opens a direct decay channel to $|0\rangle$[34].

To determine the time it takes to reset the spin, we prepare it in $|-1\rangle$ and pump it with the reset lasers for a varying duration. After a delay of $2.5\,\mu$s to ensure that no population is left in the excited or singlet states[34], we measure the population in $|0\rangle$; see Fig. 5.2A. The spin pumping process exhibits a double-exponential decay with a relative amplitude ratio for the fast and slow time scales of around 3:1, which slightly depends on the excited states used. The two timescales of this decay depend on the applied laser power. At high power, the reset timescales saturate (see Sec. 5.8.4) at 29(1) ns and 463(14) ns when driving transitions to $|A_{1,2}\rangle$ (green) and at 48(1) ns and 432(26) ns when driving transitions to $|E_{1,2}\rangle$ (yellow).

We attribute the slower timescale, which is the same for both configurations within measurement uncertainty, to the decay constant of the metastable singlet states. The fitted value is in the same range as previously reported values[35]. The faster timescale has a contribution from both direct spin flip transitions to $|0\rangle$ and transitions into the singlet states which then decay to $|0\rangle$. The difference in fast timescales between the two configurations is explained by different decay rates to the ground states and metastable singlet states from the excited states used[33]. When the laser power is reduced, we observe a gradual increase of both timescales, as shown for the $|A_{1,2}\rangle$ configuration (cyan, blue and black curves).

To obtain additional insight into the spin reset process, we measure the probabilities p_i to arrive in the states $i = |0\rangle, |-1\rangle$, and $|+1\rangle$, again $2.5\,\mu$s after applying a repump pulse of varying duration. In Fig. 5.2B we plot $1 - p_{|0\rangle}$, $p_{|-1\rangle}$, and $p_{|+1\rangle}$. We fit the data to rate equation models (solid lines), one for each repump configuration. These models assume the lifetimes of the individual states as measured in Ref. 33, a lifetime of the metastable singlet states of 440 ns (taken from the above fits), a relative singlet decay ratio R_i to the states i of $(R_{|0\rangle} : R_{|+1\rangle} : R_{|-1\rangle}) = (2:1:1)$[34], and full decay of the singlet and excited states before the ground state population is measured. The model uses equal decay of both excited states $|A_{1,2}\rangle$ to $|\pm 1\rangle$, while the states $|E_{1,2}\rangle$ decay either to $|+1\rangle$ or to $|-1\rangle$[34]. The decay rates of the excited states to $|0\rangle$ and the rate of excitation and stimulated emission caused by the repump laser are free parameters in the model. The quantitative agreement between data and the model strengthens the hypothesis that the slow timescale of the repump process is dominated by the lifetime of the metastable singlet states. The population of the metastable singlet states (before decay to the ground states) predicted by the models is shown as the green dashed curve (see Fig. 5.2).

5.4. SINGLE-NUCLEAR-SPIN QUANTUM MEMORY

We now turn to the dephasing of single nuclear spin qubits induced by the stochastic trajectory of the electronic spin state during reset. Using recently developed techniques[29], we first initialize one of the five controlled nuclear spins by a projective measurement (see Sec. 5.8.1). Ideally, this prepares the nuclear spin superposition state $\frac{1}{\sqrt{2}}(|\downarrow\rangle + |\uparrow\rangle)$. We then perform N repetitions of the remote entanglement sequence. We omit the short optical π pulses, as they are expected to induce negligible nuclear spin dephasing since they preserve the electronic spin eigenstate and can be timed such that the detrimental effect of occasional spin flips ($p_{\text{Flip}} < 1\,\%$)[23] is mitigated by the dynamical decoupling sequence. In addition, the fast optical pulses only lead once per sequence to a population of the excited state, whose spin projection is zero and whose 12 ns lifetime is short compared to the reset procedure. We track the dephasing of the nuclear spins by measuring the length of their Bloch vector projection onto the XY plane. We do not include the Z projection as it remains small. In addition, we discard the small fraction of experimental runs in which the NV electronic spin is ionized (Sec. 5.8.4).

We first investigate and optimize the timings t and τ of the dynamical decoupling sequence shown in Fig. 5.1C. We find that the dephasing rate shows a clear minimum when t equals the Larmor period of the nuclear spins (see Sec. 5.8.2), in which case the effect of entanglement between electronic and nuclear spins caused by the tilted rotation axis, as shown in Fig. 5.1B, is minimized. We therefore set $t = \frac{2\pi}{\omega_0} \simeq 2.3\,\mu$s. We then repeat the entanglement sequence $N = 200$ times and vary the time τ. Assuming an exponential distribution of the repumping time t_r, one expects to obtain the best possible decoupling when τ is equal to $\langle t_r \rangle$[32]. As can be seen in Fig. 5.3A, we observe a broad Gaussian distribution centered around an optimal value of $\tau \approx 0.44\,\mu$s for all four measured nuclear spins, in good agreement with the slow timescale of the initialization process shown in Fig. 5.2A. As mentioned, we attribute this timescale to the decay of the metastable singlet states. At first sight, it is surprising that a singlet state which has zero spin projection and thus no hyperfine coupling would induce dephasing. A possible explanation is that the orbital angular momentum of an E-symmetric singlet state induces a magnetic moment

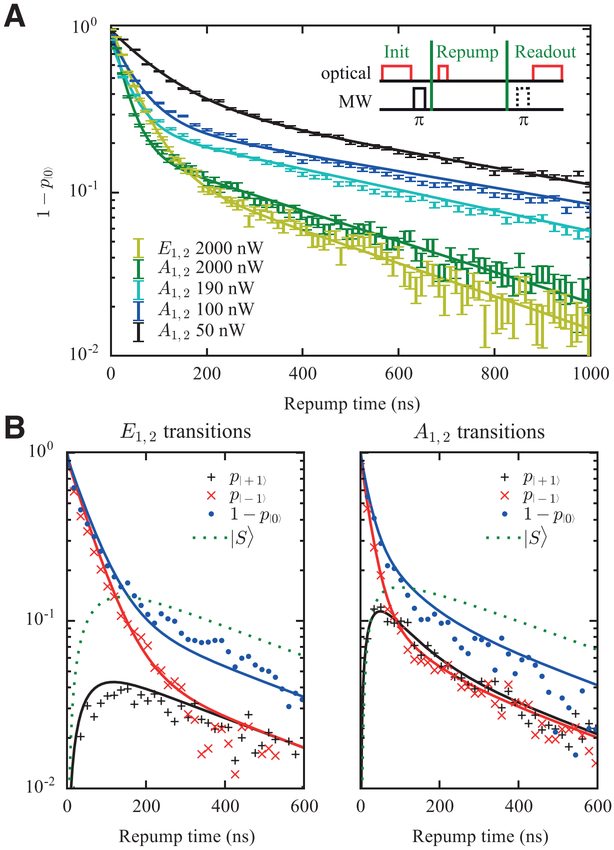

Figure 5.2 | NV electronic spin initialization. (**A**) Probability that the electronic spin is pumped to $|0\rangle$ as a function of the repump laser pulse duration when the spin is initially prepared in $|-1\rangle$. The inset shows the used pulse sequence. We observe a double exponential decay (solid fit curves), with a timescale and relative amplitude that depends on the used "Reset" transition. Reduced laser power leads to slower initialization timescales. (**B**) Probability that the NV is found in state $|0\rangle$, $|+1\rangle$, and $|-1\rangle$ for 2000–nW repump power in the $|E_{1,2}\rangle$ (left) or $|A_{1,2}\rangle$ (right) configuration. The solid lines are calculated using a rate equation model described in the text. For long repumping time, the calculated population in the metastable singlet states (green dashed line) dominates the repumping process.

that is comparable to that of the electronic spin ground states.

Additional dephasing can result from experimental imperfections. To prevent errors caused by imperfect spin initialization, e.g. when the laser power drifts over time, we apply the repump laser longer than required for the initialization curves to saturate below 0.01, which is 2 μs (1.5 μs) for the $|E_{1,2}\rangle$($|A_{1,2}\rangle$) repump configuration at 2000 nW, respectively. To prevent errors caused by imperfect MW pulses, we employ a Hermite pulse

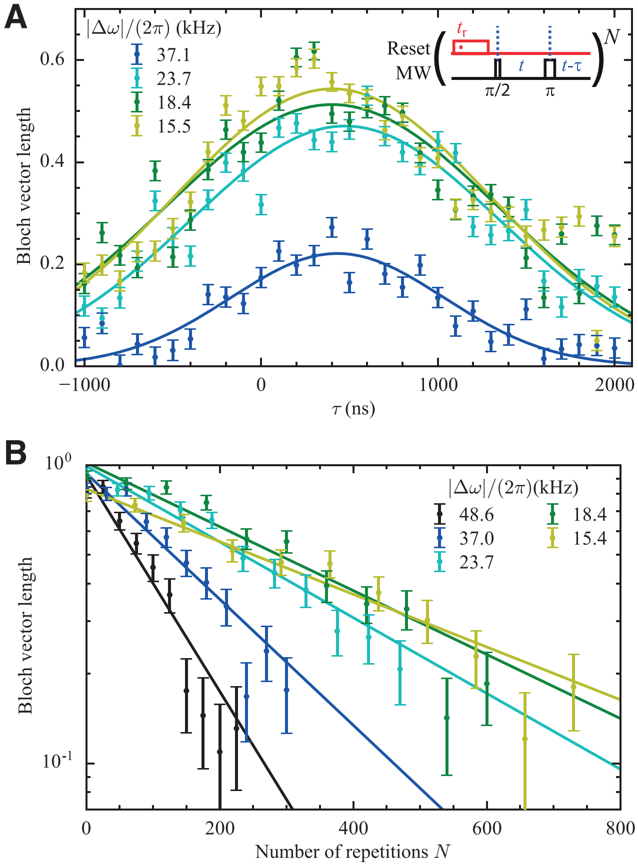

Figure 5.3 | Dephasing of ^{13}C nuclear spins. (**A**) Optimization of the dynamical decoupling sequence timing. Different nuclear spins (colors) are initialized in a balanced superposition state and the entanglement sequence is performed N = 200 times. The duration of the second wait interval is swept and the length of the Bloch vector XY projection is measured. All measured nuclear spins exhibit the same broad optimum around $0.4\,\mu$s, as can be seen from the Gaussian fit curves. (**B**) Dephasing of nuclear spins when the number of random reset processes is increased. The data shows measurement results of all five individually controlled nuclear spins, where increasing coupling strength leads to steeper decay curves. The solid lines are exponential fits.

envelope with a broad spectrum in order to drive the $|0\rangle \leftrightarrow |-1\rangle$ transition irrespective of the spin state of the nitrogen nucleus of the NV center. We employ this pulse in a BB1 composite pulse sequence[36], consisting of five pulses of less than $0.2\,\mu$s duration each, to further suppress pulse errors. In this way, we are able to exclude experimental imperfections as a relevant source of the observed dephasing (see Sec. 5.8.3 for details).

With the optimized timings and pulses, we then vary the number of repetitions N of the remote entanglement sequence. For all five nuclear spins, we observe an exponential decay of the single-qubit coherence with N; see Fig. 5.3B. Even for the nuclear spin with the largest parallel hyperfine coupling — for which the dephasing is fastest — more than $N = 100$ repetitions of the entanglement sequence can be run before the Bloch vector length drops to 1/e. For the nuclear spin with the smallest coupling strength, this number increases to $N \approx 500$. Further improvements could be achieved by using nuclear spins with even lower parallel hyperfine coupling, although this would generally come at the price of an increased duration of local control operations.

5.5. DECOHERENCE-PROTECTED SUBSPACE QUANTUM MEMORY

Motivated by the observation that the memory dephasing is mainly determined by the parallel hyperfine coupling strength, we investigate a different approach to increasing the maximum number of repetitions before a qubit is dephased. Instead of encoding the qubit in a single nuclear spin, we can encode in a decoherence-protected subspace (DPS) [37] of two or more nuclear spins. In this way, the net parallel hyperfine coupling can be strongly reduced while the speed of the individual quantum gates remains the same.

A natural choice for a DPS with reduced dephasing is given by the basis states $|\downarrow_i\uparrow_j\rangle$ and $|\uparrow_i\downarrow_j\rangle$ of nuclear spins i and j with comparable parallel hyperfine coupling strength. An encoded qubit will then to first order dephase at a rate that is determined by the coupling strength *difference* $\Delta\omega \simeq 2\pi \times (A_{\parallel,i} - A_{\parallel,j})$, which can be much smaller than the individual coupling strengths. On the other hand, encoding a qubit in the states $|\uparrow_i\uparrow_j\rangle$ and $|\downarrow_i\downarrow_j\rangle$ will lead to increased dephasing rates.

To experimentally verify these expectations, we create the states $(|\downarrow_i\uparrow_j\rangle + |\uparrow_i\downarrow_j\rangle)/\sqrt{2}$ and $(|\uparrow_i\uparrow_j\rangle + |\downarrow_i\downarrow_j\rangle)/\sqrt{2}$ (see Sec. 5.8.1 and Ref. 29) and measure the qubit state projection onto the XY plane of the Bloch sphere under the remote entangling protocol. Fig. 5.4A shows the results obtained for nuclear spins 2 and 3. When initializing the qubit in a decoherence-protected (decoherence-enhancing) two-spin state, we observe a strong improvement (reduction) of the maximum number of repetitions. In the DPS case, we can perform more than one thousand repetitions before the Bloch vector length drops to 1/e. This decay constant can be fully explained by the intrinsic dephasing time T_2^* of the nuclear spins (see Sec. 5.8.5). This shows that the dephasing induced by the entanglement protocol has become negligible in this DPS quantum memory.

The coherence of a DPS with small effective coupling strength might also be limited by the population decay (T_1) of the individual spins induced by the entanglement protocol. For the current sample, we find an exponential decay of population with N with decay constants in the range of 1000 to 10000 repetitions, depending on the individual nuclear spins used (see Sec. 5.8.5). We note that this effect is not limiting the coherence of the two-qubit DPS investigated here, but we expect it to become relevant for the smallest investigated coupling strengths once the intrinsic dephasing (with T_2^* times of a few milliseconds in the current sample; see Table 5.1) is canceled by an echo.

5.6. SCALING OF THE DEPHASING RATE WITH HYPERFINE COUPLING STRENGTH AND REPUMP DURATION

Finally, we perform an extensive quantitative investigation of the scaling of dephasing with the coupling strength and with the time it takes to reset the electronic spin. Fig. 5.4B shows the number of entanglement sequence repetitions $N_{1/e}$ for which the state fidelity of a balanced superposition state decays to 1/e of the initial value [i.e. the fitted decay constant in 5.4A]. We investigate all 5 individual nuclear spins (open circles) and all 20 possible two-spin subspaces (filled circles), whose coupling strength is the sum or difference of the individual ones. The depicted five data sets correspond to the different values of the repumping time constants shown in Fig. 5.2. To ensure that we only investigate the scaling of the dephasing with coupling strength and repump duration, we correct for the effects of T_2^* decay, which becomes dominant for the leftmost three data points (see Sec. 5.8.5) and could be compensated by a suited echo sequence on the nuclear spins[26].

We compare the data to the model of Blok et al.[32], which assumes an exponentially distributed repump timescale and that the NV stays in the ground state $|-1\rangle$ until it is reset. When the value of τ used in the dynamical decoupling sequence is equal to the average repump time $\langle t_r \rangle$, a nuclear spin has acquired a phase shift of $\Delta\omega(t_r-\tau)$ until the electronic spin is reset to $|0\rangle$. In the limit of large N, the binomial probability distribution of required electronic spin resets can be approximated by a Gaussian distribution. For a balanced superposition input state, as investigated here, this leads to a predicted qubit fidelity of

$$F = \frac{1}{2} + \frac{1}{2^{N+1}}(1+\mathrm{e}^{-\Delta\omega^2\tau^2/2})^N. \tag{5.3}$$

Thus, the model correctly predicts the observed exponential dephasing of the qubit with increasing number of repetitions N. As expected, the decay constant depends on the hyperfine coupling strength of the nuclear spin with a faster decay for increased coupling strength. However, the prediction of the model when inserting the measured optimal value of $\tau = 0.44\,\mu$s (red dotted line) does not exhibit quantitative agreement with the measured data. A possible explanation is that the model neglects the double-exponential reset time distribution and the time spent in $|+1\rangle$, in one of the excited states or in the meta-stable singlet states. These assumptions are certainly not justified in the present experiment.

To account for this, we leave τ in Eq. 5.3 as a free parameter and introduce an offset parameter C to the coupling strength, $\Delta\omega \to (\Delta\omega + C)$. Setting C to $\approx 2\pi \times 15$ kHz leads to reasonable agreement of the model (solid curves in Fig. 5.4B) with the data. The observed fit values ($\tau = 0.43(3)\,\mu$s for the $|E_{1,2}\rangle$ and $\tau = 0.46(1)\,\mu$s for the $|A_{1,2}\rangle$ repumping configuration) agree within error with both the measured slow repumping timescale, see

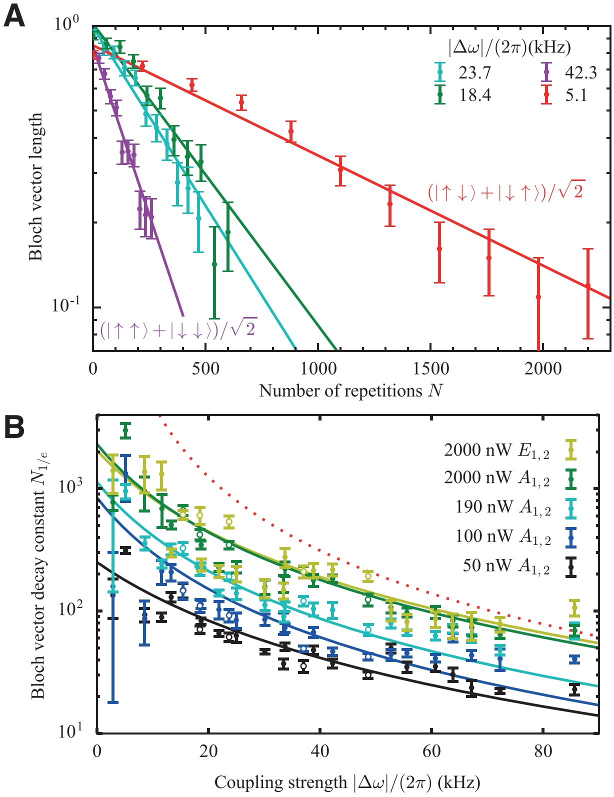

Figure 5.4 | Encoding of a quantum bit in decoherence-protected subspaces. (**A**) Encoding in nuclear spin 2 or 3 (cyan and green) shows similar decay with increasing N. Encoding in a decoherence-protected (decoherence-enhanced) subspace leads to strongly decreased (enhanced) dephasing shown in red (magenta). The initial fidelity in the two-spin case is slightly reduced because encoding and readout require more control operations on the nuclear spins. (**B**) Number of sequence repetitions that are possible before the nuclear qubit Bloch vector length drops to 1/e of its initial value, for qubits encoded in single nuclear spins (empty circles) and in two-spin states (filled circles) of different effective coupling strengths $\Delta\omega$. The four depicted data sets are taken for increasing repump duration, caused by a reduced repump laser power. The solid curves are fits according to the model presented in the text.

Fig. 5.2A, and the optimal value of τ in Fig. 5.3A.

5.7. CONCLUSION AND OUTLOOK

We have studied a prototype quantum network node consisting of nuclear spin qubits hyperfine coupled to an optically active electronic spin in a diamond with natural isotope abundance. Repeated application of a remote entangling protocol is observed to cause dephasing of the nuclear spin qubits. We found that this dephasing can be mitigated by using nuclear spins with small parallel hyperfine coupling strengths, and, even more effectively, by encoding in decoherence-protected subspaces of multiple spins. For the smallest coupling strengths investigated here, the storage of quantum states is robust to more than 1000 remote entangling attempts. We expect that our experimental findings can be generalized to other physical systems[38] and other quantum protocols in which a repeated reset of an ancilla qubit with always-on coupling to a memory is required.

In the future, the implementation of high quality optical cavities should allow for a further reduction of the time it takes to reset the electronic spin, as the Purcell effect[39] induced by such resonator increases the probability of direct spin-flips without populating the singlet states. In addition, the development of techniques to measure the electronic spin state non-destructively or within a decoupling sequence might fully eliminate the need for probabilistic repumping. Finally, the realization of quantum networking protocols that are based on photon absorption[40–42] rather than photon emission may reduce the number of required electronic spin resets until a successful entanglement event is heralded. Even in the absence of such future improvements, we anticipate that the current results will enable first demonstrations of the purification of remote entanglement[15,43] and proof-of-principle operation of a quantum repeater[16] based on NV centers in diamond[17].

CONTRIBUTIONS

A.R. and N.K. prepared the experimental apparatus, carried out the experiments and analysed the data. The diamond substrates were grown by D.J.T. and M.M. A.R. wrote the original version of the manuscript with input from N.K., R.H. and all other authors. The project was supervised by R.H.

5.8. SUPPLEMENTARY INFORMATION

5.8.1. ^{13}C SPIN INITIALIZATION AND READOUT

In this section, we explain the procedures used to initialize and readout the ^{13}C spins using the NV electronic spin as an ancilla[29]. We first describe how a single nuclear spin is prepared in the state $|X\rangle \equiv (|\downarrow\rangle + |\uparrow\rangle)/\sqrt{2}$. We employ the gate sequence shown in Fig. 5.5A. The electronic spin is first reset to $|0\rangle$ using a laser pulse on the repump transitions (see Fig. 5.1). Subsequently, it is rotated to $(|0\rangle + |1\rangle)/\sqrt{2}$ by a single $\pi/2$ microwave (MW) pulse. Then, a sequence of MW π pulses performs a selective rotation on one of the nuclear spins, which is initially in a mixed state ρ_m. The rotation is conditional on the initial electronic spin state, as described in detail in Ref. 28. In this way, the nuclear and electronic spins are correlated. After another MW $\pi/2$ pulse, a measurement of the electronic spin projects the nuclear spin to $|\pm X\rangle$, where the sign depends on the measurement result.

In our experiment, the readout fidelity of the ancilla qubit is asymmetric: If a photon is detected, the NV is with a very high probability (> 99%) in the fluorescent state $|0\rangle$. Therefore, we repeat the initialization sequence until $|0\rangle$ is measured, which prepares the nuclear spin in $|X\rangle$. The same procedure can be used to initialize all controlled nuclear spins sequentially.

The procedure to initialize a single nuclear spin in $|\downarrow\rangle$ is shown in Fig. 5.5B. Here, the electronic spin is prepared in $|0\rangle$. We then apply a reduced swap operation, which consists of two MW rotations of the electronic spin and two rotations of the nuclear spin that are conditional on the electronic spin. Ideally, this deterministically transfers the electronic spin $|0\rangle$ state to the nuclear spin state $|\downarrow\rangle$ [29].

Finally, we describe the pulse sequence used to prepare a single qubit in a two-spin decoherence-protected subspace. Here, the nuclear spins are prepared in $|\downarrow\downarrow\rangle$ by sequential application of the scheme described above. Then, the gate sequence shown in Fig. 5.5C prepares the nuclear spins either in $(|\downarrow\downarrow\rangle + |\uparrow\uparrow\rangle)/\sqrt{2}$ or in $(|\uparrow\downarrow\rangle + |\downarrow\uparrow\rangle)/\sqrt{2}$, again depending on the measurement result [29]. To avoid errors caused by the asymmetric electron readout fidelity, we again condition the start of the experiment on the detection of a photon, and we insert a MW π pulse before readout if we want to prepare the other nuclear spin state.

The techniques to do tomography on the nuclear spin consist of the same set of operations as those for initialization. They are described in detail in the supplementary information of Ref. 29.

To characterize the control we achieve over the five individual nuclear spins, we prepare each of them separately in $|X\rangle$ and then perform tomography using the electronic spin as an ancilla. We correct for ancilla readout errors. The combined nuclear spin initialization and readout fidelity $F_{i,r}$ is the overlap of the reconstructed nuclear spin density matrix ρ with the ideally expected state, i.e. $F_{i,r} = \langle X|\rho|X\rangle$. We emphasize that measuring $F_{i,r}$ involves several two-qubit quantum gates and single-qubit rotations. The individual fidelity of each of these operations is expected to be higher than the combined value.

5.8.2. OPTIMIZATION OF THE DYNAMICAL DECOUPLING SEQUENCE

As can be seen in Fig. 5.1B, the hyperfine coupling of the NV electronic and the ^{13}C nuclear spins leads to two effects: first, a change of the nuclear spin precession frequency, and second, a tilt of the precession axis. In the limit of large magnetic fields, the latter is quadratically suppressed. At the magnetic field used in the experiments, however, the nuclear spins may become partly entangled with the electronic spin in each repetition of the entanglement sequence. This induces decoherence upon projection of the latter.

To minimize this decoherence, two strategies can be explored in order to minimize the entanglement. First, keeping the entanglement sequence very short by minimizing the time t between the pulses, such that the overall nuclear spin evolution during the sequence remains small. Second, the timing of the sequence can be adjusted such that it

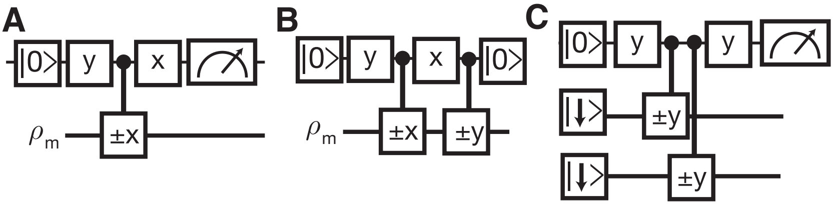

Figure 5.5 | Gate sequences used for initialization of ^{13}C spin quantum memories. x(y) denotes a MW pulse that rotates the electronic spin by an angle of $\pi/2$ around the x(y) axis in the Bloch sphere picture. For an explanation of the used sequences; see text. (**A**) Initialization of a ^{13}C nuclear spin in $(|\uparrow\rangle + |\downarrow\rangle)/\sqrt{2}$. (**B**) Initialization in $|\downarrow\rangle$. (**C**) Initialization in $(|\uparrow\downarrow\rangle + |\downarrow\uparrow\rangle)/\sqrt{2}$ or $(|\uparrow\uparrow\rangle + |\downarrow\downarrow\rangle)/\sqrt{2}$.

is matched to one of the nuclear spin precession frequencies, i.e. $t = \frac{2\pi}{\omega_{-1}}$ or $t = \frac{2\pi}{\omega_0}$. In this case, the nuclear spins have approximately undergone two full rotations (one around the magnetic field and one around the tilted axis) and end up at the same projection along the Z axis as they started, which minimizes entanglement between electronic and nuclear spin.

Fig. 5.6 shows a measurement in which this theoretical expectation is observed. The measurement uses the sequence shown in the inset of Fig. 5.3A. Single ^{13}C spins are initialized in $|\downarrow\rangle$ and the entanglement sequence is applied $N = 450$ times. We then measure the length of the Bloch vector Z projection for several values of the wait time t in the dynamical decoupling sequence. We observe two distinct maxima, one at short t and one around the inverse of the nuclear spin precession frequency. The position of the latter slightly depends on the sign and magnitude of the hyperfine coupling. We use $t = \frac{2\pi}{\omega_0} \simeq 2.3\,\mu$s (red dashed line) in all experiments presented in the main text.

5.8.3. INFLUENCE OF ELECTRONIC SPIN REINITIALIZATION AND MW PULSE ERRORS

In addition to the sources of dephasing described in the main text, also experimental imperfections such as MW pulse errors and imperfect electronic spin reinitialization in $|0\rangle$ might lead to decoherence.

To investigate the effect of the former, we repeat the measurement of the DPS with the smallest dephasing, formed by nuclear spins 2 and 3, but this time with single MW pulses rather than the BB1 pulses used in the main text. Albeit this leads to a reduced MW pulse fidelity, we observe no decrease of the decay constant. In addition, we perform a measurement in which we replace the MW $\pi/2$ pulse of the entanglement sequence by a π pulse, such that the electronic spin ends up in $|0\rangle$ at the end of the sequence and no repumping is required. We observe that the dephasing now follows a Gaussian decay and is strongly reduced compared to the case of an initial $\pi/2$ pulse. The observed decay can be fully explained by the independently measured nuclear spin dephasing time T_2^*,

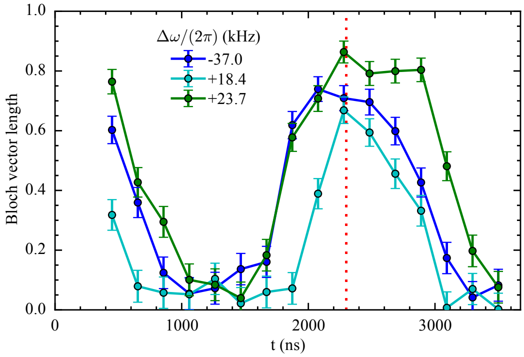

Figure 5.6 | Optimization of the dynamical decoupling sequence. Three single ^{13}C nuclear spins are individually prepared along the Z axis and the entanglement sequence is repeated N = 450 times. The state of the encoded qubit is best preserved when the timing t of the dynamical decoupling sequence matches the nuclear spin precession period (red dashed line).

which testifies that the electronic spin reset is the dominant dephasing mechanism in our experiment.

Effects from imperfect reinitialization in $|0\rangle$ seem unlikely from the remaining population in $|\pm 1\rangle$, $p_{\pm 1} < 0.2(2)\,\%$, measured after optical pumping for $1.5\,\mu$s using $2\,\mu$W of laser power. This expectation is confirmed by the observation of an unchanged decay constant upon stepwise increasing the duration of the repumping laser pulse up to $5.5\,\mu$s. Similarly, an additional delay of several μs after the repumping, which would increase the time spent in a state that causes dephasing whenever the pumping process is not perfect, has no discernible effect.

We therefore conclude that the dephasing caused by experimental imperfections is negligible in the measurements presented in the main text.

5.8.4. POWER DEPENDENCE OF THE OPTICAL PUMPING TIMESCALES AND NV DEIONIZATION PROBABILITY

In the main text, we demonstrate that a fast reset of the electronic spin is required to minimize decoherence of the coupled nuclear spins. The reset is doubly exponential, with timescales that depend on the applied laser power. Fig. 5.7A shows the power dependence of these timescales measured in the $|A_{1,2}\rangle$ repump laser configuration. We observe a saturation at ~ 500 nW of applied laser power. To ensure the fastest possible reset even in the case of NV position or laser power drift, we use $2\,\mu$W, which is well above saturation, in all measurements presented in the main text except where mentioned otherwise.

Such comparably high repump power has the unwanted effect that the NV can be transferred to the neutral charge state, which leads to a detectable (and thus heralded) loss of the nuclear spin qubit. This deionization is likely a two-photon process[34], such that we expect its probability to increase quadratically with applied laser power.

To investigate the effects of varying reset timescales and hyperfine coupling strengths on the nuclear spin dephasing without added noise, we post-select the analysis of the results presented in the main text to experimental runs in which the NV has not been deionized. To this end, we measure the NV charge state after completion of the experimental sequence by applying resonant lasers on both the cycling and repump transitions for 50 μs. If the NV is in the negative charge state, we detect on average more than 10 photons in this time interval. If we detect less than two photons, the NV has likely been deionized.

To characterize the influence of NV deionization on the results presented in the main text, we measure the deionization probability as a function of the number of electron resets when applying 2 μW of laser power in the $|A_{1,2}\rangle$ repump configuration, i.e. we study the highest powers used in the main text. Note that in this experiment the electron is prepared in $|-1\rangle$ and thus reset in *every* repetition. As can be seen in Fig. 5.7B, we observe an exponential decay of the probability to remain in the negatively charged state, p_{NV^-}, with a decay constant of $N_d = 2.82(8) \times 10^3$ repetitions. In the entanglement sequence, where repumping is required in 50 % of all trials (on average), we expect the decay to be two times slower. Albeit the resulting decay is larger than all observed dephasing constants, it becomes evident that a further reduction of the induced decoherence (e.g. via the use of decoherence-protected subspaces with even smaller coupling strengths than the ones investigated in the main text) will likely require a reduction of the maximally applied laser power.

5.8.5. NUCLEAR SPIN POLARIZATION DECAY AND NATURAL DEPHASING CORRECTION

As explained in the main text, we expect that the dominant decoherence mechanism of the nuclear spins when applying the entanglement sequence is dephasing which is induced by the electronic spin reset. In contrast, the nuclear spin population is expected to be much less sensitive. To investigate this, we initialize a qubit in the eigenstates $|\downarrow\rangle$ for each single nuclear spin and in $|\downarrow\downarrow\rangle$ and $|\uparrow\downarrow\rangle$ for each investigated two-spin configuration. We then repeat the entanglement sequence many times and measure the exponential decay of the qubit Z projection. As can be seen in Fig. 5.8, the population decay (red) is typically much smaller than the dephasing shown in black (data identical to Fig. 5.4B).

In addition to the decoherence that is induced by repeatedly applying the entanglement sequence, the nuclear spins also exhibit natural dephasing. In Ref. 29, this dephasing was shown to lead to a Gaussian decay of the state fidelity with a timescale T_2^* that is

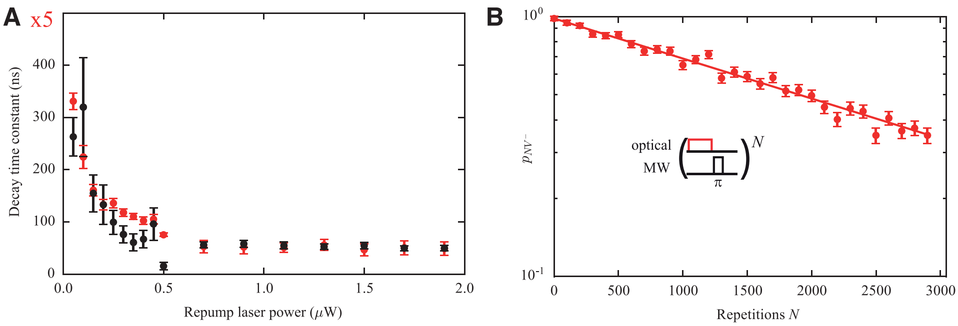

Figure 5.7 | (**A**) Power dependence of the NV electronic spin reset timescales (black: short, red: long) in the $|E_{1,2}\rangle$ repump configuration. (**B**) Fraction of experimental runs in which the NV center is not deionized to the neutral charge state as a function of the number of electron resets when applying 2 μW of laser power in the sequence shown as inset. We observe an exponential decay with a decay constant $2.82(8) \times 10^3$.

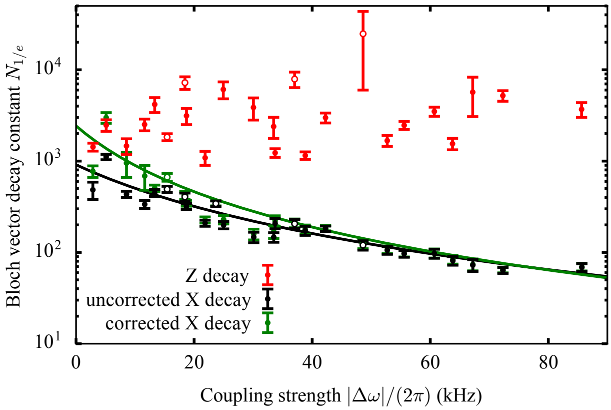

Figure 5.8 | Decay of the nuclear spin Bloch vector length with increasing coupling strength for 2μW repump laser power applied in the $|A_{1,2}\rangle$ configuration (see Fig. 5.1D). The open circles are single nuclear spins, while the filled circles are two-spin subspaces. The red data shows the population decay of a qubit that is encoded in an eigenstate, i.e. along the axis of the external magnetic field. This decay is typically much smaller than the dephasing of a qubit prepared in a superposition state (black and green). The black and green curve show the same measurements, analyzed either with (green) or without (black) applying a correction for the intrinsic nuclear spin dephasing time T_2^* (see text). A significant deviation is only observed for the leftmost data points.

different for each measured ^{13}C spin, c.f. Table 5.1. This dephasing can be mitigated by a suited dynamical decoupling sequence on the nuclear spins, which can e.g. be implemented by using radio-frequency pulses that are resonant to the nuclear spin Larmor frequency[26].

In our experiments, we do not implement such nuclear spin decoupling sequence. Instead, before fitting the decay we correct the obtained data points for their natural dephasing. To this end, we divide by the factor $\exp(-(\frac{t_N}{T_2^*})^2)$, where t_N is the absolute time elapsed after doing N repetitions of the entanglement sequence and T_2^* is the effective natural dephasing time. For single nuclear spins, we take the measured value of T_2^*, whereas we extrapolate the value for a DPS that is formed by the spins i and j as $T_{2,ij}^* \approx \frac{1}{\sqrt{(1/T_{2,i}^*)^2+(1/T_{2,j}^*)^2}}$. In Fig. 5.8, we show both the corrected (green) and uncorrected (black) data, where it becomes evident that natural dephasing only becomes relevant for DPSs with very low effective coupling strengths.

REFERENCES

[1] H. J. Kimble, *The quantum internet,* Nature **453**, 1023 (2008).

[2] L.-M. Duan and C. Monroe, *Colloquium: Quantum networks with trapped ions,* Reviews of Modern Physics **82**, 1209 (2010).

[3] N. Sangouard, C. Simon, H. de Riedmatten and N. Gisin, *Quantum repeaters based on atomic ensembles and linear optics,* Reviews of Modern Physics **83**, 33 (2011).

[4] A. Reiserer and G. Rempe, *Cavity-based quantum networks with single atoms and optical photons,* Reviews of Modern Physics **87**, 1379 (2015).

[5] J.-D. Bancal *et al., Quantum non-locality based on finite-speed causal influences leads to superluminal signalling,* Nature Physics **8**, 867 (2012).

[6] P. Kómár *et al., A quantum network of clocks,* Nature Physics **10**, 582 (2014).

[7] N. H. Nickerson, Y. Li and S. C. Benjamin, *Topological quantum computing with a very noisy network and local error rates approaching one percent,* Nature Communications **4**, 1756 (2013).

[8] S. Barz *et al., Demonstration of Blind Quantum Computing,* Science **335**, 303 (2012).

[9] A. Ekert and R. Renner, *The ultimate physical limits of privacy,* Nature **507**, 443 (2014).

[10] J. Hofmann *et al., Heralded Entanglement Between Widely Separated Atoms,* Science **337**, 72 (2012).

[11] D. Hucul *et al., Modular entanglement of atomic qubits using photons and phonons,* Nature Physics **11**, 37 (2015).

[12] W. B. Gao, A. Imamoglu, H. Bernien and R. Hanson, *Coherent manipulation, measurement and entanglement of individual solid-state spins using optical fields,* Nature Photonics **9**, 363 (2015).

[13] B. Hensen *et al.*, *Loophole-free Bell inequality violation using electron spins separated by 1.3 kilometres,* Nature **526**, 682 (2015).

[14] A. Delteil *et al.*, *Generation of heralded entanglement between distant hole spins,* Nature Physics **12**, 218 (2016).

[15] C. H. Bennett *et al.*, *Purification of Noisy Entanglement and Faithful Teleportation via Noisy Channels,* Physical Review Letters **76**, 722 (1996).

[16] H.-J. Briegel, W. Dür, J. I. Cirac and P. Zoller, *Quantum Repeaters: The Role of Imperfect Local Operations in Quantum Communication,* Physical Review Letters **81**, 5932 (1998).

[17] L. Childress, J. M. Taylor, A. S. Sørensen and M. D. Lukin, *Fault-Tolerant Quantum Communication Based on Solid-State Photon Emitters,* Physical Review Letters **96**, 070504 (2006).

[18] A. G. Fowler *et al.*, *Surface Code Quantum Communication,* Physical Review Letters **104**, 180503 (2010).

[19] L.-M. Duan, M. D. Lukin, J. I. Cirac and P. Zoller, *Long-distance quantum communication with atomic ensembles and linear optics,* Nature **414**, 413 (2001).

[20] H. Bernien *et al.*, *Heralded entanglement between solid-state qubits separated by three metres,* Nature **497**, 86 (2013).

[21] W. Pfaff *et al.*, *Unconditional quantum teleportation between distant solid-state quantum bits,* Science **345**, 532 (2014).

[22] M. V. G. Dutt *et al.*, *Quantum Register Based on Individual Electronic and Nuclear Spin Qubits in Diamond,* Science **316**, 1312 (2007).

[23] L. Robledo *et al.*, *High-fidelity projective read-out of a solid-state spin quantum register,* Nature **477**, 574 (2011).

[24] G.-Q. Liu, H. C. Po, J. Du, R.-B. Liu and X.-Y. Pan, *Noise-resilient quantum evolution steered by dynamical decoupling,* Nature Communications **4**, 2254 (2013).

[25] G. Waldherr *et al.*, *Quantum error correction in a solid-state hybrid spin register,* Nature **506**, 204 (2014).

[26] P. C. Maurer *et al.*, *Room-Temperature Quantum Bit Memory Exceeding One Second,* Science **336**, 1283 (2012).

[27] S. D. Barrett and P. Kok, *Efficient high-fidelity quantum computation using matter qubits and linear optics,* Physical Review A **71**, 060310 (2005).

[28] T. H. Taminiau, J. Cramer, T. van der Sar, V. V. Dobrovitski and R. Hanson, *Universal control and error correction in multi-qubit spin registers in diamond,* Nature Nanotechnology **9**, 171 (2014).

[29] J. Cramer *et al.*, *Repeated quantum error correction on a continuously encoded qubit by real-time feedback,* Nature Communications **7**, 11526 (2016).

[30] T. H. Taminiau *et al.*, *Detection and Control of Individual Nuclear Spins Using a Weakly Coupled Electron Spin,* Physical Review Letters **109**, 137602 (2012).

[31] L. Jiang *et al.*, *Coherence of an Optically Illuminated Single Nuclear Spin Qubit,* Physical Review Letters **100**, 073001 (2008).

[32] M. S. Blok, N. Kalb, A. Reiserer, T. H. Taminiau and R. Hanson, *Towards quantum networks of single spins: Analysis of a quantum memory with an optical interface in diamond,* Faraday Discussions **184**, 173 (2015).

[33] M. L. Goldman *et al.*, *Phonon-Induced Population Dynamics and Intersystem Crossing in Nitrogen-Vacancy Centers,* Physical Review Letters **114**, 145502 (2015).

[34] M. W. Doherty *et al.*, *The nitrogen-vacancy colour centre in diamond,* Physics Reports **528**, 1 (2013).

[35] L. Robledo, H. Bernien, I. van Weperen and R. Hanson, *Control and Coherence of the Optical Transition of Single Nitrogen Vacancy Centers in Diamond,* Physical Review Letters **105**, 177403 (2010).

[36] L. M. K. Vandersypen and I. L. Chuang, *NMR techniques for quantum control and computation,* Reviews of Modern Physics **76**, 1037 (2005).

[37] D. A. Lidar, I. L. Chuang and K. B. Whaley, *Decoherence-Free Subspaces for Quantum Computation,* Physical Review Letters **81**, 2594 (1998).

[38] D. D. Awschalom, L. C. Bassett, A. S. Dzurak, E. L. Hu and J. R. Petta, *Quantum Spintronics: Engineering and Manipulating Atom-Like Spins in Semiconductors,* Science **339**, 1174 (2013).

[39] E. Purcell, *Spontaneous emission probabilities at radio frequencies,* Physical Review **69**, 681 (1946).

[40] N. Kalb, A. Reiserer, S. Ritter and G. Rempe, *Heralded Storage of a Photonic Quantum Bit in a Single Atom,* Physical Review Letters **114**, 220501 (2015).

[41] S. Yang *et al.*, *High-fidelity transfer and storage of photon states in a single nuclear spin,* Nature Photonics **10**, 507 (2016).

[42] C. Jones, D. Kim, M. T. Rakher, P. G. Kwiat and T. D. Ladd, *Design and analysis of communication protocols for quantum repeater networks,* New Journal of Physics **18**, 083015 (2016).

[43] E. T. Campbell and S. C. Benjamin, *Measurement-Based Entanglement under Conditions of Extreme Photon Loss,* Physical Review Letters **101**, 130502 (2008).

6

DEPHASING MECHANISMS OF DIAMOND-BASED NUCLEAR-SPIN MEMORIES FOR QUANTUM NETWORKS

N. Kalb, P.C. Humphreys, J.J. Slim and R. Hanson

We probe dephasing mechanisms within a quantum network node consisting of a single nitrogen-vacancy centre electron spin that is hyperfine coupled to surrounding ^{13}C nuclear-spin quantum memories. Previous studies have analysed memory dephasing caused by the stochastic electron-spin reset process, which is a component of optical internode entangling protocols. Here, we find, by using dynamical decoupling techniques and exploiting phase matching conditions in the electron-nuclear dynamics, that control infidelities and quasi-static noise are the major contributors to memory dephasing induced by the entangling sequence. These insights enable us to demonstrate a 19-fold improved memory performance which is still not limited by the electron reinitialization process. We further perform pump-probe studies to investigate the spin-flip channels during the optical electron spin reset. We find that spin-flips occur via decay from the meta-stable singlet states with a branching ratio of 8(1):1:1, in contrast with previous work. These results allow us to formulate straightforward improvements to diamond-based quantum networks and similar architectures.

The results in this chapter have been submitted for publication. arXiv:1802.05996.

6.1. INTRODUCTION

The creation of a general-purpose quantum network will enable distributed quantum computation and long-distance quantum communication[1]. A quantum network is composed of individual nodes each hosting a number of qubits that are commonly separated into two groups: communicators and memories. Communicators have an efficient optical interface that allows for the generation of spin-photon entanglement and ultimately the creation of inter-node entanglement. Memories on the other hand are robust qubits that allow for intra-node interfacing with the communicators and thus grant access to multi-qubit protocols and the creation of highly-linked many-body quantum states across complex network architectures.

To date quantum network primitives have been demonstrated on several experimental platforms by creating point-to-point entangling links between nodes that either were comprised of one communicator each[2–8] or of one communicator and one additional memory in one of the nodes that would rapidly dephase during internode entanglement generation[9,10]. Very recently, nitrogen-vacancy (NV) centres in diamond have been able to perform network protocols that demand the storage and processing of two entangled states[11], i.e. one communicator was linked with one fully coherent memory (Fig. 6.1A). Nodes combining communicator and memory qubits are readily available in diamond of natural isotopic composition as NV centres are surrounded by a dilute bath of ^{13}C nuclear spins ($I = \frac{1}{2}$, 1.1% abundance). Each NV electron spin can selectively address nuclear spins in the near vicinity via dynamical decoupling techniques[12–14] thus making it a natural communicator surrounded by nuclear-spin memories.

The NV electron spin and the nuclear spins interact via the always-on magnetic hyperfine interaction. Uncontrolled electron spin flips therefore translate into uncontrolled shifts of the nuclear precession frequency giving rise to nuclear-spin dephasing. Previous work analysed the impact of stochastic NV reinitialization, a key ingredient for current probabilistic NV-NV entangling sequences, on nuclear-spin decoherence[15,16]. It was implicitly assumed in these works that this constituted the dominant decoherence pathway. In contrast, here we find that several other mechanisms in fact constitute the dominant sources of decoherence during entanglement generation. We show that electron spin control errors during entangling attempts in combination with quasi-static noise overshadow dephasing from the NV reinitialization. These insights enable accurate modelling of the system and as a result uncover direct paths to improved memory robustness through shortened entangling sequences and increased magnetic fields.

This work is structured as follows. In Sec. 6.2, we describe the NV system, the interaction Hamiltonian with surrounding nuclear spins and the sources of nuclear-spin dephasing introduced by repetitive entangling attempts on the electron spin. Section 6.3 provides evidence for the introduction of additional quasi-static noise during entangling attempts by observing that a nuclear-spin inversion enhances the memory robustness. Section 6.4 combines nuclear-spin inversion rotations with time-tailored entangling attempts that render the sequence robust with respect to microwave control errors. Using these entangling sequences we investigate two nuclear spin memories and observe an order of magnitude improved memory performance. In Sec. 6.5, the electron reinitialization process is investigated via nanosecond-resolved pump-probe experiments. We quantify into electron spin-flip mechanisms and branching ratios from the meta-stable singlet states to the NV ground state. In Sec. 6.6, the memory performance is further optimized by exploring the entangling-attempt parameter space. We find that the investigated memories are not limited by the stochastic repumping process but rather by a combination of intrinsic decoherence, slowly-fluctuating noise, electron-spin initialization errors and depolarization noise. In Sec. 6.7, nuclear-spin dephasing due to electron-spin initialization errors is investigated. While noticeable effects of initialization failure are observed, the magnitude of this noise source does not suffice to solely explain the previously observed limitations to nuclear spin memory robustness. We conclude with Sec. 6.8 by inferring favourable parameter regimes from a Monte-Carlo simulation and by suggesting future experimental directions.

6.2. EXPERIMENTAL SYSTEM

All experiments were performed on a type IIa chemical-vapor deposition diamond sample that was cut along the $\langle 111\rangle$ crystal axis and grown by Element Six. We milled a solid immersion lens around the positions of single NV centres to enhance photon collection efficiencies and use an additionally grown Al_2O_3 anti-reflection coating[17]. Lithographically-defined gold microstructures allow for the on-chip delivery of amplitude-shaped Hermite microwave pulses for NV electron spin control at a magnetic field of 414 G aligned with the NV symmetry axis. The sample is situated in a home-built cryogenic confocal microscope setup ($T = 4\,\mathrm{K}$) to allow for resonant single-shot readout of the electron spin state at the $|0\rangle \equiv |m_s = 0\rangle \rightarrow |\mathrm{E_x}\rangle$ excitation frequency (Fig. 6.1B; all shown data throughout this work are corrected for electron read-out infidelities and NV ionization events)[16,18]. We use a second laser beam resonant with the optical transitions $|m_s = \pm 1\rangle \equiv |\pm 1\rangle \rightarrow |E'\rangle$ for fast electron spin initialization into the $|0\rangle$ spin state. Note that the symbol $|E'\rangle$ is used as a shorthand to denote the two optically excited states $|E_{1,2}\rangle$. Before each experimental run we monitor the NV fluorescence under optical excitation to ensure the required resonance conditions and charge-state occupation[18]. We further use time-tailored dynamical decoupling sequences on the NV electron spin to selectively address and control nuclear spins in the vicinity[14].

Nuclear spins are natural quantum memories due to their long coherence times while the electron spin remains idle[19]. If, however, states are stored on the nuclei while the electron spin is manipulated then electron-spin control errors can propagate onto the nuclear spin state via the hyperfine interaction. The electron-nuclear Hamiltonian in an appropriately rotating frame and secular approximation is

$$H = \omega_0 I_\mathrm{z} + (A_\parallel S_\mathrm{z} I_\mathrm{z} + A_\perp S_\mathrm{z} I_\mathrm{x}) \tag{6.1}$$

with the nuclear and electronic spin operators I_j and S_j, the bare Larmor frequency arising from the external magnetic field $\omega_0 = 2\pi\gamma|\vec{B}| = 443275\,\mathrm{Hz}$ and the parallel (perpendicular) hyperfine coupling strength $A_\parallel$ ($A_\perp$). The Hamiltonian of Eq. (6.1) gives rise to electron-spin-dependent nuclear precession frequencies ω_0 (electron spin in $|0\rangle$) and

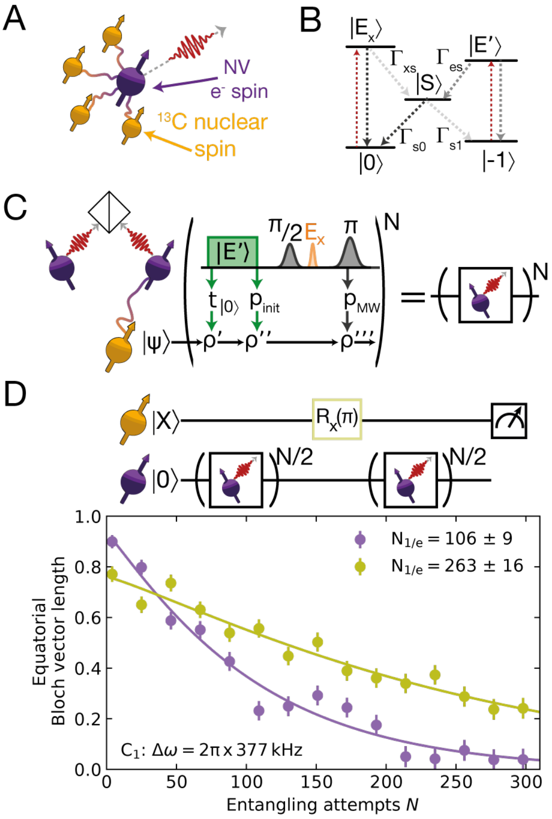

Figure 6.1 |NV centres in diamond as multi-qubit nodes for quantum networks. (**A**) The NV electron spin (purple) serves as optical interface (red wavepacket) to establish remote entangling links. The surrounding ^{13}C nuclear spins (orange) are hyperfine coupled to the electron spin (wiggly lines) and serve as quantum memories. (**B**) Relevant level structure of the NV centre. The NV allows for spin-selective optical transitions to $|\mathrm{E_x}\rangle$ and $|\mathrm{E}'\rangle$. These states may decay to the meta-stable singlet states summarized as $|S\rangle$. The transition rates Γ_i are qualitatively indicated by the opacity of the dashed arrows. (**C**) Repeated attempts are made to create remote NV-NV entanglement until success is heralded. Each entangling attempt consists of electron spin manipulations via laser (green/orange) and microwave pulses (grey). Electron spin operations fail with probability p_i, thus leaving the electron spin in a mixed state. Nuclear spins with initial state $|\psi\rangle$ will acquire an electron-state-dependent phase which results in a mixed state (ρ', see Eq. (6.1)). Further nuclear decoherence is induced by the optical electron spin reset ($|\mathrm{E}'\rangle$), a stochastic process with randomly distributed projection times $t_{|0\rangle}$. (**D**) Top: Experimental sequence. Bottom: Memory coherence decay of nuclear spin $\mathrm{C_1}$ ($\Delta\omega = 2\pi \times 377\,\mathrm{kHz}$) with (yellow) and without (purple) interleaved π-rotation to probe quasi-static noise. See legend for fitted decay constants $N_{1/\mathrm{e}}$. Error bars represent one standard deviation.

$\omega_{\pm1} = \sqrt{(\omega_0 \pm A_\parallel)^2 + A_\perp^2}$ (electron in $|m_s = \pm1\rangle$). It is therefore evident that unaccounted electron spin flips will decohere nuclear-spin memories due to a shift in nuclear precession frequency $\Delta\omega = |\omega_0 - \omega_{\pm1}|$.

The generation of long-distance entangled states is a central source of electron spin state uncertainty and thus nuclear spin decoherence (Fig. 6.1C). Independent of the entangling scheme[20–22], each entangling attempt involves error-prone operations such as microwave spin rotations, optical excitation (E_x) and optical spin reinitialization into $|0\rangle$ (E'). The timing of these operations is typically optimized to preserve the coherence of both the nuclear and electron spin[16]. Any residual imperfections in these operations will however give rise to dephasing of nuclear spin superposition states. Moreover the electron spin reinitialization relies on optical pumping, an inherently stochastically-timed process that poses a limit on the number of entangling attempts a nuclear spin of a certain coupling strength $\Delta\omega$ can preserve a quantum state for. In the experiments described here we use entangling sequences that contain all necessary electron-spin operations apart from the generation of spin-photon entanglement (E_x). We expect the impact of undesired electron spin flips ($p \approx 0.005$) after an optical excitation to E_x to be negligible when compared to other sources of error because the timing of these optical excitation pulses can be chosen such that the spurious nuclear spin phases upon flipping are small[16].

6.3. PERFORMANCE OF A STRONGLY-COUPLED NUCLEAR SPIN MEMORY

We first examine the coherence of nuclear spin C_1, a particularly strongly coupled nuclear spin in close proximity to our NV centre (Table 6.1 lists the key numbers for seven addressable carbon nuclear spins). The spin is initialized into the superposition state $|X\rangle \equiv (|\uparrow\rangle + |\downarrow\rangle)/\sqrt{2}$ and after a number of entangling attempts (duration of one attempt: $7\,\mu$s), the nuclear spin coherence is measured by evaluating the remaining length of the Bloch vector in the equatorial plane of the Bloch sphere $\sqrt{\langle\sigma_x\rangle^2 + \langle\sigma_y\rangle^2}$ (Fig. 6.1D), with the Pauli spin operators σ_i. We find an exponential decay of the nuclear coherence with a $1/e$ decay constant of 106(9) attempts for a consecutive stream of entangling attempts (purple data in Fig. 6.1D). By further employing a Hahn-echo π rotation ($R_x(\pi)$) on the nuclear spin after half the attempts to cancel quasi-static noise, we obtain an improved decay constant of 263(16) attempts (yellow data). Here $R_i(\theta)$ corresponds to a rotation around axis i with angle θ. These coherence decays are remarkable since the coupling strength $\Delta\omega$ for this spin is an order of magnitude larger than the nuclear spin memories used for the recent demonstration of entanglement distillation, yet a comparable decoherence rate is observed[11]. These results therefore provide a key first indication that the model of Refs. 15, 16 does not fully capture the decoherence dynamics of the NV-nuclear system.

The increased $1/e$ decay constant for an interleaved nuclear $R_x(\pi)$ rotation points to-

	C$_1$	C$_2$	C$_3$	C$_4$	C$_5$	C$_6$	C$_7$
$\frac{\Delta\omega}{2\pi}$ (kHz)	376.5	62.4	77.0	32.4	26.6	20.9	12.2
T_2^* (ms)	9.9(2)	9.9(1)	9.5(2)	11.2(3)	17.3(6)	4.5(1)	7.0(1)

Table 6.1 |Coupling strength $\Delta\omega$ and free-induction decay T_2^* for seven addressable nuclear spins in the vicinity of the NV. Note that the NV used in this work does not correspond to the NV used in Ref.[16].

wards quasi-static noise introduced by the repeated performance of entangling attempts as a large component of the nuclear spin decoherence. Such quasi-static noise may originate from slow intensity fluctuations of the repumping laser at the position of the NV which may, for example, be induced by mechanical vibrations of the optical set-up. Intuitively, the distribution of electron-spin-reset times will fluctuate in accordance with the laser intensity at the NV-position. Fluctuating electron-spin-reset times directly translate into a fluctuation of the average phase per entangling attempt imprinted onto the nuclear spins[16]. In the future, the exact origin of the quasi-static noise could be probed by measuring the pointing stability of the impinging beam with respect to the NV and employing active laser-intensity stabilization methods.

The coupling strength $\Delta\omega$ and nuclear decoherence due to NV reinitialization are related via the model of Blok et al.[15]. In this model a decay constant τ is invoked to model the decoherence of nuclear spins with a given coupling strength $\Delta\omega$. This model will further apply to any noise source that induces stochastic noise in the timing of the NV spin population. Note that τ becomes the mean of the exponentially-distributed electron-spin repumping time under the assumption that this repumping process is the dominant noise source. The expected equatorial Bloch vector length is a function of τ, $\Delta\omega$, the number of entangling attempts N and the probability $p_{|1\rangle}$ that the electron spin is in $|\pm 1\rangle$ at the end of the entangling attempt

$$\sqrt{\langle\sigma_\mathrm{x}\rangle^2 + \langle\sigma_\mathrm{y}\rangle^2} = (1 - p_{|1\rangle} + p_{|1\rangle} e^{-\Delta\omega^2\tau^2/2})^N. \tag{6.2}$$

Using Eq. (6.2) we obtain $\tau \approx 52$ ns for the best dataset (Fig. 6.1D, yellow), which is a factor of 8 faster and therefore at odds with the observed data in Ref. 16. We hypothesize that this discrepancy arises as τ originates not only from the reinitialization process, but is also impacted by other NV control infidelities. This motivates the further investigations in the following sections.

6.4. MICROWAVE CONTROL ERRORS

We next consider the influence of microwave control errors and their impact on the nuclear spin coherence. All entangling sequences contain a microwave-induced π-rotation to preserve the electron coherence upon successfully creating entanglement and to render the acquired phase of the nuclear spin electron-state-independent. This is because the time spent in both electron states equalizes for a perfect π-rotation and the nuclear

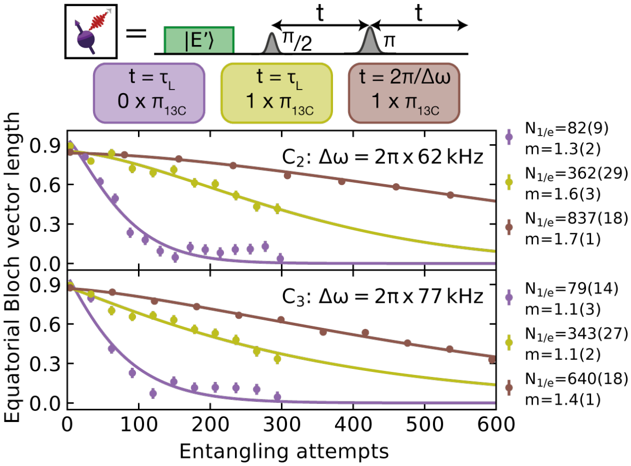

Figure 6.2 |Impact of microwave pulse errors on memory performance. We measure the decay of a superposition state on two different nuclear spins C_2, C_3 for three different scenarios (see legend and main text). We find maximal decay constants of 837(18) and 640(18) respectively which corresponds to $\tau = 177\,\mathrm{ns}/163\,\mathrm{ns}$ according to Blok et al.[15]. Solid lines are exponentially decaying fits to the data sets with $A \times \mathrm{Exp}[-(N/N_{1/e})^m]$. Error bars are one s.d.

spin picks up a phase according to the average frequency $\bar{\omega} = (\omega_0 + \omega_{-1})/2$ and the inter-pulse delay t. Microwave π-rotations however fail with a probability p_{MW} such that the rotation can be described as a mixture of two processes $p_{\mathrm{MW}} \times \mathrm{R_x}(0) + (1 - p_{\mathrm{MW}}) \times \mathrm{R_x}(\pi)$. The nuclear spin therefore acquires a phase φ depending on the success or failure of the microwave π pulse and the projected electron state after the initial $\pi/2$ microwave rotation (Fig. 6.2). The probabilities : phases for the different possible outcomes are

$$\begin{aligned} (|0\rangle;|0\rangle) &\quad 0.5\,p_{\mathrm{MW}} : \varphi_0 = 2\omega_0 t \\ (|-1\rangle;|-1\rangle) &\quad 0.5\,p_{\mathrm{MW}} : \varphi_1 = 2\omega_{-1} t \\ (|0\rangle;|-1\rangle) &\quad 1 - p_{\mathrm{MW}} : \bar{\varphi} = 2\bar{\omega} t. \end{aligned} \tag{6.3}$$

We additionally list the electron spin state in brackets (|before⟩;|after⟩) before and after the pulse has been applied. The inter-pulse delay t can be chosen such that the acquired phase equalizes in all cases $\bar{\varphi} - \varphi_0 \,(\mathrm{mod}\, 2\pi) = \bar{\varphi} - \varphi_1 \,(\mathrm{mod}\, 2\pi)$. This condition is fulfilled for $t = 2\pi/\Delta\omega$.

We use these phase-matched entangling attempts to unveil the impact of microwave pulse errors. We choose two nuclear spins with intermediate coupling strengths (C_2: $\Delta\omega = 2\pi \times 62\,\mathrm{kHz}$ and C_3: $\Delta\omega = 2\pi \times 77\,\mathrm{kHz}$ respectively) and measure their decoherence rate in three different scenarios (Fig. 6.2). First, the standard setting of Ref. 16 with an inter-pulse delay corresponding to the inverse of the nuclear spin Larmor frequency $t = \tau_{\mathrm{L}} = 2\pi/\omega_0$ (purple). Second, with a single interleaved nuclear π-rotation to overcome quasi-static sources of dephasing and $t = \tau_L$ (yellow). And finally with an optimized inter-pulse delay $t = 2\pi/\Delta\omega$ (Eq. (6.3), brown). All data are fit with an exponentially decaying function $A \times \text{Exp}[-(N/N_{1/e})^m]$ with free parameters A, $N_{1/e}$ and m.

We find an increase in robustness by an order of magnitude when comparing the optimized sequence (brown) to the standard sequence (purple). In addition, the optimized sequence outperforms the standard sequence with inversion rotation (yellow) therefore demonstrating the role of microwave pulse errors during the entangling sequence. The coherence decay of C_2 and C_3 deviates from the exponential decay observed for C_1 and predicted by Ref. 15. We still use Eq. (6.2) to associate the observed $1/e$-decay constants with τ therefore establishing a basis for performance comparisons between nuclear spins. We find $\tau = 177\,\text{ns}$ ($163\,\text{ns}$) for C_2 (C_3) which is still larger than the earlier obtained value of 52 ns for C_1. We note that C_1 did not show a changed decay behaviour for the optimized entangling sequence ($N_{1/e} = 265(28)$ and $m = 1.0(2)$; data not shown) leading us to conclude that the dominant noise source of C_1 is indeed the stochastic electron spin reinitialization. These elevated decay constants for C_2 and C_3 require a deeper understanding of the NV electron spin repumping process and the exploration of the entangling attempt parameter space to yield further improvements in memory robustness.

6.5. SPIN-FLIP MECHANISMS OF THE NV ELECTRON SPIN

We next investigate spin-flip mechanisms of the NV electron spin during the optical pumping process. Spin-flips are expected to either be direct, i.e. they occur via spin-mixing in the excited state, or indirect via NV specific intersystem crossing (ISC) to the orbital singlet states (summarized here as $|\text{S}\rangle$; Fig. 6.1B). The electron spin then decays from $|\text{S}\rangle$ back to the NV spin ground-state triplet of $m_s = 0$ and $m_s = \pm 1$ with the branching ratio $\Gamma_{s0}/\Gamma_{s1} : 1 : 1$ [23].

We prepare the NV centre in $|-1\rangle$ and use a calibrated optical π pulse to excite the NV to $|\text{E}'\rangle$ with a Gaussian intensity envelope that has a full width at half maximum of 2.6 ns. We next apply a 40 ns long optical pulse on the E_y transition to detect fluorescence of the $|0\rangle$ ground-state and therefore spin flips during the optical cycle. By varying the delay between both laser pulses we are able to monitor spin flips to $|0\rangle$ in a time-resolved fashion. The data set is generalized by using DC Stark tuning[24] to induce a range of frequency shifts of $|\text{E}_\text{x}\rangle$ ($1 - 4.5\,\text{GHz}$) in the NV excited state. All measurements are normalized to interleaved experimental runs where no optical π pulse is applied and the NV is either prepared in $|0\rangle$ or $|-1\rangle$.

We observe an exponential increase of the probability to be in $|0\rangle$ with a strain-averaged time scale of 368(12) ns (Fig. 6.3) which is consistent with the literature value for the singlet lifetime of single NV centres 371 ns [25] and in reasonable agreement with ensemble measurements[26]. Only a negligible fraction of the spin population resides in $|0\rangle$ for short pump-probe delays, therefore ruling out direct decay from $|E'\rangle$ to $|0\rangle$ as dominant electron spin-flip mechanism. Since the probe window has a finite length (40 ns) the observed direct spin-flip probability (1(1) %) represents an upper bound. We are therefore able to identify the decay from $|S\rangle$ to the ground state triplet as the major spin-flip mechanism. The measured singlet lifetime allows us to estimate the expected decoherence if the singlet states were to couple significantly to the nuclear spins. In this case, we would expect much faster spin decay than observed[15], allowing us to rule out such an effect as a significant decoherence mechanism in our experiments.

The data in Fig. 6.3 allow for the determination of the spin-flip probability per optical excitation to $|\mathrm{E}'\rangle$ and — together with the measured ISC rate Γ_{es} — the branching ratio from the singlet states $|\mathrm{S}\rangle$ to the NV ground state. Following the methods of Ref. 27 we experimentally determine the ISC rate Γ_{es} for the $|\mathrm{E}'\rangle$ states. We quote strain-averaged values as we assume no significant strain dependence (all fitted values are given in Table 6.2). By measuring the radiative lifetime of $|\mathrm{E_x}\rangle$ and $|\mathrm{E}'\rangle$ via resonant optical excitation and time-resolved fluorescence monitoring in the phonon sideband we obtain strain-averaged lifetimes $t_{\mathrm{Ex}} = 12.3(1)\,\mathrm{ns}$ and $t_{\mathrm{E}'} = 7.4(1)\,\mathrm{ns}$ (Fig. 6.3 inset). From the measured lifetimes and the assumption that the transition rate from $|\mathrm{E_x}\rangle$ to $|\mathrm{S}\rangle$ is $\Gamma_{\mathrm{xs}} \approx 0$, we extract a strain-averaged ISC rate for E′ of $\Gamma_{\mathrm{es}} = 2\pi \cdot 8.2(3)\,\mathrm{MHz}$ in good agreement with earlier results[27].

From the measurements described in this section (Γ_{es}, t_{Ex}, $t_{\mathrm{E}'}$) we obtain a strain-averaged probability of $p_s = 0.41(1)$ to transfer to $|S\rangle$ per excitation cycle on $|\mathrm{E}'\rangle$. The probability for double excitation to $|\mathrm{E}'\rangle$ may obscure the estimate of the singlet branching ratio[28]. We use a quantum jump simulation to estimate this probability with $t_{\mathrm{E}'}$, t_{Ex} and the intensity profile of the excitation pulse as input parameters[28]. Our simulation results in a double excitation probability of $\sim 5\,\%$, which we take into account when computing p_s.

From p_s, the measured probability to be in $|0\rangle$ after one excitation and the assumption that the decay rate from $|S\rangle$ to $|\pm 1\rangle$ is symmetric[16] we are able to extract the branching ratios from $|S\rangle$ to $|0\rangle$:$|+1\rangle$:$|-1\rangle$. We find a strain-averaged branching ratio of 8(1):1:1. This value is significantly different from the literature value (2:1:1) for NV centres at ambient temperatures[23]. The relatively large uncertainty originates from the spread in $F(|0\rangle)$ for long delay times and may be explained by imperfect optical π excitations. We emphasize that the lowest extracted branching ratio is 5(1) : 1 : 1 while the largest obtained branching ratio is 13(3) : 1 : 1 therefore validating a data set that is systematically above the literature value (see Table 6.2). This result is in accordance with Ref. 29 which found a higher spin polarization at cryogenic temperatures upon off-resonant excitation. Note that the observed branching ratio also suffices to explain the electron spin reinitialization data of Ref. 16 without invoking direct spin-flip channels. In the future, the experimental tools developed in this section can be used to study the temperature dependence of the singlet branching ratio on single NV centres.

6.6. CURRENT LIMITS TO MEMORY ROBUSTNESS

We investigate factors that currently limit the nuclear spin coherence for spins C_2 and C_3. To this end we initialize the nuclear spin in a balanced superposition and measure the remaining coherence $\sqrt{\langle\sigma_{\mathrm{x}}\rangle^2 + \langle\sigma_{\mathrm{y}}\rangle^2}$ after a number of entangling attempts while changing several key attributes of the repeated electron-spin entangling sequence. First,

$\Delta_\perp$ (GHz)	lifetime (ns)	p_s	$\|0\rangle$:$\|+1\rangle$:$\|-1\rangle$
0.9	379(17)	0.41(1)	11(2):1:1
1.3	340(18)	0.39(1)	13(3):1:1
1.7	403(26)	0.39(2)	5(1):1:1
2.7	343(32)	0.43(2)	5(1):1:1
4.6	372(37)	0.42(2)	6(1):1:1

Table 6.2 |Results of the singlet pump-probe experiments. Ordered according to the electric-field-induced frequency shift $\Delta_\perp$ of $|E_x\rangle$. We give the inferred cumulative singlet lifetime, the probability of transfering to the singlet p_s after one excitation pulse and the branching ratio from the singlet states into the ground-state spin triplet.

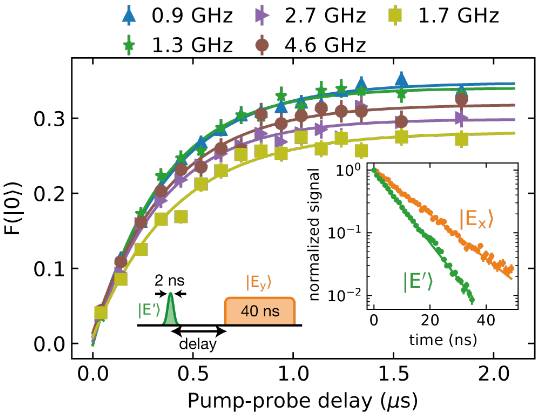

Figure 6.3 |Results of a pump-probe experiment on the $|-1\rangle \rightarrow |E'\rangle$ transition. We measure the radiative lifetimes of both states (inset) and infer $\Gamma_{es}/2\pi = 8.2(3)$ MHz. Besides, we infer from this a strain-averaged singlet branching ratio of $8(1):1:1$. See legend for the strain-induced frequency shifts at which each data set was taken.

we remove the intermediary electron $R_x(\pi)$ rotation and set the time after the first microwave pulse ($R_x(\alpha)$) to $t \sim 2\pi/\Delta\omega$ (Eq. (6.3) and Fig. 6.4) which removes the dependency of the acquired nuclear spin phase on the electronic spin state. This allows us to effectively half the entangling attempt duration while still applying electron spin reinitialization events repetitively. Second, we sweep the intensity of the optical pumping beam to obtain the influence of the electronic reinitialization speed on the nuclear spin coherence for each data set. In addition, the influence of quasi-static noise is further probed by either interleaving a single (purple data) or two (yellow data) nuclear spin inversions at an appropriate timing. Note that all previous experiments were conducted with a reinitialization intensity of $6\,\mu$W and a repumping duration of $2\,\mu$s.

Figure 6.4 shows the inferred decay constants $N_{1/e}$ when fitting the data with the function $A \times \mathrm{Exp}[-(N/N_{1/e})^m]$ with free parameters A, $N_{1/e}$, m. We use entangling attempts

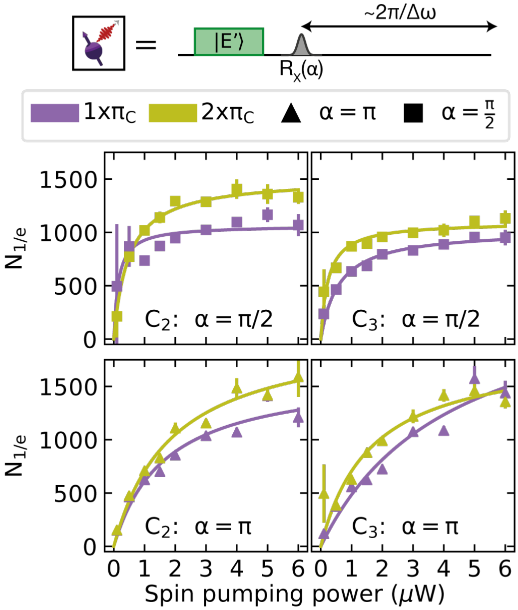

Figure 6.4 |Nuclear spin decay constants as a function of optical spin-pumping power and different sequence configurations. Purple (yellow) data uses one (two) nuclear spin π rotations to mitigate quasi-static noise. The microwave pulse during each entangling sequence rotates the electron by an angle α which we set to $\alpha = \pi/2$ (squared, top panels) or $\alpha = \pi$ (triangles, bottom panels). Solid lines are fits to the function $N_{\text{sat}} \cdot P/(P + P_{\text{sat}})$ with the optical power P and the free parameters N_{sat} and P_{sat}.

with $\alpha = \pi/2$ to set $p_{|1\rangle} = 0.5$ (top panels, squares) and find that using two nuclear π-rotations (yellow data) outperforms the use of a single π-rotation (purple data). This indicates that the previously identified quasi-static noise is not fully mitigated by a single π rotation on the probed timescales of $\sim 20\,$ms.

We fit saturation curves $N_{\text{sat}} \cdot P/(P + P_{\text{sat}})$ with the optical pumping power P and the free parameters N_{sat} and P_{sat} to the measured decay constants (solid lines). The average fitted saturation power of $P_{\text{sat}} = 366(68)\,$nW is consistent with measurements that were directly carried out on the electron spin under similar experimental conditions[16]. The best achievable $N_{1/e}$ decay constants for $\alpha = \pi/2$ are $N_{\text{sat},C_2} = 1511(38)$ and $N_{\text{sat},C_3} = 1097(40)$. This yields a 19-fold increase in memory robustness for C_2 when compared to the standard performance in Fig. 6.2 (purple data).

We next choose $\alpha = \pi$ (preparing the NV in $|-1\rangle$) such that optical electron spin initialization occurs after each entangling attempt, thus amplifying the phase noise due to the reinitialization process. Repeating the measurements as described above for both nuclear spins (Fig. 6.5, lower panels) results in an average saturation power of $P_{\text{sat}} = 2.4(8)\,\mu$W and maximal $N_{1/e}$ decay constants of $N_{\text{sat},C_2} = 2045(136)$ and $N_{\text{sat},C_3} = 2207(278)$.

The measured ratios of N_{sat} for $\alpha = \pi/2$ and $\alpha = \pi$ are 1.35 (C_2) and 2.01 (C_3). These ratios are inconsistent with Eq. (6.2) which predicts a ratio of $N_{\text{sat},\pi}/N_{\text{sat},\pi/2} = 0.5$. The increased performance of the nuclear spins when setting $\alpha = \pi$ therefore provides further evidence that the memory decay is not dominated by the stochastic reinitialization process. The discrepancy in saturation powers between the two data-sets will spur further investigations.

Entangling sequences using electron $\pi/2$ rotations may cause additional noise due to off-axis rotations of the nuclear spin[16] and the lack of a frozen core if the electron spin is in $|0\rangle$ thus allowing for resonant nuclear-nuclear flip-flop events that translate to lower nuclear coherence times[30]. Depolarizing noise is investigated by initializing both nuclear spins in the eigenstate $|\uparrow\rangle$ and setting $\alpha = \pi/2$. We obtain decay constants for these eigenstates of $\gtrsim 3500$. Environmental dephasing due to the fluctuating spin bath and off-resonant pumping from $|0\rangle$ to $|\pm 1\rangle$ is investigated by measuring the nuclear coherence decay T_2 without microwave pulses in the entangling attempts. We obtain $T_2 \gtrsim 3000$ entangling attempts for both spins at the highest spin pumping powers. We additionally point out that the fitted average exponent for the two nuclear spins differs [$m_{C_2} = 1.89(0.14)$ and $m_{C_3} = 1.49(0.03)$] which implies differing dominant decay mechanisms for each nuclear spin. Note that the entangling sequences of this section are suitable for single-photon entangling protocols[11,28] because the entangling sequence duration is well within $T_{2,\text{Hahn}}$ of the electron spin; the required electron π-rotation can be applied once the entanglement generation is successfully heralded.

6

The observed decay constants in this section are in-line with the best-performing decoherence-protected subspaces formed from two nuclear spin memories therefore indicating that the robustness of these low-coupling ($\Delta\omega \sim$ kHz) subspaces may be further improved by more than an order of magnitude[16]. These results further establish that the majority of addressable nuclear spins are suitable quantum memories for quantum networks.

6.7. ELECTRON SPIN INITIALIZATION ERRORS

The nuclear spin coherence may be restricted by unsuccessful electron reinitialization attempts which we explore in this section. As shown in Sec. 6.5, reinitialization of the electron spin occurs by optical pumping of the states $|\pm 1\rangle$ to the intermediate singlet states $|S\rangle$ from where the electron spin either decays to the final state $|0\rangle$ or with equal probability to the other spin states $|\pm 1\rangle$, thus repeating the pumping cycle. Optical pumping is a stochastic process that, when applied for a finite duration of time, is accompanied by a failure probability p_{init} with which the NV electron spin is either left in $|+1\rangle$ or $|-1\rangle$.

We probe electron spin initialization failure by running 700 entangling attempts with a $R_x(\pi/2)$ rotation on the electron spin that is timed such that it fulfils the earlier discovered phase matching condition of $t = 2\pi/\Delta\omega$ (Fig. 6.5A). We further vary a waiting time T between the end of the repumping laser pulse and the microwave rotation on the elec-

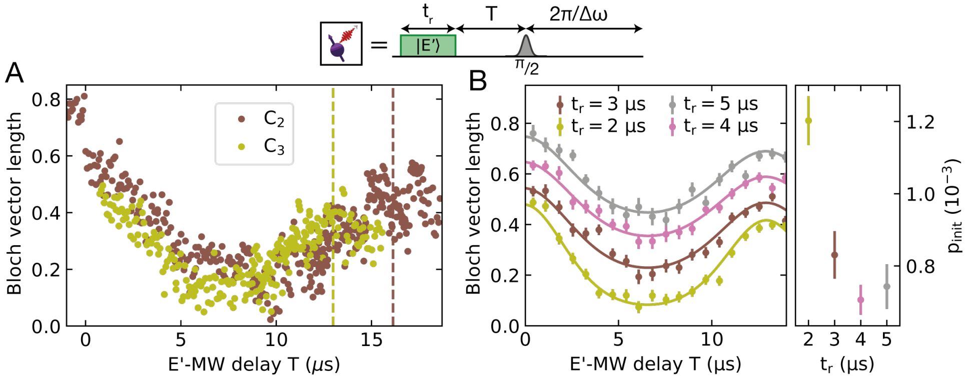

Figure 6.5 |Memory sensitivity with respect to NV initialization errors. (**A**) Top: Entangling sequence performed on the NV electron spin while the nuclear spin is idling in a superposition state. Bottom: Measured equatorial Bloch vector length as a function of the delay T between repumping pulse and microwave $R_x(\frac{\pi}{2})$ rotation. We use $t_r = 2\,\mu$s. Dashed lines are the expected phase matching conditions $T = 2\pi/\Delta\omega$ for the respective spin (see legend). (**B**) Left: Coherence of C$_3$ for various spin pumping durations t_r (see legend). Solid lines are fits with the probability of initialization failure p_{init} as free parameter. The data have been offset for better visibility. Right: Extracted initialization infidelity as a function of repumping duration. Rate calculations suggest that a minimum of $3.3\,\mu$s repumping is required to achieve an infidelity of 10^{-4} under the assumption of fully saturating the NV and negligible off-resonant excitation.

tron spin. The absolute change in precession frequency of a nuclear spin $|\Delta\omega|$ is almost identical for both electron states $|\pm 1\rangle$, as can be seen from the Hamiltonian in Eq. (6.1) and the fact that we operate in the regime $(\omega_0 \pm A_\parallel)^2 \gg A_\perp^2$. This means that there is a phase cancellation condition for T at which electron initialization failure does not invoke a phase shift on the nuclear spin. The repumping duration t_r was chosen to be $2\,\mu$s and the optical pumping power was $4\,\mu$W. The nuclear spins are initialized in $|X\rangle$ and inverted midway through the sequence. Finally the quantity $\sqrt{\langle\sigma_\text{x}\rangle^2 + \langle\sigma_\text{y}\rangle^2}$ is measured to evaluate the remaining nuclear spin coherence.

Figure 6.5A shows the measured Bloch vector lengths as a function of T. We observe a decrease in Bloch vector length and a revival of the nuclear spin coherence for both examined nuclear spins (yellow and brown data). Both nuclear spins experience a revival in coherence at the expected phase matching condition $T = 2\pi/\Delta\omega$ (dashed lines). The data at negative delays were used to calibrate the delay between the end of the repumping pulse and the start of the microwave rotation on the electron spin (duration of 50 ns).

This technique allows us to estimate the initialization failure probability p_{init}. We measure the nuclear spin coherence of C$_3$ for four different repumping durations t_r and a repumping power of $4\,\mu$W (Fig. 6.5B). The nuclear-spin expectation values $\sigma_{\text{x,y}}$ after N entangling attempts are described by assuming binomially distributed initialization failures that occur with probability p_{init}. Each failure is assumed to have equal probability for the electron spin to end up in $|\pm 1\rangle$. We use the shorthand notation $b_{mn}(p) = \binom{m}{n}(1-p)^{m-n}p^n$ which results in

$$\langle\sigma_x\rangle = A\sum_{i=0}^{N} b_{Ni}(p_{\text{init}})\sum_{j=0}^{i} b_{ij}(\frac{1}{2})\cos\left[(N-i)\phi_0 + j\phi_{-1} + (i-j)\phi_{+1}\right] \tag{6.4}$$

where the phases $\phi_{+1,-1,0}$ solely depend on the nuclear spin frequencies for the respective electron spin state and the timing of the used entangling attempts. Analytically evaluating this expression allows us to derive a fit function with two free parameters: p_{init} and an amplitude A that encompasses other sources of infidelity (solid lines). The best fitted initialization failure probability is $p_{\text{init}} = (7.1 \pm 0.4)\cdot 10^{-4}$ for $t_r = 4\,\mu$s (Fig. 6.5B, right panel). We attribute the saturation of p_{init} for longer repumping durations to off-resonant optical excitation of the NV electron spin.

The inferred initialization failure probabilities are used to find an upper-bound to the coherence decay constants of C_2 and C_3 (see 6.6). Using a Monte-Carlo simulation of the nuclear-electron dynamics and the assumptions $p_{\text{MW}} = 0$, negligible quasi-static noise and an average spin reinitialization time of 52 ns we find: $N_{1/e,C_2} = 5300$ and $N_{1/e,C_3} = 3338$. These decay constants are well beyond the experimentally observed decay constants of 1511 and 1097 (Sec. 6.6). These results therefore support the existence of additional noise sources that limit the memory performance in this regime of $\Delta\omega$.

Future experiments may trade off repumping duration and off-resonant excitation to obtain improved NV initialization fidelities. The techniques presented in this section allow for the certification of NV initialization errors at the 10^{-5} level. Off-resonant excitation might be further tackled by utilizing DC Stark tuning to steer the excited state level structure and excitation frequency spectrum of the NV electron spin[24].

6.8. DISCUSSION AND OUTLOOK

In summary, we performed a detailed study of decoherence mechanisms within a quantum network node consisting of an NV centre as optical interface and surrounding ^{13}C nuclear spins as quantum memories. Instead of the earlier suspected stochastic NV reinitialization process, we found that control infidelities and quasi-static noise constitute the major contributors to nuclear-spin decoherence for spins with coupling strengths below $2\pi \times 400$ kHz. These insights lead to the demonstration of a 19-fold improved memory robustness which is still not limited by the inherently stochastic electron reinitialization process.

In Fig. 6.6A we plot the decay constant data of Ref.[16] (purple circles) as a function of $\Delta\omega$. The data set for all seven nuclear spins that are available around the NV used in this work, including two-nuclear-spin subspace configurations, is shown in addition (purple squares) and found to be consistent with the data of Ref.[16]. We compare all measured decay constants to a phenomenological model that comprises the repumping process and the control infidelities $p_{\text{init}} = 1.2\cdot 10^{-3}$ and $p_{\text{MW}} = 8\cdot 10^{-3}$ (estimated from electron

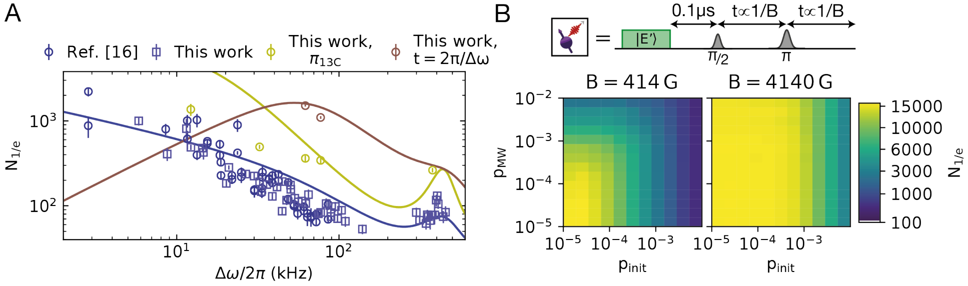

Figure 6.6 |(**A**) Comparison between experimentally obtained decay constants (see legend) as a function of coupling strength $\Delta\omega$ and a phenomenological model (solid lines). (**B**) Monte-Carlo simulation of a nuclear spin memory with $\Delta\omega = 26\,\mathrm{kHz}$. We vary the error probabilities for NV electron spin rotations p_{MW} and unfaithful initialization p_{init} and estimate the $1/e$-decay constant $N_{1/e}$ of the memory for two magnetic fields B. We use $\tau = 100\,\mathrm{ns}$ resulting in an optimal decay constant of $\sim 15\times10^3$ which is limited by the stochastic electron reinitialization process[15]. Our simulation suggests that larger errors are tolerable in a regime of higher magnetic field as the sequence duration of each entangling attempt may be shortened which in turn reduces the accumulated nuclear-spin phase upon error. For a magnetic field of $4.14\,\mathrm{kG}$ the time between microwave pulses becomes $256\,\mathrm{ns} = 2\pi/\omega_0$ while the required microwave frequency for electron spin manipulation becomes $8.7\,\mathrm{GHz}$. Both values are obtainable with state-of-the-art technology.

spin measurements). The quasi-static noise is hypothesized to originate from laser intensity fluctuations at the electron-spin position and therefore dephasing noise with a phenomenological $\Delta\omega$-dependence is incorporated. We further show the decay constants when interleaving a nuclear π-rotation (yellow, see Figs. 6.1,6.2) and when utilizing the phase-matching sequences of Sec. 6.6 (brown) while the respective modelled decay constants are shown as solid lines of the same colour. We find reasonable agreement between our model and experimental data when incorporating the Gaussian nuclear coherence decay with $T_{2,\mathrm{Hahn}} = 60\,\mathrm{ms}$ which stems from the fluctuating spin bath.

Our results point towards straightforward improvements to show that memory performance can be greatly increased. The spurious phases acquired by nuclear spins during entangling sequences scale with $\Delta\omega$ and the entangling sequence duration. This duration is dictated by the Larmor period $\tau_L = 2\pi/\omega_0 \propto 1/B$ of the nuclear spin bath: decoupling the electron with an inter-pulse delay equal to τ_L preserves the electron spin coherence upon entangling success and induces minimal depolarization noise on the nuclear spin memories by avoiding undesired off-axis rotations[16]. It is therefore desirable to increase the magnetic field and in turn shorten the critical phase-sensitive parts of the entangling sequence.

To underpin this hypothesis we perform a Monte-Carlo simulation of our experiment for two differing magnetic fields. Our Monte-Carlo simulation builds on the simple model of Ref. 15 by exponentially distributing electron reinitialization times $t_{|0\rangle}$. We choose the mean of this distribution as $\tau = 100\,\mathrm{ns}$, in accordance with the best measured τ for nuclear spins C_2 and C_3 in Sec. 6.5. We additionally keep track of the electron state during each entangling attempt and randomly draw microwave and initialization failure events with probabilities p_{MW} and p_{init}.

Figure 6.6B presents the simulated decay constants for a nuclear spin with $\Delta\omega = 2\pi \times 26\,\mathrm{kHz}$. We chose this value for $\Delta\omega$ because nuclear spins in this coupling regime still have an experimental track record of high addressability[11,16,31,32] while we expect them to outperform the memories in this work ($\Delta\omega > 2\pi \times 60\,\mathrm{kHz}$). Our simulation predicts a steep increase in memory robustness for higher magnetic fields at already demonstrated error rates while a memory with the chosen $\Delta\omega$ at current magnetic fields ($B = 414\,\mathrm{G}$) would only unfold its full potential at the highest-level of experimental control achieved to date[33,34]. Moreover operating at an elevated magnetic field will further suppress depolarizing noise originating from the perpendicular hyperfine coupling $A_\perp$ [16].

Decreasing the entangling duration to enhance memory robustness trivially works for short distances between network nodes such that successful entanglement generation events can be heralded within hundreds of nanoseconds. For larger distances between network nodes one may achieve similar results by employing multiple inversion pulses on the electron spin, potentially in conjunction with pulse error cancelling dynamical decoupling sequences[35,36]. One can additionally mitigate faulty initialization into the electron spin triplet state that is not part of the qubit subspace by using a dedicated continuous light field that couples this unused state to the optically excited state.

In conclusion, we have shown that quantum superposition states on weakly-coupled nuclear spins ($\Delta\omega < 2\pi \times 80\,\mathrm{kHz}$) are robust against a large number of entangling attempts on the NV electron spin (>1000) and identified quasi-static noise and microwave control errors as the previously limiting factors. The exact composition of the currently limiting noise sources for the memory performance remains elusive, but could be further investigated by employing fast laser-intensity stabilization techniques in combination with more nuclear spin inversion rotations and increased magnetic fields. The obtained results are readily generalized to other solid-state defects and quantum information processing platforms that utilize always-on interactions[30,37–42]. The majority of nuclear spins surrounding NVs in diamond of natural isotopic composition therefore have a robustness which is comparable to the inverse success probability of generating entanglement at close distances (10^{-3}-10^{-4}) [28]. These results further unlock the potential of NV centres as highly-coherent multi-qubit network nodes and may lead to the proof-of-principle demonstrations of an NV-based quantum repeater[43,44] and distributed quantum computation[45].

CONTRIBUTIONS

N.K., P.C.H. and J.J.S. prepared and characterized the experimental apparatus. N.K. collected and analysed the data with the help of P.C.H. and R.H. N.K. wrote the chapter with input from all authors.

REFERENCES

[1] H. J. Kimble, *The Quantum Internet,* Nature **453**, 1023 (2008).

[2] D. L. Moehring *et al.*, *Entanglement of Single-Atom Quantum Bits at a Distance,* Nature **449**, 68 (2007).

[3] S. Ritter *et al.*, *An Elementary Quantum Network of Single Atoms in Optical Cavities,* Nature **484**, 195 (2012).

[4] J. Hofmann *et al.*, *Heralded Entanglement Between Widely Separated Atoms,* Science **337**, 72 (2012).

[5] H. Bernien *et al.*, *Heralded Entanglement between Solid-State Qubits Separated by Three Metres,* Nature **497**, 86 (2013).

[6] T. E. Northup and R. Blatt, *Quantum Information Transfer Using Photons,* Nature Photonics **8**, 356 (2014).

[7] A. Narla *et al.*, *Robust Concurrent Remote Entanglement Between Two Superconducting Qubits,* Physical Review X **6**, 031036 (2016).

[8] R. Stockill *et al.*, *Phase-Tuned Entangled State Generation between Distant Spin Qubits,* Physical Review Letters **119**, 010503 (2017).

[9] W. Pfaff *et al.*, *Unconditional Quantum Teleportation between Distant Solid-State Quantum Bits,* Science **345**, 532 (2014).

[10] D. Hucul *et al.*, *Modular Entanglement of Atomic Qubits Using Photons and Phonons,* Nature Physics **11**, 37 (2015).

[11] N. Kalb *et al.*, *Entanglement Distillation between Solid-State Quantum Network Nodes,* Science **356**, 928 (2017).

[12] N. Zhao *et al.*, *Sensing Single Remote Nuclear Spins,* Nature Nanotechnology **7**, 657 (2012).

[13] S. Kolkowitz, Q. P. Unterreithmeier, S. D. Bennett and M. D. Lukin, *Sensing Distant Nuclear Spins with a Single Electron Spin,* Physical Review Letters **109**, 137601 (2012).

[14] T. H. Taminiau, J. Cramer, T. van der Sar, V. V. Dobrovitski and R. Hanson, *Universal Control and Error Correction in Multi-Qubit Spin Registers in Diamond,* Nature Nanotechnology **9**, 171 (2014).

[15] M. S. Blok, N. Kalb, A. Reiserer, T. H. Taminiau and R. Hanson, *Towards Quantum Networks of Single Spins: Analysis of a Quantum Memory with an Optical Interface in Diamond,* Faraday Discussions **184**, 173 (2015).

[16] A. Reiserer *et al.*, *Robust Quantum-Network Memory Using Decoherence-Protected Subspaces of Nuclear Spins,* Physical Review X **6**, 021040 (2016).

[17] T. K. Yeung, D. Le Sage, L. M. Pham, P. L. Stanwix and R. L. Walsworth, *Anti-Reflection Coating for Nitrogen-Vacancy Optical Measurements in Diamond,* Applied Physics Letters **100**, 251111 (2012).

[18] L. Robledo *et al.*, *High-Fidelity Projective Read-out of a Solid-State Spin Quantum Register,* Nature **477**, 574 (2011).

[19] S. Yang *et al.*, *High-Fidelity Transfer and Storage of Photon States in a Single Nuclear Spin,* Nature Photonics **10**, 507 (2016).

[20] C. Cabrillo, J. I. Cirac, P. García-Fernández and P. Zoller, *Creation of Entangled States of Distant Atoms by Interference,* Physical Review A **59**, 1025 (1999).

[21] S. D. Barrett and P. Kok, *Efficient High-Fidelity Quantum Computation Using Matter Qubits and Linear Optics,* Physical Review A **71**, 060310 (2005).

[22] E. T. Campbell and S. C. Benjamin, *Measurement-Based Entanglement under Conditions of Extreme Photon Loss,* Physical Review Letters **101**, 130502 (2008).

[23] M. W. Doherty *et al.*, *The Nitrogen-Vacancy Colour Centre in Diamond,* Physics Reports **528**, 1 (2013).

[24] P. Tamarat *et al.*, *Stark Shift Control of Single Optical Centers in Diamond,* Physical Review Letters **97**, 083002 (2006).

[25] L. Robledo, H. Bernien, T. van der Sar and R. Hanson, *Spin Dynamics in the Optical Cycle of Single Nitrogen-Vacancy Centres in Diamond,* New Journal of Physics **13**, 025013 (2011).

[26] V. M. Acosta, A. Jarmola, E. Bauch and D. Budker, *Optical Properties of the Nitrogen-Vacancy Singlet Levels in Diamond,* Physical Review B **82**, 201202 (2010).

[27] M. L. Goldman *et al.*, *Phonon-Induced Population Dynamics and Intersystem Crossing in Nitrogen-Vacancy Centers,* Physical Review Letters **114**, 145502 (2015).

[28] P. C. Humphreys *et al.*, *Deterministic delivery of remote entanglement on a quantum network,* arXiv , 1712.07567 (2017).

[29] S. Felton *et al.*, *Hyperfine Interaction in the Ground State of the Negatively Charged Nitrogen Vacancy Center in Diamond,* Physical Review B **79**, 075203 (2009).

[30] M. Zhong *et al.*, *Optically Addressable Nuclear Spins in a Solid with a Six-Hour Coherence Time,* Nature **517**, 177 (2015).

[31] J. Cramer *et al.*, *Repeated Quantum Error Correction on a Continuously Encoded Qubit by Real-Time Feedback,* Nature Communications **7**, 11526 (2016).

[32] N. Kalb *et al.*, *Experimental Creation of Quantum Zeno Subspaces by Repeated Multi-Spin Projections in Diamond,* Nature Communications **7**, 13111 (2016).

[33] J. P. Gaebler *et al.*, *High-Fidelity Universal Gate Set for ${{{̂9}\mathrm{Be}}}{̂+}$ Ion Qubits,* Physical Review Letters **117**, 060505 (2016).

[34] T. P. Harty *et al.*, *High-Fidelity Preparation, Gates, Memory, and Readout of a Trapped-Ion Quantum Bit,* Physical Review Letters **113**, 220501 (2014).

[35] G. de Lange, Z. H. Wang, D. Ristè, V. V. Dobrovitski and R. Hanson, *Universal Dynamical Decoupling of a Single Solid-State Spin from a Spin Bath,* Science **330**, 60 (2010).

[36] M. H. Abobeih *et al.*, *One-second coherence for a single electron spin coupled to a multi-qubit nuclear-spin environment,* arXiv , 1801.01196 (2018).

[37] R. Kolesov *et al.*, *Optical Detection of a Single Rare-Earth Ion in a Crystal,* Nature Communications **3**, 1029 (2012).

[38] D. J. Christle *et al.*, *Isolated Electron Spins in Silicon Carbide with Millisecond Coherence Times,* Nature Materials **14**, 160 (2015).

[39] D. D. Sukachev *et al.*, *Silicon-Vacancy Spin Qubit in Diamond: A Quantum Memory Exceeding 10 ms with Single-Shot State Readout,* Physical Review Letters **119**, 223602 (2017).

[40] T. Iwasaki *et al.*, *Tin-Vacancy Quantum Emitters in Diamond,* arXiv:1708.03576 (2017).

[41] K. J. Morse *et al.*, *A Photonic Platform for Donor Spin Qubits in Silicon,* Science Advances **3**, e1700930 (2017).

[42] H.-J. Lim, S. Welinski, A. Ferrier, P. Goldner and J. J. L. Morton, *Coherent spin dynamics of ytterbium ions in yttrium orthosilicate,* arXiv , 1712.00435 (2017).

[43] H.-J. Briegel, W. Dür, J. I. Cirac and P. Zoller, *Quantum Repeaters: The Role of Imperfect Local Operations in Quantum Communication,* Physical Review Letters **81**, 5932 (1998).

[44] F. Rozpędek *et al.*, *Realistic Parameter Regimes for a Single Sequential Quantum Repeater,* arXiv , 1705.00043 (2017).

[45] N. H. Nickerson, J. F. Fitzsimons and S. C. Benjamin, *Freely Scalable Quantum Technologies Using Cells of 5-to-50 Qubits with Very Lossy and Noisy Photonic Links,* Physical Review X **4**, 041041 (2014).

7

LOOPHOLE-FREE BELL INEQUALITY VIOLATION USING ELECTRON SPINS SEPARATED BY 1.3 KILOMETRES

B. Hensen, H. Bernien, A.E. Dréau, A. Reiserer, N. Kalb, M.S. Blok,
J. Ruitenberg, R.F.L. Vermeulen, R.N. Schouten, C. Abellán, W. Amaya,
V. Pruneri, M.W. Mitchell, M. Markham, D.J. Twitchen, K. Goodenough,
D. Elkouss, S. Wehner, T.H. Taminiau and R. Hanson

For more than 80 years, the counterintuitive predictions of quantum theory have stimulated debate about the nature of reality[1]. In his seminal work[2], John Bell proved that no theory of nature that obeys locality and realism can reproduce all the predictions of quantum theory. In any local realist theory the correlations between distant measurements satisfy an inequality that can be violated according to quantum theory if the measurements are performed on entangled particles. In the past decades, numerous ingenious Bell inequality tests have been reported[3–14]. However, because of experimental limitations, all experiments to date required additional assumptions to obtain a contradiction with local realism, resulting in loopholes[14–17]. Here we report on a Bell experiment that is free of any such additional assumption and thus directly tests the principles underlying Bell's inequality. We employ an event-ready scheme[18–20] that enables the generation of robust entanglement between distant electron spins. Efficient spin readout avoids the fair sampling assumption[15,16], while the use of fast random basis selection and readout combined with a spatial separation of 1.3 km ensure the required locality conditions[14]. In two experimental tests we find strong evidence against the null-hypothesis that a local-realist model for space-like separated sites could produce data with a violation at least as large as we observe, even when allowing for memory[17,21] in the devices.

Part of the results in this chapter have been published in Nature **526**, 682 (2015) and Scientific Reports **6**, 30289 (2016).

7.1. BELL TESTS AND LOOPHOLES IN EXPERIMENTAL DEMONSTRATIONS

We consider a Bell test in the form proposed by Clauser, Horne, Shimony and Holt (CHSH)[25] (Fig. 7.1A). The test involves two boxes labelled A and B. Each box accepts a binary input (0 or 1) and subsequently delivers a binary output (+1 or −1). In each trial of the Bell test, a random input bit is generated on each side and input to the respective box. The random input bit triggers the box to produce an output value that is recorded. The test concerns correlations between the output values (labelled x and y for boxes A and B, respectively) and the input bits (labelled a and b for A and B, respectively) generated within the same trial.

The discovery made by Bell is that in any theory of physics that is both local (physical influences do not propagate faster than light) and realistic (physical properties are defined before, and independent of, observation) these correlations are bounded more strongly than they are in quantum theory. In particular, if the input bits can be considered free random variables (condition of 'free will') and the boxes are sufficiently separated such that locality prevents communication between the boxes during a trial, then the following inequality holds under local realism:

$$S = \left|\langle x\cdot y\rangle_{(0,0)} + \langle x\cdot y\rangle_{(0,1)} + \langle x\cdot y\rangle_{(1,0)} - \langle x\cdot y\rangle_{(1,1)}\right| \leq 2 \tag{7.1}$$

where $\langle x\cdot y\rangle_{(\mathrm{a,b})}$ denotes the expectation value of the product of x and y for input bits a and b. A mathematical formulation of the concepts underlying Bell's inequality is found in, for example, ref. 26.

Quantum theory predicts that the Bell inequality can be significantly violated in the following setting. We add one particle, for example an electron, to each box. The spin degree of freedom of the electron forms a two-level system with eigenstates $|\uparrow\rangle$ and $|\downarrow\rangle$. For each trial, the two spins are prepared into the entangled state $|\psi^-\rangle = (|\uparrow\downarrow\rangle - |\downarrow\uparrow\rangle)/\sqrt{2}$. The spin in box A is then measured along direction Z (for input bit $a = 0$) or X (for $a = 1$) and the spin in box B is measured along $(-Z+X)/\sqrt{2}$ (for $b = 0$) or $(-Z-X)/\sqrt{2}$ (for $b = 1$). If the measurement outcomes are used as outputs of the boxes, then quantum theory predicts a value of $S = 2\sqrt{2}$, which shows that the combination of locality and realism is fundamentally incompatible with the predictions of quantum mechanics.

Bell's inequality provides a powerful recipe for probing fundamental properties of nature: all local-realist theories that specify where and when the free random input bits and the output values are generated can be experimentally tested against it.

Violating Bell's inequality with entangled particles poses two main challenges: excluding any possible communication between the boxes (locality loophole[14]) and guaranteeing efficient measurements (detection loophole[15,16]). First, if communication is possible, a box can in principle respond using knowledge of both input settings, rendering the Bell inequality invalid. The locality conditions thus require boxes A and B and their respective free-input-bit generations to be separated in such a way that signals travelling at the

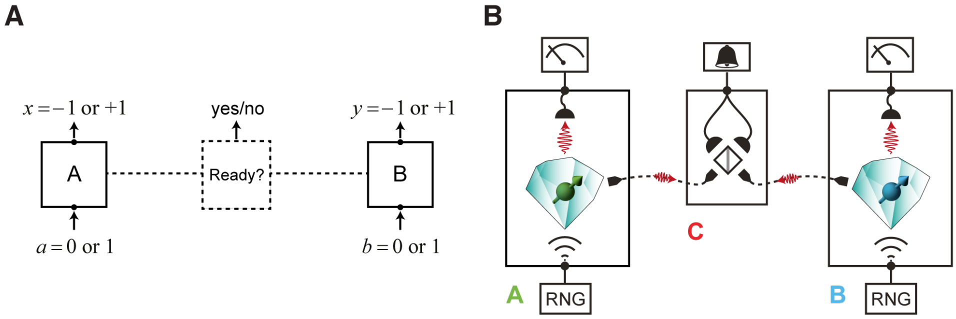

Figure 7.1 | **Bell-test schematic and experimental equivalent**. (**A**) Bell-test setup: two boxes, A and B, accept binary inputs (a, b) and produce binary outputs (x, y). In an event-ready scenario, an additional box C gives a binary output signalling that A and B were successfully prepared. (**B**) Experimental realization. The set-up consists of three separate laboratories, A, B and C. The boxes at locations A and B each contain a single NV centre in diamond. A quantum random-number generator (RNG) is used to provide the input. The NV electronic spin is read out in a basis that depends on the input bit, and the resultant signal provides the output. A box at location C records the arrival of single photons that were previously emitted by, and entangled with, the spins at A and B.

speed of light (the maximum allowed under special relativity) cannot communicate the local input setting of box A to box B, before the output value of box B has been recorded, and vice versa. Second, disregarding trials in which a box does not produce an output bit (that is, assuming fair sampling) would allow the boxes to select trials on the basis of the input setting. The fair sampling assumption thus opens a detection loophole[15,16]: the selected subset of trials may show a violation even though the set of all trials may not.

The locality loophole has been addressed with pairs of photons separated over a large enough distance, in combination with fast settings changes[4] and later with settings determined by fast random number generators[5,9]. However, these experiments left open the detection loophole, owing to imperfect detectors and inevitable photon loss during the spatial distribution of entanglement. The detection loophole has been closed in different experiments[6–8,10,12,13], but these did not close the locality loophole. So far, no experiment has closed all the loopholes simultaneously.

A Bell test that closes all experimental loopholes at the same time — commonly referred to as a loophole-free Bell test[16,20] — is of foundational importance to the understanding of nature. In addition, a loophole-free Bell test is a critical component for device-independent quantum security protocols[22] and randomness certification[23,24]. In such adversarial scenarios, all loopholes are ideally closed because they allow for security breaches in the system[27].

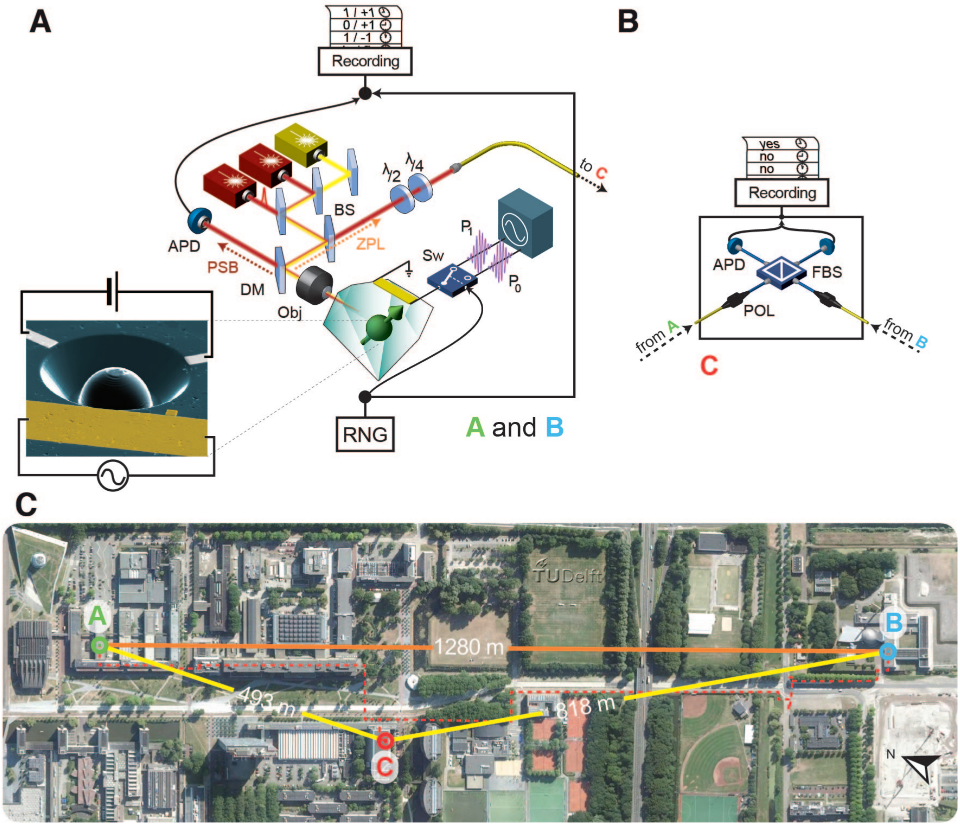

Figure 7.2 | **Experimental Setup**. (**A**) Experimental set-up at A and B. The NV centre is located in a low-temperature confocal microscope (Obj.). Depending on the output of the RNG, a fast switch (Sw.) transmits one of two different microwave pulses (P0 and P1) into a gold line deposited on the diamond surface (inset, scanning electron microscope image). Pulsed red and yellow lasers are used to resonantly excite the optical transitions of the NV centre. The emission (dashed arrows) is spectrally separated into an off-resonant part (phonon side band, PSB) and a resonant part (zero-phonon line, ZPL), using a dichroic mirror (DM). The PSB emission is detected with a single-photon counter (APD). The ZPL emission is transmitted through a beam-sampler (BS, reflection ≤ 4%) and wave plates ($\lambda/2$ and $\lambda/4$), and sent to location C through a single-mode fibre. (**B**) Set-up at location C. The fibres from A and B are connected to a fibre-based beam splitter (FBS) after passing a fibre-based polarizer (POL). Photons in the output ports are detected and recorded. (**C**) Aerial photograph of the campus of Delft University of Technology indicating the distances between locations A, B and C. The red dotted line marks the path of the fibre connection. Aerial photograph by Slagboom en Peeters Luchtfotografie BV.

7.2. EXPERIMENTAL REALIZATION

One approach for realizing a loophole-free set-up was proposed by Bell himself[18]. The key idea is to record an additional signal (dashed box in Fig. 7.1A) to indicate whether the required entangled state was successfully shared between A and B, that is, whether the boxes were ready to be used for a trial of the Bell test. By conditioning the validity of a Bell-test trial on this event-ready signal, failed entanglement distribution events are excluded upfront from being used in the Bell test.

We implemented an event-ready Bell set-up[19,20] with boxes that use the electronic spin associated with a single nitrogen-vacancy (NV) defect centre in a diamond chip (Fig. 7.1B). The diamond chips are mounted in closed-cycle cryostats ($T = 4\,\mathrm{K}$) located in distant laboratories named A and B (Fig. 7.2A). We control the electronic spin state of each NV centre with microwave pulses applied to on-chip striplines (Fig. 7.2A, inset). The spins are initialized through optical pumping and read out along the Z axis via spin-dependent fluorescence[28]. The readout relies on resonant excitation of a spin-selective cycling transition (12 ns lifetime), which causes the NV centre to emit many photons when it is in the bright $m_\mathrm{s} = 0$ spin state, while it remains dark when it is in either of the $m_\mathrm{s} = \pm 1$ states. We assign the value +1 ($m_\mathrm{s} = 0$) to the output if we record at least one photo-detector count during the read-out window, and the value −1 ($m_\mathrm{s} = \pm 1$) otherwise. Read-out in a rotated basis is achieved by first rotating the spin, followed by read-out along Z.

We generate entanglement between the two distant spins by entanglement swapping[19] in the Barrett–Kok scheme[29,30] using a third location C (roughly midway between A and B; see Fig. 7.2B and Fig. 7.2C). First we entangle each spin with the emission time of a single photon (time-bin encoding). The two photons are then sent to location C, where they are overlapped on a beam-splitter and subsequently detected. If the photons are indistinguishable in all degrees of freedom, then the observation of one early and one late photon in different output ports projects the spins at A and B into the maximally entangled state $|\psi^-\rangle = (|\uparrow\downarrow\rangle - |\downarrow\uparrow\rangle)/\sqrt{2}$, where $m_\mathrm{s} = 0 \equiv |\uparrow\rangle$ and $m_\mathrm{s} = -1 \equiv |\downarrow\rangle$. These detections herald the successful preparation and play the role of the event-ready signal in Bell's proposed set-up. As can be seen in the space–time diagram in Fig. 7.3A, we ensure that this event-ready signal is space-like separated from the random input-bit generation at locations A and B.

The separation of the spins by 1,280 m defines a 4.27-μs time window during which the local events at A and B are space-like separated from each other (see the space–time diagram in Fig. 7.3B). To comply with the locality conditions of the Bell test, the choice of measurement bases and the measurement of the spins should be performed within this time window. For the basis choice we use fast random-number generators with real-time randomness extraction[31]. We reserve 160 ns for the random basis choice, during which time one extremely random bit is generated from 32 partially random raw bits (see Sec. 7.8). The random bit sets the state of a fast microwave switch that selects one out of two preprogrammed microwave pulses implementing the two possible read-out bases (Fig. 7.2C). Adding the durations of each of the above steps yields a maximum time from

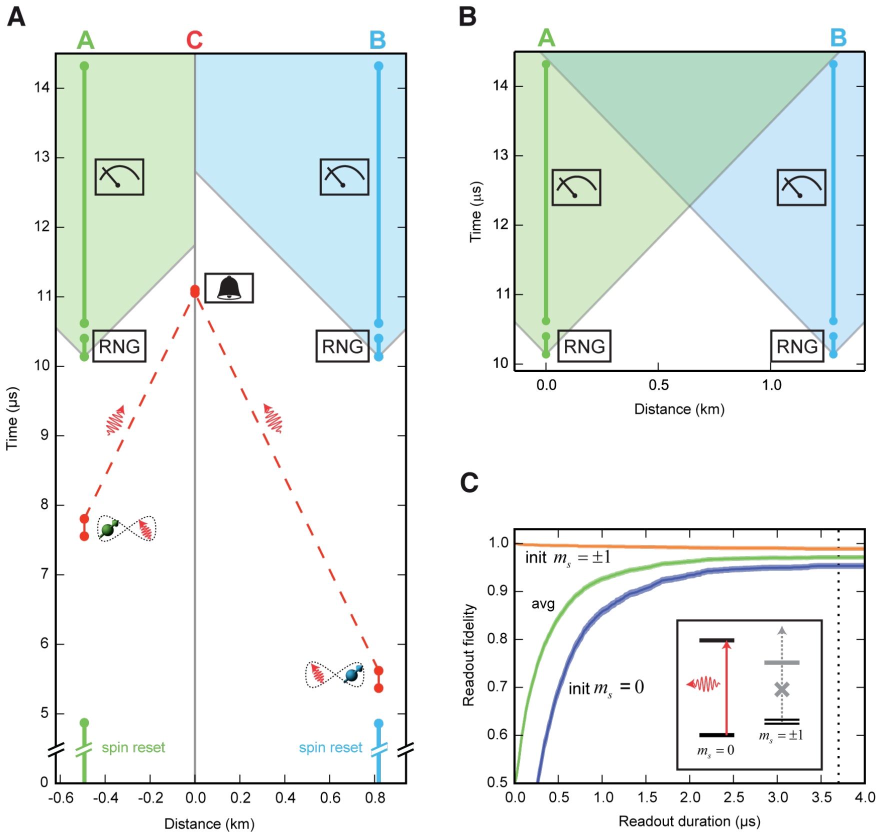

Figure 7.3 | Space–time analysis of the experiment. (**A**) Space–time diagram of a single repetition of the entanglement generation. The x axis denotes the distance along the lines AC and CB. After spin initialization, spin-photon entanglement is generated, such that the two photons from A and B arrive simultaneously at C where the detection time of the photons is recorded. Successful preparation of the spins is signalled (bell symbol) by a specific coincidence detection pattern. Independent of the event-ready signal, the setups at locations A and B choose a random basis (RNG symbol), rotate the spin accordingly and start the optical spin read-out (measurement symbol). Vertical bars indicate durations. The event-ready signal lies outside the future light cone (coloured regions) of the random basis choices of A and B. (**B**) Space–time diagram of the Bell test. The x axis denotes the distance along the line AB. The read-out on each side is completed before any light-speed signal can communicate the basis choice from the other side. The uncertainty in the depicted event times and locations is much smaller than the symbol size. (**C**) Single-shot spin read-out fidelity at location A as a function of read-out duration (set by the latest time that detection events are taken into account). Blue (orange) line, fidelity of outcome +1 (−1) when the spin is prepared in $m_S = 0$ ($m_S = \pm1$); green line, average read-out fidelity; dotted line, read-out duration used (3.7 μs). The inset shows the relevant ground and excited-state levels (not to scale).

the start of the basis choice to the start of the read-out of 480 ns. We choose the read-out duration to be 3.7 μs, which leaves 90 ns to cover any uncertainty in the distance between the laboratories and the synchronization of the set-up (estimated total error is at most 16 ns; see Sec. 7.8). For this read-out duration, the combined initialization and single-shot read-out fidelity of sample A is $(97.1 \pm 0.2)\%$ (Fig. 7.3C); sample B achieves $(96.3 \pm 0.3)\%$. In summary, the use of the event-ready scheme enables us to comply with the strict locality conditions of the Bell set-up by using photons to distribute entanglement, while simultaneously using the single-shot nature of the spin read-out to close the detection loophole.

7.3. SET-UP CHARACTERIZATION

Before running the Bell test we first characterized the set-up and the preparation of the spin–spin entangled state. Fig. 7.4A displays correlation measurements on the entangled spin-photon states to be used for the entanglement swapping. For both locations A and B we observe near-unity correlations between spin state and photon time bin when spin read-out errors are accounted for. We then estimate the degree of indistinguishability of the single photons emitted at locations A and B in a Hong–Ou–Mandel[32] two-photon-interference experiment at location C, that is, after the photons have travelled through a combined length of 1.7 km of fibre. Using the observed two-photon interference contrast of 0.90 ± 0.06 and the spin-photon correlation data, we estimate that the fidelity to the ideal state ψ^- of the spin–spin entangled states generated in our set-up is 0.92 ± 0.03 (Sec. 7.8.3). Combined with measured read-out fidelities, the generated entangled state is thus expected to violate the CHSH–Bell inequality with $S = 2.30 \pm 0.07$.

As a final characterization we ran the full Bell sequence including random number generation and fast read-out, but with co-linear measurement bases (ZZ and XX) such that spin–spin correlations could be observed with optimal contrast. To test the fast basis selection and rotation, the Z (X) basis measurements are randomly performed along the $+Z$ ($+X$) and $-Z$ ($-X$) axis. The observed correlations, shown in Fig. 7.4C (orange bars), are consistent with the estimated quantum state and the independently measured read-out fidelities (dotted bars), which confirms that the set-up is performing as expected and that the desired entangled state is generated.

We find a success probability per entanglement generation attempt of about $6.4 \cdot 10^{-9}$, which yields slightly more than one event-ready signal per hour. Compared to our previous heralded entanglement experiments over 3 m (ref. 30), this probability is reduced, mainly owing to additional photon loss (8dB km^{-1}) in the 1.7-km optical fibre. To ensure the required long-term operation, we exploit active stabilization on different relevant timescales via automated feedback loops (Sec. 7.8). We note that the distance between the entangled electrons is nearly two orders of magnitude larger than it was in any previous experiment[7,10,30,33] with entangled matter systems.

Using the results of the characterization measurements we determine the optimal read-out bases for our Bell test. A numerical optimization yields the following angles for the read-out bases with respect to Z: 0 (for $a = 0$), $+\pi/2$ (for $a = 1$), $-3\pi/4 - \epsilon$ (for $b = 0$) and

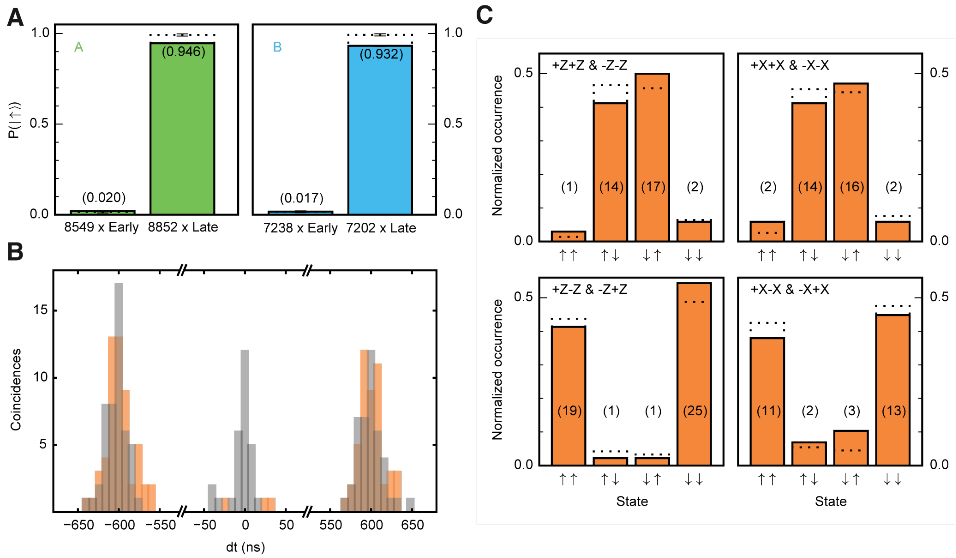

Figure 7.4 | Characterization of the set-up and the entangled state. (**A**) The probability to obtain spin state $|\uparrow\rangle$ at location A (left panel) or B (right panel) when a single photon is detected in the early or late time bin at location C. In the left (right) panel, only emission from A (B) was recorded. Dotted bars are corrected for finite spin read-out fidelity and yield remaining errors of 1.4% ± 0.2% (1.6% ± 0.2%) and 0.8% ± 0.4% (0.7% ± 0.4%) for early and late detection events, respectively, from set-up A (B). These errors include imperfect rejection of the excitation laser pulses, detector dark counts, microwave-pulse errors and off-resonant excitation of the NV. (**B**) Two-photon quantum interference signal, with dt the time between the two photo-detection events. When the NV centres at A and B emit indistinguishable photons, coincident detections of two photons, one in each output arm of the beam-splitter at C, are expected to vanish. The observed contrast between the cases of indistinguishable (orange) and distinguishable (grey) photons (3 versus 28 events in the central peak) yields a visibility of (90 ± 6)% (Sec. 7.8.2). (**C**) Characterization of the Bell set-up using (anti-)parallel read-out angles. The spins at A (left arrows on the x axis) and B (right arrows on the x axis) are read out along the ±Z axis (left panels) or the ±X axis (right panels). The numbers in brackets are the raw number of events. The dotted lines represent the expected correlations on the basis of the characterization measurements presented in (**A**) and (**B**) (Sec. 7.8.2). The data yield a strict lower bound[30] on the state fidelity to $|\psi^-\rangle$ of 0.83 ± 0.05. Error bars are 1 s.d.

$3\pi/4+\epsilon$ (for $b=1$), with $\epsilon = 0.026\pi$. Adding the small angle ϵ is beneficial because of the stronger correlations in ZZ compared to XX. Furthermore, we use the characterization data to determine the time window for valid photon-detection events at location C to optimally reject reflected laser light and detector dark counts. We choose this window conservatively to optimize the entangled-state fidelity at the cost of a reduced data rate. These settings are then fixed and used throughout the actual Bell test. As a final optimization we replaced the photo-detectors at location C with the best set we had available.

7.4. FIRST EXPERIMENTAL TRIAL

We ran 245 trials of the Bell test during a total measurement time of 220 h over a period of 18 days. Fig. 7.5A summarizes the observed data, from which we find $S = 2.42$, in violation of the CHSH–Bell inequality $S \leq 2$. We quantify the significance of this violation for two different scenarios (see Fig. 7.5B). First, similar to previous work[4–9], we analyse the data under the assumptions that the Bell trials are independent of each other, that the recorded random input bits have zero predictability and that the outcomes follow a Gaussian distribution. This analysis (which we term 'conventional') yields a standard deviation of 0.20 on S. In this case, the null hypothesis that a local-realist model for space-like separated sites describes our experiment is rejected with a P value of 0.019 (see Supplementary Information of ref.[34]).

The assumptions made in the conventional analysis are not justified in a typical Bell experiment. For instance, although the locality conditions outlined earlier are designed to ensure independent operation during a single trial, the boxes can in principle have access to the entire history including results from all previous trials and adjust their output to it[17,21]. Our second analysis (which we term 'complete') allows for arbitrary memory, takes the partial predictability of the random input bits into account and also makes no assumption about the probability distributions underlying the data (see Supplementary Information of ref. 34). In this case, the null hypothesis that an arbitrary local-realist model of space-like separated sites governs our experiment is rejected with a P value of 0.039 (Fig. 7.5B).

7.5. SECOND EXPERIMENTAL TRIAL

After finishing the first loophole-free Bell experiment in July 2015, both the A(lice) and B(ob) setups were modified and used in various local experiments. In December 2015, we rebuilt the Bell setup for performing a second run of the Bell test, with three small modifications compared to the first run.

First, we add a source of classical random numbers for the input choices[35]. A random basis choice is now made by applying an XOR operation between a quantum random bit generated as previously[31,36,37] and classical random bits based on Twitter messages, as proposed by Pironio[38]. In particular, we generate two sets of classical random numbers, one for the basis choice at A, and one for the basis choice at B. At each location, 8 of these bits are fed into an FPGA. Just before the random basis rotation, the 8 Twitter bits and 1 quantum random bit are combined by subsequent XOR operations. The resulting bit is used as the input of the same microwave switch as used in the first run[34]. The XOR operation takes 7 ns of additional time, shifting the start of the readout pulse to a later time by the same amount. We leave the end of the readout window unchanged, resulting in the same locality conditions as in the first test.

We note that the Twitter-based classical random bits by themselves cannot close the locality loophole: the raw data is available on the Internet well before the trials and the

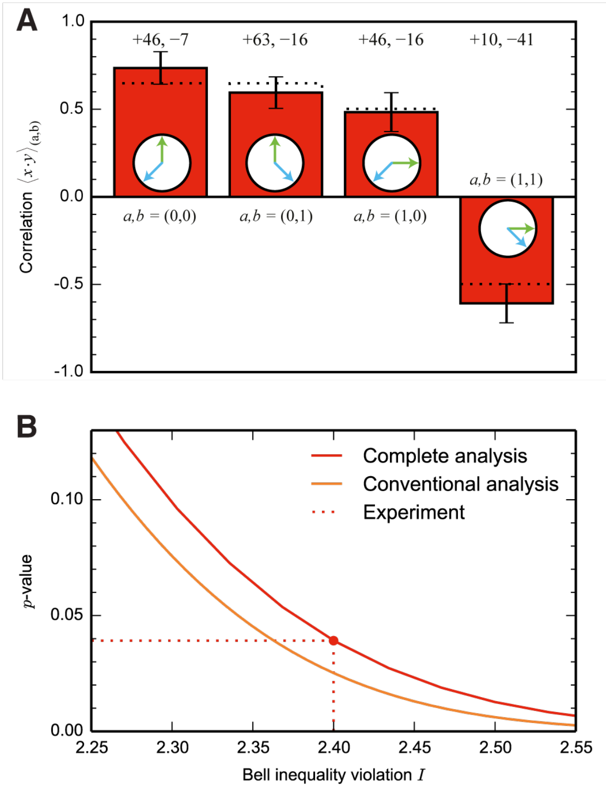

Figure 7.5 | Loophole-free Bell inequality violation. (**A**) Summary of the data and the CHSH correlations. The read-out bases corresponding to the input values are indicated by the green (for A) and blue (for B) arrows. Dotted lines indicate the expected correlation on the basis of the spin read-out fidelities and the characterization measurements presented in Fig. 7.4 (Sec. 7.8.3). Numbers above the bars represent the number of correlated and anti-correlated outcomes, respectively. Error bars shown are $\sqrt{1-\langle x\cdot y\rangle^2_{(\mathrm{a,b})}/n_{a,b}}$, with $n_{a,b}$ the number of events with inputs $(a,\ b)$. (**B**) Statistical analysis for $n=245$ trials. For the null-hypothesis test performed (Sec. 7.8.5), the dependence of the P value on the I value is shown (complete analysis, red). Here $I=8(\frac{k}{n}-\frac{1}{2})$, with k the number of times $(-1)^{(a\cdot b)}x\cdot y=1$. (For equal $n_{(a,b)}$, $I=S$ with S defined in Eq. (7.1).) A small P value indicates strong evidence against the null hypothesis. We find $k=196$, which results in a rejection of the null hypothesis with a $P\leq 0.039$. For comparison, we also plot the P value for an analysis (conventional analysis, orange) assuming independent and identically distributed (i.i.d.) trials, Gaussian statistics, no memory and perfect random-number generators.

protocol to derive the bits is deterministic and programmed locally. The only operations that are performed in a space-like separated manner are the XOR operations between 8 stored bits. Therefore, strictly speaking only the quantum-RNG is providing fresh random bits. Since a loophole-free Bell test is described solely by the random input bit generation and the outcome recording at A and B (and in our case the event-ready signal recording at C), the second run can test the same null hypothesis as the first run as these events are unchanged. That being said, the use of the Twitter-based classical randomness puts an additional constraint on local-hidden-variable models attempting to explain our data.

Second, we set larger (i.e. less conservative) heralding windows at the event-ready detector in order to increase the data rate compared to the first experiment. We start the heralding window about 700 picoseconds earlier, motivated by the data from the first test. We predefine a window start of 5426.0 ns after the sync pulse for channel 0, and 5425.1 ns for channel 1. We set a window length of 50 ns.

Finally, we also use the ψ^+-Bell state, which is heralded by two photo-detection events in the *same* beam-splitter output arm at the event-ready station. In general the fidelity of this Bell state is lower than that of ψ^- due to detector after-pulsing[30] (note that for ψ^- the after-pulsing is not relevant because ψ^- is heralded by photo detection events in different beam-splitter output arms). However, we found the after-pulsing effect to be small enough for the detectors used in this run. We set an adapted window length of the second window of 4 ns and 2.5 ns for channels 0, 1 respectively, where the exponentially decaying NV emission is still large relative to the after-pulsing probability. We can combine the ψ^--related and ψ^+-related Bell trials into a single hypothesis test[39] (see also Sec. 7.9.2).

Apart from these modifications, all settings, analysis software, calibrations and stabilisation routines were identical to those in the first run[34].

In this test we set the total number of Bell trials $n_2 = 300$. After 210 hours of measurement over 22 days during 1 month, we find $S_2 = 2.35 \pm 0.18$, with S_2 the weighted average of $S_{\psi^-} = \langle x \cdot y \rangle_{(0,0)} + \langle x \cdot y \rangle_{(0,1)} + \langle x \cdot y \rangle_{(1,0)} - \langle x \cdot y \rangle_{(1,1)}$ for ψ^- heralded events (different detectors clicked), and $S_{\psi^+} = \langle x \cdot y \rangle_{(0,0)} + \langle x \cdot y \rangle_{(0,1)} - \langle x \cdot y \rangle_{(1,0)} + \langle x \cdot y \rangle_{(1,1)}$ for ψ^+ (same detector clicked). See Fig. 7.6. This yields a P-value of 0.029 in the conventional analysis[34] (a non-loophole-free analysis that assumes independent trials, perfect random number generators and Gaussian statistics), and with $k_2 = 237$ a P-value of 0.061 in the complete analysis[34].

7.6. COMBINED P-VALUE FOR THE TWO TESTS

We now turn to analysing the statistical significance of the two runs combined. Let us first note that there are many methods for combining hypothesis tests and P-values, each with its own assumptions. Extending the conventional analysis, we take the weighted sum of the CHSH parameters obtained for both tests to find $S_{\text{combined}} = 2.38 \pm 0.136$, yielding a P-value of $2.6 \cdot 10^{-3}$. For the complete analysis, we give here two example cases. The first case is where the tests are considered to be fully independent; the P-values can then be combined using Fisher's method, resulting in a joint P-value of $1.7 \cdot 10^{-2}$ for the complete analysis. As a second example the two runs are considered to form a single test; the data can then be combined, $k_1 + k_2 = 433$ for $n_1 + n_2 = 545$, resulting in a joint

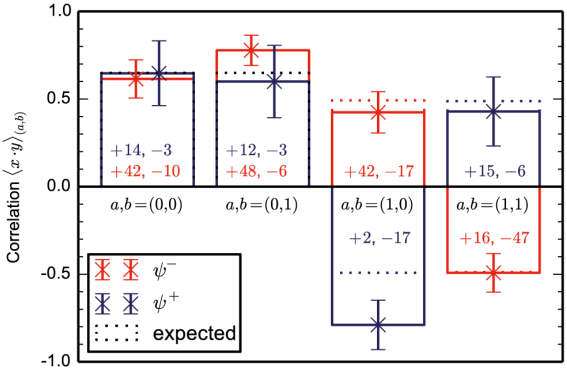

Figure 7.6 | Second loophole-free Bell test results: Summary of the measured CHSH correlations. We record a total of $n_2 = 300$ trials of the Bell test. Dotted lines indicate the expected correlation based on the spin readout fidelities and the characterization measurements presented in Sec. 7.8.3. Shown are data for both ψ^- heralded events (red, two clicks in different APD's at location C), and for ψ^+ heralded events (blue, two clicks in the same APD). Numbers in bars represent the amount of correlated and anti-correlated outcomes respectively, for ψ^- (red) and ψ^+ (orange). Error bars shown are $\sqrt{1-\langle x \cdot y \rangle^2_{(\mathrm{a,b})}/n_{a,b}}$, with $n_{(a,b)}$ the number of events with inputs $(a,\ b)$.

P-value of $8.0 \cdot 10^{-3}$ for the complete analysis. We emphasize that these are extreme interpretations of a subtle situation and these P-values should be considered accordingly.

7.7. CONCLUSION

Our experiment realizes the first Bell test that simultaneously addresses both the detection loophole and the locality loophole. Being free of the experimental loopholes, the set-up tests local-realist theories of nature without introducing extra assumptions such as fair sampling, a limit on (sub-)luminal communication or the absence of memory in the set-up. Our observation of a statistically significant loophole-free Bell inequality violation thus indicates rejection of all local-realist theories that accept that the number generators produce a free random bit in a timely manner and that the outputs are final once recorded in the electronics.

Strictly speaking, no Bell experiment can exclude all conceivable local-realist theories, because it is fundamentally impossible to prove when and where free random input bits and output values came into existence[14]. Even so, our loophole-free Bell test opens the possibility to progressively bound such less-conventional theories: by increasing the distance between A and B (for example, to test theories with increased speed of physical influence); by using different random input bit generators (to test theories with specific free-will agents, for example, humans); or by repositioning the random input bit generators (to test theories where the inputs are already determined earlier, sometimes referred to as 'freedom-of-choice'[9]). In fact, our experiment already enables tests of all models that predict that the random inputs are determined a maximum of 690 ns before we record them (Sec. 7.8)

Combining the presented event-ready scheme with higher entangling rates (for example, through the use of optical cavities) provides prospects for the implementation of device-independent quantum key distribution[22] and randomness certification[23,24]. In combination with quantum repeaters, this might enable the realization of large-scale quantum networks that are secured through the very same counterintuitive concepts that inspired one of the most fundamental scientific debates for 80 years[1,2].

CONTRIBUTIONS

First run B.H., H.B. and R.H. devised the experiment. B.H., H.B., A.E.D., A.R., M.S.B., J.R., R.F.L.V. and R.N.S. built and characterized the experimental set-up. M.W.M., C.A. and V.P. designed the quantum random-number generators (QRNGs), M.W.M. and C.A. designed the randomness extractors, and W.A. and C.A. built the interface electronics and the QRNG optics, the latter with advice from V.P. C.A. and M.W.M. designed and implemented the QRNG statistical metrology. C.A. designed and implemented the QRNG output tests. M.M. and D.J.T. grew and prepared the diamond device substrates. H.B. and M.S.B. fabricated the devices. B.H., H.B., A.E.D., A.R. and N.K. collected and analysed the data, with support from T.H.T. and R.H. D.E. and S.W. performed the theoretical analysis. R.H. supervised the project.

Second run B.H. and R.H. devised the experiment. B.H., N.K., A.E.D., A.R., M.S.B., R.F.L.V. and R.N.S. built and characterized the experimental set-up. K.G. compiled the random Twitter datasets. M.M. and D.J.T. grew and prepared the diamond device substrates. M.S.B. fabricated the devices. B.H., N.K., A.E.D., A.R. and M.S.B. collected and analysed the data, with support from T.H.T. and R.H. D.E. and S.W. performed the theoretical analysis. R.H. supervised the project.

The underlying manuscripts were written by B.H., A.R., T.H.T., D.E., S.W. and R.H. and ultimately adapted for this thesis by N.K.

7.8. SUPPLEMENTARY INFORMATION

For the supplementary information contained in this thesis we limit us to the description of the experimental setup and sequence as well as the estimation of the generated entangled state. In the following we give an overview of the available information attached to refs. 40, 41.

- Descriptions of the tested models and their properties[40,41].
- A detailed description of the 'complete analysis' which incorporates memory of the devices, partial predictability of the generated random numbers and additionally makes no assumption on the probability distributions that underlie the

data[40]. A summary of the P-valuecomputation is given in Sections 7.8.5,7.9.2.

- Details on the fast random number generation[40] and the introduction of classical randomness based on Twitter messages[41].
- Details on data recording and processing as well as synchronization of the experimental set-ups[40].
- Frequency stabilization of the two excitation lasers[40].
- The implementation of adaptive optics at Node A to enhance the photon collection efficiency[40].
- Determination of locations and distances between the laboratories[40].
- Determination of the event-ready signal settings[40].
- Analysis of the Bell violation when changing the event-ready signal settings[41].
- Examination of the observed violation for changed read out window settings[40].
- A statistical analysis of the obtained read out settings choices[41].

7.8.1. EXPERIMENTAL SETUP

The experiments are performed on individual NV centres that are naturally present in high purity type IIa chemical-vapor deposition diamond samples (Element Six), with a ⟨111⟩ crystal orientation. In its negative charge state, the NV centre ground state is an electronic spin triplet with total spin 1. The zero-field splitting separates the $|m_s = 0\rangle$ and $|\mathrm{m}_s = \pm 1\rangle$ levels by 2.88 GHz. Additionally we split the $|\mathrm{m}_s = \pm 1\rangle$ levels by 0.14 GHz using a static magnetic field applied along the defect axis. We use the two levels $|m_s = 0\rangle$ and $|m_s = -1\rangle$, denoted as $|\uparrow\rangle$ and $|\downarrow\rangle$, respectively. We use microwave control pulses, applied via a gold stripline deposited on the sample surface, to rotate the electronic ground state spin. The carrier frequency of the pulses is resonant with the $|\mathrm{m}_s = 0\rangle$ to $|\mathrm{m}_s = -1\rangle$ ground state transition. The electronic spin resonance spectrum of both NV centres is split into three lines by the hyperfine interaction with the host nitrogen nuclear spin of the defect. Therefore, we chose a Hermite pulse envelope shape, which provides a broad and flat spectral distribution. In this way, we achieve a π rotation within 180 ns with a fidelity exceeding 99.8% without initializing the nitrogen nuclear spin state.

The samples are kept at a temperature of 4 K in closed-cycle cryostats (Montana Instruments) to enable resonant optical excitation of spin-dependent transitions. This enables fast single-shot readout and high-fidelity optical initialization of the electronic spin state. The design of the electronics and optical setup is described in detail in previous work[30,42]. To initialize the electronic spin into $|\downarrow\rangle$, we apply resonant excitation on the $|\mathrm{m}_s = \pm 1\rangle \leftrightarrow |E'\rangle$ optical transition, achieving an initialization fidelity of more than 99.8% within 5 μs. Electronic spin readout is accomplished by resonant excitation of the $E_x(E_y)$ transition for the sample in setup A (B). To guarantee a high readout fidelity by minimizing the spin mixing in the excited state, we chose samples with low transversal strain splitting and additionally use d.c. Stark tuning by applying d.c. electric fields to the on-chip electrodes (Fig. 7.2A inset). The average strain splitting during the experiment was 1.8 (2.3) GHz in sample A (B).

A high photon collection efficiency is a prerequisite for high fidelity optical single-shot readout and high-efficiency entanglement. To overcome the limitation of total internal reflection of the emitted photons, we fabricate solid immersion lenses in the diamond surface around preselected NVs (oriented along the $\langle 111 \rangle$ crystal direction) using a focused ion beam. In addition, we deposit a single-layer aluminium oxide anti-reflection coating. We select devices with a particularly high phonon-sideband (PSB, wavelength > 640 nm) photon collection efficiency in our home-built confocal microscope setups, which we measure to be $(13 \pm 2)\%$. Note that this value includes the 80% quantum efficiency of the detectors. The zero-phonon line (ZPL) photon emission of each NV is separated from the PSB using a dichroic long-pass and an additional tunable bandpass filter. Per optical excitation, we collect on average $2.9 \cdot 10^{-4}$ $(1.7 \cdot 10^{-4})$ ZPL photons at location C after propagation through a single-mode fibre from location A (B). Measured fiber losses are 6 dB from A to C and 9 dB from B to C.

On setup A, we use adaptive optics to couple the ZPL emission into the single-mode fiber, increasing the efficiency by about a factor of two, compared to using standard optics. We use two polarisers at C to block unwanted reflections from the excitation pulse. To compensate for polarization drift inside the fibers, an automated polarization control feedback loop adjusts two waveplates in front of the fiber couplers at A and B.

7.8.2. TWO-PHOTON QUANTUM INTERFERENCE (FIG. 7.4B)

Measurement of photon coincidences in different output ports of a beam splitter has become a standard tool to investigate the indistinguishability of single photons generated by different sources. To account for potentially unequal efficiency of the sources, one can compare the case where the photons are indistinguishable to one where they are made distinguishable on purpose. In our experimental system, using orthogonal polarization is prohibited by in-line fibre polarisers. We instead program the experimental sequence such that setup A generates photons in an ‘early’ time window and setup B in a ‘late’ time window which is delayed with respect to the early one by 300 ns. Since this is much longer than the optical lifetime of the NV centre, this allows us to clearly distinguish which of the setups has emitted a given detected photon. During the measurement this distinguishable setting is alternated (every 3750 excitation pulses) with the indistinguishable setting, in which both setups produce photons that arrive at the same time at the beamsplitter.

In the data analysis for the distinguishable setting the arrival times of the photons in the late time window (coming from setup B) are shifted back by 300 ns in order to overlap them with those from setup A. In this way, we can present the data in a more familiar way (Fig. 7.4B). Note also that the data in Fig. 7.4B is taken on a different NV pair than the one used in the other experiments; the two pairs are very similar and are therefore expected to yield equivalent results.

7.8.3. MODEL OF THE ENTANGLED STATE (FIGURES 7.4C AND 7.5A)

We estimate the readout fidelities of NV A and B from the daily calibration measurements during the recording of the XX and ZZ entanglement data (Fig. 7.4C). We find: $F_0^A = 0.9536 \pm 0.0030$, $F_1^A = 0.9940 \pm 0.0011$, $F_0^B = 0.9390 \pm 0.0034$, $F_1^B = 0.9982 \pm 0.0006$. Using these values, we correct the spin-photon correlation data of Fig. 7.4A for readout errors[42], to obtain the residual errors made in the spin-photon correlation, $e^{A,B}_{\text{early,late}}$ presented in the caption of Fig. 7.4A.

To obtain an estimate for the fidelity of the generated entangled state, we model the state of the two NVs after a successful heralding event by a density matrix of the following form (See SI of ref. 42):

$$\rho = \frac{1}{2}\begin{pmatrix} 1-F_z & 0 & 0 & 0 \\ 0 & F_z & -V & 0 \\ 0 & -V & F_z & 0 \\ 0 & 0 & 0 & 1-F_z \end{pmatrix}. \tag{7.2}$$

Here we set

$$F_z = \frac{1}{2}\left((1-e^A_{\text{early}})(1-e^B_{\text{late}}) + (1-e^B_{\text{early}})(1-e^A_{\text{late}})\right), \tag{7.3}$$

V can be estimated from the measured interference contrast in Fig. 7.4B, in combination with the expected 3% reduction in phase coherence from the instability in excitation laser frequency. The statistical uncertainty in the estimated V is large because of the small number of events in the interference experiment. Our best estimate is $V \approx 0.9 * 0.97 = 0.873 \pm 0.060$. This yields an estimate for the state fidelity $\langle\Psi^-|\rho|\Psi^-\rangle = 0.92 \pm 0.03$. To get the expected correlation values for Fig. 7.4C, we numerically perform the corresponding final basis rotations $U_{a,b}$ on ρ and apply the expected readout-errors on the obtained density matrix. We use the same model to numerically find the best basis settings for the Bell experiment and to calculate the expected correlators in Fig. 7.5A. This results in an expected S-parameter of 2.30 ± 0.07.

7.8.4. DYNAMICAL DECOUPLING SEQUENCE

The coherence of the NV centre spins is limited by the interaction with a bath of ^{13}C nuclear spins, resulting in a dephasing time T_2^* of a few μs. To counteract this dephasing we apply a dynamical decoupling sequence that consists of two microwave (MW) π-pulses with appropriate spacing. The full experimental pulse sequence is shown in Fig. 7.7. To quantify the remaining detrimental effect of spin dephasing during the experiment, we omit the two optical π-pulses used to generate the spin-photon entanglement and replace the last MW rotation by a $\pi/2$ pulse. Ideally, this sequence should bring the spin to the state $|\downarrow\rangle$. The measured probability to end up in this state is above 99% showing that decoherence is efficiently mitigated.

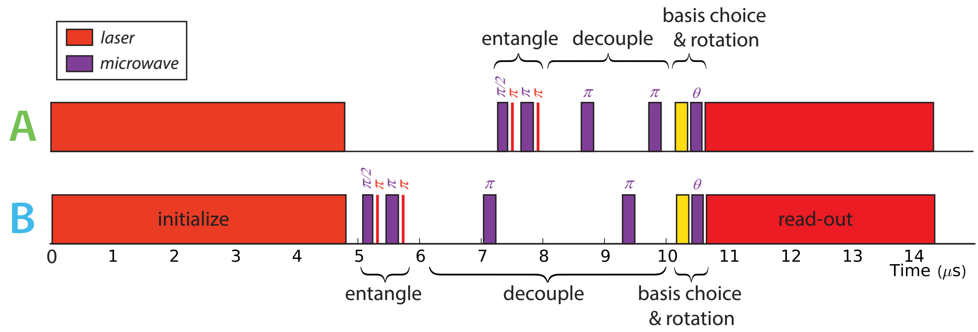

Figure 7.7 | Pulse sequence of the experiment. First, the spins at A (top) and B (bottom) are initialized by optical pumping. Then we perform the entangling sequence, consisting of two microwave and two optical pulses, followed by a dynamical decoupling sequence consisting of two microwave π-pulses that preserves the spin coherence. Finally, the readout basis is chosen and implemented and the spins are read out.

7.8.5. HOW TO COMPUTE THE P-VALUE

See Fig. 7.1A; an event-ready Bell experiment consisted of m entanglement attempts. Let $\mathbf{t}^m = (t_i)_{i=1}^m$ denote the output signal of the “event-ready”-box, where the tag $t_i = 0$ corresponds to a failure (no, not ready) event, and $t_i = 1$ to a successful preparation (yes, ready) of the boxes A and B [*]. We will reserve the word *trial* for the attempts that correspond to a successful preparation. Throughout, we use superscripts m to remind ourselves a sequence $\mathbf{t}^m$ has m elements.

Let $\mathbf{a}^m = (a_i)_{i=1}^m, \mathbf{b}^m = (b_i)_{i=1}^m$ denote the inputs to boxes A and B in Fig. 7.1a, where $a_i, b_i \in \{0,1\}$. Furthermore, let $\mathbf{x}^m = (x_i)_{i=1}^m, \mathbf{y}^m = (y_i)_{i=1}^m$ with $x_i, y_i \in \{\pm 1\}$ denote the output of boxes A and B.

We denote by $|\mathbf{t}^m|$ the number of ones in the binary sequence $\mathbf{t}^m$. Since we will use only the attempts where $t_i = 1$, let us define

$$n := |\mathbf{t}^m| = \sum_{i=1}^{m} t_i \tag{7.4}$$

to be the number of attempts in which $t_i = 1$, where n is fixed as discussed below. Given the observed values $\mathbf{a}^m, \mathbf{b}^m, \mathbf{x}^m, \mathbf{y}^m$, and $\mathbf{t}^m$ recorded in the experiment, we can compute the CHSH function

$$k := \sum_{i=1}^{m} t_i \cdot \frac{(-1)^{a_i b_i} x_i y_i + 1}{2} \; . \tag{7.5}$$

Note that k is the number of times that $(-1)^{a_i b_i} x_i y_i = 1$. When viewing CHSH as a non-local game [14], k is thus the number of times that Alice and Bob win the CHSH game. For large n, and uniform distribution of the inputs, we have $k \approx n(S+4)/8$, where S is the

---

[*] For readers that are familiar with non-local games we note that the ‘event-ready’ box could be seen as a third player that receives no question as input.

value of the familiar CHSH correlator. The supplement of ref. 34 in conjunction with ref. 39 rigorously prove that

$$P\text{-value} \leq P_{n,k}(\mathbb{B}_\xi) = \sum_{j=k}^{n} \binom{n}{j} \xi^j (1-\xi)^{n-j}\,, \tag{7.6}$$

where $P_{n,k}(\mathbb{B}_\xi)$ is the probability that n i.i.d. (independent and identically distributed) Bernoulli trials with probability

$$\xi = 3/4 + 3(\tau + \tau^2) \tag{7.7}$$

have at least k successes. Here τ denotes a partial predictability of the inputs given the history of the experiment[40] (in our case $\tau \approx 10^{-5}$). We remark that n is fixed in this analysis, i.e., we stop the experiment if a certain number n of trials have been collected, where n was decided independently of the data observed.

Even though we allowed that the LHVM could depend on previous attempts, thus making no extra assumptions on the memory of the devices, the upper bound is the tail probability of an i.i.d. distribution. This is not at all uncommon for sums of random variables, and there are many other examples where such a simplification occurs (see for instance ref. 43 and ref. 44).

7.9. SUPPLEMENTARY INFORMATION - SECOND EXPERIMENTAL TRIAL

7.9.1. APD REPLACEMENT

After 5 days of measurement, the APD at location C corresponding to channel 0 broke down during the daily calibration routine and was subsequently replaced. To take into account the changed detection-to-output delay for the event-ready filter settings, the laser pulse arrival time was recorded for the new APD before proceeding. We adapted the start of the event-ready window for channel 0 accordingly, and used this for all the data taken afterwards.

7.9.2. JOINT P-VALUEFOR ψ^- AND ψ^+ HERALDED EVENTS

Here we expand the statistical analysis used for the first run[34] to incorporate the ψ^- and ψ^+ events into one hypothesis test. For each of these states we perform a different variant of the CHSH game, and then use the methods of Elkouss and Wehner[39] to combine the two: The output signal of the "event-ready"-box $\mathbf{t}^m = (t_i)_{i=1}^m$ now has three possible outcomes, where the tag $t_i = 0$ still corresponds to a failure (no, not ready) event. We now distinguish two different successful preparations of the boxes A and B: $t_i = -1$ corresponds to a successful preparation of the ψ^- Bell state, and $t_i = +1$ to a ψ^+ Bell state. In terms of non-local games, Alice and Bob are playing two different games, where in case $t_i = -1$ they must have $(-1)^{a_i b_i} x_i y_i = 1$ in order to win, and in case of $t_i = +1$ they must have $(-1)^{a_i (b_i \oplus 1)} x_i y_i = 1$ to win. Note that both games have the same maximum winning probabilities. This means that we can take $k := k_- + k_+$, with k_- the number of times $(-1)^{a_i b_i} x_i y_i = 1$, and k_+ the number of times $(-1)^{a_i (b_i \oplus 1)} x_i y_i = 1$; the remainder of the analysis remains the same and in particular the obtained bound to the P-value is unchanged (see Elkouss and Wehner[39], page 20). We then have for the adapted CHSH function (see Supplementary Information of Hensen et al.[34]):

$$k' := \sum_{i=1}^{m} |t_i| \cdot \frac{(-1)^{a_i (b_i + \frac{t_i+1}{2})} x_i y_i + 1}{2} \tag{7.8}$$

and adapted total number of events then becomes:

$$n' := \left|\mathbf{1}\, t^m\right| = \sum_{i=1}^{m} |t_i|. \tag{7.9}$$

REFERENCES

[1] A. Einstein, B. Podolsky and N. Rosen. Can quantum-mechanical description of physical reality be considered complete? *Physical Review* **47**, 777 (1935).

[2] J. Bell. On the einstein-podolsky-rosen paradox. *Physics* **1**, 195 (1964).

[3] S. J. Freedman and J. F. Clauser. Experimental test of local hidden-variable theories. *Physical Review Letters* **28**, 938 (1972).

[4] A. Aspect, J. Dalibard and G. Roger. Experimental test of bell's inequalities using time- varying analyzers. *Physical Review Letters* **49**, 1804 (1982).

[5] G. Weihs, T. Jennewein, C. Simon, H. Weinfurter and A. Zeilinger. Violation of bell's inequality under strict einstein locality conditions. *Physical Review Letters* **81**, 5039 (1998).

[6] M. A. Rowe *et al.* Experimental violation of a bell's inequality with efficient detection. *Nature* **409**, 791 (2001).

[7] D. N. Matsukevich, P. Maunz, D. L. Moehring, S. Olmschenk and C. Monroe. Bell inequality violation with two remote atomic qubits. *Physical Review Letters* **100**, 150404 (2008).

[8] M. Ansmann *et al.* Violation of bell's inequality in josephson phase qubits. *Nature* **461**, 504 (2009).

[9] T. Scheidl *et al.* Violation of local realism with freedom of choice. *Proceedings of the National Academy of Sciences* **107**, 19708 (2010).

[10] J. Hofmann *et al.* Heralded entanglement between widely separated atoms. *Science* **337**, 72 (2012).

[11] W. Pfaff *et al.* Demonstration of entanglement-by-measurement of solid-state qubits. *Nature Physics* **9**, 29 (2013).

[12] M. Giustina *et al.* Bell violation using entangled photons without the fair-sampling assumption. *Nature* **497**, 227 (2013).

[13] B. G. Christensen *et al.* Detection-loophole-free test of quantum nonlocality, and applications. *Physical Review Letters* **111**, 130406 (2013).

[14] N. Brunner, D. Cavalcanti, S. Pironio, V. Scarani and S. Wehner. Bell nonlocality. *Reviews of Modern Physics* **86**, 419 (2014).

[15] A. Garg and N. D. Mermin. Detector inefficiencies in the einstein-podolsky-rosen experiment. *Physical Review D* **35**, 3831 (1987).

[16] P. H. Eberhard. Background level and counter efficiencies required for a loophole-free einstein-podolsky-rosen experiment. *Physical Review A* **47**, R747 (1993).

[17] J. Barrett, D. Collins, L. Hardy, A. Kent and S. Popescu. Quantum nonlocality, bell inequalities, and the memory loophole. *Physical Review A* **66**, 042111 (2002).

[18] J. S. Bell. Bertlmann's socks and the nature of reality. *Le Journal de Physique Colloques* **42**, C2 (1981).

[19] M. Żukowski, A. Zeilinger, M. A. Horne and A. K. Ekert. Event-ready-detectors" bell experiment via entanglement swapping. *Physical Review Letters* **71**, 4287 (1993).

[20] C. Simon and W. T. M. Irvine. Robust long-distance entanglement and a loophole-free bell test with ions and photons. *Physical Review Letters* **91**, 110405 (2003).

[21] R. D. Gill. Time, finite statistics, and bell's fifth position. *Proc. of "Foundations of Probability and Physics - 2.* Växjö Univ. Press (2003), *Ser. Math. Modelling in Phys., Engin., and Cogn. Sc.*, volume 5, 179–206.

[22] A. Acín *et al.* Device-independent security of quantum cryptography against collective attacks. *Physical Review Letters* **98**, 230501 (2007).

[23] R. Colbeck. *Quantum and Relativistic Protocols for Secure Multi-Party Computation.* Ph.D. thesis, University of Cambridge (2007).

[24] S. Pironio *et al.* Random numbers certified by bell's theorem. *Nature* **464**, 1021 (2010).

[25] J. F. Clauser, M. A. Horne, A. Shimony and R. A. Holt. Proposed experiment to test local hidden-variable theories. *Physical Review Letters* **23**, 880 (1969).

[26] J. S. Bell. *Speakable and Unspeakable in Quantum Mechanics: Collected Papers on Quantum Philosophy.* Cambridge University Press, 2 edition (2004).

[27] I. Gerhardt *et al.* Experimentally faking the violation of bell's inequalities. *Physical Review Letters* **107**, 170404 (2011).

[28] L. Robledo *et al.* High-fidelity projective read-out of a solid-state spin quantum register. *Nature* **477**, 574 (2011).

[29] S. D. Barrett and P. Kok. Efficient high-fidelity quantum computation using matter qubits and linear optics. *Physical Review A* **71**, 060310 (2005).

[30] H. Bernien *et al.* Heralded entanglement between solid-state qubits separated by three metres. *Nature* **497**, 86 (2013).

[31] C. Abellán, W. Amaya, D. Mitrani, V. Pruneri and M. W. Mitchell. Generation of fresh and pure random numbers for loophole-free bell tests. *Physical Review Letters* **115**, 250403 (2015).

[32] C. K. Hong, Z. Y. Ou and L. Mandel. Measurement of subpicosecond time intervals between two photons by interference. *Physical Review Letters* **59**, 2044 (1987).

[33] S. Ritter *et al.* An elementary quantum network of single atoms in optical cavities. *Nature* **484**, 195 (2012).

[34] B. Hensen *et al.* Loophole-free bell inequality violation using electron spins separated by 1.3 kilometres. *Nature* **526**, 682 (2015).

[35] L. K. Shalm *et al.* Strong Loophole-Free Test of Local Realism*. *Physical Review Letters* **115**, 250402 (2015).

[36] C. Abellán *et al.* Ultra-fast quantum randomness generation by accelerated phase diffusion in a pulsed laser diode. *Optics Express* **22**, 1645 (2014).

[37] M. W. Mitchell, C. Abellan and W. Amaya. Strong experimental guarantees in ultra-fast quantum random number generation. *Physical Review A* **91**, 012314 (2015).

[38] S. Pironio. Random 'choices' and the locality loophole. *arXiv:1510.00248 [quant-ph]* (2015).

[39] D. Elkouss and S. Wehner. (Nearly) optimal P values for all Bell inequalities. *npj Quantum Information* **2**, npjqi201626 (2016).

[40] B. Hensen *et al.* Loophole-free Bell inequality violation using electron spins separated by 1.3 kilometres. *Nature* **526**, 682 (2015).

[41] B. Hensen *et al.* Loophole-free Bell test using electron spins in diamond: Second experiment and additional analysis. *Scientific Reports* **6**, srep30289 (2016).

[42] W. Pfaff *et al.* Unconditional quantum teleportation between distant solid-state quantum bits. *Science* **345**, 532 (2014).

[43] V. Bentkus. On Hoeffding's inequalities. *Annals of probability* 1650–1673 (2004).

[44] I. Pinelis. Binomial upper bounds on generalized moments and tail probabilities of (super) martingales with differences bounded from above. *High dimensional probability*, Institute of Mathematical Statistics, 33–52 (2006).

8

DETERMINISTIC DELIVERY OF REMOTE ENTANGLEMENT ON A QUANTUM NETWORK

P.C. Humphreys*, N. Kalb*, J.P.J. Morits, R.N. Schouten, R.F.L. Vermeulen, M. Markham, D.J. Twitchen and R. Hanson

Large-scale quantum networks promise to enable secure communication, distributed quantum computing, enhanced sensing and fundamental tests of quantum mechanics through the distribution of entanglement across nodes[1–7]. Moving beyond current two-node networks[8–13] requires the rate of entanglement generation between nodes to exceed their decoherence rates. Beyond this critical threshold, intrinsically probabilistic entangling protocols can be subsumed into a powerful building block that deterministically provides remote entangled links at pre-specified times. Here we surpass this threshold using diamond spin qubit nodes separated by 2 metres. We realise a fully heralded single-photon entanglement protocol that achieves entangling rates up to 39 Hz, three orders of magnitude higher than previously demonstrated two-photon protocols on this platform[14]. At the same time, we suppress the decoherence rate of remote entangled states to 5 Hz by dynamical decoupling. By combining these results with efficient charge-state control and mitigation of spectral diffusion, we are able to deterministically deliver a fresh remote state with average entanglement fidelity exceeding 0.5 at every clock cycle of ~100 ms without any pre- or post-selection. These results demonstrate a key building block for extended quantum networks and open the door to entanglement distribution across multiple remote nodes.

The results in this chapter have been submitted for publication. arXiv:1712.07567

*Equally contributing authors

8.1. THE QUANTUM LINK EFFICIENCY

The power of future quantum networks will derive from entanglement that is shared between the network nodes. Two critical parameters for the performance of such networks are the entanglement generation rate r_{ent} between nodes and the entangled-state decoherence rate r_{dec}. Their ratio, that we term the quantum link efficiency $\eta_{\text{link}} = r_{\text{ent}}/r_{\text{dec}}$[8,15], quantifies how effectively entangled states can be preserved over the timescales necessary to generate them. Alternatively, from a complementary perspective, the link efficiency determines the average number of entangled states that can be created within one entangled state lifetime. Achieving a link efficiency of unity therefore represents a critical threshold beyond which entanglement can be generated faster than it is lost. Exceeding this threshold is central to allowing multiple entangled links to be created and maintained simultaneously, as required for the distribution of many-body quantum states across a network[6,15].

Consider an elementary entanglement delivery protocol that delivers states at pre-determined times. This can be achieved by making multiple attempts to generate entanglement, and then protecting successfully generated entangled states from decoherence until the required delivery time (Fig. 8.1a, steps 1, 2 & 3). If we try to generate entanglement for a period t_{ent}, the cumulative probability of success will be $p_{\text{succ}} = 1 - e^{-r_{\text{ent}} t_{\text{ent}}}$. For a given p_{succ}, the average fidelity F_{succ} of the successfully generated states is solely determined by the quantum link efficiency η_{link} (Sec. 8.6.1). We plot F_{succ} versus p_{succ} for several values of η_{link} in Fig 8.1b.

This protocol allows entangled states to be delivered at specified times, but with a finite probability of success. By delivering an unentangled state (state fidelity $F_{\text{unent}} \leq \frac{1}{2}$) in cycles in which all entanglement generation attempts failed, the protocol can be cast into a fully deterministic black-box (Fig 8.1a, step 4). The states output from such a black-box will have a fidelity with a Bell state of

$$F_{\text{det}} = p_{\text{succ}} F_{\text{succ}} + (1 - p_{\text{succ}}) F_{\text{unent}}. \tag{8.1}$$

The maximum achievable fidelity $F_{\text{det}}^{\text{max}}$ of this deterministic state delivery protocol, found by optimising p_{succ}, is also only determined by the quantum link efficiency η_{link}. For $F_{\text{unent}} = \frac{1}{4}$ (fully mixed state), we find (see Fig 8.1c):

$$F_{\text{det}}^{\text{max}} = \frac{1}{4}\left(1 + 3\eta_{\text{link}}{}^{\frac{1}{1-\eta_{\text{link}}}}\right). \tag{8.2}$$

Beyond the threshold $\eta_{\text{link}} \gtrsim 0.83$, there exists a combination of p_{succ} and F_{succ} high enough to compensate for cycles in which entanglement is not heralded, allowing for the deterministic delivery of states that are on-average entangled ($F_{\text{det}}^{\text{max}} \geq \frac{1}{2}$). Demonstrating deterministic entanglement delivery therefore presents a critical benchmark of a network's performance, certifying that the network quantum link efficiency is of order unity or higher. Furthermore, the ability to specify in advance the time at which entangled states are delivered may assist in designing multi-step quantum information tasks such as entanglement routing[16,17].

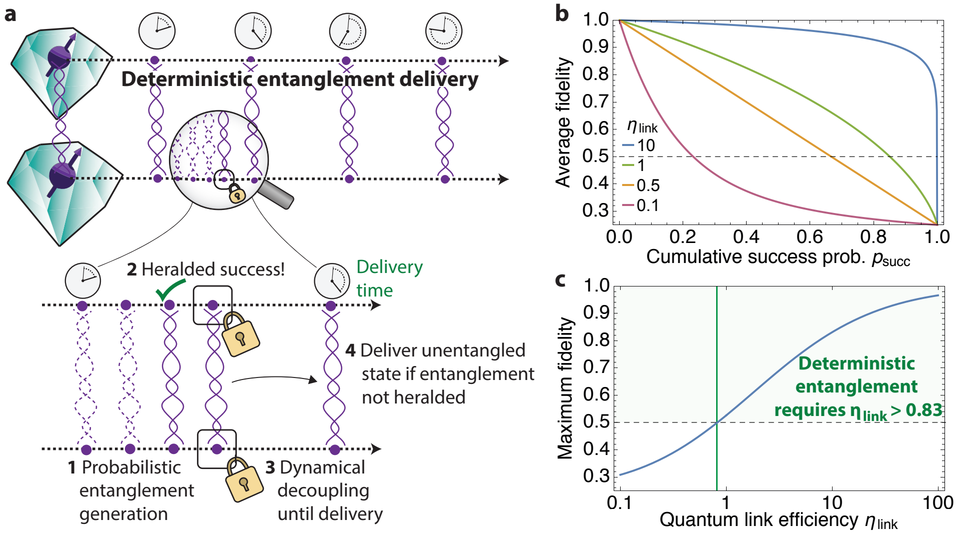

Figure 8.1 |**Deterministic remote entanglement delivery.** **a**, Deterministic entanglement delivery guarantees the output of states with average entanglement fidelity exceeding 0.5 at pre-specified times. In our protocol, underlying this deterministic delivery is a probabilistic but heralded entanglement process. Repeated entangling attempts are made and then, upon heralded success, the entangled state is protected from decoherence until the specified delivery time. If no attempt at entanglement generation succeeds within one cycle, an unentangled state must be delivered. **b**, For the underlying entanglement generation and state preservation protocol (steps 1, 2 & 3 in (a)), the effectiveness of the trade-off between the average fidelity of the delivered entangled state and the success probability is determined by the quantum link efficiency η_{link}. **c**, Plotted is the maximum fidelity of deterministically delivered states as a function of η_{link}. A critical threshold $\eta_{\text{link}} \gtrsim 0.83$ must be surpassed in order to render the underlying probabilistic process deterministic and deliver an on-average entangled state at every cycle.

To date, this threshold has remained out of reach for solid-state quantum networks. Quantum dots have demonstrated kHz entanglement rates r_{ent}, but tens of MHz decoherence rates r_{dec} limit their achieved quantum link efficiencies to $\eta_{\mathrm{link}} \sim 10^{-4}$ [18,19]. Nitrogen vacancy (NV) centres, point-defects in diamond with a long-lived electron spin and bright optical transitions, have demonstrated entanglement rates r_{ent} of tens of mHz[10,14] and, in separate experiments, decoherence rates r_{dec} of order 1 Hz[20], which would together give $\eta_{\mathrm{link}} \sim 10^{-2}$.

8.2. SINGLE-PHOTON ENTANGLING PROTOCOL

Here we achieve η_{link} well in excess of unity by realising an alternative entanglement protocol for NV centres in which we directly use the state heralded by the detection of a single photon (Fig. 8.2)[21,22]. The rate for such single-photon protocols scales linearly with losses, which, in comparison with previously used two-photon-mediated protocols[9,14], provides a dramatic advantage in typical remote entanglement settings. Recent experiments have highlighted the potential of such single-photon protocols by generating local entanglement[23,24], and remote entanglement in post-selection[18,19]. By realising a single-photon protocol in a fully heralded fashion and protecting entanglement through dynamical decoupling, we achieve the deterministic delivery of remote entangled states on a ~10 Hz clock.

Our experiment employs NV centres residing in independently operated cryostat setups separated by 2 metres (see Sec. 8.6.2). We use qubits formed by two of the NV centre ground-state spin sub-levels ($|\uparrow\rangle \equiv |m_s = 0\rangle, |\downarrow\rangle \equiv |m_s = -1\rangle$). Single-photon entanglement generation (Fig. 8.2a) proceeds by first initialising each node in $|\uparrow\rangle$ by optical pumping[25], followed by a coherent rotation using a microwave pulse[26] to create the state

$$|NV\rangle = \sqrt{\alpha}|\uparrow\rangle + \sqrt{1-\alpha}|\downarrow\rangle. \tag{8.3}$$

We then apply resonant laser light to selectively excite the 'bright' state $|\uparrow\rangle$ to an excited state, which rapidly decays radiatively back to the ground state by emitting a single photon. This entangles the spin state of the NV with the presence $|1\rangle$ or absence $|0\rangle$ of a photon in the emitted optical mode:

$$|NV, \text{optical mode}\rangle = \sqrt{\alpha}|\uparrow\rangle|1\rangle + \sqrt{1-\alpha}|\downarrow\rangle|0\rangle. \tag{8.4}$$

Emitted photons are transmitted to a central station at which a beamsplitter is used to remove their which-path information. Successful detection of a photon at this station indicates that at least one of the NVs is in the bright state $|\uparrow\rangle$ and therefore heralds the creation of a spin-spin entangled state. However, given the detection of one photon, the conditional probability that the other NV is also in the state $|\uparrow\rangle$, but the photon it emitted was lost, is given by $p = \alpha$ (in the limit that the photon detection efficiency $p_{\mathrm{det}} \ll 1$). This degrades the heralded state from a maximally-entangled Bell state $|\psi\rangle = \frac{1}{\sqrt{2}}(|\uparrow\downarrow\rangle + |\downarrow\uparrow\rangle)$ to

$$\rho_{NV,NV} = (1-\alpha)|\psi\rangle\langle\psi| + \alpha|\uparrow\uparrow\rangle\langle\uparrow\uparrow|. \tag{8.5}$$

The probability of successfully heralding entanglement is given by $2\,p_{\mathrm{det}}\alpha$. The state fidelity $F = 1 - \alpha$ can therefore be directly traded off against the entanglement rate. The corresponding success probability of a two-photon protocol is given by $\frac{1}{2}p_{\mathrm{det}}^2$; for a given acceptable infidelity α, single-photon protocols will thus provide a rate increase of $4\,\alpha/p_{\mathrm{det}}$. For example, for our system's $p_{\mathrm{det}} \sim 4\times10^{-4}$, if a 10% infidelity is acceptable, the rate can be increased by three orders of magnitude over two-photon protocols.

The primary challenge in implementing single-photon entanglement is that the resulting entangled state depends on the optical phase acquired by the laser pulses used to create spin-photon entanglement at each node, as well as the phase acquired by the emitted single photons as they propagate (Fig 8.2b). The experimental setup therefore acts as an interferometer from the point at which the optical pulses are split to the point at which the emitted optical modes interfere. For a total optical phase difference of $\Delta\theta$, the entangled state created is given by

$$|\psi_{0/1}(\Delta\theta)\rangle = |\uparrow\downarrow\rangle \pm e^{\mathrm{i}\Delta\theta}|\downarrow\uparrow\rangle, \tag{8.6}$$

where 0/1 (with corresponding ± phase factor) denotes which detector at the central station detected the incident photon. This optical phase difference must be known in order to ensure that entangled states are available for further use.

We overcome this entangled-state phase sensitivity by interleaving periods of optical-phase stabilisation with our entanglement generation. During phase stabilisation we input bright laser light at the same frequency as the NV excitation light and detect the light reflected from the diamond substrate using the same detectors that are used to herald entanglement. The measured optical phase, estimated from the detected counts, is used to adjust the phase back to our desired value using a piezoelectric fibre stretcher. We achieve an average steady-state phase stability of 14.3(3)°, limited by the mechanical oscillations of the optical elements in our experimental setup (see Sec. 8.6.5).

To demonstrate the controlled generation of entangled states, we run the single-photon entangling protocol with a bright-state population of $\alpha = 0.1$. After entanglement is heralded, we apply basis rotations and single-shot state readout[25] at each node to measure $\langle\sigma_i^A\sigma_j^B\rangle$ correlations between the nodes, where the standard Pauli matrices will be referred to here in the shorthand $\sigma_X,\sigma_Y,\sigma_Z = X,Y,Z$. We observe strong correlations both for $\langle XX\rangle$ and $\langle YY\rangle$, and, when sweeping the readout basis for node A, oscillations of these coherences as expected from the desired entangled state (Fig. 8.2c, left panel). In combination with the measured $\langle ZZ\rangle$ correlations (Fig. 8.2c, right panel), this unambiguously proves the establishment of entanglement between our nodes.

We explore the tradeoff between the entangled state fidelity and the entanglement rate by measuring $\langle XX\rangle$, $\langle YY\rangle$ and $\langle ZZ\rangle$ correlations for a range of different initial bright-state populations α. Using these correlations, we calculate the fidelity of the heralded state to the desired maximally entangled Bell state for each value of α (Fig. 8.2d), along with the measured success rate (Fig. 8.2e). As predicted, the fidelity increases with decreasing α as the weight of the unentangled state $|\uparrow\uparrow\rangle\langle\uparrow\uparrow|$ diminishes (Eqn. 8.5). For

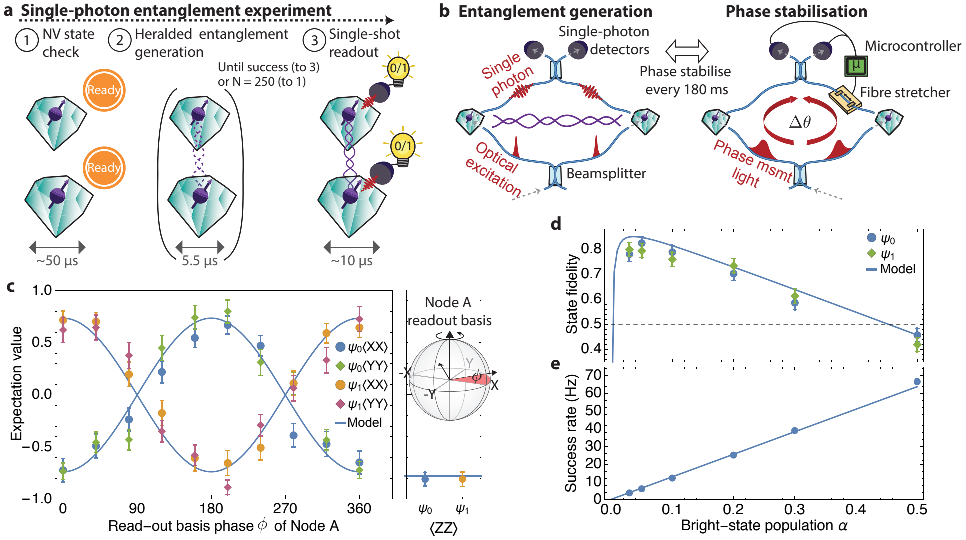

Figure 8.2 |Benchmarking single-photon entanglement generation. **a**, The single-photon entanglement experiment consists of several steps: ① Before entanglement generation, the NV centre must be in the correct charge state (NV^-) and resonant with the excitation laser. An NV state check is employed to ensure this (see Sec. 8.6.2), and is repeated until the check passes. ② Single-photon entanglement generation is attempted until success is heralded, in which case we continue to readout. If 250 attempts have been made without success, we revert to step 1. ③ Upon heralded success, the spin states are read out in a chosen basis by using microwaves to rotate the state followed by single-shot readout. **b**, The optical phase difference $\Delta\theta$ acquired in an interferometer formed by the two nodes must be known. For the data reported in this figure, we stabilise the phase difference every 180 ms. **c**, For α of 0.1, we plot the measured $\langle XX\rangle$ and $\langle YY\rangle$ correlations (left panel) for $\psi_{0/1}$ (where 0/1 denotes the heralding detector) as the phase of the microwave pulse before readout is swept at node A. This changes the readout basis of this node to $\cos(\phi)X+\sin(\phi)Y$. Right panel shows the measured $\langle ZZ\rangle$ correlations. **d**, Fidelity of the heralded states with a Bell state and **e**, entanglement generation success rate, for different values of α. The success rate is calculated by dividing the entangling attempt duration (5.5 μs) by the probability of successfully heralding entanglement. Solid lines in each plot give the predictions of our model solely based on independently determined parameters (see Sec. 8.6.3).

small α, the fidelity saturates because the detector dark-count rate becomes comparable to the detection rate.

Choosing α to maximise fidelity, we find that our protocol allows us to generate entanglement with a fidelity of 0.81(2) at a rate of $r_{\text{ent}} = 6$ Hz (for $\alpha = 0.05$). Alternatively, by trading the entanglement fidelity for rate, we can generate entanglement at $r_{\text{ent}} = 39$ Hz with an associated fidelity of 0.60(2) ($\alpha = 0.3$). This represents a two orders of magnitude increase in the entangling rate over all previous NV experiments[10] and a three orders of magnitude increase in rates over two-photon protocols under the same conditions[14].

Compared to the maximum theoretical fidelity for $\alpha = 0.05$ of 0.95, the states we generate have a 3% reduction in fidelity due to residual photon distinguishability, 4% from double excitation, 3% from detector dark counts, and 2% from optical-phase uncertainty (see Sections 8.6.5, 8.6.6 & 8.6.7).

8.3. NV-STATE PROTECTION BY DYNAMICAL DECOUPLING

In order to reach a sufficient link efficiency η_{link} to allow for deterministic entanglement delivery, the single-photon protocol must be combined with robust protection of the generated remote entangled states. To achieve this, we carefully shielded our NVs from external noise sources including residual laser light and microwave amplifier noise, leaving as the dominant noise the slowly-fluctuating magnetic field induced by the surrounding nuclear spin bath.

We mitigate this quasi-static noise by implementing dynamical decoupling with XY8 pulse sequences (Fig. 8.3a, see Sec. 8.6.8). The fixed delay between microwave pulses in these sequences is optimised for each node. Varying the number of decoupling pulses allows us to protect the spins for different durations. This dynamical decoupling extends the coherence time of Node A and B from a T_2^* of $\sim 5\,\mu$s to 290(20) ms and 680(70) ms respectively, as shown in Fig. 8.3b. The difference in coherence times for the two nodes is attributed to differing nuclear spin environments and microwave pulse fidelities.

To investigate the preservation of remote entangled states, we incorporate dynamical decoupling for varying time durations after successful single-photon entanglement generation (Fig. 8.3c). We find an entangled state coherence time of 200(10) ms (decoherence rate r_{dec} of 5.0(3) Hz). The observed entangled-state fidelities closely match the predictions of our model, which is solely based on independently determined parameters (see Sec. 8.6.3). In particular, the decoherence of the remote entangled state is fully explained by the combination of the individual decoherence rates of the individual nodes.

The combination of dynamical decoupling with the single-photon entanglement protocol achieves a quantum link efficiency of $\eta_{\text{link}} \sim 8$ (comparable to the published state-of-the-art in ion traps[8], $\eta_{\text{link}} \sim 5$), pushing the NV-based platform well beyond the critical threshold of $\eta_{\text{link}} \gtrsim 0.83$.

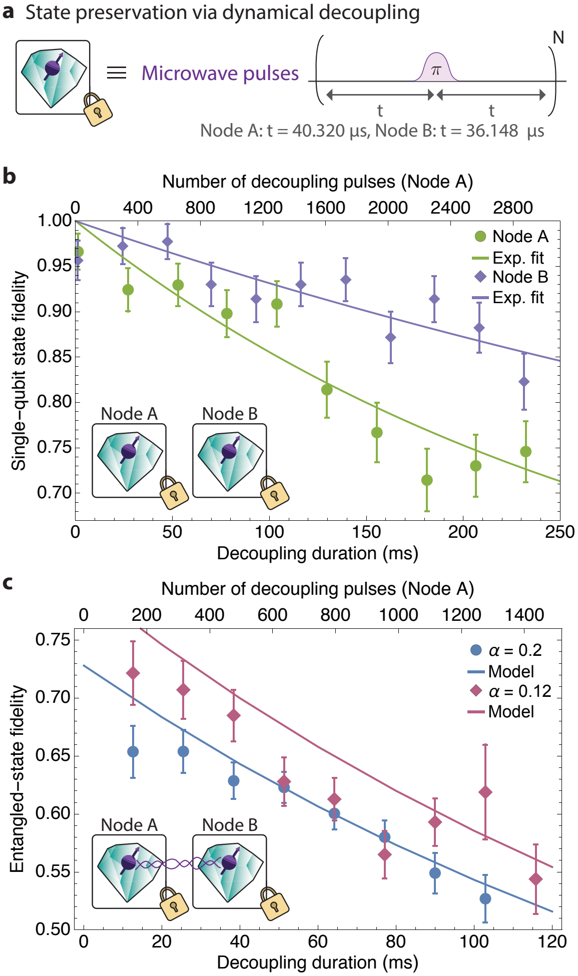

Figure 8.3 |**Coherence protection of remote entangled states.** **a**, Dynamical decoupling protects the state of the NV spins from quasi-static environmental noise. Applying N pulses allows us to dynamically decouple the NV state for a time $2Nt$. **b**, Fidelity with the initial state for dynamical decoupling of the single-qubit state $|\uparrow\rangle + |\downarrow\rangle$ at our two NV nodes. Solid lines show exponential fits with coherence times of $290(20)$ ms and $680(70)$ ms for nodes A and B respectively. **c**, Dynamical decoupling of entangled states created using the single-photon entanglement protocol for bright-state populations $\alpha = 0.12$ and $\alpha = 0.2$. Solid lines show the predictions of our model based on the coherence times measured in (b), from which the effective entangled state coherence time is expected to be $\tau = 200(10)$ ms.

8.4. DETERMINISTIC ENTANGLEMENT GENERATION

We capitalise on these innovations to design a deterministic entanglement delivery protocol that guarantees the delivery of entangled states at specified intervals, without any post-selection of results or pre-selection based on the nodes being in appropriate conditions (Fig. 8.4a). Phase stabilisation occurs at the start of each cycle, after which there is a preset period before an entangled state must be delivered. This window must therefore include all NV state checks (necessary to mitigate spectral diffusion via feedback control and verify the charge-state and resonance conditions[9]), entanglement generation attempts and dynamical decoupling necessary to deliver an entangled state (further details are given in Sec. 8.6.2).

We run our deterministic entanglement delivery protocol at two values of α (0.2 & 0.12) and for delivery rates ranging from 7-12 Hz. We divide the experiment into runs of 1500 cycles (i.e. 1500 deterministic state deliveries), for a total data set of 42000 cycles.

We first confirm that heralded entanglement occurs with the expected probabilities (Fig. 8.4a) by determining the fraction of cycles in which entanglement is heralded, in which no entangling attempts succeed, and in which entanglement attempts do not occur at all as the NV state check never succeeds. In order to establish reliable and useful quantum networks, it is important that entangled states can be delivered with high confidence over long periods. The nodes must therefore not be offline due, for example, to uncompensated drifts in the resonant frequencies of the optical transitions. We therefore do not stop the experiment from running once it starts and include any such offline cycles in our datasets. Their negligible contribution (0.8% of cycles) confirms the high robustness of our experimental platform and the effectiveness of our NV frequency and charge-state control (see Sections 8.6.2 & 8.6.4).

For each value of α and for each pre-set delivery interval, we determine the average fidelity of the deterministically delivered states by measuring their $\langle XX\rangle$, $\langle YY\rangle$ and $\langle ZZ\rangle$ correlations (Fig. 8.4b). We find that for $\alpha = 0.2$ and a rate of 9.9 Hz, we are able to create states with a fidelity of 0.56(1), proving successful deterministic entanglement delivery.

During cycles in which entanglement is not successfully heralded, the spin states are nonetheless delivered and readout. In these case, we deliver the state that the NVs are left in after a failed entanglement attempt, which has a low fidelity with the desired Bell state (e.g. $F_{\text{unent}} = 0.04$ for $\alpha = 0.2$). While this stringent test highlights the robust nature of our protocol, we could instead deliver a mixed state ($F_{\text{unent}} = \frac{1}{4}$) or a classically-correlated state ($F_{\text{unent}} = \frac{1}{2}$) when a successful event is not heralded. The resulting fidelities for our experimental data if classically-correlated states were delivered are also plotted in Fig. 8.4b (grey circles). In this case we would be able to deliver entangled states deterministically with fidelities of 0.62(1) at a rate of 9.9 Hz.

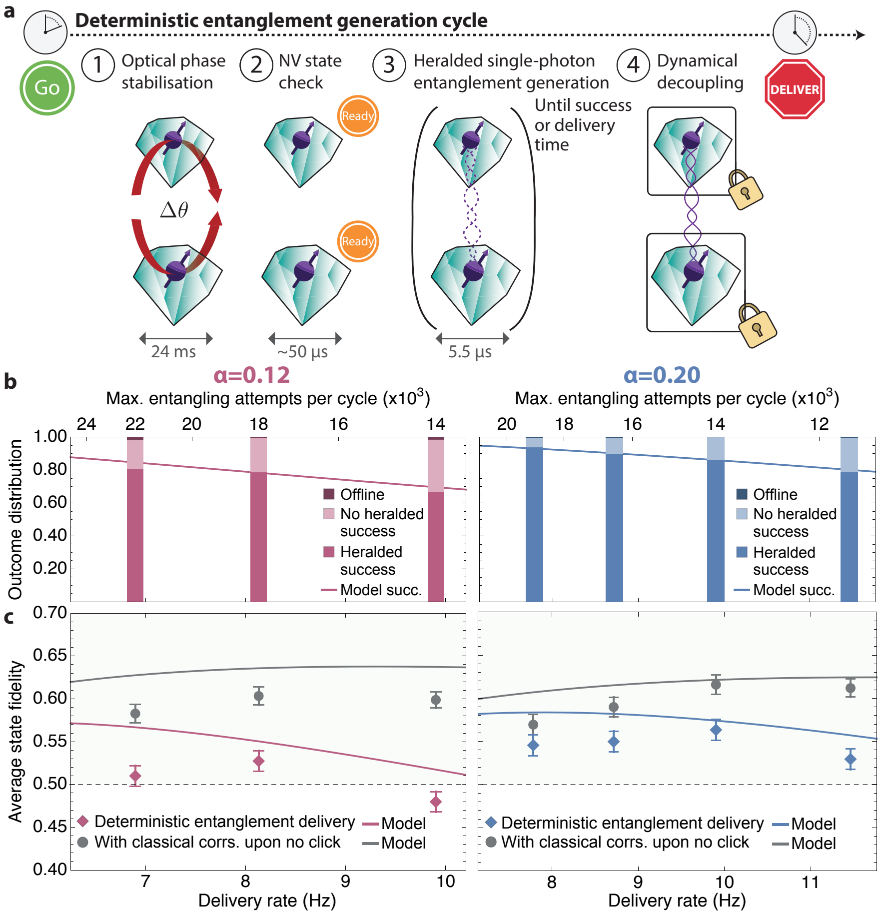

Figure 8.4 |Deterministic entanglement delivery. **a**, One cycle of deterministic entanglement delivery combines the following steps: ① Optical phase stabilisation. ② NV state checks, repeated until a threshold number of photons are detected at each node. ③ Attempts at probabilistic entanglement generation (Fig. 8.2). ④ Upon heralded entanglement success, the state is protected by dynamical decoupling until the delivery time. **b**, Distribution of deterministic entanglement delivery outcomes for $\alpha = 0.12$ & 0.2 and different delivery rates. Shown is the fraction of cycles in which a herald photon is detected (heralded success), in which no herald is detected (no heralded success), and in which the NV state checks for at least one of the NV centres fail repeatedly for the whole cycle (offline). Note that the offline fraction is often too small to be visible in the plot. The line gives the success rate predicted by our model. **c**, Average fidelity of deterministically-delivered entangled states for $\alpha = 0.12$ & 0.2 and different delivery rates (diamonds). Also plotted is the average fidelity if classically-correlated states were delivered for cycles in which no success event is heralded (circles). The associated lines plot the corresponding predictions of our model based on independently measured parameters (Sec. 8.6.3).

8.5. OUTLOOK

The deterministic entanglement delivery between remote NV centres demonstrated here is enabled by a quantum link efficiency exceeding unity. Straightforward modifications to our experiment are expected to further increase our quantum link efficiency. Refinements to the classical experimental control will allow us to reduce the entanglement attempt duration from 5.5 μs to below 2 μs, which would more than double the entangling rate. Furthermore, the entangled state coherence time could be significantly improved by exploiting long-lived nuclear spin quantum memories [10,27,28]. We anticipate that this will allow for link efficiencies in excess of 100 in the near term. Further improvements to the photon detection efficiency (including enhancement of zero-phonon line emission) [29,30] would lead to an additional increase of at least an order of magnitude.

In combination with recent progress on robust storage of quantum states during remote entangling operations [10,31], the techniques reported here reveal a direct path to the creation of many-body quantum states distributed over multiple quantum network nodes. Moreover, given the demonstrated potential for phase stabilisation in optical fibre over tens of kilometre distances [22], our results open up the prospect of entanglement-based quantum networks at metropolitan scales.

CONTRIBUTIONS

P.C.H., N.K. and J.P.J.M. prepared the experimental apparatus. P.C.H. and N.K. carried out the experiments. R.F.L.V. and R.N.S. conceived the microwave switch circuit. P.C.H. analysed the data and wrote the manuscript with input from N.K. and R.H. The diamond substrates were grown by D.J.T. and M.M. The project was supervised by R.H.

8.6. SUPPLEMENTARY INFORMATION

8.6.1. DERIVATION OF DETERMINISTICALLY DELIVERED ENTANGLED STATE FIDELITY AS A FUNCTION OF QUANTUM LINK EFFICIENCY

We assume an entanglement generation rate r_{ent} and an entangled state decoherence rate r_{dec}. If the rate at which entanglement attempts occur is much faster than r_{ent} (i.e there is a low probability of success), we can approximate entanglement generation as a continuous process. In this case, the probability density for successfully generating entanglement at a time t after beginning our attempts is given by $p_{\text{ent}}(t) = r_{\text{ent}} e^{-r_{\text{ent}} t}$. The corresponding cumulative probability of success is $p_{\text{succ}}(t) = 1 - e^{-r_{\text{ent}} t}$.

Once we succeed at creating entanglement, the state will decohere until the time at which we deliver it. For single-qubit depolarising noise at each site, the fidelity of the resulting state after storage for a time t is given by

$$F(t) = \frac{1}{4} + \frac{3}{4} e^{-r_{\text{dec}} t}. \tag{8.7}$$

If we deliver our entangled state at time $t_{\text{ent}} = \beta / r_{\text{dec}}$ (where β is simply used to parameterise the time in terms of the decoherence rate), the average fidelity of the delivered state (given a success occurred) is therefore

$$\begin{aligned} F_{\mathrm{succ}} &= \frac{1}{p_{\mathrm{succ}}(t_{\mathrm{ent}})} \int_0^{t_{\mathrm{ent}}} p_{\mathrm{ent}}(t) F(t_{\mathrm{ent}} - t) \mathrm{d}t \\ &= \frac{1}{p_{\mathrm{succ}}(t_{\mathrm{ent}})} \int_0^{t_{\mathrm{ent}}} r_{\mathrm{ent}} e^{-r_{\mathrm{ent}} t} (\frac{1}{4} + \frac{3}{4} e^{-r_{\mathrm{dec}}(t_{\mathrm{ent}} - t)}) \mathrm{d}t. \\ &= \frac{3e^{-\beta} \eta_{\mathrm{link}} + (1 - 4\eta_{\mathrm{link}}) e^{-\eta_{\mathrm{link}} \beta} + \eta_{\mathrm{link}} - 1}{4(\eta_{\mathrm{link}} - 1) p_{\mathrm{succ}}(t_{\mathrm{ent}})} \end{aligned} \tag{8.8}$$

We note that $p_{\mathrm{succ}}(t_{\mathrm{ent}}) = 1 - e^{-\beta \eta_{\mathrm{link}}}$, and therefore $\beta = -\ln(1 - p_{\mathrm{succ}}(t_{\mathrm{ent}}))/\eta_{\mathrm{link}}$. Using this, along with the shorthand $p_{\mathrm{succ}} = p_{\mathrm{succ}}(t_{\mathrm{ent}})$, we find that

$$F_{\mathrm{succ}} = \frac{3\eta_{\mathrm{link}} + p_{\mathrm{succ}} - 3\eta_{\mathrm{link}}(1 - p_{\mathrm{succ}})^{1/\eta_{\mathrm{link}}} - 4\eta_{\mathrm{link}} p_{\mathrm{succ}}}{4 p_{\mathrm{succ}}(1 - \eta_{\mathrm{link}})}. \tag{8.9}$$

As discussed in the main text, we can choose to draw a black box around this process, delivering an unentangled state (state fidelity $F_{\mathrm{unent}} \leq \frac{1}{2}$) for cycles in which no attempt at entanglement generation succeeds such that a state is always delivered. Reproducing Eq. 1 of the main text, this means that the states output from this black-box will have a fidelity with a Bell state of

$$F_{\mathrm{det}} = p_{\mathrm{succ}} F_{\mathrm{succ}} + (1 - p_{\mathrm{succ}}) F_{\mathrm{unent}}, \tag{8.10}$$

where F_{succ} is as given above. The maximum achievable fidelity when outputting a fully mixed state ($F_{\mathrm{unent}} = \frac{1}{4}$) upon failure is found by optimising F_{succ} for a given quantum link efficiency η_{link}:

$$F_{\mathrm{det}}^{\mathrm{max}} = \frac{1}{4}\left(1 + 3(\eta_{\mathrm{link}})^{\frac{1}{1-\eta_{\mathrm{link}}}}\right). \tag{8.11}$$

Note that the full state of a quantum system can only be determined experimentally using an ensemble of identical states. This means that, in the absence of information about which deterministic entanglement delivery cycles have a heralded success, the only accurate description of the output of such a black-box system is that a statistical mixture is deterministically output at each cycle.

8.6.2. EXPERIMENTAL METHODS FOR DETERMINISTIC ENTANGLEMENT DELIVERY

EXPERIMENT DESIGN

We use chemical-vapour-deposition homoepitaxially grown diamonds of type IIa with a natural abundance of carbon isotopes. Both diamonds have been cut along the ⟨111⟩ crystal axis and were grown by Element Six. They are situated in home-built confocal microscope set-ups within closed-cycle cryostats (4 K, Montana Instruments) separated by two meters. We use fast microwave switches to shield both NV centres from microwave amplifier noise and therefore increase the coherence times dramatically (Node A uses Qorvo TGS2355-SM and Node B uses Analog Devices HMC544). All other parts of the set-up and sample details have been described in the Supplementary Information of Refs. 9, 10.

One cycle of the deterministic entanglement protocol consists of optical phase stabilisation (described in detail in Sec. 8.6.5), charge-resonance checks to ensure that both NVs are in the appropriate charge state and on-resonance[25], heralded single-photon entanglement generation, and finally dynamical decoupling to protect the state of the NVs from their environment until the delivery time. The experimental sequences used in each step of this protocol (and also the single-photon entanglement generation experiment) are detailed in Fig. 8.5.

After delivery, the state of each NV is measured in a chosen basis. We use spin-selective optical read-out of the NV electron spin in a single shot via the optical E_x transition on both nodes[25]. We measure single-shot read-out fidelities of 0.959(3) (0.950(3)) for the bright $|m_s = 0\rangle \equiv |\uparrow\rangle$ ground-state and 0.995(1) (0.996(1)) for the dark $|m_s = -1\rangle \equiv |\downarrow\rangle$ state on Node A (Node B). These values are subsequently used to correct for read-out errors of the electron spins in state tomography measurements.

INDEPENDENTLY MEASURED PARAMETERS FOR THE EXPERIMENT

EXPERIMENT CONTROL AND COMMUNICATION LOGIC

Fig. 8.6 gives the decision trees and control logic for the ADwin microprocessors (Jaeger ADwin Pro II) that control the experiments. These microcontrollers are responsible for controlling all other experimental hardware and also communicate with each other to synchronise the experiment.

HERALD PHOTON DETECTION WINDOW

We use a combination of polarization and temporal filtering to separate the excitation pulse from photons emitted by the NV. This necessitates a compromise between collecting as much of the emission light as possible, while ensuring that contamination from the pulse is minimised. In this experiment, we choose a temporal filter window (Fig. 8.7) such that the pulse (assumed to have a Gaussian profile) is suppressed to the level of the detector dark counts by the beginning of the window. The end of the window at ~ 30 ns after the pulse is chosen so that, for all of the data sets taken, the rate of detected NV photons is greater than ten times the dark count rate at all points within the window. We use a complex programmable logic device (CPLD) to apply this temporal filtering during our experiment and herald the successful generation of an entangled state in real-time.

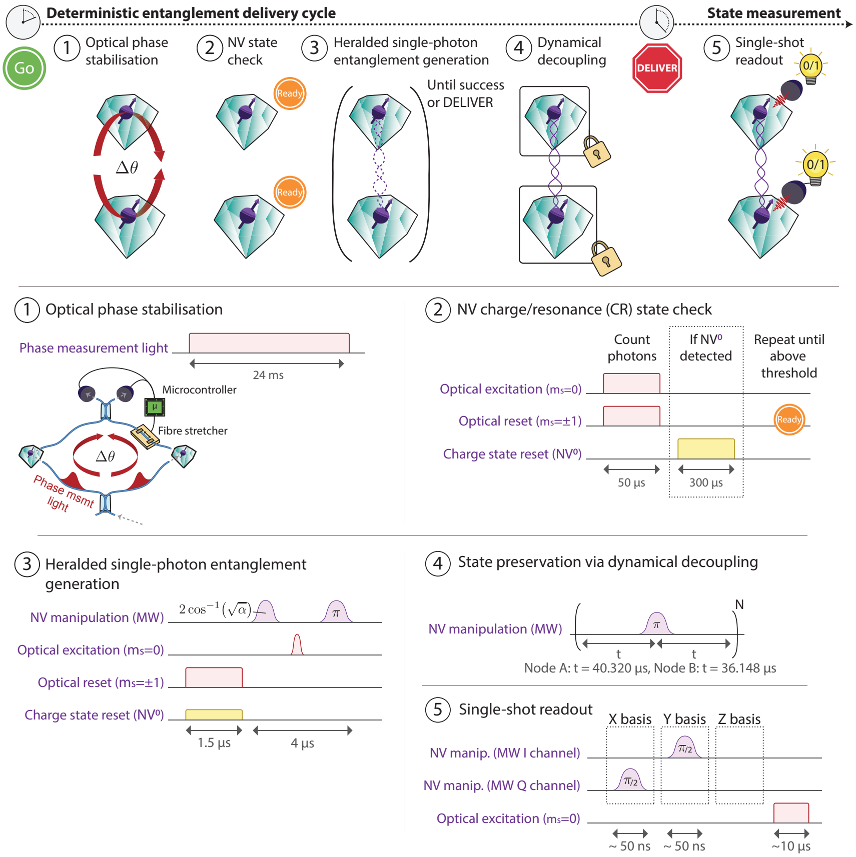

Figure 8.5 |**Deterministic entanglement delivery sequences** Pulse sequences for each step of the deterministic entanglement delivery protocol. These sequences are also employed in the single-photon entanglement generation experiment. ① **Optical phase stabilisation**: Bright light is input to measure and stabilise the interferometer (see Sec. 8.6.5). Note that the duration is different for the single-photon entanglement experiment. ② **NV state check**: By shining in two lasers that are together resonant with transitions from all of the ground states, the NV will fluoresce regardless of its ground-state occupation. By counting photons emitted by the NV we are able to verify that both NVs are in the desired charge state NV^- and that they are on resonance with the applied lasers. The NV centre is deemed to be on resonance if the number of photons detected during the CR check surpasses a certain threshold [25]. If no photons are detected, the NV is assumed to be in the NV^0 state and a resonant laser is applied to reset it to NV^-. ③ **Heralded single-photon entanglement generation:** Entanglement generation proceeds by optically repumping the spins to $|\uparrow\rangle$ (including passive charge-state stabilisation, Sec. 8.6.4) before a microwave (MW) pulse is used to create the desired bright-state population α at each node. A resonant excitation pulse then generates spin-photon entanglement. A subsequent MW π pulse is used to ensure that the NV state is refocused before the next stage should success be heralded. ④ **Dynamical decoupling**: MW pulses are used to implement dynamical decoupling (see Sec. 8.6.8). ⑤ **Single-shot readout**: The NV nodes can be readout in arbitrary bases in a single shot. If required, a MW pulse is applied to rotate the qubit state before a resonant laser is applied. Fluorescence photons from the NV are detected if the NV is in the state $|\uparrow\rangle$ [25].

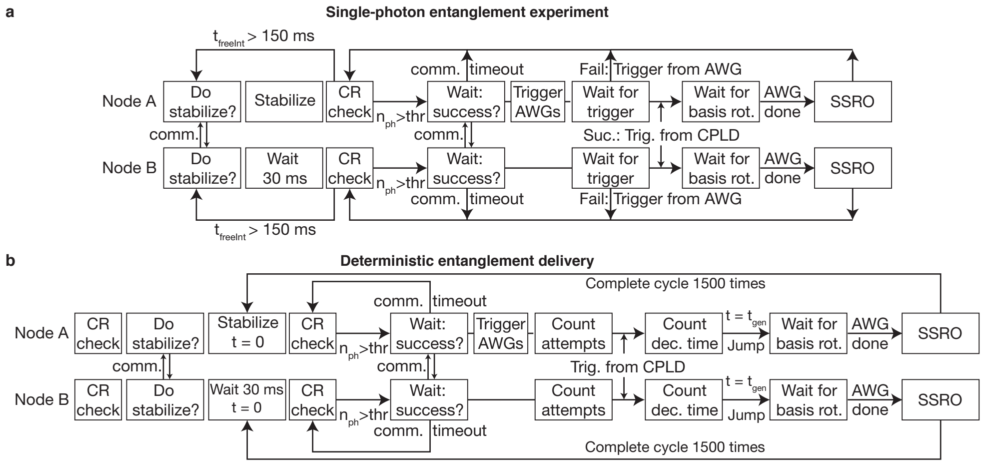

Figure 8.6 |**Flowchart of the experimental sequences.** Shown are the decision trees of the ADwin microprocessors (Jaeger ADwin Pro II) that create the overarching measurement and control loops for network nodes A and B. Both nodes use arbitrary waveform generators for microwave and laser pulse sequencing (AWG, Tektronix AWG5014C). We additionally use a complex programmable logic device (CPLD) to herald the successful generation of an entangled state in real-time (see Sec. 8.6.2). **a**. Decision tree when benchmarking the entangled state. **b**. Deterministic entanglement delivery. Here the ADwins keep track of the elapsed time since the end of the phase stabilization ($t = 0$). **CR check**: As explained in Fig. 8.5, the NV centre is deemed to be on resonance with the excitation lasers if the number of photons detected during the CR check surpasses a certain threshold n_{thr}. The CR check is repeated until this occurs. **comm. & comm. timeout:** Both ADwins exchange classical communication, such as success of the CR check, via a three-step-handshake. If one ADwin waits longer than $1\,\mathrm{ms}$ for a response from its counterpart the communication times out and we return to the previous logical step (see arrow). **Count attempts**: count the number of entangling attempts N until $N = N_{\mathrm{max}}$. **Count dec. time**: track the elapsed time since phase stabilization. If the elapsed time equals the prespecified state-generation time t_{gen} then trigger the AWG such that the local readout sequences are executed. **Wait for basis rot.**: ADwins wait for a trigger input from the AWG (AWG done) which heralds that the last MW-rotation before optical readout has been completed. **Trigger AWGs**: The ADwin of Node A triggers the AWGs of both nodes to initiate the microwave and entangling sequences. We use a single ADwin as trigger source to avoid timing jitter between both generated sequences. **SSRO**: Optical single-shot read-out. **Success: Trigger from CPLD / Fail: Trigger from AWG**: During entanglement generation, the CPLD communicates successful detection of a photon to the nodes. During the single-photon entanglement benchmarking experiment, the AWG at each node flags failure of the round after 250 entangling attempts. **Do stabilize?**: The ADwins communicate that phase stabilization will be the next step in the experimental sequence. The Node A ADwin then proceeds with the phase stabilization while the ADwin of Node B waits until the phase stabilisation has finished. The deterministic entangling sequence is run a total of 1500 times (500 times per read-out basis) before a new round is called in which starts again with the verification of resonant conditions for both NVs.

	Node A	Node B	Description
T_2 (ms)	290(20)	680(70)	Dephasing time of the electron spin state.
T_1 (s)	> 1	> 1	Relaxation time of electron spin eigenstates.
p_{det} (10^{-4})	2.8(1)	4.2(1)	Probability to detect a ZPL photon after a single excitation.
p_{ionize}	$\leq 10^{-6}$	$\leq 10^{-6}$	Probability of passive charge-state control failure per entangling attempt. See Sec. 8.6.4.
t (μs)	40.320	36.148	Optimized inter-pulse delay for state storage.
F_0	0.959(3)	0.950(3)	Fidelity of the electron read-out for $\lvert\uparrow\rangle$.
$F_{\pm 1}$	0.995(1)	0.996(1)	Fidelity of the electron read-out for $\lvert\downarrow\rangle$.
V	0.90(2)		Visibility of the two-photon quantum interference. See Sec. 8.6.6.
$p_{2\text{ph}}$	0.04		Estimated probability of double excitation during the optical π-pulse. See Sec. 8.6.7.
ν_{dark} (Hz)	20		Dark count rate per detection channel.
σ_{Int}	14.3(1)°		Initial uncertainty of the interferometric drift. See Sec. 8.6.5.
ν_{Int} (/s)	~ 20°		Estimated drift rate of the free running interferometer. See Sec. 8.6.5.

Table 8.1 |Independently measured experimental parameters for the performance of the nodes used in our experiment.

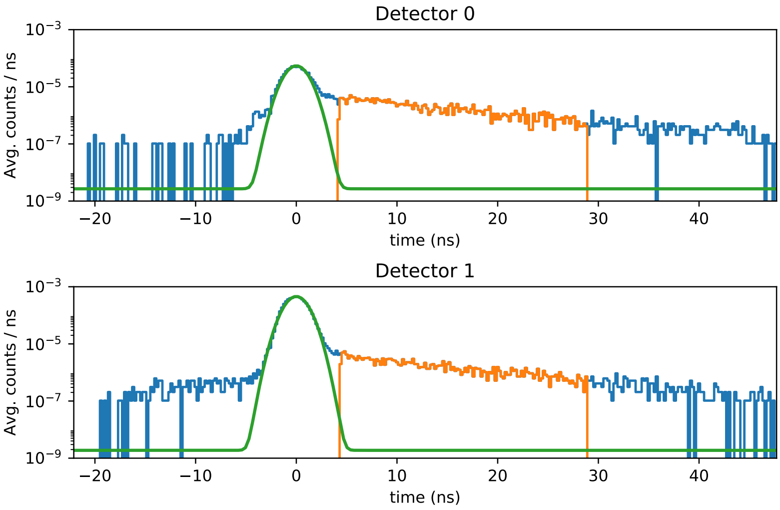

Figure 8.7 |Temporal filtering of photons. Histogram of the times at which photons are detected at each single-photon detector (blue) during a deterministic entanglement delivery experiment with bright state population $\alpha = 0.12$. The orange histograms show the photons that were detected within the temporal filter window and therefore were counted as valid entanglement events. The green line shows a gaussian fit to the pulse with a FWHM of 2.26 as measured in Fig. 8.11. This is used to estimate the contribution of residual pulse photons within the filter window.

8.6.3. THEORETICAL MODEL OF DETERMINISTIC ENTANGLEMENT DELIVERY

We developed a detailed model to determine the expected performance of the deterministic entanglement delivery experiment, based on the independently measured parameters given in Table 8.1.

Once the set-ups are determined to be ready, the core entanglement sequence begins with single-photon entanglement generation. This proceeds by first initialising each node in $|\uparrow\rangle$, followed by a coherent rotation using a microwave pulse to create the state

$$|NV\rangle = \sqrt{\alpha}|\uparrow\rangle + \sqrt{1-\alpha}|\downarrow\rangle. \tag{8.12}$$

Resonant excitation of the NV nodes excites only the 'bright' $|\uparrow\rangle$ level to an excited state, which rapidly decays radiatively back to the ground state by emitting a single photon. This entangles the state of the NV with the presence $|1\rangle$ or absence $|0\rangle$ of a photon in the emitted optical mode:

$$|NV, \text{optical mode}\rangle = \sqrt{\alpha}|\uparrow\rangle|1\rangle + \sqrt{1-\alpha}|\downarrow\rangle|0\rangle. \tag{8.13}$$

The photons emitted by each NV are transmitted to a central station at which a beam-splitter is used to remove their which-path information. Successful detection of a photon at this station indicates that at least one of the NVs is in the bright state $|\uparrow\rangle$ and therefore heralds the creation of a spin-spin entangled state. This entangled state, expressed as $|NV_{\text{Node A}}, NV_{\text{Node B}}\rangle$, is given (in unnormalised form) by

$$\rho_{\text{sc}} = |\psi^{\pm}\rangle\langle\psi^{\pm}| + p_{\uparrow\uparrow}|\uparrow\uparrow\rangle\langle\uparrow\uparrow| + p_{\downarrow\downarrow}|\downarrow\downarrow\rangle\langle\downarrow\downarrow|, \tag{8.14}$$

where

$$|\psi^{\pm}\rangle\langle\psi^{\pm}| = \begin{pmatrix} 0 & 0 & 0 & 0 \\ 0 & p_{\uparrow\downarrow} & \pm\sqrt{V p_{\uparrow\downarrow} p_{\downarrow\uparrow}} & 0 \\ 0 & \pm\sqrt{V p_{\uparrow\downarrow} p_{\downarrow\uparrow}} & p_{\downarrow\uparrow} & 0 \\ 0 & 0 & 0 & 0 \end{pmatrix}. \tag{8.15}$$

This state is parametrized by

$$\begin{aligned} p_{\uparrow\uparrow} &= \alpha^2 \left((1-p_{\text{dc}})^2 (p^A_{\text{det}}(1-p^B_{\text{det}}) + p^B_{\text{det}}(1-p^A_{\text{det}}))\right. \\ &\qquad \left. + 2(1-p_{\text{dc}})\, p_{\text{dc}}(1-p^A_{\text{det}})(1-p^B_{\text{det}})\right) \\ p_{\uparrow\downarrow} &= \alpha\,(1-\alpha)\left((1-p_{\text{dc}})^2\, p^A_{\text{det}} + 2\,p_{\text{dc}}(1-p_{\text{dc}})(1-p^A_{\text{det}})\right) \\ p_{\downarrow\uparrow} &= \alpha\,(1-\alpha)\left((1-p_{\text{dc}})^2\, p^B_{\text{det}} + 2\,p_{\text{dc}}(1-p_{\text{dc}})(1-p^B_{\text{det}})\right) \\ p_{\downarrow\downarrow} &= 2\,(1-\alpha)^2\, p_{\text{dc}}\,(1-p_{\text{dc}}) \end{aligned} \tag{8.16}$$

where V gives the visibility of two-photon interference, p_{dc} gives the dark count probability per detector (given by the product of the dark count rate ν_{dark} and the 25 ns detection window length), and p^A_{det} (p^B_{det}) gives the probability of detecting a photon emitted by Node A (B). In the limit of $p_{\text{det}} \ll 1$, for balanced detection probabilities

$p_{\text{det}} = p^A_{\text{det}} = p^B_{\text{det}}$ and no other imperfections, this tends to the expression given in the main text: $\rho_{NV,NV} = (1-\alpha)|\psi\rangle\langle\psi| + \alpha|\uparrow\uparrow\rangle\langle\uparrow\uparrow|$.

We model double excitation (Sec. 8.6.7) by applying a Pauli Z transformation to each of the NV states with probability $p_{2\text{ph}}/2$. Phase instability is modelled similarly by applying a Pauli Z transformation to one of the states with probability $\frac{1}{2}(1-e^{-\frac{1}{2}((\nu_{\text{Int}}t_p)^2+\sigma^2_{\text{Int}})})$, where t_p denotes the time elapsed since phase stabilisation.

Finally, we model the impact of dynamical decoupling by assuming that it acts as a depolarising channel for each qubit. We therefore apply single-qubit depolarising errors with a probability determined by the measured dynamical-decoupling coherence times. For decoupling for a total time duration of t_d, the total probability of a depolarising error (i.e. the application of a Pauli X, Y or Z transformation with an equal probability) is given by $\frac{3}{4}(1-e^{-t_d/T_2})$.

8.6.4. PASSIVE CHARGE-STATE STABILIZATION OF INDIVIDUAL NV CENTRES

The negatively charged NV centre (NV^-) can be ionized under optical illumination via a two-photon absorption process[32]. Due to the different level structure of the neutral charge state NV^0, the NV will remain dark if such an ionization event occurs during one of our entangling attempts. Ionization thus hampers the performance of our deterministic entangling protocol by diminishing the success rate and delivery of a separable state upon success. Previous experiments with NV centres that worked in the regime of probabilistically generated, yet heralded, remote entanglement overcame NV-ionization by frequent charge-state verification between protocols and actively converting the NV centre back to NV^- by interleaved resonant excitation of the optical transitions of NV^0[14].

Such active stabilization protocols would require additional logical overhead in our scenario where entanglement is generated deterministically. Instead we passively stabilize the charge-state during our entangling sequence by shining in an additional weak laser beam that is resonant with the optical transition of NV^0 (Fig. 8.8). This provides negligible disturbance to the spin initialization fidelity of NV^- while bringing the NV centre back into NV^- if it was converted to NV^0. We additionally identify that the optical reset beam (duration 1.5 μs) is the main cause of ionization in our system and carefully balance the power of both beams such that the spin state is still well initialized and that ionization is a negligible process for our deterministic entangling protocol (up to 15000 entangling attempts). Note that reducing the applied power further by elongating the spin reset duration would decrease the entanglement rate and limit our quantum link efficiency.

Figure 8.8 depicts the basic element that, in repetition, forms our sequence to probe the ionization rate. We use simultaneous charge and spin reset beams followed by a single microwave π rotation that brings the NV into $|1\rangle$ and thus guarantees optical excitation during the next round. The NV is then readout after a final optical reinitialisation into the

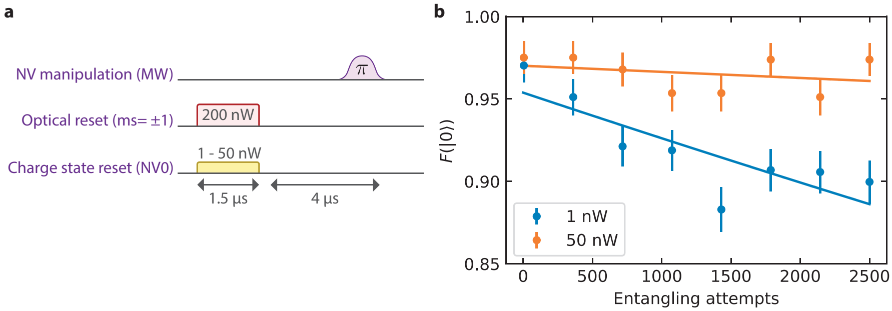

Figure 8.8 |Verifying passive charge-state stabilization into NV$^-$. **a**, Elementary sequence to probe the NV ionization rate. **b**, Applying our sequence many times results in a decay of the NV readout fidelity due to ionization. By exploring the ionization rate for different charge-reset powers we find an optimal regime in which the spin initialization of NV^- is not affected by the additional blue-detuned beam and ionization is effectively mitigated over thousands of trials.

bright state $|0\rangle$. By increasing the number of sequence repetitions, we observe a decay of the final readout fidelity that is associated with the ionization rate. By increasing the optical intensity of the charge-state reset beam we obtain a negligible decay as a function of sequence repetitions, therefore allowing us to overcome ionization in our deterministic entangling protocol. Note that the illumination strength of the charge-reset beam is weak enough to avoid inducing noticeable spectral diffusion of the NV emission as our measured entangled states are consistent with a high degree of indistinguishability for both NV emission profiles (see Secs. 8.6.6).

8.6.5. OPTICAL PHASE STABILISATION

The single-photon entanglement experiment requires that optical phase of an effective interferometer between the two nodes is known, as shown in Fig. 2 of the main text. The optical phase difference between the paths of this interferometer must be known in order to ensure that entangled states are available for further use. This is achieved by interleaving periods of optical-phase stabilisation with our entanglement generation.

For phase stabilisation we input bright laser light at the same frequency but orthogonally polarised to the light used for excitation of the NVs. The orthogonal polarisation is chosen because we use a crossed-polariser to filter out the excitation light from the NV emission. Using orthogonally polarised light for phase stabilisation therefore allows us to collect more light reflected from the diamond substrate. Before doing this, we verified that there is no measurable difference in the relative phase of the two polarisations within our interferometer.

Measurements of the phase drift (Fig. 8.9a) show a slow drift on second time scales, but several strong resonances at hundreds of hertz (Fig. 8.9b). These resonances are thought to be from mechanical elements in the path of the beam, including the microscope objective mount. As we were unable to completely suppress these resonances in the current set-ups, we need to measure the phase over a complete oscillation to estimate the mean phase reliably. The phase must therefore be measured for approximately 10 ms.

We calculate an estimate of the phase from the counts detected at the heralding single-photon detectors. This estimate is used to adjust the phase back to our desired value using a homebuilt piezoelectric fibre stretcher and a proportional-integral-derivative (PID) routine within our Adwin micro-controller. We find that it takes between 2-3 PID cycles to optimally stabilise the phase. We stabilise the phase for 3 cycles during the single-photon entanglement experiment and for 2 cycles during the deterministic entanglement experiment. This difference is because phase stabilisation occurs during every cycle of the deterministic entanglement delivery experiment (100 ms), while it only occurs every 180 ms during the single-photon entanglement experiment and therefore the phase drifts slightly less after one experimental cycle.

We achieve an average steady-state phase stability of 14.3(1)°, as measured by calibration routines spaced throughout the measurement of our data set (Fig. 8.9c,d). This stability is limited by the previously identified mechanical oscillations of the optical elements in our experimental set-up. The standard deviation of the phase averaged over a 10 ms period during active stabilisation is 4.8(1)°.

We note that optical phase stabilisation is also likely to be feasible for long-distance network links. Using long-wavelength off-resonant light for phase measurements would allow for continuous stabilisation during entanglement attempts with negligible impact upon the NV state. An experimental study[22] has shown that two network nodes separated by 36 km over a commercial fibre network would still allow for interference visibilities of 99%. For longer distances, it would also be possible to passively track the phase at the time of entanglement delivery and feed this information back to the nodes in which the state is stored, requiring only a coherence time longer than the communication time.

8.6.6. TWO-PHOTON QUANTUM INTERFERENCE

The quality of photon-mediated heralded entanglement between two emitters hinges on the indistinguishability of their emitted photons. We probe this indistinguishability by interfering emitted single photons on a beam splitter and measuring the number of events in which single-photon detectors connected to the output ports of the beam-splitter both detect a photon. For completely indistinguishable single photons, Hong-Ou-Mandel interference ensures that both photons always exit from the same port of the beamsplitter, and therefore no coincident events should be detected.

Our TPQI experiment proceeds by exciting each emitter with a series of well separated optical excitation pulses (separated by $1\,\mu$s). We collect statistics on coincidence events in which one detector registers a photon after one excitation pulse, and then the other detector registers a photon after a later excitation pulse. For an infinite pulse train, the

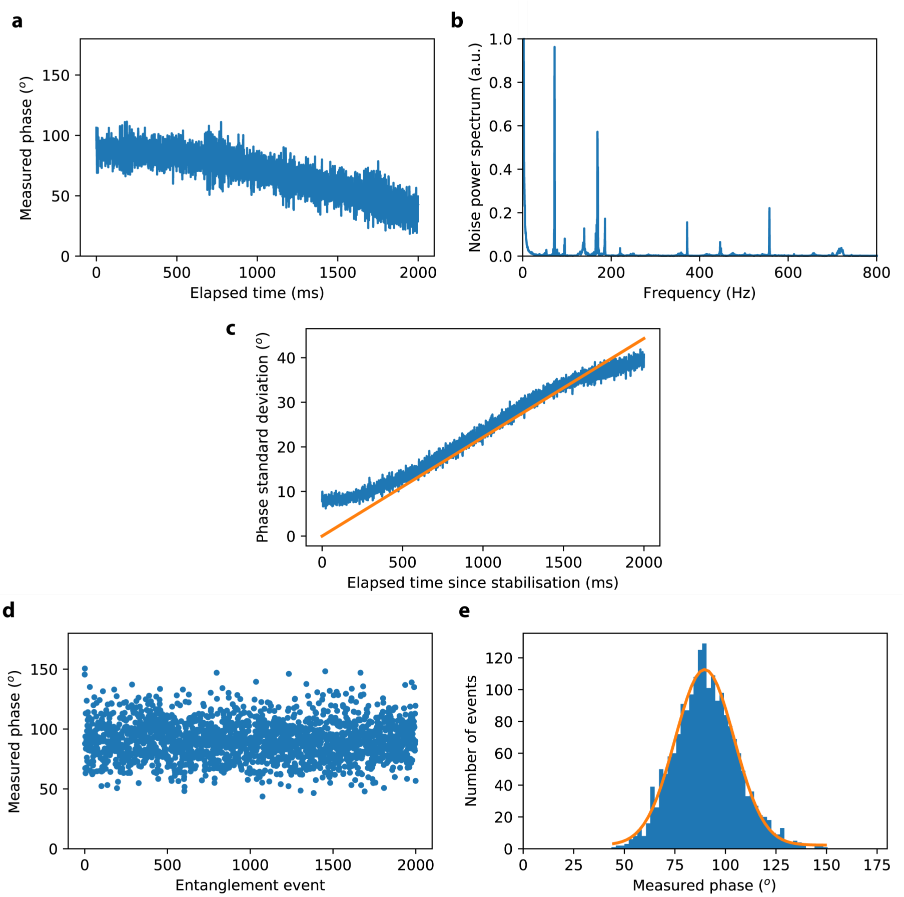

Figure 8.9 |Optical phase stabilisation. Single-photon entanglement requires that optical phase of an effective interferometer between the two nodes is known. **a**, A typical trace of the interferometer optical phase as it is passively tracked for two seconds. **b**, Power spectrum of the optical phase signal showing peaks thought to be due to mechanical resonances of components in the setup. **c**, Active phase stabilisation is used to correct for phase drifts. Here the phase is stabilised and then the interferometer is allowed to passively drift for two seconds. Plotted is the standard deviation of the phase as a function of elapsed time for a data set of 100 of these measurements. The orange line shows a linear fit, used to estimate the rate of phase drift $v_{\text{Int}} \sim 20°/s$. **d**, Here the phase is repeatedly actively stabilised every 180 ms. Entanglement generation occurs during the periods in between stabilisation. The interferometer phase is measured directly after each successful heralded entanglement event. **e**, Histogram of the measured post-entanglement optical phases. Also plotted in orange is a Gaussian fit with a standard deviation fixed to the average measured standard deviation for all entanglement data taken, $\sigma_{\text{Int}} = 14.3(1)°$.

number of coincidence events detected for each number of pulses between the detection events should be constant. However, for a finite pulse train, there are some pulses for a given pulse separation for which there is no partner excitation pulse and therefore no coincident events will be detected. This leads to a linearly decreasing number of coincidence events as a function of pulse difference (Fig. 8.10a).

We use a linear fit to the coincidence events to infer the number of coincidences that would be detected from the same pulse (pulse difference of zero), if fully distinguishable single photons were input (Fig. 8.10b). Because these are nonetheless single photons, a counting argument shows that, for balanced emission probabilities from each emitter, this expected number of events is given by half of the value of the linear fit at zero pulse difference.

The ratio r between the measured number of coincident events within the same pulse and the expected number of events for fully distinguishable photons is related to the single-photon wave function overlap $V = \left|\langle\psi_a|\psi_b\rangle\right|^2$ by $V = (1-r)$ (again for balanced emission probabilities from each emitter). Incorporating the effect of the known imbalance in emission probabilities in our experiment, we find $V = 0.90(2)$.

8.6.7. DEPHASING OF ENTANGLED STATES DUE TO DOUBLE EXCITATION

An optical rabi pulse is used to excite the NV nodes to a higher lying level via a spin-conserving transition. The NV subsequently decays back down to its original level through spontaneous emission, thereby entangling the spin state of the NV and the emitted optical mode. For optical rabi pulses of finite duration, there is a chance that the NV will spontaneously emit a photon during the optical pulse and be re-excited before the end of the pulse. the first emitted photon will be lost to the environment, as it is impossible to distinguish from the excitation light. However, if the subsequent emitted photon is detected in this double excitation process, this will falsely herald entanglement. We measured the width of our optical pulse (Fig. 8.11) and used a quantum-jump based simulation to calculate the corresponding double-excitation probability. Given that the NV emitted a photon within the detection window, the probability that double excitation occurred is $p_{2\mathrm{ph}} = 0.04$.

8.6.8. STATE STORAGE VIA DYNAMICAL DECOUPLING

The coherence time of NV centres is limited by interactions with other magnetic impurities. In our samples the dominant source of magnetic field noise is the surrounding bath of slowly fluctuating ^{13}C nuclear spins (natural abundance of 1.1 %) resulting in typical coherence times of 5 μs. We use dynamical decoupling XY8 sequences of the form $(t-\pi_X-2t-\pi_Y-2t-\pi_X-2t-\pi_Y-2t-\pi_Y-2t-\pi_X-2t-\pi_Y-2t-\pi_X-t)^{N/8}$ to elongate the coherence times of both NV centres (see Fig. 3 main text), with microwave inversion pulses π, the waiting time t and the number of pulses N (see also Fig. 8.5.4). A given decoupling duration is obtained by arbitrary combinations of t and N. We find the optimal combination for a targeted protection duration of ~ 100 ms by varying t for a fixed

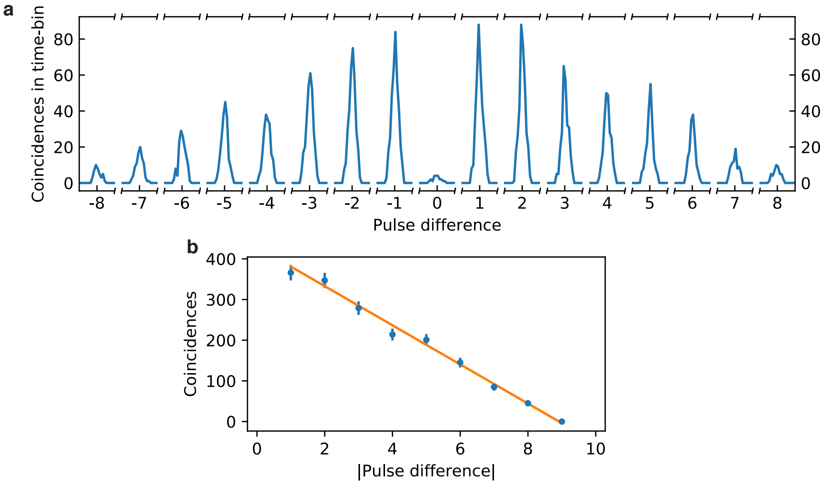

Figure 8.10 |Two-photon quantum interference. **a**. Histogram for coincident events measured by two single-photon detectors in a two-photon quantum interference experiment, measured by cross-referencing photon detection events from a pulse train of 10 optical π-pulses that excite both emitters. Hong-Ou-Mandel interference of simultaneously coinciding photons ideally results in vanishing coincidence events within a single excitation round. The time difference between individual excitation rounds is $1\,\mu$s. Histograms of coincidence counts are shown with a bin-size of $5\,$ns. **b**. Total number of coincidences as a function of the number of pulses separating the two detection events. We extrapolate the measured coincidences to infer the expected coincidences for distinguishable photons at zero pulse difference by fitting a linear regression (orange). Using this to normalise the 22 observed coincidences for zero pulse difference allows us to estimate the TPQI visibility $V = 0.90(2)$.

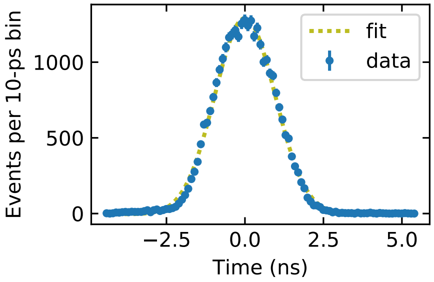

Figure 8.11 |Width of the optical π-pulse. FWHM $= 2.26\,$ns, necessary to compute the dual-excitation probability for a radiative lifetime of $12\,$ns

$N = 1024$. We specifically choose $N = 1024$ as the introduced infidelity from inversion pulse errors is still moderate for both nodes.

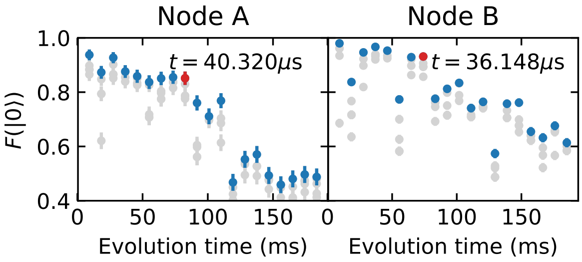

Figure 8.12 |Determining the optimal inter-pulse delay for state storage and 1024 inversion pulses. We initialize a superposition state on the NV electron spin, preserve it via dynamical decoupling and finally perform optical readout after another $\pi/2$ pulse. We probe the coherence of the NV by varying the inter-pulse delay t in steps of the Larmor period $1/\nu_L \approx 2.25\,\mu$s and additionally shifting the delay in steps of 4 ns for a total of five data points per Larmor period (grey data). For each multiple of the Larmor period we pick the best, i.e. most preserving, inter-pulse delay (blue data). We determine the optimal delay t by selecting an inter-pulse delay that provides sufficient state preservation, i.e. ~ 100 ms, for a moderate amount of pulses (red data point and text inset in both panels). Left: Node A. Right: Node B. Error bars are 1 s.d.

Figure 8.12 shows the results of our decoupling optimization procedure. We prepare the NV in a balanced superposition and choose waiting times that are integer multiples of the inverse ^{13}C-nuclear-spin Larmor frequency ν_L to avoid coupling with the nuclear spin bath (Node A: $\nu_L = 443.342$ kHz; Node B: $\nu_L = 442.442$ kHz). Following the techniques of Abobeih et al.[33], we further avoid coupling to other magnetic noise sources that result in loss of NV coherence by picking five waiting times with a total variation of 16 ns for each multiple of the inverse Larmor frequency. The data (grey) are then sorted for the waiting time with the best state preservation quality (blue) at each multiple, giving the minimal NV coherence decay for this number of inversion pulses. We then proceed to pick the waiting time that guarantees a low number of inversion pulses while still providing high-quality state protection (red).

REFERENCES

[1] H. J. Kimble, *The Quantum Internet,* Nature **453**, 1023 (2008).

[2] A. Broadbent, J. Fitzsimons and E. Kashefi, *Universal Blind Quantum Computation,* in *50th Annual IEEE Symposium on Foundations of Computer Science* (2009).

[3] L. Jiang *et al.*, *Quantum Repeater with Encoding,* Physical Review A **79**, 032325 (2009).

[4] A. Ekert and R. Renner, *The Ultimate Physical Limits of Privacy,* Nature **507**, 443 (2014).

[5] D. Gottesman, T. Jennewein and S. Croke, *Longer-Baseline Telescopes Using Quantum Repeaters,* Physical Review Letters **109**, 070503 (2012).

[6] N. H. Nickerson, J. F. Fitzsimons and S. C. Benjamin, *Freely Scalable Quantum Technologies Using Cells of 5-to-50 Qubits with Very Lossy and Noisy Photonic Links,* Physical Review X **4**, 041041 (2014).

[7] P. Kómár *et al.*, *A Quantum Network of Clocks,* Nature Physics **10**, 582 (2014).

[8] D. Hucul *et al.*, *Modular Entanglement of Atomic Qubits Using Photons and Phonons,* Nature Physics **11**, 37 (2015).

[9] B. Hensen *et al.*, *Loophole-Free Bell Inequality Violation Using Electron Spins Separated by 1.3 Kilometres,* Nature **526**, 682 (2015).

[10] N. Kalb *et al.*, *Entanglement Distillation between Solid-State Quantum Network Nodes,* Science **356**, 928 (2017).

[11] A. Reiserer and G. Rempe, *Cavity-Based Quantum Networks with Single Atoms and Optical Photons,* Reviews of Modern Physics **87**, 1379 (2015).

[12] J. Hofmann *et al.*, *Heralded Entanglement Between Widely Separated Atoms,* Science **337**, 72 (2012).

[13] T. E. Northup and R. Blatt, *Quantum Information Transfer Using Photons,* Nature Photonics **8**, 356 (2014).

[14] W. Pfaff *et al.*, *Unconditional Quantum Teleportation between Distant Solid-State Quantum Bits,* Science **345**, 532 (2014).

[15] C. Monroe *et al.*, *Large-Scale Modular Quantum-Computer Architecture with Atomic Memory and Photonic Interconnects,* Physical Review A **89**, 022317 (2014).

[16] M. Pant *et al.*, *Routing entanglement in the quantum internet,* arXiv , 1708.07142 (2017).

[17] E. Schoute, L. Mancinska, T. Islam, I. Kerenidis and S. Wehner, *Shortcuts to quantum network routing,* arXiv , 1610.05238 (2016).

[18] R. Stockill *et al.*, *Phase-Tuned Entangled State Generation between Distant Spin Qubits,* Physical Review Letters **119**, 010503 (2017).

[19] A. Delteil *et al.*, *Generation of Heralded Entanglement between Distant Hole Spins,* Nature Physics **12**, 218 (2016).

[20] N. Bar-Gill, L. M. Pham, A. Jarmola, D. Budker and R. L. Walsworth, *Solid-State Electronic Spin Coherence Time Approaching One Second,* Nature Communications **4**, 1743 (2013).

[21] C. Cabrillo, J. I. Cirac, P. García-Fernández and P. Zoller, *Creation of Entangled States of Distant Atoms by Interference,* Physical Review A **59**, 1025 (1999).

[22] J. Minář, H. de Riedmatten, C. Simon, H. Zbinden and N. Gisin, *Phase-Noise Measurements in Long-Fiber Interferometers for Quantum-Repeater Applications,* Physical Review A **77**, 052325 (2008).

[23] B. Casabone *et al.*, *Heralded Entanglement of Two Ions in an Optical Cavity,* Physical Review Letters **111**, 100505 (2013).

[24] A. Sipahigil *et al.*, *An Integrated Diamond Nanophotonics Platform for Quantum-Optical Networks,* Science **354**, 847 (2016).

[25] L. Robledo *et al.*, *High-Fidelity Projective Read-out of a Solid-State Spin Quantum Register,* Nature **477**, 574 (2011).

[26] G. D. Fuchs, V. V. Dobrovitski, D. M. Toyli, F. J. Heremans and D. D. Awschalom, *Gigahertz Dynamics of a Strongly Driven Single Quantum Spin,* Science **326**, 1520 (2009).

[27] P. C. Maurer *et al.*, *Room-Temperature Quantum Bit Memory Exceeding One Second,* Science **336**, 1283 (2012).

[28] S. Yang *et al.*, *High-Fidelity Transfer and Storage of Photon States in a Single Nuclear Spin,* Nature Photonics **10**, 507 (2016).

[29] D. Riedel *et al.*, *Deterministic Enhancement of Coherent Photon Generation from a Nitrogen-Vacancy Center in Ultrapure Diamond,* Physical Review X **7**, 031040 (2017).

[30] N. H. Wan *et al.*, *Efficient Extraction of Light from a Nitrogen-Vacancy Center in a Diamond Parabolic Reflector,* arXiv:1711.01704 [quant-ph] (2017).

[31] A. Reiserer *et al.*, *Robust Quantum-Network Memory Using Decoherence-Protected Subspaces of Nuclear Spins,* Physical Review X **6**, 021040 (2016).

[32] N. Aslam, G. Waldherr, P. Neumann, F. Jelezko and J. Wrachtrup, *Photo-Induced Ionization Dynamics of the Nitrogen Vacancy Defect in Diamond Investigated by Single-Shot Charge State Detection,* New Journal of Physics **15**, 013064 (2013).

[33] M. H. Abobeih *et al.*, *One-second coherence for a single electron spin coupled to a multi-qubit nuclear-spin environment,* arXiv , 1801.01196 (2018).

9

ENTANGLEMENT DISTILLATION BETWEEN SOLID-STATE QUANTUM NETWORK NODES

N. Kalb*, A.A. Reiserer*, P.C. Humphreys*, J.J.W. Bakermans,
S.J. Kamerling, N.H. Nickerson, S.C. Benjamin, D.J. Twitchen,
M. Markham and R. Hanson

The impact of future quantum networks hinges on high-quality quantum entanglement shared between network nodes. Unavoidable imperfections necessitate means to improve remote entanglement by local quantum operations. We realize entanglement distillation on a quantum network primitive of distant electron-nuclear two-qubit nodes. The heralded generation of two copies of a remote entangled state is demonstrated through single-photon-mediated entangling of the electrons and robust storage in the nuclear spins. After applying local two-qubit gates, single-shot measurements herald the distillation of an entangled state with increased fidelity that is available for further use. The key combination of generating, storing and processing entangled states should enable the exploration of multi-particle entanglement on an extended quantum network.

The results in this chapter have been published in Science **356**, 928 (2017).

*Equally contributing authors

9.1. INTRODUCTION

Future quantum networks connecting nodes of long-lived stationary qubits through photonic channels may enable secure communication, quantum computation and simulation, and enhanced metrology[1–9]. The power of these applications fundamentally derives from quantum entanglement shared between the network nodes. The key experimental challenge is therefore to establish high-quality remote entanglement in the presence of unavoidable errors such as decoherence, photon loss and imperfect quantum control. Remarkably, by only using classical communication and local quantum operations, a high-fidelity remote entangled state can be distilled from several lower-fidelity copies[10,11] (Fig. 9.1A). Success of this intrinsically probabilistic distillation can be non-destructively heralded by measurement outcomes such that the distilled state is available for further use, a critical requirement for scalable networks. Owing to these unique features, entanglement distillation (or purification) has become a central building block of quantum network proposals[6–9,12,13].

9.2. DISTILLATION OF REMOTE ENTANGLED STATES

To run entanglement distillation on a quantum network, several copies of a raw entangled state must first be shared between the nodes. This can be achieved using a network primitive of two nodes with two qubits each: a communication qubit with an optical interface for generating remote entanglement and a memory qubit for storage (Fig. 9.1B). First the communication qubits run the entangling protocol, which due to photon loss is intrinsically probabilistic. After photon detection heralds the generation of a raw entangled state on the communication qubits, this state is swapped onto the memory qubits. The communication qubits are then used to generate a second raw entangled state. At this point, the network nodes share two nominally identical copies of the raw state, from which an entangled state of higher fidelity can be distilled. This protocol thus exploits the combination of heralded generation of remote entanglement with robust quantum state storage, high-fidelity quantum logic gates and non-demolition qubit readout within each node.

These demanding experimental requirements have so far limited the exploration of distillation on entangled qubits to four ions within a single node[14] and to all-photonic protocols without memories in which the distilled state was unavoidably lost upon success[15–17]. As an important step towards the desired quantum network, heralded entanglement between distant stationary qubits has recently been achieved with ions, atoms, nitrogen-vacancy (NV) defect centers, quantum dots and superconducting qubits[18–23]. However, the potential memory qubits investigated so far in conjunction with these protocols[24,25] suffered from rapid dephasing during remote entangling attempts due to unwanted couplings, thus precluding the generation of multiple remote entangled states as required for distillation.

We realize the distillation of entangled states on an elementary quantum network consisting of a pair of two-qubit solid-state nodes separated by two meters (Fig. 9.1B). We implement a single-photon-based entangling protocol using diamond electron-spin qubits

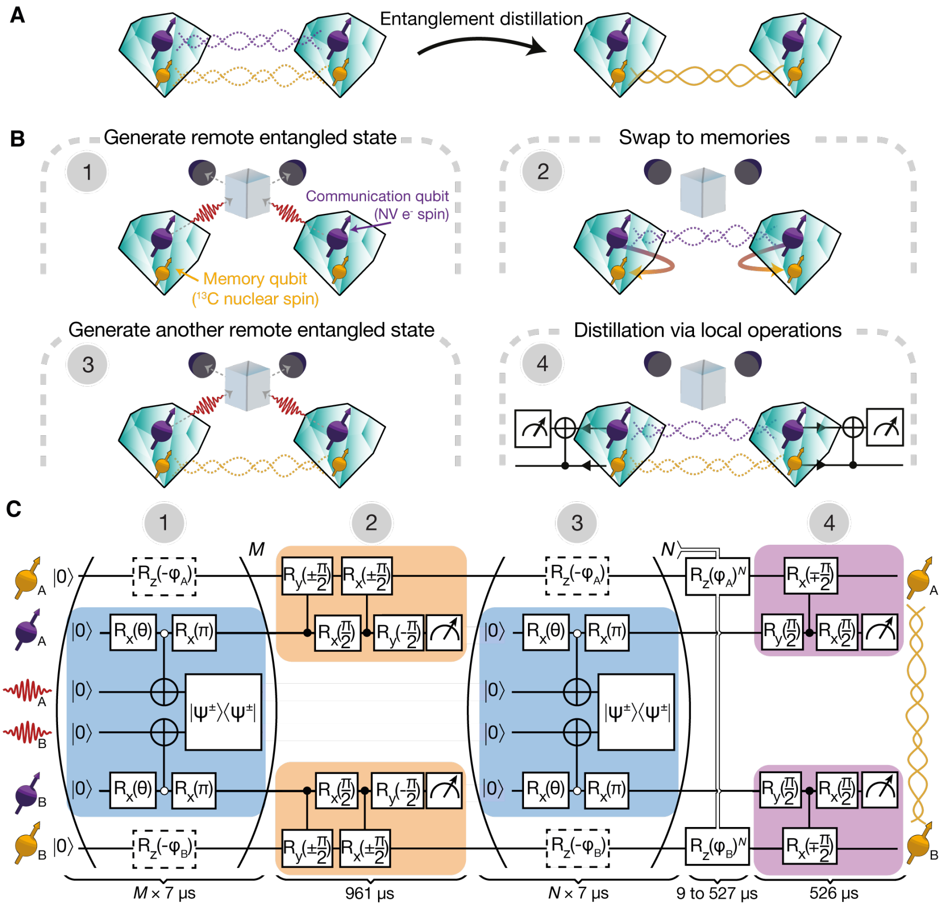

Figure 9.1 |**Entanglement distillation on a quantum network.** (**A**) Working principle: a remote entangled state of higher quality (right) is distilled via local operations and classical communication from several lower-quality states (left) that are shared between remote qubits (depicted as colored spins). (**B**) Protocol overview. Each network node consists of a communication qubit (purple) and a memory qubit (yellow). First, the communication qubits are prepared in a remote entangled state by generating entanglement between a photon (red wave packet) and the spin, interfering the optical modes on a beam splitter (gray cube) and subsequently detecting a single photon ①. Next, the remote entangled state (purple waves represent entanglement) is swapped onto the memory qubits ②, followed by another round of entangled state generation ③. Finally, local operations (black circuit) distill a state of higher fidelity ④. (**C**) Gate circuit implementing steps ①-④.We include the photonic modes of each setup (red wave packets) in which a qubit is encoded such that vacuum and a single photon represent $|0\rangle$ and $|1\rangle$ respectively. Entanglement between the electron spin and photonic mode is experimentally realized by an optical π-pulse (depicted as CNOT symbol). The photonic Bell-state projection $|\Psi^{\pm}\rangle\langle\Psi^{\pm}|$ is probabilistically realized by a beam splitter and subsequent detection of a single photon. Dashed-bordered gates indicate phase-shifts of the memory due to free evolution during entangling attempts. Colored boxes indicate logical blocks of the circuit and are used throughout the manuscript.

(communication qubits) while capitalizing on recent progress on quantum control[26] and robust state storage[27] in nuclear-spin-based quantum memories. Real-time feedback is implemented to compensate memory qubit phase-shifts induced by the probabilistic nature of the remote entangling protocol. As an immediate advantage, the demonstrated protocol distinctly increases the efficiency of entanglement generation compared to the standard two-photon-coincidence protocols used in earlier works[25,28], while removing the optical path-length dependence of stand-alone probabilistic single-photon protocols[22,29].

9.3. QUANTUM NETWORK NODES

Our quantum network nodes comprise an NV electron spin in diamond as a communication qubit and a nearby carbon-13 nuclear spin as a memory qubit. The diamond chips holding these qubits reside in individual closed-cycle cryostats ($T = 4\,\mathrm{K}$) that are separated by two meters (Sec. 9.9.1). The electron spin state is manipulated using amplitude-shaped microwave pulses. Electron spin decoherence occurs on timescales exceeding a millisecond and has negligible impact on the presented results. Spin-selective resonant optical excitation enables high-fidelity initialization and single-shot non-demolition readout of the electron spin[30], as well as generation of spin-photon entanglement for connecting distant nodes[20] (see also Fig. 9.9). We use nuclear spins with intrinsic dephasing times T_2^* of 3.4(1) ms and 16.2(3) ms for node A and B, respectively (Sec. 9.9.1). We implement universal control on each of these nuclear spin qubits by exploiting its hyperfine coupling to the electron spin through recently developed dynamical-decoupling-based gate sequences[31]. This complete quantum toolbox enables the implementation of all four steps in the distillation protocol.

Fig. 9.1C shows the compilation of the full gate circuit into the quantum control operations of our platform. This compilation maximizes the repetition rate and minimizes the number of local quantum gates following the generation of the first remote state. In particular, by initializing the memory qubit at the start of the protocol we are able to implement the SWAP operation with just two conditional quantum gates instead of the three that would be required for arbitrary input states (Sec. 9.9.3). Note that our SWAP implementation maps the communication qubit energy eigenstates onto memory superposition states $|\pm X\rangle \equiv (|0\rangle \pm |1\rangle)/\sqrt{2}$.

To benchmark the performance of the local quantum logic we execute a combination of the SWAP (orange box in Fig. 9.1C) and the gates of the distillation step (purple box in Fig. 9.1C) to generate a maximally-entangled Bell-state between the communication and memory qubits (see Fig. 9.2A). The full density matrix of the resulting two-qubit state is reconstructed via quantum state tomography (QST, see Sec. 9.9.11 for further details). We find a fidelity with the ideal Bell state of 0.96(1) [0.98(1)] for node A [B] indicating high-quality operations in both nodes (Fig. 9.2B).

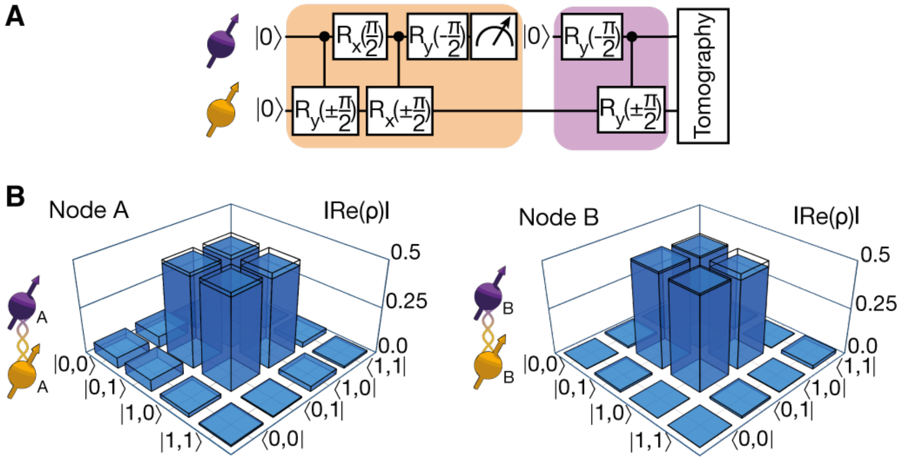

Figure 9.2 |**Benchmarking local control.** (**A**) Gate circuit for entanglement generation within one node. All local operations of the distillation circuit are used to generate an entangled state between communication and memory qubit. Color coding of local operations corresponds to Fig. 9.1C. (**B**) Absolute value of the real part of the local density matrix obtained via sequential QST (see Fig. 9.14). We find fidelities with the desired entangled state of 0.96(1) (node A) and 0.98(1) (node B). Transparent bars give the values of the ideal state.

9.4. ROBUST STORAGE OF QUANTUM INFORMATION

A critical capability for the network nodes is the robust storage of quantum information in the memories while the communication qubits are used to generate remote entangled states. This requires the memory qubits to have long coherence times and be resilient to operations on the communication qubit. The generation of remote entanglement, in particular, poses two challenges as its probabilistic nature means that an a priori unknown number of attempts is required.

First, each failed entangling attempt leaves the communication qubits in an unknown state which necessitates a reset by optical pumping. This reset is a stochastic process which, in combination with the always-on hyperfine interaction between communication and memory qubit, causes dephasing of stored memory states[27,32]. Memories with a small parallel hyperfine coupling are used so that the precession frequency of these memories exhibits only a weak dependency $\Delta\omega$ on the state of the communication qubit during the repumping process of a few hundred nanoseconds [$\Delta\omega_{\mathrm{A}} = 2\pi\cdot 22.4(1)$ kHz and $\Delta\omega_{\mathrm{B}} = 2\pi\cdot 26.6(1)$ kHz]. Decoherence via the perpendicular hyperfine component is suppressed by an applied magnetic field of about 40 mT.

Second, the interaction between communication and memory qubit leads to a deterministic phase-shift $\varphi_{A/B}$ on the memory per entangling attempt. Because it is unknown which entangling attempt will herald success, real-time feedback on the memory is required to compensate for these phase-shifts before the final two-qubit gate of Fig. 9.1C is applied. In addition, the feedback must preserve the coherence of the communication qubit as it holds the second copy of the raw entangled state. We realize such real-time feedback through dynamical decoupling of the electron spin synced with the nuclear spin precession frequency that induces an electron-state-independent phase gate on the memory[31]. At each node, the number of entangling attempts until success N is tracked by a microprocessor that terminates the subsequent decoupling sequence when the desired rotation $\mathrm{R}_\mathrm{Z}(\varphi_{A/B})^N$ has been applied. Ideally, this leaves the memory with the desired phase relation regardless of the number of entangling attempts. We calibrate and verify this feedback at each node separately (see Fig. 9.3A and Fig. 9.3B) and measure a negligible effect on the memory state fidelity while the state of the communication qubit is preserved as desired.

With this feedback realized, we investigate the robustness of the memory as a function of the elapsed entangling attempts. The memory is initialized in one of the six cardinal states of the Bloch sphere ($|0\rangle, |1\rangle, |\pm\mathrm{X}\rangle$ and $|\pm\mathrm{Y}\rangle \equiv (|0\rangle \pm i|1\rangle)/\sqrt{2}$), execute a number of entangling attempts followed by phase-feedback and measure the relevant memory expectation value (see Fig. 9.3C). Dephasing-sensitive states $|\pm\mathrm{X}\rangle, |\pm\mathrm{Y}\rangle$ decay with $1/e$-values of 273(5) (272(4)) entangling attempts in node A (node B) whereas the energy eigenstates $|0\rangle, |1\rangle$ are preserved with high fidelity as expected. The memories thus provide faithful storage during remote entangling attempts.

9.5. EXPERIMENTAL ENTANGLEMENT DISTILLATION

With local control and storage in place, we now turn towards the execution of the full distillation protocol (Figs. 9.6 and 9.7). Following Campbell's protocol[33], we generate the remote states that provide the resources for distillation by first initializing both communication qubits in a superposition with variable angle θ, $|\theta\rangle \equiv \sin\theta|0\rangle - i\cos\theta|1\rangle$. Subsequent optical excitation for state $|0\rangle$ and overlap of the emission of both communication qubits on a beam splitter (see steps 1 and 3 of Fig. 9.1C and histograms in Fig. 9.8) generates the raw remote state ρ_raw if a single photon is detected[33]. For equal and small detection probabilities for both nodes and negligible dark counts, ρ_raw reads:

$$\rho_\mathrm{raw} = \left(1 - \sin^2\theta\right)|\Psi^\pm_\phi\rangle\langle\Psi^\pm_\phi| + \sin^2\theta\,|0,0\rangle\langle 0,0|. \tag{9.1}$$

The states $|\Psi^\pm_\phi\rangle \equiv (|01\rangle \pm e^{i\phi}|10\rangle)/\sqrt{2}$ are entangled states, with a relative phase depending on which detector clicked (±) and an additional internal phase ϕ due to the unknown path length between both emitters and the beam splitter. The fraction of the non-entangled admixture $|0,0\rangle\langle 0,0|$ can be directly controlled through the choice of the initial communication qubit state $|\theta\rangle$; note that the choice of $|\theta\rangle$ also affects the probability of successful entanglement generation (scaling as $\sin^2\theta$). We next swap the raw state onto the memories such that the communication qubit is free for another round of remote state generation (step 2 in Fig. 9.1C). Once a second state is successfully generated (step 3), we apply a conditional quantum gate within each node and read out the

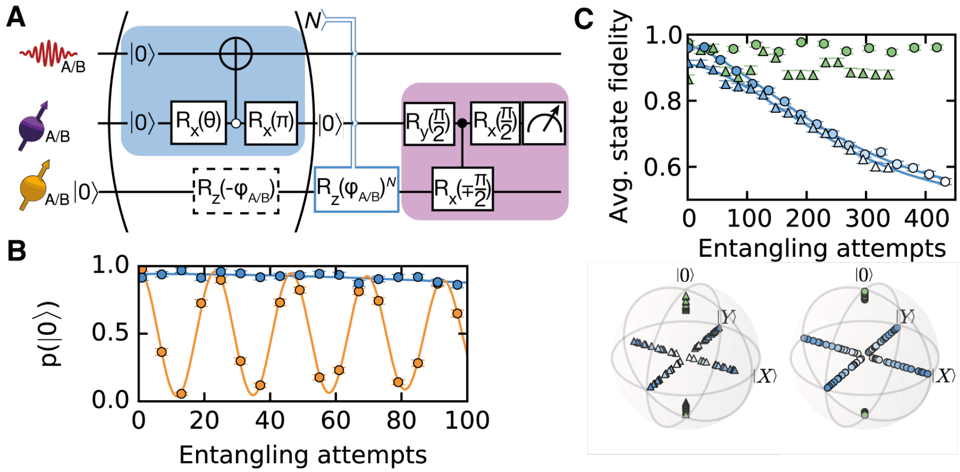

Figure 9.3 |Quantum state storage during entangling operations. (**A**) Real-time feedback circuit for memory qubits. We initialize memory A/B, which then experiences a phase-shift of $-\varphi_{\mathrm{A/B}}$ per executed entangling attempt. After reinitialization of the communication qubit, the distillation step of the protocol is performed (Fig. 9.1C). Blue-rimmed gate indicates the feedback. (**B**) Memory state as a function of the number of entangling attempts. The oscillation observed without feedback (orange) is successfully compensated (blue) by the feedback. Solid lines are fits to the data. (**C**) Memory lifetime of node A (triangles) and node B (circles). We initialize the memory in one of the six cardinal states of the Bloch sphere (see right panel), sweep the number of entangling attempts, apply feedback, and read-out the expectation value that is relevant for the estimation of the state fidelity with the initial cardinal state. Note that all fidelity-irrelevant expectation values are set to zero, i.e. we depict projections of the state onto the respective axis in the Bloch sphere picture. The average state fidelities are separately plotted for phase-sensitive superposition states (blue) and phase-insensitive eigenstates (green). Blue solid lines depict a generalized exponential fit (Sec. 9.9.1). The decay is limited by the stochastic repumping process, microwave pulse errors and/or environmental dephasing. The color gradient of the left and right panel match to facilitate comparisons. Error bars represent one standard deviation.

communication qubits in a single shot. Owing to the quantum non-demolition nature of this readout the memory qubits do not experience additional dephasing during this step[30]. Readout of the communication qubit projects the memories into one of four states depending on the readout results (Sec. 9.9.6):

$$
\begin{aligned}
(0_A, 0_B) &\quad : \quad \tfrac{1}{2}\cos^4\theta\, U|\Psi_0^\pm\rangle\langle\Psi_0^\pm|U^\dagger, \\
(0_A, 1_B) &\quad : \quad \tfrac{1}{2}\sin^2\theta\cos^2\theta\, U(|0,1\rangle\langle 0,1| + |1,1\rangle\langle 1,1|)U^\dagger, \\
(1_A, 0_B) &\quad : \quad \tfrac{1}{2}\sin^2\theta\cos^2\theta\, U(|1,0\rangle\langle 1,0| + |1,1\rangle\langle 1,1|)U^\dagger, \\
(1_A, 1_B) &\quad : \quad \sin^4\theta\, U|1,1\rangle\langle 1,1|U^\dagger + \tfrac{1}{2}\cos^4\theta\, U|\Psi_{2\phi}^\pm\rangle\langle\Psi_{2\phi}^\pm|U^\dagger.
\end{aligned}
$$

Here the states are left unnormalized; their traces indicate their probabilities of occurrence. The unitary U corresponds to a Hadamard gate on each memory that arises from the swapping operation in each node. Observation of the readout combination $(0_A, 0_B)$ heralds successful distillation and leaves the system in the state

$$|\psi\rangle_\mathrm{c} \otimes |\psi\rangle_\mathrm{m} = e^{i\phi}|0,0\rangle \otimes U|\Psi_0^\pm\rangle \tag{9.2}$$

with the relative phase of the final Bell state given by the photon detection signature, i.e. the photons in step 1 and 3 were detected in the same (+) or in different (-) output ports. Importantly, the protocol is agnostic to correlated dephasing of the raw states and is therefore only sensitive to optical path length drifts that occur within an individual run of the protocol (see Fig. 9.12)[33]. This is in stark contrast to probabilistic single-photon protocols[22,23,29,34] that require path length stabilization over the full course of data acquisition.

The experimental implementation of entanglement generation requires that the communication qubits' optical transitions are kept on resonance despite shot-to-shot fluctuations and long-term drifts of the respective local charge environments. An automatic feedback loop and resonance search routine is used to compensate for charge jumps such that the experiment is push-button and runs without human intervention. To further optimize the data rate the number of remote entangling attempts is bounded to 1000 for step 1 and up to 500 rounds for step 3, leading to event rates (i.e. two remote states were successfully generated) of around 10 Hz. These bounds are a compromise between maximizing the success probability (favoring more attempts) and minimizing effects of drifts and of memory decoherence (favoring fewer attempts).

9.6. DISTILLATION RESULTS

We start by running the complete protocol using $\theta = \pi/6$ and perform full quantum state tomography on the distilled state. This way, using the complete information obtained on the resulting output, we can verify whether the protocol works as desired. Fig. 9.4A shows the resulting data for a maximum of 50 entangling attempts in the second round of state generation. This truncation yields optimal state storage during each run of the protocol. Quantitatively, the measured fidelity with the ideal Bell state of 0.65(3) > 0.5 proves entanglement of the distilled state. Furthermore, the density matrix has high populations in the Bell-state-subspace only, showing that the distillation successfully diminishes the separable admixture.

To gain further insight into the performance of the protocol we measure the fidelity of the distilled state for different amounts of the separable admixture in the raw states; i.e. for different θ (see Fig. 9.4B, blue dots). The results are again truncated after a maximum of 50 entangling attempts in the second round. The state fidelities are averaged over both detection signatures.

The hallmark of successful distillation is an increase in fidelity of the distilled state compared to that of the raw states. Whereas in the textbook description both raw states are assumed to be equal, in our experiment they are different due to imperfections in the swap operation and memory storage that only affect the raw state held by the memories, and path length variations on short timescales that only affect the raw state held by the communication qubits. To make a meaningful comparison we therefore consider the state fidelities of each of these raw states separately.

Because of the unreferenced internal phase of the raw states, all coherences are washed out due to optical path length variations. Direct tomography will therefore yield state fidelities that cannot surpass 0.5. As a result, the measured fidelities of the distilled states far exceed the electron state fidelities measured after step 1 (Fig. 9.4B, purple dots). Although these numbers reflect the current experiment, we now turn to a more strict comparison by taking into account that the internal phase may become accessible in future experiments through optical path stabilization.

We model the raw state fidelities at the start of the distillation step (step 4) using independently determined parameters under the assumption of a perfectly known initial path length difference (Fig. 9.4B, solid purple line for raw state on the electrons and solid orange line for raw state on the nuclei; Sec. 9.9.7). For small values of θ (small separable admixtures) the fidelity increase due to distillation is offset by the errors introduced with the additional quantum operations of the distillation step. However, we find that for larger values of θ the distilled state fidelity significantly surpasses both of the raw state fidelities (see also Fig. 9.15 and Sec. 9.9.12 for hypothesis test). This result demonstrates the realization of entanglement distillation on our elementary quantum network.

For a more detailed understanding of the different error sources contributing to the measured fidelity, we develop an extensive model of the full protocol using independently measured quantities and two free parameters: one factor accounting for additional memory control errors and the second for phase fluctuations of the raw states (Sec. 9.9.6). We find good agreement between the modeled fidelity and the data for each of the different separable admixtures (see Fig. 9.4B blue dashed line and Sec. 9.9.7) and for the evolution of the correlations with number of entangling attempts (Fig. 9.4C). The model

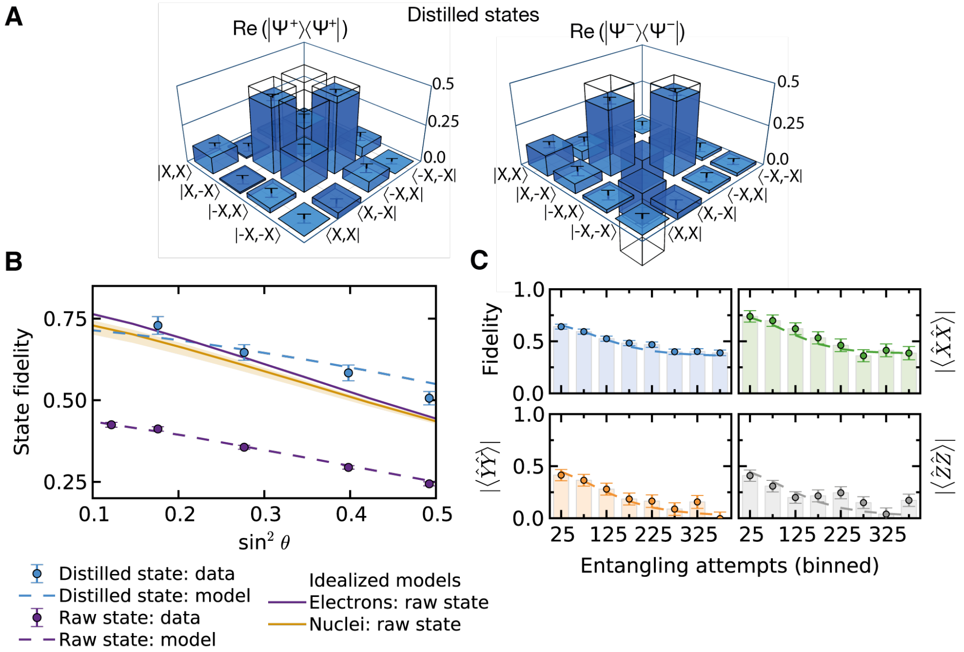

Figure 9.4 |Experimental realization of entanglement distillation. (**A**) Two-qubit density matrices for $\theta = \pi/6$ and a maximum of 50 entangling attempts in the second round. Right panel: different detectors clicked. Left panel: the same detector clicked twice. We find a fidelity with the ideal state of 0.65(3) for both states. Transparent bars represent the ideal state. (**B**) Fidelity with the ideal state as a function of θ for a maximum of 50 entangling attempts in the second round. Blue data is the two-memory state fidelity. Dashed lines are derived from our model (Sec. 9.9.7). Purple data is the measured raw state fidelity on the communication qubits. Solid orange (purple) line is the modeled fidelity of the raw state on the memories (communication qubits) that would be obtained if the initial internal phase was known. The memory state is calculated for the average number of entangling attempts until success (25). The orange shaded region is the modeled memory fidelity for minimal (0 attempts) and maximal (50 attempts) dephasing. The θ-dependence of the distilled state fidelity is explained by the finite probability of misidentifying a separable state (the presence of which scales with θ) as a successfully distilled entangled state due imperfect quantum control and decoherence of the stored state. Fidelities were obtained by measuring the expectation values $\langle\hat{X}\hat{X}\rangle$, $\langle\hat{Y}\hat{Y}\rangle$ and $\langle\hat{Z}\hat{Z}\rangle$. We denote the Pauli operators as $\hat{X}$, $\hat{Y}$ and $\hat{Z}$. (**C**) State decay for $\theta = \pi/6$. Data are binned according to the number of second entanglement generation attempts until success. Shown are the state fidelity (blue) and the absolute value of the relevant expectation values. The dashed lines are derived from our theoretical model (see Fig. 9.10). Error bars represent one standard deviation.

indicates that the state fidelities are mainly limited by memory qubit dephasing and control errors as well as non-zero two-photon distinguishability. The latter effect, quantified by a measured two-photon interference visibility of 0.73(3) (see Fig. 9.11), is especially harmful in the above comparison with the raw state, as this occurs twice for the distillation protocol but only once for the raw state generation. A visibility of 0.9 as observed on different NV center pairs[28] would thus yield an even stronger entanglement enhancement.

9.7. EBIT RATE

Previously demonstrated entangling protocols based on two-photon coincidences[25,28] require steps 1 and 3 to succeed in subsequent attempts leading to a success probability scaling with the square of the photon detection probability p_{det}. In contrast, the distillation protocol allows step 3 to succeed in one of many attempts following success in step 1, leading to a success probability scaling linearly with p_{det} in the ideal case. Given that in a typical quantum network setting p_{det} will be small (in our case $p_{\text{det}} \approx 10^{-3}$), the distillation protocol can provide a distinct rate advantage despite the overhead of the additional local quantum logic.

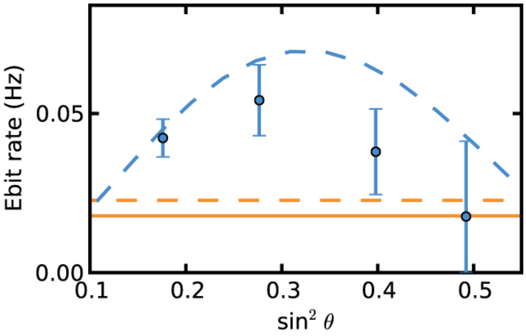

Figure 9.5 |**Ebit rate comparison.** Ebit rate as a function of excitation angle θ. The blue data is derived from the measured success rates and state fidelity over the entire data set (see Fig. 9.13). The blue dashed line is the estimated ebit rate for distillation including the overhead of local operations. The solid (dashed) orange line gives the estimated ebit rate of a standard two-photon protocol including (excluding) imperfections. All data are averaged over both detection signatures. Error bars represent one standard deviation.

To quantitatively compare our results with two-photon-coincidence protocols we upper bound the rate r of entangled bit (ebit) generation for each protocol using $r = \nu E_N$ with the logarithmic negativity E_N and the rate of success ν. Fig. 9.5 compares the ebit rate of the presented distillation protocol to the modeled rate of the Barrett-Kok two-photon-coincidence protocol[35] used in earlier experiments on NV centers[20,28]. We find that the distillation protocol (blue dots) outperforms the two-photon-coincidence protocol for identical experimental conditions, not only when assuming the measured two-photon indistinguishability (orange solid line) but even for the case that the two-photon-coincidence protocol would be able to access perfect two-photon indistinguishability (orange dashed line).

9.8. TOWARDS MULTI-NODE QUANTUM NETWORKS

The combination of generating, storing and processing remote entangled qubits as demonstrated in the current distillation experiment provides a universal primitive for realizing extended quantum networks. The distillation itself is a powerful method to counteract unavoidable decoherence as entanglement is distributed throughout the network. Also, the protocol enables a speedup of entanglement generation that can be harnessed in related platforms such as other solid-state defect centers[36] and trapped ions[37]. Improvements can be expected by encoding qubits into decoherence-protected subspaces[27], by using isotopically purified materials with longer qubit dephasing times[38–40], by implementing a faster reset or a measurement-based reset of the communication qubit and by increasing the entangling rates through photonic cavities[41,42]. Furthermore, the techniques used in recent demonstrations of multi-qubit control and quantum error correction on a 4-qubit node[26,43] are fully compatible with the current experiment, thus highlighting the potential for scaling to more qubits and extending network functionality in the near future. Finally, the methods developed provide the toolkit to explore and utilize many-particle entanglement on a multi-node quantum network.

CONTRIBUTIONS

N.K., A.R. and R.H. devised the experiment. N.K., A.R., P.C.H., J.J.W.B. and S.J.K. prepared and characterized the experimental apparatus. D.J.T. and M.M. grew the diamond substrates. N.H.N. and S.C.B. provided theoretical support. N.K. and P.C.H. collected the data. P.C.H. and N.K. analysed the data with the help of R.H. N.K. wrote the original form of this chapter with input from all authors which was then adapted by N.K. for this thesis.

9.9. SUPPLEMENTARY INFORMATION

9.9.1. EXPERIMENTAL DESIGN

We use chemical-vapour-deposition homoepitaxially grown diamonds of type IIa with a natural abundance of carbon isotopes. Both diamonds have been cut along the ⟨111⟩ crystal axis and were grown by Element Six. They are situated in home-built confocal microscope setups within closed-cycle cryostats (4 K, Montana Instruments) separated by two meters. We additionally employ a magnetic field (Node A: 418.248(5) G; node B: 413.980(5) G) approximately aligned with the NV symmetry axis in both setups by placing a permanent magnet within the respective sample chamber and compensating slight alignment-deviations with additional permanent magnets from the outside (few cm distance). Microwave pulses are applied via a gold stripline (thickness of 200 nm) that has been deposited onto the surface of the sample. We shape these pulses to a Hermite amplitude envelope for robustness against qubit frequency detunings (≈ MHz) such as arising from the hyperfine interaction with the host nitrogen nuclear spin[28]. To generate short optical excitation pulses, we use an electro-optic modulator (Jenoptik) in a homebuilt, temperature stabilized, enclosure which, in conjunction with an upstream acousto-optic modulator (Gooche & Housego), creates a laser pulse with high on/off ratio and Gaussian temporal envelope. This pulse is split into two using a polarization maintaining fiber beam splitter (Evanescent Optics) for excitation of both NV centers (see also Section 9.9.5). Optical transition frequencies of each NV center are tuned by applying voltages to gold electrodes on the diamond surface.

We employ a single-layer anti-reflection coating for 637 nm light (Al_2O_3) and solid immersion lenses around the position of the NVs to increase optical collection efficiencies. This in conjunction with the cryogenic environment allows for spin-selective optical read-out of the NV electron spin in a single-shot via the optical E_x (E_y) transition on node A (node B). We measure read-out fidelities of 0.9379(6) (0.8985(7)) for the bright $|m_s = 0\rangle \equiv |0\rangle$ ground-state and 0.9932(2) (0.9962(1)) for the dark $|m_s = +1\rangle \equiv |1\rangle_\mathrm{A}$ ($|m_s = -1\rangle \equiv |1\rangle_\mathrm{B}$) state on node A (node B). These values are subsequently used to correct for read-out errors of the electron spins in state tomography measurements. Node A additionally uses adaptive optics to compensate for imperfections in the solid immersion lens, which leads to an improved collection efficiency of zero-phonon-line (ZPL) photons[28].

We utilize each electron spin to control an adjacent nuclear spin ($I = \frac{1}{2}$) associated with a ^{13}C atom in the diamond lattice via dynamical decoupling sequences that are resonant with the electron-nuclear dynamics, optimizing the gate parameters to maximize the fidelity of our operations. The parameters for a full entangling operation between nuclear and electron spin are given in Table 9.1. Furthermore we characterize the strength of the magnetic hyperfine interaction between nuclear spin and electron as well as nuclear dephasing times with the electron spin idling in one of the two relevant states ($|0\rangle$ or $|1\rangle$). The decay of the memories when performing entangling attempts are best fit with exponential functions of the form $e^{-(t/T)^n}$ with T the $1/e$ decay constant and with exponents $n = 1.7(1), 1.48(5)$ for nodes A and B respectively. We correct for tomography errors on the nuclear spin state by employing previously developed methods that rely on a symmetric initialization and read-out of the respective nuclear spin[26,43]. The measured quantities are given in Table 9.1.

9.9.2. EXPERIMENTAL SEQUENCE

Remote entangled electron spin states are generated by initializing the superposition state $|\theta\rangle$ on both sides (we use a 2 μs long repumping laser pulse followed by a microwave pulse) and subsequent optical excitation from a common laser source which guarantees relative frequency-stability. The sequence duration is 7 μs. A photo-detection event heralds the desired raw state of Eq. (9.4). We obtain single-photon detection probabilities of $p_\mathrm{a} = 8\cdot 10^{-4}$ ($p_\mathrm{b} = 4\cdot 10^{-4}$) for node A (node B). A final microwave π-pulse preserves electron coherence and decouples the magnetic hyperfine interaction with the memory[27].

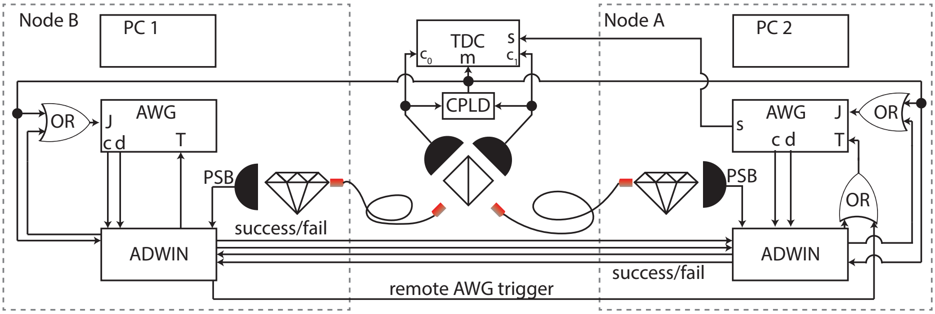

Figure 9.6 |Control schematic of the experimental setup. Complex programmable logic device (CPLD) outputs a trigger upon detection of a ZPL photon (see Section 9.9.4 for timing). Time-to-digital converter (TDC, PicoQuant HydraHarp 400) with time-tagged channels (c_0 and c_1), a marker for ZPL photon detection events (m), and a sync channel (s). We use microprocessors for decision making (Jäger ADwin Pro II (ADwin)) and arbitrary waveform generators (Tektronix AWG5014c (AWG)) which have input channels for jump (J) and trigger (T) commands. Outputs of the AWGs are used to have the respective local ADwin count the number of entangling events (c) and to determine whether a part of the logical sequence (see Fig. 9.7) has finished (d). Besides, AWGs and ADwins control all laser and microwave pulses of the respective setup. Personal computers (PCs 1&2) are used for sequence programming, hardware control and monitoring during measurements. ADwins record electron-spin readout via luminescence in the phonon sideband (PSB) and communicate success or failure of logical steps within the sequence with a three-way handshake that utilizes two digital input and two digital output channels on each device (success/fail). See Fig. 9.7 for further details on the sequence. The start of the AWG sequences is triggered via one ADwin to mitigate timing jitter between both AWG outputs.

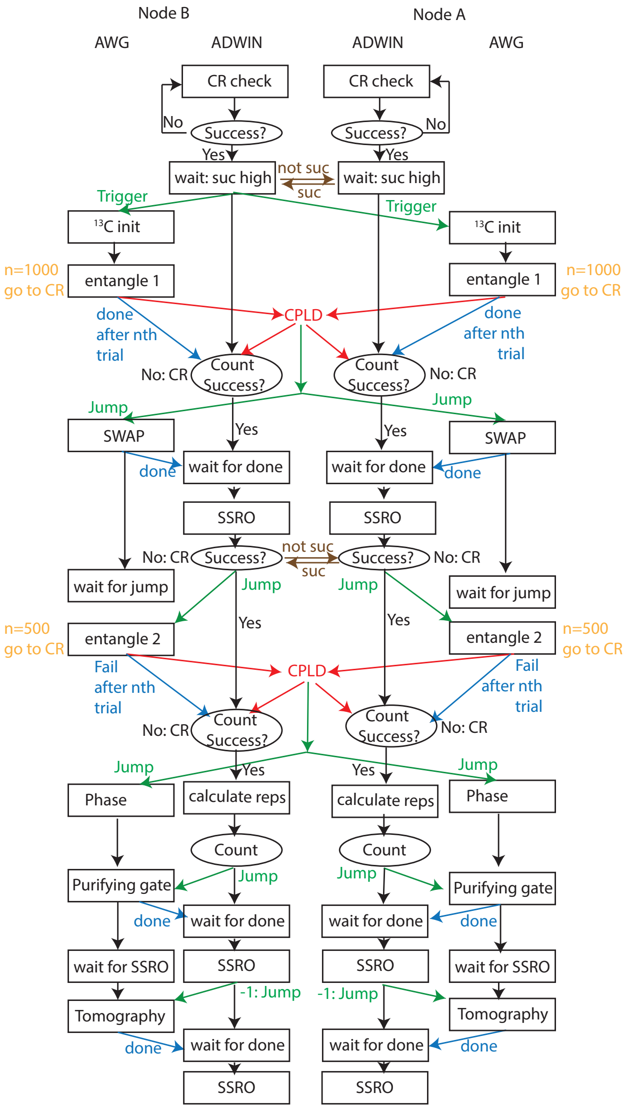

Figure 9.7 |Logical blocks for the AWG and ADwin of each setup during one round of distillation. For a wire diagram of the experimental logic see Fig. 9.6. Boxes give logical steps within the sequence (see also Fig. 9.1C). Conditional actions and feedback are implied by ellipses. Before each experimental run we verify that both electron spins are on resonance via a charge-resonance (CR) check[44]. Unless indicated otherwise, black arrows represent an unconditional advance of the sequence even if no communication signal was received. The absence of a black arrow indicates a restart of the sequence upon failure. We additionally provide a glossary of all used terms in Tab. 9.2.

	Node A	Node B	Description
$A_{\parallel}$ (kHz)	$-2\pi\cdot 30(1)$	$2\pi\cdot 33(1)$	Parallel hyperfine coupling with electron spin.
$A_{\perp}$ (kHz)	$2\pi\cdot 88(1)$	$2\pi\cdot 35(1)$	Perpendicular hyperfine coupling with electron spin.
N	12	34	Number of inversion pulses on electron for nuclear spin gate.
τ (μs)	21.772	12.812	Optimized interpulse delay for nuclear spin gate.
F_{tomo}	0.973(3)	0.978(2)	Correction factor for gate errors in the tomography sequence.
$T_{2,0}^{*}$ (ms)	3.4(1)	19.4(3)	Nuclear dephasing time with the electron idle in $\lvert m_s = 0\rangle$.
$T_{2,1}^{*}$ (ms)	3.4(1)	16.2(3)	Nuclear dephasing time with the electron idle in $\lvert m_s = \pm 1\rangle$.
σ	273(5)	272(4)	fitted $1/e$ value of the memory decay in entangling attempts.

Table 9.1 |Measured experimental parameters of the nuclear spins.

Generating remote entangled states with low detection efficiencies requires complex logic operations to limit overhead and guarantee a time-efficient execution of the sequence. We implement charge resonance checks for pre-selection of and feedback on the current NV emission frequencies as well as multiple logical stages in the sequence at which both nodes communicate local success or failure. Combined success events advance the sequence one step further whereas failure causes a restart. A schematic of the electrical wiring is depicted in Fig. 9.6. Figure 9.7 gives an overview of all communication steps between the involved instruments.

9.9.3. CONFIRMATION HERALD FOR A HIGH FIDELITY SWAP

The fidelity of the local swap operation is improved by constructing a confirmation herald. Prior to the swap the memory is initialized in the phase-insensitive eigenstate $\lvert 0\rangle$ which gets mapped onto the fluorescing electron state $\lvert 0\rangle$ by the applied gate sequence. Measuring the electron in the state $\lvert 0\rangle$ by detection of a photon after the swap sequence therefore suppresses infidelities at negligible cost in efficiency (measured success probability of 0.89(1)).

9.9.4. TEMPORAL FILTERING & CPLD TIMING

We determine the relative timing of clicks originating from avalanche photodiodes (APDs) 1 and 2 by creating histograms of all detection events registered from each APD by the

Term	Description
CR check	charge-resonance check[44].
Success?	ADwin verifies whether a condition of success is fulfilled or not.
wait: suc high	ADwin waits until success is signaled by the other ADwin.
not / suc	ADwin-ADwin communication via a three-way handshake.
wait for done	ADwin waits for the AWG signaling the end of a subsequence.
SSRO	single-shot readout of the NV electron spin[30,44].
Trigger	Signals the AWG to start with the sequence.
Fail/done after nth trial	AWG signals the respective ADwin the end of entangle 1 or 2.
Jump	Event jump channel of the AWG that induces a jump to the next subsequence.
^{13}C init	Initialization of the memory into the state $\|0\rangle$.
entangle 1 and entangle 2	Generate long-distance entanglement.
Count	ADwin counts the number of repetitions of a specific sequence element.
wait for jump	AWG waits for a jump command from the ADwin. If no jump (e.g. signifying a failed SWAP on one of both sides) is sent within the prespecified waiting time we return to the beginning of the sequence.
SWAP	Subsequence to swap the NV state onto the memory.
Phase	Nuclear phase feedback via dynamical decoupling of the electron spin.
calculate reps	ADwin calculates the number of dynamical decoupling cycles to obtain the desired memory phase.
Purifying gate	Step 4 of the experimental protocol (see Fig. 9.1).
wait for SSRO	AWG waits until ADwins have obtained a SSRO result.
-1 : Jump	Go to a phase-adjusted tomography sequence if communication qubit was measured in $\|1\rangle$.
Tomography	One of the gate sequences depicted in Fig. 9.14.

Table 9.2 |Glossary for all terms and abbreviations contained in Fig. 9.7.

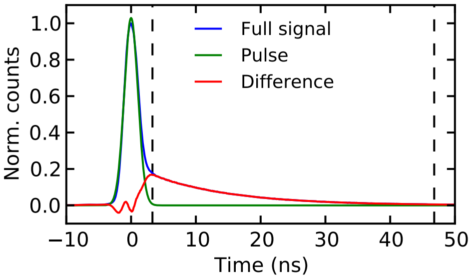

Figure 9.8 |Plotted in blue is the histogram of the timings of all APD clicks registered by our time-to-digital converter (blue). We fit a Gaussian profile to the beginning of this histogram (green), as this profile is known to closely correspond to the temporal shape of our excitation pulse. The profile of the NV emission (red) is estimated by taking the difference between the full histogram of counts and the photons assumed to originate from the excitation pulse. Dashed lines indicate the beginning and end of the detection window. Time is given with respect to the fitted center of the laser pulse.

TDC. The maximum of the auto-correlation between these histograms indicates the timing delay at which the two temporal distributions are best overlapped.

Once this timing is determined, we fit a Gaussian profile to the beginning of the histogram of all overlapped data (Fig. 9.8). This Gaussian profile is known to closely correspond to our excitation pulse profile. We use this fit to estimate the point in time beyond which the ratio between photons from the excitation laser and the integrated residual NV emission is less than 0.001. This independently determined time set the beginning of the temporal filter in our analysis of the distillation results. We choose this conservative criterion in order to mitigate any potential impact of non-Gaussian tails in the laser profile.

In order to minimize the impact of dark counts, we set the end of the temporal filter to be 40 ns after the start of the window. This filtering is chosen because, for times longer than 40 ns after the excitation pulse, the ratio between dark counts and NV photon detections is estimated to increase above 0.1 for the most sensitive case ($\theta = \pi/8$). A live temporal filter through the CPLD (see Figs. 9.6 and 9.7) allows us to exclude 36.6% of all events on-the-fly.

9.9.5. OPTICAL TRANSITION FREQUENCIES OF THE NV IN A MAGNETIC FIELD

Lateral crystal strain modifies the eigenstates and respective eigenenergies of the NV excited electronic states. Fig. 9.9 shows the optical transition frequencies ω_{Ex} for $|m_s = 0\rangle \rightarrow |E_x\rangle$ and $\omega_{\pm 1}$ for the transitions $|m_s = \pm 1\rangle \rightarrow |A_1\rangle$, as a function of lateral strain. The transition $|m_s = 0\rangle \rightarrow |E_x\rangle$ is of particular interest as it remains spin conserving even under large lateral strain fields (no deterioration was found for strain induced frequency

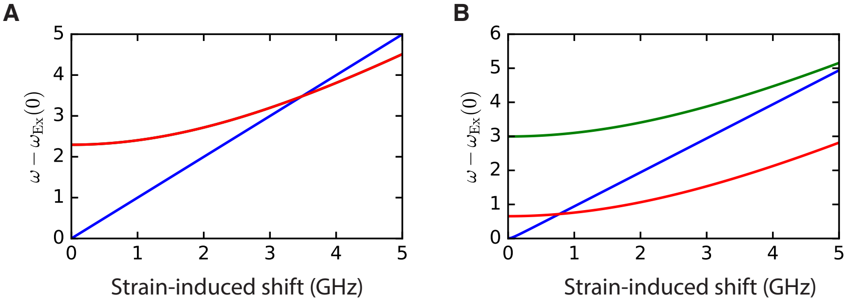

Figure 9.9 |Optical transition frequencies of the NV electron spin as a function of lateral strain with and without magnetic field. (**A**) without magnetic field and (**B**) with magnetic field along the NV axis (B = 418.2 G). In the latter case the excitation frequencies $\omega_{\pm1}$ are no longer degenerate. Blue: transition from $|m_s = 0\rangle$ to $|E_x\rangle$. Red (green): transition from $|m_s = +1\,(-1)\rangle$ to the optically excited state $|A_1\rangle$. Red and green lines overlap in panel A.

shifts up to 5 GHz). Without magnetic field the ground states $|m_s \pm 1\rangle$ are degenerate and $\omega_{+1} = \omega_{-1}$. In this case, at a lateral strain-induced frequency shift around 3.5 GHz ω_{Ex} and $\omega_{\pm1}$ are nearly degenerate which hampers the quality of spin-photon entanglement. Applying a sufficiently large magnetic field along the NV axis splits the ground states due to the Zeeman effect; therefore ω_{Ex} is degenerate with ω_{+1} and ω_{-1} in distinct strain regimes and there is always a choice of qubit states in the ground state triplet of the NV center that allows for high-quality spin-photon entanglement. In our experiment node A operates at a lateral strain-induced frequency shift of ~ 4 GHz such that we choose $|1\rangle \equiv |m_s = +1\rangle$. These considerations are not a factor for node B, as in this case we are using the transition $|m_s = 0\rangle \rightarrow |E_y\rangle$.

9.9.6. DISTILLATION PROTOCOL

We entangle distant NV spins by employing single photons as flying qubits in a probabilistic measurement-based entanglement (MBE) protocol. After initializing each NV in the $|m_s = 0\rangle$ ground state, which we will label $|0\rangle$, a microwave pulse is used to rotate the spin into a superposition of this state and one of the $|m_s = \pm1\rangle$ states, here labeled $|1\rangle$. This prepares each NV in the state

$$|\theta\rangle = \sin\theta|0\rangle - i\cos\theta|1\rangle. \tag{9.3}$$

Subsequent spin-selective resonant excitation of the NVs leads to the emission of a single photon if the NV is in the $|0\rangle$ state, creating spin-photon entangled states at each node. These single photons are transmitted to a central node and subsequently interfered on a beam splitter. In the ideal case, detection of a single photon after this beam splitter projects the NVs onto the entangled state $|\Psi^{\pm}\rangle = -i(|01\rangle \pm |10\rangle)/\sqrt{2}$ (where the sign depends on which detector clicked).

We do not stabilize the phase of the excitation laser at the position of the NVs, nor the optical path length traversed by the emitted photons from the NVs to the central node. These differences between the two optical paths apply an unknown phase ϕ to the entangled state. In addition, the NVs only emit photons 3% of the time in the usable zero-phonon line (ZPL), and the optical channels have finite transmissivities. This leads to a reduced probability p_d of successfully detecting a single photon given that one of the NVs was in the $|0\rangle$ state. These dominant imperfections mean that we actually produce the state

$$\rho_\mathrm{raw}(\phi) = \eta|\Psi^\phi\rangle\langle\Psi^\phi| + (1-\eta)|00\rangle\langle 00|, \tag{9.4}$$

where $|\Psi^\phi\rangle = (|01\rangle + e^{\mathrm{i}\phi}|10\rangle)/\sqrt{2}$ and η depends on both θ and p_d.

Each communication qubit is flipped by applying $R_\mathrm{x}(\pi)$ as part of our dynamical decoupling sequence and then (following[8,33]) swapped onto local memories at each node. This allows us to reuse the NVs to produce a second entangled state between the nodes. Upon success, our overall state is then given by $\rho_\mathrm{raw}(\phi_2) \otimes \rho'_\mathrm{raw}(\phi_1)$, where ϕ_2 and ϕ_1 depend on the phase differences at the two different times that the states were created (for pedagogical clarity, here we assume that the same detector clicked). Due to the particular swapping operation we employ, the memory state $\rho'_\mathrm{raw}(\phi_1)$ is a rotated version of the initial state $\rho_\mathrm{raw}(\phi_1)$, such that $\rho'_\mathrm{raw}(\phi_1) = U\rho_\mathrm{raw}(\phi_1)U^\dagger$. Therefore, for readability, in the following text we redefine the memory qubit states in a rotated basis such that the states $|0\rangle_m$ and $|1\rangle_m$ are superpositions of the energy eigenstates $|0\rangle$ and $|1\rangle$ that are employed in the main text.

$$\begin{aligned}
(|10\rangle_c + e^{\mathrm{i}\phi_2}|01\rangle_c) \otimes (|10\rangle_m + e^{\mathrm{i}\phi_1}|01\rangle_m) &\rightarrow (|11\rangle_c + e^{\mathrm{i}\phi_2}|00\rangle_c) \otimes |10\rangle_m + \\
&\quad + e^{\mathrm{i}\phi_1}(|00\rangle_c + e^{\mathrm{i}\phi_2}|11\rangle_c) \otimes |01\rangle_m, \\
(|10\rangle_c + e^{\mathrm{i}\phi_2}|01\rangle_c) \otimes |11\rangle_m &\rightarrow (|10\rangle_c + e^{\mathrm{i}\phi_2}|01\rangle_c) \otimes |11\rangle_m, \\
|11\rangle_c \otimes (|10\rangle_m + e^{\mathrm{i}\phi_1}|01\rangle_m) &\rightarrow |10\rangle_c \otimes |10\rangle_m + e^{\mathrm{i}\phi_1}|01\rangle_c \otimes |01\rangle_m, \\
|11\rangle_c \otimes |11\rangle_m &\rightarrow |11\rangle_c \otimes |11\rangle_m
\end{aligned} \tag{9.5}$$

Measurement of both communication qubits in the $|00\rangle_c$ state heralds successful distillation. For a balanced superposition state ($\theta = \pi/4$) and high photon loss ($p_\mathrm{d} \ll 1$), in which case $\eta = 1/2$, the distillation succeeds with probability $\frac{1}{8}$. It can be seen that this projects the memories into the pure state $\frac{1}{\sqrt{2}}(e^{\mathrm{i}\phi_1}|01\rangle_m \otimes + e^{\mathrm{i}\phi_2}|10\rangle_m)$, and so the $|11\rangle\langle 11|$ contamination has been removed.

In addition, if the phase drift over the duration of the experiment is sufficiently small, such that $\phi_1 \approx \phi_2$, one obtains the desired entangled state $|\Psi^+\rangle = \frac{1}{\sqrt{2}}(|01\rangle_m + |10\rangle_m)$. If different detectors clicked in the first and second rounds of entanglement generation, it can be easily shown that the resulting state is instead $|\Psi^-\rangle = \frac{1}{\sqrt{2}}(|01\rangle_m - |10\rangle_m)$.

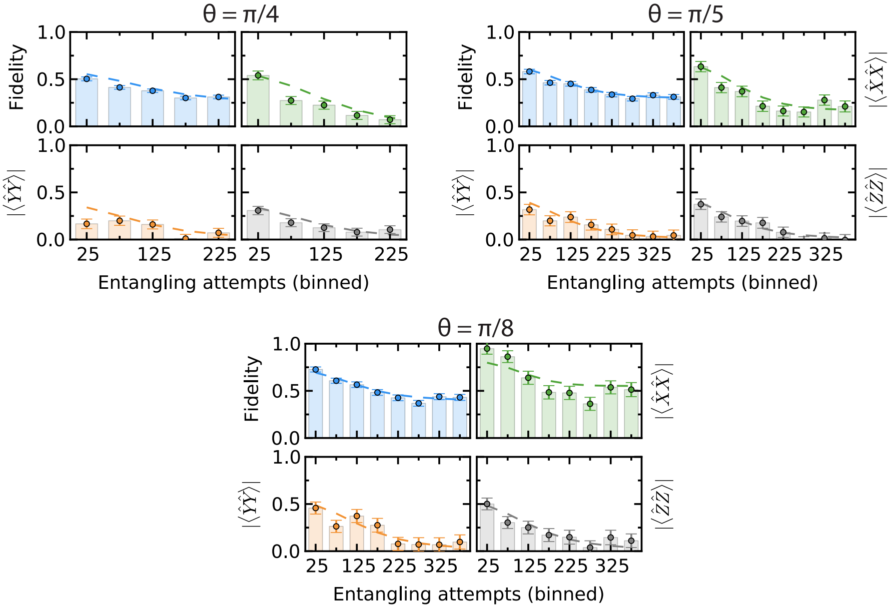

Figure 9.10 |Modeled (dashed lines) and measured correlations and state fidelities for all remaining excitation angles. See Fig. 9.4C for the data of $\theta = \pi/6$.

In reality, our experiment has further experimental imperfections beyond optical phase drifts, and so the state that is actually produced by the distillation protocol deviates from this ideal entangled state. In our experiment, the primary imperfections are given in Table 9.3, along with independent estimates of their magnitudes. We incorporate these parameters into an analytical model of the experiment, as is outlined in the following section.

The independently estimated parameters are not sufficient to completely explain the obtained state fidelities. We therefore introduce two phenomenological parameters: an initial amplitude damping implemented via a dephasing operation ($p = 0.08$) on the memory qubits and additional interferometric drift of the setup per entangling attempt. We fit our model to the combined dataset for all excitation angles. The resulting fit (3.4 mrad per entangling attempt) suggests an increased drift of the relative phase between both raw states which could be caused by a deviating interferometric stability at the time of data acquisition. In order to make a conservative comparison, these additional experimental infidelities are excluded for the modeled stored raw state that we compare with the distilled state in Fig. 9.4B. Fig. 9.10 shows the state decay for all measured superposition angles and the result from fitting the model to the combined data set.

9.9.7. EXPERIMENTAL MODEL

RAW STATE

The raw entangled state in our model is given by

$$\rho_{\mathrm{raw}} = p_{00}|00\rangle\langle 00| + p_{11}|11\rangle\langle 11| + |\Psi^{\pm}\rangle\langle\Psi^{\pm}| \tag{9.6}$$

where

$$|\Psi^{\pm}\rangle\langle\Psi^{\pm}| = \begin{pmatrix} \frac{1}{2}p_{\mathrm{s}}(p_{01}+p_{10}) & 0 & 0 & 0 \\ 0 & p_{01}(1-p_{\mathrm{s}}) & \pm\sqrt{V\,p_{01}\,p_{10}}\,(1-p_{\mathrm{s}})e^{\mathrm{i}\phi} & 0 \\ 0 & \pm\sqrt{V\,p_{01}\,p_{10}}\,(1-p_{\mathrm{s}})e^{-\mathrm{i}\phi} & p_{10}(1-p_{\mathrm{s}}) & 0 \\ 0 & 0 & 0 & \frac{1}{2}p_{\mathrm{s}}(p_{01}+p_{10}) \end{pmatrix}. \tag{9.7}$$

This state is parametrized by

$$\begin{aligned} p_{11} &= 2\cos^4\theta\, p_{\mathrm{dc}}\,(1-p_{\mathrm{dc}}) \\ p_{10} &= \sin^2\theta\,\cos^2\theta\,((1-p_{\mathrm{dc}})^2\,p_{\mathrm{d2}} + 2\,p_{\mathrm{dc}}(1-p_{\mathrm{dc}})(1-p_{\mathrm{d2}})) \\ p_{01} &= \sin^2\theta\,\cos^2\theta\,((1-p_{\mathrm{dc}})^2\,p_{\mathrm{d1}} + 2\,p_{\mathrm{dc}}(1-p_{\mathrm{dc}})(1-p_{\mathrm{d1}})) \\ p_{00} &= \sin^4\theta\,((1-p_{\mathrm{dc}})^2(p_{\mathrm{d1}}(1-p_{\mathrm{d2}}) + p_{\mathrm{d2}}(1-p_{\mathrm{d1}})) + 2(1-p_{\mathrm{dc}})\,p_{\mathrm{dc}}(1-p_{\mathrm{d1}})(1-p_{\mathrm{d2}})). \end{aligned} \tag{9.8}$$

Param.	Value	Description
V	0.72	Indistinguishability between photons produced by the two NVs (Section 9.9.8).
p_{s}	0.01	Failure probability for classical spin-photon correlations[28].
p_{d1}	$8 \cdot 10^{-4}$	Single-photon detection probability after the central beam splitter, given that NV_1 is in $\|0\rangle$.
p_{d2}	$4 \cdot 10^{-4}$	Single-photon detection probability after the central beam splitter, given that NV_2 is in $\|0\rangle$.
p_{dc}	$2.5 \cdot 10^{-6}$	Dark count probability within detection window.
p_{gate}	0.0163	Error rate for electron-nuclear-spin two-qubit gates.
p_{proj}	0.985	Probability that the NV is left in $\|m_s = 0\rangle$, given the corresponding SSRO measurement result.
ϕ		First entangled state phase. The ideal protocol is insensitive to this parameter.
$\Delta\phi$	Section 9.9.9	Difference in phase between the two entangled states.
p_{m}	Sections 9.9.1 & 9.9.7	Memory dephasing probability during the interval between the generation of the two entangled states.

Table 9.3 |Measured experimental parameters used in our error model.

PROTOCOL

We model the swap gate that transfers the entangled state to the nuclear spins at each node by assuming that this gate causes random two-qubit Pauli noise with a probability $2 \times p_{\text{gate}}$. As in the experiment, this swap gate stores the entangled state in a rotated basis, such that the initial electronic state is transformed by a Hadamard gate as it is stored.

After this swap, the stored state experiences dephasing noise due to the second round of entanglement attempts. This is modeled by applying a $R_z(\pi)$ rotation independently to each of the stored states with a probability p_{m}. For Gaussian dephasing noise (such as decoherence), in which the fidelity of a stored state degrades as $F = \frac{1}{2}(1 + e^{-\frac{n^2}{2\tau^2}})$, $p_{\text{m}} = 1 - F \equiv \frac{1}{2}(1 - e^{-\frac{n^2}{2\tau^2}})$. For exponential damping noise (such as the stochastic repumping process used to reset our NV spins[27]) , p_{m} is given by $\frac{1}{2}(1 - e^{-\frac{n}{\tau}})$. Besides the induced dephasing due to the electron spin reset, we find that our feedback resolution is limited by systematic drifts of the required feedback phase per entangling attempt. Analyzing all calibration data results in an additional phase uncertainty of 0.87(3) mrad per entangling trial per node which is taken into account via a Gaussian decay channel.

We introduce a second raw entangled state, modeling the optical phase drift since the first state was generated by applying a $R_z(\pi)$ rotation to one of the qubits with a probability determined by the expected phase drift $\Delta\phi$ per attempt (Section 9.9.9).

The distillation operation consists of another two-qubit gate between the electron and the nuclear spin at each node, and again is modeled by assuming random two-qubit Pauli noise, this time with a probability p_{gate}. Finally, we calculate the state of the nuclear spins after a noisy measurement of the electron spin, with a failure probability given by p_{proj}.

9.9.8. TWO-PHOTON QUANTUM INTERFERENCE

We are able to estimate the degree of indistinguishability between the single photons emitted by each NV by aggregating the full set of detection events from the distillation data set. Using the same temporal filtering as for the distillation analysis, we calculate the number of events within this data set in which both APDs detect a photon within the same entanglement generation element. This is normalized by calculating the number of events in which one APD clicked in a given entanglement generation element, while the other APD clicked in the next entanglement generation element.

For fully distinguishable single-photon emission and balanced emission probabilities, the ratio r between coincident clicks to clicks in successive elements should be 0.5, while for fully indistinguishable photons no coincident clicks will be detected due to two-photon Hong-Ou-Mandel quantum interference[45]. This is because this quantum interference effect ensures that the two photons will always emerge from the same port of the beam splitter, and so both APDs will never click during the same round. For partially indistinguishable photons and again assuming balanced emission probabilities, r

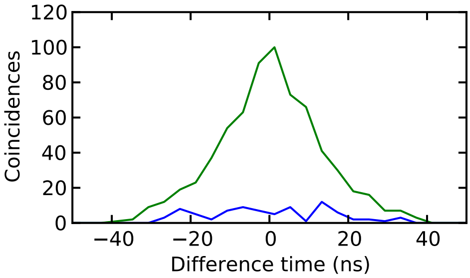

Figure 9.11 |Two-photon quantum interference between indistinguishable single photons leads to bunching at the output of a beam splitter This is reflected in a suppressed probability of detecting coincident clicks at each APD during the same entanglement generation element (blue). This interference is not present for events in which one APD clicks during one entanglement generation element, while the other APD clicks during the next entanglement generation element (green).

is related to the wave function overlap $V = \left|\langle\psi_a|\psi_b\rangle\right|^2$ by $V = (1-2r)$. Incorporating the effect of the known imbalance in emission probabilities in our experiment, we find $V = 0.72(3)$. This is substantially lower than measured in Refs.[24,28]. We hypothesize that this is due to fast spectral diffusion of one of our NVs, which is not picked up by our charge resonance checks as they confirm resonant conditions on a time scale of 100μs. In the future further insight into the emission properties of single NVs could be obtained by interfering photons from a single emitter in an unbalanced interferometer[46].

9.9.9. PHASE STABILITY

As mentioned in Section 9.9.7, in order to create the initial spin-photon entanglement, resonant laser pulses are used to selectively excite the $|m_s = 0\rangle$ state to a higher level; this excited state then spontaneously decays, emitting a single photon. In this way, the photon-number occupation of the emission optical mode becomes entangled with the state of the NV. This resonant excitation process imprints the phase of the excitation laser onto the resulting spin-photon state. As the optical mode propagates towards the beam splitter, it also picks up an additional phase that depends on the optical path length that it traverses. After the optical modes from each NV interfere on the beam splitter and a photon is detected, the resulting spin-spin entangled state has a phase ϕ that depends on the total phase difference between the two spin-photon states.

Since we derive the resonant excitation pulses from the same laser, the full setup effectively acts as an optical interferometer (Fig 9.12A), starting from where the excitation pulses are split, and ending at the beam splitter at which the photons are interfered. The phase sensitivity of the resulting spin-spin entangled state is the same as for classical light traversing the same paths, but reflecting off of the NV sample instead of exciting the NV. By probing the stability of the interferometer using classical light, we can therefore determine the expected difference between ϕ_1 and ϕ_2 for subsequent entangled states. This allows us to determine how much the interferometer phase stability will impact the fidelity of the resulting distilled state.

Fig. 9.12B shows measurements of the output intensity of one port of the beam splitter, measured using a photodiode. As the interferometer is not phase stabilized, the output fluctuates over time. The noise spectral density for this signal is shown in Fig. 9.12C. Several clear resonances can be seen below 1 kHz; these dominate the dynamics of the interferometer.

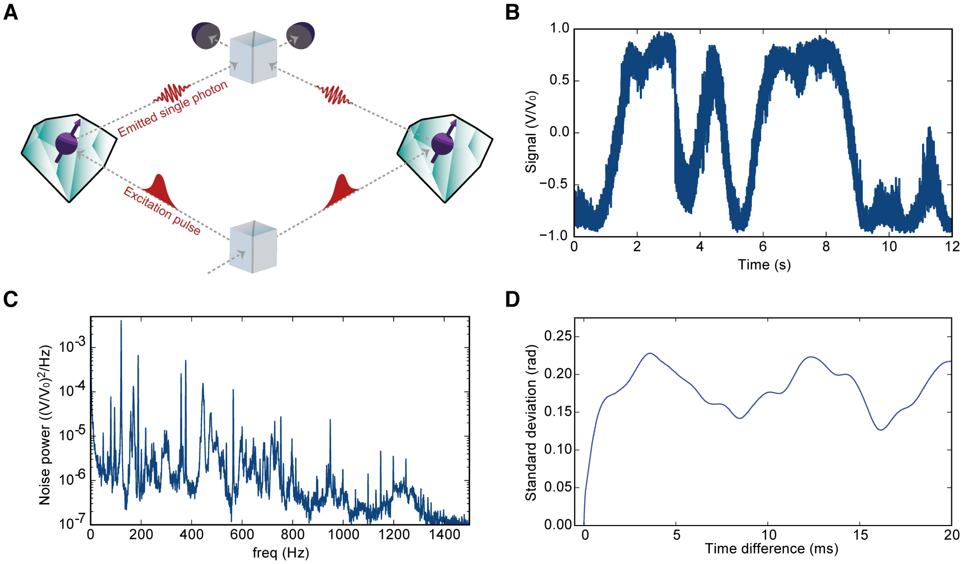

Figure 9.12 |(**A**) The entanglement protocol imprints a phase on the entangled state that depends on the relative phase of the excitation laser pulses, as well as the difference in the phase acquired by the single photons as they propagate from the NVs to a central beam splitter This creates an effective interferometer, starting where the excitation pulses are separated at an initial beam splitter, and ending at the final beam splitter. (**B**) Classical light traversing the interferometer, but reflecting off of the NV sample instead of exciting the NV, is subject to the same phase fluctuations as the entangled states. This allows us to easily probe the expected phase stability of the protocol. Here classical light is inserted into the interferometer, and the output intensity is measured at one output port of the final beam splitter using a photodiode. Fluctuations in the output intensity over time are seen due to changes in the relative path length. (**C**) Noise spectral density of the interferometer output showing many several sharp resonances below 1 kHz. (**D**) Standard deviation of the inferred phase difference between sets of sample points separated by a fixed time difference. As can be seen, a phase difference is rapidly acquired within about 1 ms, but then the dynamics are dominated by a few resonant frequencies that periodically increase and then decrease the phase difference.

A useful measure for quantifying the phase stability of the interferometer is the stan-

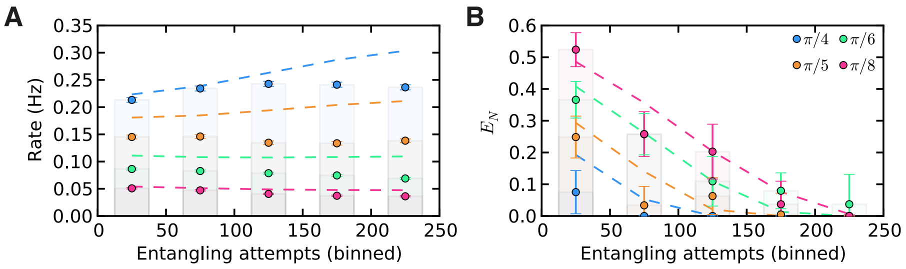

Figure 9.13 |(**A**) The corresponding estimated protocol success rate (error bars are smaller than the points). Also shown in both plots are the predictions of our model (dashed lines). We partially attribute the deviation of the model to ionization of the NV electron spin while trying to generate entanglement. (**B**) The experimentally estimated distillable entanglement E_N of the distilled state as a function of θ and elapsed second round entanglement generation attempts.

dard deviation $\Delta\phi$ of the phase difference $\delta\phi(\tau) = \phi(t+\tau) - \phi(t)$ between two sample points separated by a fixed time difference τ, measured for all t in the sample. This is plotted in Fig. 9.12D. As can be seen, the standard deviation $\Delta\phi$ grows rapidly for the first millisecond, and then oscillates more slowly. These oscillations are caused by several resonant frequencies that dominate the noise spectrum of the interferometer, as is shown in Fig. 9.12C.

Once the first entangled state is created, the swap operations take 0.961 ms. For the data of Fig. 9.12, this would lead to an initial phase deviation of $\Delta\phi \approx 0.18$ rad. Each entanglement generation attempt during the second stage takes 7μs. We do not try more than 500 times to generate an entangled state the second time, and so the phase deviation would not increase beyond $\Delta\phi \approx 0.24$ rad. Therefore, for the data in Fig. 9.12, we find an estimated dephasing probability of 0.018. Since the interferometer is not monitored during the experiment, these estimates can only serve as a guide. In our modeling we use the phase stability as a free parameter, fitting a linearly increasing phase deviation with $\Delta\phi = 0.49$ rad after 1 ms, which is larger but of the same order as that measured in Fig. 9.12.

9.9.10. EBIT RATE ESTIMATES

DISTILLATION

From our experimental data, we can determine the total number of successful events n_s, as well as the total number of entangling attempts made n_a. From these numbers and the duration of an entanglement attempt $t_e = 7\,\mu$s, we can estimate the instantaneous rate $r = n_s/(n_a t_e)$ at which the protocol succeeds (i.e. the rate assuming that both NVs are on resonance, a condition which is necessary for any network protocol). As shown in Fig. 9.13A, this rate is a function of the superposition angle θ.

The distillable entanglement of a state ρ is upper bounded by its logarithmic negativity $E_N(\rho)$, an easily computable entanglement measure[47]. $E_N(\rho)$ is determined by the sum of the singular values of the partial transpose of ρ. We do not have access to the full density matrix ρ for all of the θ values that we measure. However, we can make an estimate of $E_N(\rho)$ by assuming that all off-diagonal elements of the density matrix are zero, apart from the coherence c between $|01\rangle$ and $|10\rangle$. This assumption is supported by our measurements of the density matrix for $\theta = \pi/6$ (shown in Fig. 9.4A), in which other off-diagonal terms were indeed negligible. Under this assumption, it is possible to calculate $E_N(\rho)$ using only our measurements of the correlations $\langle \hat{X}\hat{X} \rangle$, $\langle \hat{Y}\hat{Y} \rangle$ and $\langle \hat{Z}\hat{Z} \rangle$. Parameterizing ρ as

$$\left(() \begin{matrix} 1-r-p_{11} & 0 & 0 & 0 \\ 0 & r-p_{10} & c & 0 \\ 0 & c^* & p_{10} & 0 \\ 0 & 0 & 0 & p_{11} \end{matrix} \right), \tag{9.9}$$

$$E_N(\rho) = \log_2 \left(r + \frac{1}{\sqrt{2}} \left(\sqrt{\alpha + (1-r)(1-r+\beta)} + \sqrt{\alpha + (1-r)(1-r-\beta)} \right) \right) \tag{9.10}$$

$$\text{where } \alpha = 2|c|^2 + 2p_{11}^2 - 2p_{11}(1-r), \quad \beta = \sqrt{4|c|^2 + (1-r-2p_{11})^2}.$$

The logarithmic negativity is plotted in Fig. 9.13B for different values of θ.

Multiplying the success rate by the distillable entanglement gives us the ebit rate. Since the number of ebits available depends on the number of second round entanglement attempts needed to succeed, we carry out this calculation for different sets of our experimental results, binned by the number of second round attempts. We choose bins separated by fifty entangling attempts. This represents a compromise between having enough experimental results in each bin to calculate the correlations with reasonable accuracy, while not averaging too broadly over the different outcomes.

EXPERIMENTAL MODEL

Independent measurements allow us to estimate the probabilities of detecting a single photon given that one or other of the NVs was in the $|0\rangle$ state (Table 9.3). From these probabilities, we can estimate the probability p_1 of an entanglement generation attempt succeeding in the first round of the protocol. This in turn allows us to estimate $p_2 = p_1(1-p_1)^{n-1}$, the probability of a second entanglement event occurring after a specified number of attempts n, given that the first round succeeded. In addition to these parameters, our model (Section 9.9.7) allows us to predict the probability of the local distillation gate succeeding, given the overall electron nuclear-spin state resulting from a specified number of second round entanglement generation attempts. Combining these numbers with the probability of a successful read-out after the distillation gate (0.9 on each side) gives us the average number of attempts (and therefore the time) necessary to produce a successful entanglement event. Our model also allows us to directly calculate $E_N(\rho)$ from the simulated density matrix ρ. The rate and E_N predictions of our model are plotted alongside the experimental data in Fig. 9.13. This information is used to provide the theoretical lines in Fig. 9.5.

COMPARISON TO BARRETT AND KOK PROTOCOL

The single-photon detection probabilities can also be used to estimate the rate that would be achieved for a conventional Barrett-Kok (BK) protocol[35] running on our experimental apparatus. Given these probabilities (Table 9.3), the BK success probability is given by $\frac{1}{2} p_{\mathrm{d1}} p_{\mathrm{d2}}$. As each entanglement attempts takes $7\,\mu s$, this gives a rate of 16 mHz.

In order to calculate the number of ebits available for the BK protocol, we assume that the generated state is perfect, apart from a reduced coherence $c = V/2$ resulting from the imperfect indistinguishability V of our photons. In this case

$$\begin{aligned} E_N(\rho) &= \log_2(1+2|c|) \\ &= \log_2(1+V). \end{aligned} \tag{9.11}$$

The estimated rate and number of ebits are combined to give the BK ebit rates shown in Fig. 9.5.

9.9.11. NUCLEAR INITIALIZATION AND READ-OUT SEQUENCES

Nuclear spins in each setup are initialized and read-out by employing conditional electron-nuclear gates and single-shot quantum measurements of the electron. Fig. 9.14 shows all relevant circuit diagrams for initialization and read-out of the nuclei. The directions of the rotations induced on the memory qubits by the controlled $\pm\pi/2$ gates are determined by the communication qubit states.

Besides using established gate circuits for the tomography of single nuclear spins, we employ a sequential tomography for the combined electron-nuclear Bell states of Fig. 9.2. Here, we first rotate the electron spin by applying one of six suitable microwave pulses followed by a single-shot read-out measurement. We continue with the tomography sequence of the nuclear spin if the electron was successfully measured to be in $|m_s = 0\rangle$. This guarantees a high projectivity of the NV spin and allows for the implementation of the nuclear-spin read-out sequence with high fidelity.

9.9.12. P-VALUES FOR DISTILLATION

As noted in the main text, successful distillation requires that the distilled state is increased in fidelity as compared to the raw states. In order to provide evidence that this is the case, we calculate P-values for the measured state fidelities shown in Fig. 9.4B (replotted in Fig. 9.15), taking as a null hypothesis that the states do not show an increase in fidelity from the highest fidelity raw state. These P-values are given in Table 9.4.

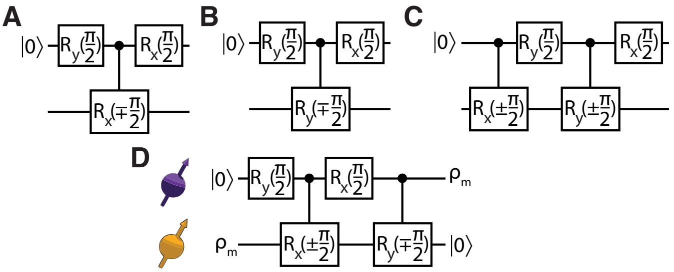

Figure 9.14 |Panels **A**-**C** Read-out sequences of the nuclear spin expectation values $\hat{X}$, $\hat{Y}$, $\hat{Z}$[26] . All gate circuits are followed by a single-shot measurement of the electron spin. (**D**) Nuclear spin initialization sequence. $\rho_{\mathrm{m}} = \mathbb{I}/2$ is the mixed state.

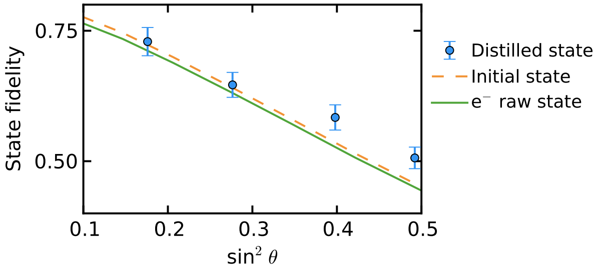

Figure 9.15 |Distilled state fidelities (blue) and communication qubit raw state fidelities (green) reproduced from Fig. 9.4B. Also shown is the best-case fidelity of the raw state if the optical phase was perfectly known at all points of the protocol (dashed orange).

9

Also calculated are the P-values showing evidence for distillation in the most stringent possible case, in which the raw states were generated in a completely stable interferometer with no phase drifts whatsoever (dashed orange line in Fig. 9.15). In this case the only imperfections on the raw states result from imperfect two-photon quantum interference, imbalanced optical losses, and dark counts. All of these quantities are independently characterized for our experiment.

9.9.13. MEASURED DENSITY MATRICES

For completeness we present all numerical entries of all measured density matrices in this section. The matrices were directly reconstructed from the measurement outcomes via linear inversion. From Fig. 9.2B for node A:

$\sin^2(\theta)$	P-value comm. qubit state	P-value phase-stable state
$\pi/8$	0.26	0.41
$\pi/6$	0.26	0.41
$\pi/5$	0.0095	0.023
$\pi/4$	0.0032	0.0086

Table 9.4 |P-values for the null hypothesis that the final state fidelity is not increased from the highest-fidelity raw state.

$$\begin{pmatrix} 0.06(1) & 0.06(1)+i0.00(1) & 0.02(1)-i0.02(1) & 0.01(1)+i0.00(1) \\ 0.06(1)+i0.00(1) & 0.48(1) & -0.48(1)+i0.00(1) & -0.01(1)+i0.01(1) \\ 0.02(1)+i0.02(1) & -0.48(1)+i0.00(1) & 0.47(1) & -0.03(1)+i0.00(1) \\ 0.01(1)+i0.00(0) & -0.01(1)-i0.01(1) & -0.03(0)+i0.00(1) & -0.01(1) \end{pmatrix}. \tag{9.12}$$

and node B:

$$\begin{pmatrix} 0.00(1) & 0.01(1)+i0.02(1) & 0.00(1)-i0.02(1) & 0.00(1)+i0.01(1) \\ 0.01(1)-i0.02(1) & 0.51(1) & -0.49(1)-i0.02(1) & -0.01(1)+i0.03(1) \\ 0.00(1)+i0.02(1) & -0.49(1)+i0.02(1) & 0.47(1) & 0.00(1)-i0.02(1) \\ 0.00(1)-i0.01(1) & -0.01(1)-i0.03(1) & 0.00(1)+i0.02(1) & 0.02(1) \end{pmatrix}. \tag{9.13}$$

The density matrices of Fig. 9.4A are given in the following:

$$\begin{pmatrix} 0.11(2) & -0.01(3)+i0.02(3) & 0.03(3)+i0.01(3) & 0.00(3)-i0.02(4) \\ -0.01(3)-i0.02(3) & 0.43(2) & 0.20(3)+i0.03(4) & -0.04(3)-i0.03(3) \\ 0.03(3)-i0.01(3) & 0.20(3)-i0.03(4) & 0.46(2) & 0.07(3)-i0.05(3) \\ 0.00(3)+i0.02(4) & -0.04(3)+i0.03(3) & 0.07(3)+i0.05(3) & 0.00(2) \end{pmatrix} \tag{9.14}$$

$$\begin{pmatrix} 0.13(2) & 0.06(3)-i0.05(3) & 0.02(3)+i0.05(3) & 0.00(3)+i0.05(3) \\ 0.06(3)+i0.05(3) & 0.40(2) & -0.21(3)+i0.01(3) & -0.04(3)-i0.03(3) \\ 0.02(3)-i0.05(3) & -0.21(3)-i0.01(3) & 0.45(2) & 0.02(3)-i0.01(3) \\ 0.00(3)-i0.05(3) & -0.04(3)+i0.03(3) & 0.02(3)+i0.01(3) & 0.02(2) \end{pmatrix} \tag{9.15}$$

Numbers in brackets represent one standard deviation.

REFERENCES

[1] H. J. Kimble, *The quantum internet,* Nature **453**, 1023 (2008).

[2] M. Ben-Or, C. Crepeau, D. Gottesman, A. Hassidim and A. Smith, *Secure Multiparty Quantum Computation with (Only) a Strict Honest Majority,* in *47th Annual IEEE Symposium on Foundations of Computer Science* (2006).

[3] A. Broadbent, J. Fitzsimons and E. Kashefi, *Universal Blind Quantum Computation,* in *50th Annual IEEE Symposium on Foundations of Computer Science* (2009).

[4] L. Jiang *et al.*, *Quantum repeater with encoding,* Physical Review A **79**, 032325 (2009).

[5] A. Ekert and R. Renner, *The ultimate physical limits of privacy,* Nature **507**, 443 (2014).

[6] J. I. Cirac, A. K. Ekert, S. F. Huelga and C. Macchiavello, *Distributed quantum computation over noisy channels,* Physical Review A **59**, 4249 (1999).

[7] D. Gottesman, T. Jennewein and S. Croke, *Longer-Baseline Telescopes Using Quantum Repeaters,* Physical Review Letters **109**, 070503 (2012).

[8] N. H. Nickerson, J. F. Fitzsimons and S. C. Benjamin, *Freely Scalable Quantum Technologies Using Cells of 5-to-50 Qubits with Very Lossy and Noisy Photonic Links,* Physical Review X **4**, 041041 (2014).

[9] P. Kómár *et al.*, *A quantum network of clocks,* Nature Physics **10**, 582 (2014).

[10] C. H. Bennett *et al.*, *Purification of Noisy Entanglement and Faithful Teleportation via Noisy Channels,* Physical Review Letters **76**, 722 (1996).

[11] D. Deutsch *et al.*, *Quantum Privacy Amplification and the Security of Quantum Cryptography over Noisy Channels,* Physical Review Letters **77**, 2818 (1996).

[12] W. Dür, H.-J. Briegel, J. I. Cirac and P. Zoller, *Quantum repeaters based on entanglement purification,* Physical Review A **59**, 169 (1999).

[13] L. Childress, J. M. Taylor, A. S. Sørensen and M. D. Lukin, *Fault-Tolerant Quantum Communication Based on Solid-State Photon Emitters,* Physical Review Letters **96**, 070504 (2006).

[14] R. Reichle *et al.*, *Experimental purification of two-atom entanglement,* Nature **443**, 838 (2006).

[15] J.-W. Pan, S. Gasparoni, R. Ursin, G. Weihs and A. Zeilinger, *Experimental entanglement purification of arbitrary unknown states,* Nature **423**, 417 (2003).

[16] P. G. Kwiat, S. Barraza-Lopez, A. Stefanov and N. Gisin, *Experimental entanglement distillation and 'hidden' non-locality,* Nature **409**, 1014 (2001).

[17] J.-W. Pan *et al.*, *Multiphoton entanglement and interferometry,* Reviews of Modern Physics **84**, 777 (2012).

[18] D. L. Moehring *et al.*, *Entanglement of single-atom quantum bits at a distance,* Nature **449**, 68 (2007).

[19] J. Hofmann *et al.*, *Heralded Entanglement Between Widely Separated Atoms,* Science **337**, 72 (2012).

[20] H. Bernien *et al.*, *Heralded entanglement between solid-state qubits separated by three metres,* Nature **497**, 86 (2013).

[21] A. Narla *et al.*, *Robust Concurrent Remote Entanglement Between Two Superconducting Qubits,* Physical Review X **6**, 031036 (2016).

[22] A. Delteil *et al.*, *Generation of heralded entanglement between distant hole spins,* Nature Physics **12**, 218 (2016).

[23] R. Stockill *et al.*, *Phase-Tuned Entangled State Generation between Distant Spin Qubits,* Physical Review Letters **119**, 010503 (2017).

[24] W. Pfaff *et al.*, *Unconditional quantum teleportation between distant solid-state quantum bits,* Science **345**, 532 (2014).

[25] D. Hucul *et al.*, *Modular entanglement of atomic qubits using photons and phonons,* Nature Physics **11**, 37 (2015).

[26] J. Cramer *et al.*, *Repeated quantum error correction on a continuously encoded qubit by real-time feedback,* Nature Communications **7**, 11526 (2016).

[27] A. Reiserer *et al.*, *Robust Quantum-Network Memory Using Decoherence-Protected Subspaces of Nuclear Spins,* Physical Review X **6**, 021040 (2016).

[28] B. Hensen *et al.*, *Loophole-free Bell inequality violation using electron spins separated by 1.3 kilometres,* Nature **526**, 682 (2015).

[29] L. Slodička *et al.*, *Atom-Atom Entanglement by Single-Photon Detection,* Physical Review Letters **110**, 083603 (2013).

[30] M. S. Blok *et al.*, *Manipulating a qubit through the backaction of sequential partial measurements and real-time feedback,* Nature Physics **10**, 189 (2014).

[31] T. H. Taminiau, J. Cramer, T. van der Sar, V. V. Dobrovitski and R. Hanson, *Universal control and error correction in multi-qubit spin registers in diamond,* Nature Nanotechnology **9**, 171 (2014).

[32] L. Jiang *et al.*, *Coherence of an Optically Illuminated Single Nuclear Spin Qubit,* Physical Review Letters **100**, 073001 (2008).

[33] E. T. Campbell and S. C. Benjamin, *Measurement-Based Entanglement under Conditions of Extreme Photon Loss,* Physical Review Letters **101**, 130502 (2008).

[34] C. Cabrillo, J. I. Cirac, P. García-Fernández and P. Zoller, *Creation of entangled states of distant atoms by interference,* Physical Review A **59**, 1025 (1999).

[35] S. D. Barrett and P. Kok, *Efficient high-fidelity quantum computation using matter qubits and linear optics,* Physical Review A **71**, 060310 (2005).

[36] D. J. Christle *et al.*, *Isolated electron spins in silicon carbide with millisecond coherence times,* Nature Materials **14**, 160 (2015).

[37] C. Monroe and J. Kim, *Scaling the Ion Trap Quantum Processor,* Science **339**, 1164 (2013).

[38] G. Balasubramanian *et al.*, *Ultralong spin coherence time in isotopically engineered diamond,* Nature Materials **8**, 383 (2009).

[39] P. C. Maurer *et al.*, *Room-Temperature Quantum Bit Memory Exceeding One Second,* Science **336**, 1283 (2012).

[40] A. M. Tyryshkin *et al.*, *Electron spin coherence exceeding seconds in high-purity silicon,* Nature Materials **11**, 143 (2012).

[41] A. Faraon, P. E. Barclay, C. Santori, K.-M. C. Fu and R. G. Beausoleil, *Resonant enhancement of the zero-phonon emission from a colour centre in a diamond cavity,* Nature Photonics **5**, 301 (2011).

[42] A. Sipahigil *et al.*, *An integrated diamond nanophotonics platform for quantum-optical networks,* Science **354**, 847 (2016).

[43] N. Kalb *et al.*, *Experimental creation of quantum Zeno subspaces by repeated multi-spin projections in diamond,* Nature Communications **7**, 13111 (2016).

[44] L. Robledo *et al.*, *High-fidelity projective read-out of a solid-state spin quantum register,* Nature **477**, 574 (2011).

[45] C. K. Hong, Z. Y. Ou and L. Mandel, *Measurement of subpicosecond time intervals between two photons by interference,* Physical Review Letters **59**, 2044 (1987).

[46] T. Legero, T. Wilk, M. Hennrich, G. Rempe and A. Kuhn, *Quantum Beat of Two Single Photons,* Physical Review Letters **93**, 070503 (2004).

[47] M. B. Plenio, *Logarithmic Negativity: A Full Entanglement Monotone That is not Convex,* Physical Review Letters **95**, 090503 (2005).

10

CONCLUSIONS AND OUTLOOK

10.1. SUMMARY

The experimental demonstrations in this thesis cover multi-qubit control as well as the exploration of three different entangling schemes. We summarize the results of this thesis organized by chapter.

In **Chapter 3** we show that single NV centres act as a quantum bus that coherently connects several nuclear spins. A single NV centre is used to perform multi-partite quantum nondemolition measurements of up to three nuclear spins and thus invoke the quantum Zeno effect.

Chapter 4 theoretically investigates and **Chapter 5** experimentally demonstrates the use of nuclear spins as quantum memories in an NV-based quantum network setting. We find that weakly-coupled nuclear spins constitute memories that can withstand hundreds of entangling attempts.

Chapter 6 experimentally revisits nuclear spin quantum memories for quantum networks by isolating and investigating individual sources of decoherence. We find that the memory robustness can be enhanced by more than an order of magnitude when realizing improved experimental control or time-tailored entangling sequences.

Chapter 7 uses a two-node quantum network and a two-photon entangling scheme to provide strong evidence that local-realist models are incompatible with the obtained measurement outcomes in a loophole-free manner.

Chapter 8 expands our toolbox of entangling schemes by realizing an efficient single-photon entangling protocol. This means that the entangling rate on our network significantly surpasses the decoherence rate of an entangled state which in turn allows for the deterministic delivery of entangled states.

Chapter 9 realizes a memory-assisted remote entangling scheme. This scheme requires two raw input states for the creation of a single entangled state of higher fidelity thus demonstrating entanglement distillation.

10.2. EXPERIMENTAL PLATFORMS FOR QUANTUM NETWORKS

Quantum networks will be a universal tool to realize quantum information protocols. Such a network is composed of nodes that share a complex many-body quantum state by receiving, manipulating and sending quantum information with high fidelity and efficiency. This concept has sparked a race across many experimental platforms to realize the ultimate quantum network node. Ideally, a network node fulfils the following criteria:

- Efficient optical interface with high photon-extraction efficiency.
- Emission or conversion of emission into the telecom band for low-loss photon

transmission over large distances.

- High-quality quantum control and interfacing to memory qubits that can withstand many entangling attempts.
- Operation at liquid-helium temperature or above (for reasons of experimental simplicity).

In the following we give an overview of the contenders at the forefront of quantum networks.

Individual *trapped ions* are one of the prime candidates for quantum networks and quantum computation[1,2]. In particular, trapped ions were the first system to demonstrate the generation of heralded remote entanglement[3]. Meanwhile significant advances have led to entangling rates on the order of ∼ Hz[4]. In contrast to NV-based systems, there is no always-on interaction that would deteriorate adjacent quantum memories. Instead interactions are enabled by laser-driven gates that exploit the mutual coulomb interaction between the ions. However, global disturbances by external control fields that are resonant with all ions have to be mitigated by the use of mixed atomic isotopes or species with different optical resonances in one trap[5–7]. This adds to the required experimental complexity per network node. Besides, there are ongoing efforts to combine trapped ions with an efficient cavity-based photonic interface[8,9].

Individual *trapped atoms* operate in a similar manner to their ionic counterpart and have recently been used to demonstrate the loophole-free violation of Bell's inequality[10,11]. Interactions between an array of neutral atoms are technically demanding yet realizable via Rydberg blockade[12], exchange interaction in optical tweezers[13] or by reflecting photons off an optical cavity to which all addressed atoms couple[14]. Especially the latter approach has synergies with quantum networks since the optical interface of the atoms is already enhanced by the cavity[15]. Using this reflection-based mechanism[16], which has also been demonstrated in microscopic cavity architectures[17–19], could propel this system from initial post-selected entanglement generation procedures[20] to heralded state transfers[21] and network protocols. Yet for conceptual multi-qubit network nodes a suitable mechanism of hiding quantum information within memory qubits from external light fields remains elusive.

As compared to trapped individual particles, solid-state based systems provide the advantage of lower experimental overhead because the system of interest is already localized but in turn is usually subject to unwanted interactions with the host material. *Quantum dots* are conveniently incorporated into on-chip cavities allowing them to access the same tools as trapped neutral atoms[22]. Rapid heralded entanglement generation[23,24] and heralded photonic absorption[25] have been demonstrated with such systems but the coherence time of these systems needs improvement to allow for multiple entangled links. *Rare-earth ion doped crystals* have been a workhorse as ensemble-based optical quantum memories[26]. Recently this system has demonstrated long coherence times[27,28] and reduced ensemble sizes by coupling to photonic-crystal cavities[29] bringing efficient individual addressing within reach[30].

A large variety of optically-active *single defect centres* in the solid-state are currently being investigated[31–35]. Arguably the most prominent contenders for the title of most fruitful quantum network node among these systems are the negatively-charged silicon vacancy (SiV) in diamond[36] and NVs as discussed in this thesis. Being unaffected by local charge fluctuations and having most of the emission unaccompanied by phonons grants SiV a, in principle, superior optical interface. The dominant path from the optically excited state is however non-radiative, thus limiting the photon output and elevating requirements on cavity-based implementations[37,38]. Besides making full use of SiV as a qubit requires environmental temperatures around ~ 100 mK to obtain long coherence times[39,40].

At the time of writing this thesis, none of the described platforms has gone beyond elementary point-to-point quantum networks. In the following sections we describe near-term milestones on the road towards NV-based networks. We finally elucidate the main challenges for the NV platform and point out concrete routes towards improved performance.

10.3. NV-BASED THREE-NODE NETWORKS

It is clear that the next conceptual step for NV-based quantum networks is the establishment of multi-node entanglement. Having realized a third node in our lab a first benchmark for the network performance can be obtained in a three-fold photon interference experiment. To this end one would use a fiber-based beamsplitter with three in- and outputs[41,42]. The entanglement generation would work in a similar fashion to the single-photon scheme used in Chapter 8, therefore generating a W-state. The requirements on the experimental apparatus are essentially the same as in Chapter 8 with the additional difficulty that two path length differences have to stabilized instead of one. Such an experimental set-up would also allow the measurement of triad phases with true single-photons (albeit with very low success probabilities $\sim 10^{-9}$).

This single-click state generation scheme can be extended to more nodes and therefore larger networks. We additionally provide geometries in Fig. 10.1A which may substitute the multi-port inteference devices with a regular chain of beam-splitters. Such a beam-splitter-based realization is commercially available for any number of nodes which is in stark contrast to, for instance, interference devices with four input and output ports. For larger network systems active switching instead of passive optics networks might be desirable. The generated states are ideally of the form $|\mathrm{W_N}\rangle = \sum_i |0_1 \cdots 1_i \cdots 0_N\rangle / \sqrt{N}$. Due to photon loss and the nature of our single-click entangling scheme the created states will have imperfections as a function of the initial bright state population α (see 2). We calculate the fidelity of the expected state with the ideal state as a function of α and observe that high fidelity state generation is possible for moderate values of α and several network nodes (Fig. 10.1B).

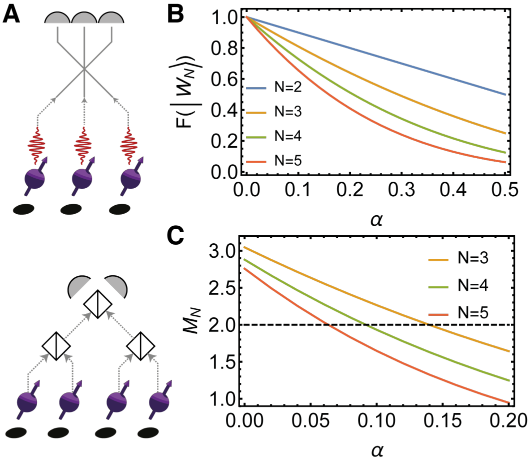

Figure 10.1 | (**A**) Linear optics networks for the generation of N-partite W states $|\mathrm{W_N}\rangle = \sum_i |0_1 \cdots 1_i \cdots 0_N\rangle / \sqrt{N}$ for three (top) and four (bottom) network nodes. (**B**) Upper bound on the fidelity of the generated state with an ideal W state (see also Chapter 8 for experimental results on 2 nodes). All fidelities are given for a varying network size and as a function of the initial bright state probability α (see Sec. 2.4). Note that the success rate of this scheme will be just as high as the scheme used in Ch. 8 since it still only requires a single detection event to herald entanglement. (**C**) We additionally give the resulting sum of the third to fifth-order Mermin polynomial $\mathrm{M_N}$ to violate an N-partite Bell-type inequality with a normalized classical threshold value of 2 (dashed line)[43].

A validation for the generation of entanglement is the violation of Bell's inequality. Leaping from two-partite to multi-partite systems allows for an experimental violation of Bell-type inequalities for multi-partite systems[44]. To this end, we investigate the performance of the W states with Bell-type inequalities that are built up from Mermin polynomials M_N, see Ref. 45. These polynomials rely on measurements of two dichotomic observables A_j and A'_j with outcomes a_j and a'_j where the subscript j is run over all participating network nodes. M_N is recursively defined as

$$M_N = \frac{1}{2} M_{N-1}(a_N + a'_N) + M'_{N-1}(a_N - a'_N) \tag{10.1}$$

with $M_1 = a_1$ and using M'_k as a shorthand notation for the kth order polynomial that has all a and a' exchanged. Experimentally one measures the expectation values of all correlators in M_N with the quantum mechanical bound $M_N^{QM} = 2^{N-1}$ and the bound according to local hidden-variable models (LHVM) $M_{N,\mathrm{odd}}^{lv} = 2^{(N-1)/2}$ for N odd and $M_{N,\mathrm{even}}^{lv} = 2^{N/2}$. The LHVM bounds are maximally violated by GHZ states but can also be overcome by the type of W state considered here. We estimate the optimal outcomes for M_N by considering the measurement operators $A = \sin\theta\,\sigma_\mathrm{x} + \cos\theta\,\sigma_\mathrm{z}$ and $A' = \sin\theta'\,\sigma_\mathrm{x} + \cos\theta'\,\sigma_\mathrm{z}$ and numerically optimizing M_N for the angles θ and θ' (Fig. 10.1C).

Creating three-node set-ups with current devices would additionally open up the ex-

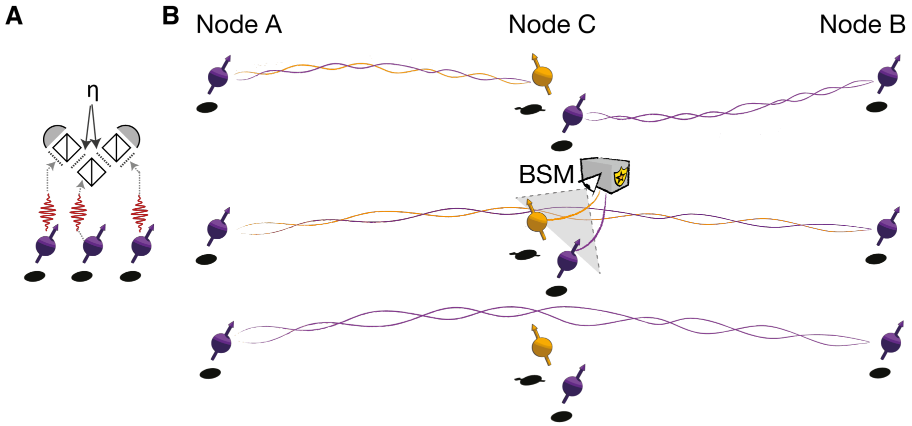

Figure 10.2 | (**A**) Linear optics network for the realization of a quantum repeater type experiment with neutral density filters to simulate the channel loss η. (**B**) Schematic sequence to perform entanglement swapping in a three-node network. Node C establishes entangling links with nodes A and B via the single-photon entangling protocol (Ch. 8) over a total channel transmittance η. Once successful, a local Bell-state-measurement (BSM) at node C creates an entangling link between nodes A and B over a channel with a total transmittance η^4.

ploration of quantum repeater schemes[46]. Quantum key distribution, enabling secure communication, is one of the primary applications of quantum networks. Simple point-to-point quantum key distribution schemes[47] suffer from transmission probabilities that scale exponentially with distance therefore strongly hampering success probabilities at large distances. This exponential scaling is encompassed in the Takeoka-Guha-Wilde (TGW) bound[48] which describes the maximum extractable bits per channel use for a given channel transmittance η. Note that this bound was later improved upon by Pirandola et al.[49]. Quantum repeaters can surpass this bound by building a linear chain of entangling links between two communicating parties.

Once the entangled links A↔C and C↔B are established, local entanglement swapping can create a direct entangling link between the communicating parties therefore conceptually overcoming the exponential scaling with distance (Fig. 10.2). More specifically, a quantum repeater is demonstrated if the delivered bit number per channel use surpasses the TGW bound at the measured loss rate[50]. Theoretical proposals have already been analyzed, taking into account experimental details, for a memory-assisted source-in-the-middle situation[51] and more optimistic parameters for cavity-based systems[52].

10

We argue that a three-node experiment which builds on the theoretical results of ref. 51 with current NV technology might already be on the verge of beating the TGW bound. The main ingredients here are a central repeater node with a quantum memory that allows for thousands of entangling attempts before decohering. This could be realized by using isotopically purified diamond samples which allow access to ^{13}C spins with very weak coupling strengths ($\sim 1\,$kHz instead of $\sim 20\,$kHz)[53,54] or by using decoherence-protected subspaces as demonstrated in Chapter 5. One would then combine the techniques shown in Chapters 9,8 to demonstrate all ingredients of a quantum repeater in one experiment (see Fig. 10.2B). In addition, the set-up could operate in a benchmarking mode where the rate of direct communication between Nodes A and B is compared to the rate of success in the quantum repeater setting for a given total channel loss[55].

10.4. FUTURE DIRECTIONS

Besides the near-term goal of three-node networks there are two complementary visions for NV centres in quantum computation and quantum networks. Individual small-scale ion-trap quantum nodes[56,57] and NVs acting as multi-qubit registers[58] have already performed simple computational algorithms. The two main ideas to scale these systems rely either on increasing the number of qubits in a monolithic architecture or on linking few-qubit nodes in a distributed fashion. Recent theoretical developments in distributed quantum computation point towards surface-code-like architectures where each cell — or node — houses multiple qubits[59,60]. Cells are linked up by photonic channels and stabilizer measurements between cells are performed on shared GHZ states during each clock cycle. Such an architecture can tolerate infidelities of the entangling links on the 10 %-level while requiring intra-node gate infidelities below 1 %. Making such an NV-based computing architecture would require additional improvements in the entangling rate and ^{13}C memory resilience.

Alternatively NVs can form the backbone of a long-distance quantum communication network which may be used to demonstrate several networking protocols that have so far remained elusive or were only realized in a laboratory setting[61–64]. Such a network would stretch across tens of kilometres, which is below the largest achieved distances for simple QKD schemes[65], but would provide desirable additional functionalities due to the ability to store and manipulate quantum information. The main challenge here is to keep entangling rates high despite the increased distance and therefore channel loss. One particularly promising technology to overcome the signal attenuation of 8 db/km at a wavelength of 637 nm[66] is to convert NV-emitted photons to telecommunication wavelengths[67] which may yield losses as low as 0.2 db/km[68].

Distributed computation and long-distance quantum communication with NVs will require further sophistication of the experimental platform. In the following sections we will target key parameters of the system and propose research directions which promise improvement. We group advancements according to their most beneficial properties, but note that the proposed technologies may yield progress across several key parameters of NV-based systems.

10.4.1. IMPROVING THE QUANTUM LINK EFFICIENCY

The quantum link efficiency is the product of the entangled-state decoherence rate and the entangling rate itself. The link efficiency gives the number of entangled states one can create within the lifetime of another entangled state. It is therefore a benchmark number for the achievable complexity within a quantum network. Note that link efficiencies commonly relate to time scales but a redefinition for multi-qubit nodes might replace decoherence rates with the number of entangling attempts a stored entangled state survives. While Chapter 8 demonstrated link efficiencies up to 8, further improvement is required.

Optical cavities have been a widespread tool to realize efficient optical interfaces with individual quantum systems. Cavities improve collection efficiencies by providing preferential emission into a well-defined spatial mode. They additionally benefit the NV in particular by enhancing the probability of emission into the ZPL via the Purcell effect[69].

Early efforts to build nanoscale cavities around NVs showed enhancement of the emission into the ZPL[70,71]. But they have failed to meet the strict requirements on the spectral properties of the emission due to the need for near-surface NVs and the electric field sensitivity of the NV emission frequencies. Alternative approaches based on low-mode-volume Fabry-Perot cavities that encapsulate μm-thin diamond membranes[72,73] have delivered first promising results with marginal broadening of the NV emission spectrum[74].

In addition, these low-mode-volume cavities are in a parameter regime where the earlier mentioned reflection-based mechanism might already become feasible[16]. This would then ideally allow for NV state measurements by monitoring the reflection off the cavity, without ever exciting the NV centre itself. Such a readout mechanism would clearly elevate readout fidelities and could ultimately be used to initialize the NV centre by measurement without direct optical excitation and therefore without inducing dephasing on the surrounding nuclear spin memories.

10.4.2. INTRA-NODE GATE FIDELITIES

All diamond samples used in this thesis were of natural isotopic composition. Future devices should exploit the engineerability of diamond to exclude additional noise sources such as the remote nuclear spin bath. An ideal scenario involves isotopically purified diamond with a delta-doped layer of ^{13}C atoms to realize a well localized resource. Alternatively ^{13}C spins could also be implanted at certain locations close to NVs. This type of dilute spin bath eliminates unwanted interactions with remote spins during gate sequences and should therefore increase local gate fidelities and coherence times while retaining full capabilities.

So far we relied on nuclear-electron gates that are realized by solely addressing the NV spin at prespecified times. There is a wide range of gate mechanisms that promise to achieve higher fidelities. These mechanisms either rely on simultaneous addressing of electron and nuclear spins[75], asymmetrically-timed dynamical decoupling sequences[76] or continuous driving of the NV-spin[77]. Note that some of these techniques are highly sensitive to the inter-pulse delay. One can however overcome timing resolution limitiations by pulse-amplitude-shaping to realize inter-pulse delays with ∼ ps-resolution and commercially available waveform generators[78].

10.4.3. QUANTUM MEMORY ROBUSTNESS

The presented quantum memories in Chapter 9 can withstand hundreds of entangling attempts. In the future it is desirable to increase their resilience such that multiple entangled states can be generated and stored reliably. Chapter 6 demonstrates that quasi-static noise and microwave pulse errors during entangling attempts are currently the limiting factor to memory performance. This calls for a sophisticated approach to engineer the delivery of microwave signals to the NV. Besides changing the on-chip lithographic gold structures to impedance matched transmission lines, one could employ optimal control algorithms to elevate fidelities[79] or gate set tomography to identify systematic gate errors[80]. Further, active intensity stabilization of laser pulses has led to single-qubit gate infidelities of 10^{-5}; see Refs. 81, 82. Analogous stabilization methods can be implemented with NVs by monitoring the microwave throughput amplitudes on the fly.

A straight forward increase of the memory resilience is obtained by reducing the coupling strength to the NV. Three strategies exist to achieve this. First, as demonstrated in Ch. 5 decoherence-protected subspaces can synthesize lower coupling strengths from multiple nuclear spins. Second, isotopically purified samples may grant direct access to very weakly coupled nuclear spins[53]. Finally, long-range dipolar NV-NV coupling[83] may enable coherent state transfer between two NVs. One NV would then act as optical interface while the other NV facilitates state storage in nuclear spin memories that are far removed from the optical interface.

10.4.4. REMOTE ENTANGLED STATE FIDELITIES

Table 10.1 provides an overview of the remote entangling schemes, including the scaling of the success probability p_{success} with the probability to detect a single photon p_{det}. Straightforward technical improvements exist for most of the given sources of error and most of them are combated by a combination of the proposed technologies above. NVs in optical cavities, for instance, may display a higher luminosity and therefore render detector dark counts less relevant.

The distinguishability of the NV emission may need special attention. The limiting factors to the indistinguishability of the NV emission in our system are currently unknown. We therefore call for a systematic study of the DC Stark-tuning behaviour and of spectral diffusion on short time scales. To this end, subsequent photons emitted by a single NV centre may be interfered in an unbalanced interferometer[87]. Since this experiment does not require microwave control one could perform it on NVs without metallic leads in the vicinity which may lead to a visible reduction of high-frequency charge noise.

Entangling scheme	Ref. [84]	Ref. [85]	Ref. [86]
Realized in	Ch. 8	Ch. 7	Ch. 9
p_{success}	$2\alpha p_{\text{det}}$	$p_{\text{det}}^2/2$	$\propto \alpha^2 p_{\text{det}}^2$ to $\propto \alpha p_{\text{det}}$
TQPI visibility V	$\propto \sqrt{1-V}$	$\propto 1-V$	$\propto 1-V$
Dark counts (20 Hz)	$9\cdot10^{-3}$	$2\cdot10^{-3}$	$2\cdot10^{-3}$
Double excitation (Sec. 8.6.7)	0.04	0.075	0.075
Interferometric instability (Sec. 8.6.5)	0.014	~0	0.014
Bright state population α (Sec. 2.4)	$\propto \alpha$	0	0

Table 10.1 | We present key numbers and scaling behaviour of the demonstrated entangling schemes in this thesis. In addition, sources of systematic error with their proportional or numerical contribution to state infidelities were estimated with parameters of current devices. We further assume ZPL photon detection probabilities of 10^{-3} and, where applicable, $\alpha = 0.05$. Dark count rates are given per detector. The probability of double excitation is estimated for Gaussian pulses of 2.2 ns width (see Sec. 8.6.7). The memory-assisted entangling protocol[86] is moreover subject to control errors and dephasing of nuclear spins such that a full summary of all infidelities — and their dependencies on parameters such as α — is demanding. Here we limit ourselves to high-fidelity local operations. In this regime all second order dependencies cancel such that a quantification of the protocol performance becomes straightforward. The proportionality of the success probability depends on the quantum memory robubstness and is given for the worst-case (full decoherence after a single entangling attempt) and best-case (no decoherence) scenarios.

10.5. CONCLUSION

Quantum networks will enable distributed computation and secure long-distance communication. The NV centre is among the prime candidates for the realization of such a network. All earlier mentioned challenges have no fundamental limit and the proposed strategies may yield fruitful results in overcoming these hurdles. Extraordinary scientific achievements such as the realization of a quantum repeater will be demonstrated during the grander research effort to obtain a fully-fledged quantum network.

REFERENCES

[1] L.-M. Duan and C. Monroe, *Colloquium: Quantum networks with trapped ions,* Reviews of Modern Physics **82**, 1209 (2010).

[2] C. Monroe and J. Kim, *Scaling the Ion Trap Quantum Processor,* Science **339**, 1164 (2013).

[3] D. L. Moehring *et al.*, *Entanglement of single-atom quantum bits at a distance,* Nature **449**, 68 (2007).

[4] D. Hucul *et al.*, *Modular entanglement of atomic qubits using photons and phonons,* Nature Physics **11**, 37 (2015).

[5] C. J. Ballance *et al.*, *Hybrid quantum logic and a test of Bell's inequality using two different atomic isotopes,* Nature **528**, 384 (2015).

[6] T. R. Tan *et al.*, *Multi-element logic gates for trapped-ion qubits,* Nature **528**, 380 (2015).

[7] I. V. Inlek, C. Crocker, M. Lichtman, K. Sosnova and C. Monroe, *Multispecies Trapped-Ion Node for Quantum Networking,* Physical Review Letters **118**, 250502 (2017).

[8] M. Steiner, H. M. Meyer, C. Deutsch, J. Reichel and M. Köhl, *Single Ion Coupled to an Optical Fiber Cavity,* Physical Review Letters **110**, 043003 (2013).

[9] T. E. Northup and R. Blatt, *Quantum information transfer using photons,* Nature Photonics **8**, 356 (2014).

[10] J. Hofmann *et al.*, *Heralded Entanglement Between Widely Separated Atoms,* Science **337**, 72 (2012).

[11] W. Rosenfeld *et al.*, *Event-Ready Bell Test Using Entangled Atoms Simultaneously Closing Detection and Locality Loopholes,* Physical Review Letters **119**, 010402 (2017).

[12] M. Saffman, T. G. Walker and K. Mølmer, *Quantum information with Rydberg atoms,* Reviews of Modern Physics **82**, 2313 (2010).

[13] A. M. Kaufman *et al.*, *Entangling two transportable neutral atoms via local spin exchange,* Nature **527**, 208 (2015).

[14] S. Welte, B. Hacker, S. Daiss, S. Ritter and G. Rempe, *Cavity Carving of Atomic Bell States,* Physical Review Letters **118**, 210503 (2017).

[15] A. Reiserer and G. Rempe, *Cavity-based quantum networks with single atoms and optical photons,* Reviews of Modern Physics **87**, 1379 (2015).

[16] L.-M. Duan and H. J. Kimble, *Scalable Photonic Quantum Computation through Cavity-Assisted Interactions,* Physical Review Letters **92**, 127902 (2004).

[17] T. G. Tiecke *et al.*, *Nanophotonic quantum phase switch with a single atom,* Nature **508**, 241 (2014).

[18] I. Shomroni *et al.*, *All-optical routing of single photons by a one-atom switch controlled by a single photon,* Science **345**, 903 (2014).

[19] J. Volz, M. Scheucher, C. Junge and A. Rauschenbeutel, *Nonlinear π phase shift for single fibre-guided photons interacting with a single resonator-enhanced atom,* Nature Photonics **8**, 965 (2014).

[20] S. Ritter *et al.*, *An elementary quantum network of single atoms in optical cavities,* Nature **484**, 195 (2012).

[21] N. Kalb, A. Reiserer, S. Ritter and G. Rempe, *Heralded Storage of a Photonic Quantum Bit in a Single Atom,* Physical Review Letters **114**, 220501 (2015).

[22] S. Sun, H. Kim, G. S. Solomon and E. Waks, *A quantum phase switch between a single solid-state spin and a photon,* Nature Nanotechnology **11**, 539 (2016).

[23] R. Stockill *et al.*, *Phase-Tuned Entangled State Generation between Distant Spin Qubits,* Physical Review Letters **119**, 010503 (2017).

[24] A. Delteil *et al.*, *Generation of heralded entanglement between distant hole spins,* Nature Physics **12**, 218 (2016).

[25] A. Delteil, Z. Sun, S. Fält and A. Imamoğlu, *Realization of a Cascaded Quantum System: Heralded Absorption of a Single Photon Qubit by a Single-Electron Charged Quantum Dot,* Physical Review Letters **118**, 177401 (2017).

[26] A. I. Lvovsky, B. C. Sanders and W. Tittel, *Optical quantum memory,* Nature Photonics **3**, 706 (2009).

[27] M. Zhong *et al.*, *Optically addressable nuclear spins in a solid with a six-hour coherence time,* Nature **517**, 177 (2015).

[28] M. Rančić, M. P. Hedges, R. L. Ahlefeldt and M. J. Sellars, *Coherence time of over a second in a telecom-compatible quantum memory storage material,* Nature Physics **advance online publication** (2017).

[29] T. Zhong *et al.*, *Nanophotonic rare-earth quantum memory with optically controlled retrieval,* Science **357**, 1392 (2017).

[30] R. Kolesov *et al.*, *Optical detection of a single rare-earth ion in a crystal,* Nature Communications **3**, 1029 (2012).

[31] M. Widmann *et al.*, *Coherent control of single spins in silicon carbide at room temperature,* Nature Materials **14**, 164 (2015).

[32] K. J. Morse *et al.*, *A photonic platform for donor spin qubits in silicon,* Science Advances **3**, e1700930 (2017).

[33] B. C. Rose *et al.*, *Observation of an environmentally insensitive solid state spin defect in diamond,* arXiv:1706.01555 (2017).

[34] T. Iwasaki *et al.*, *Tin-Vacancy Quantum Emitters in Diamond,* arXiv:1708.03576 (2017).

[35] M. K. Bhaskar *et al.*, *Quantum Nonlinear Optics with a Germanium-Vacancy Color Center in a Nanoscale Diamond Waveguide,* Physical Review Letters **118**, 223603 (2017).

[36] J. N. Becker and C. Becher, *Coherence Properties and Quantum Control of Silicon Vacancy Color Centers in Diamond,* Physica Status Solidi A , 1700586 (2017).

[37] J. Riedrich-Möller *et al.*, *Deterministic Coupling of a Single Silicon-Vacancy Color Center to a Photonic Crystal Cavity in Diamond,* Nano Letters **14**, 5281 (2014).

[38] A. Sipahigil *et al.*, *An integrated diamond nanophotonics platform for quantum-optical networks,* Science **354**, 847 (2016).

[39] D. D. Sukachev *et al.*, *The silicon-vacancy spin qubit in diamond: Quantum memory exceeding ten milliseconds and single-shot state readout,* arXiv:1708.08852 (2017).

[40] J. N. Becker *et al.*, *All-optical control of the silicon-vacancy spin in diamond at millikelvin temperatures,* arXiv:1708.08263 (2017).

[41] A. J. Menssen *et al.*, *Distinguishability and Many-Particle Interference,* Physical Review Letters **118**, 153603 (2017).

[42] S. Agne *et al.*, *Observation of Genuine Three-Photon Interference,* Physical Review Letters **118**, 153602 (2017).

[43] D. Alsina and J. I. Latorre, *Experimental test of Mermin inequalities on a 5-qubit quantum computer,* Physical Review A **94** (2016).

[44] A. Cabello, *Bell's theorem with and without inequalities for the three-qubit Greenberger-Horne-Zeilinger and W states,* Physical Review A **65**, 032108 (2002).

[45] N. D. Mermin, *Extreme quantum entanglement in a superposition of macroscopically distinct states,* Physical Review Letters **65**, 1838 (1990).

[46] H.-J. Briegel, W. Dür, J. I. Cirac and P. Zoller, *Quantum Repeaters: The Role of Imperfect Local Operations in Quantum Communication,* Physical Review Letters **81**, 5932 (1998).

[47] C. H. Bennett and G. Brassard, *Quantum cryptography: Public key distribution and coin tossing,* Proceedings of IEEE International Conference on Computers, Systems and Signal Processing **175**, 8 (1984).

[48] M. Takeoka, S. Guha and M. M. Wilde, *Fundamental rate-loss tradeoff for optical quantum key distribution,* Nature Communications **5**, 5235 (2014).

[49] S. Pirandola, R. Laurenza, C. Ottaviani and L. Banchi, *Fundamental limits of repeaterless quantum communications,* Nature Communications **8**, 15043 (2017).

[50] D. Luong, L. Jiang, J. Kim and N. Lütkenhaus, *Overcoming lossy channel bounds using a single quantum repeater node,* Applied Physics B **122**, 96 (2016).

[51] F. Rozpędek *et al.*, *Realistic parameter regimes for a single sequential quantum repeater,* arXiv:1705.00043 (2017).

[52] N. L. Piparo, M. Razavi and W. J. Munro, *Memory-Assisted Quantum Key Distribution with a Single Nitrogen Vacancy Center,* arXiv:1708.06532 (2017).

[53] P. C. Maurer *et al.*, *Room-Temperature Quantum Bit Memory Exceeding One Second,* Science **336**, 1283 (2012).

[54] M. S. Blok, *Quantum Measurement and Real-Time Feedback with a Spin-Register in Diamond*, Ph.d. thesis, Delft University of Technology (2015).

[55] M. Uphoff, M. Brekenfeld, G. Rempe and S. Ritter, *An integrated quantum repeater at telecom wavelength with single atoms in optical fiber cavities,* Applied Physics B **122**, 46 (2016).

[56] T. Monz *et al.*, *Realization of a scalable Shor algorithm,* Science **351**, 1068 (2016).

[57] S. Debnath *et al.*, *Demonstration of a small programmable quantum computer with atomic qubits,* Nature **536**, 63 (2016).

[58] L. Robledo *et al.*, *High-fidelity projective read-out of a solid-state spin quantum register,* Nature **477**, 574 (2011).

[59] N. H. Nickerson, Y. Li and S. C. Benjamin, *Topological quantum computing with a very noisy network and local error rates approaching one percent,* Nature Communications **4**, 1756 (2013).

[60] N. H. Nickerson, J. F. Fitzsimons and S. C. Benjamin, *Freely Scalable Quantum Technologies Using Cells of 5-to-50 Qubits with Very Lossy and Noisy Photonic Links,* Physical Review X **4**, 041041 (2014).

[61] G. Smith and J. Yard, *Quantum Communication with Zero-Capacity Channels,* Science **321**, 1812 (2008).

[62] M. Ben-Or and A. Hassidim, *Fast Quantum Byzantine Agreement,* in *Proceedings of the Thirty-Seventh Annual ACM Symposium on Theory of Computing*, STOC '05 (ACM, New York, NY, USA, 2005) pp. 481–485.

[63] M. Ben-Or, C. Crepeau, D. Gottesman, A. Hassidim and A. Smith, *Secure Multiparty Quantum Computation with (Only) a Strict Honest Majority,* in *47th Annual IEEE Symposium on Foundations of Computer Science* (2006).

[64] S. Barz *et al.*, *Demonstration of Blind Quantum Computing,* Science **335**, 303 (2012).

[65] J. Yin *et al.*, *Satellite-based entanglement distribution over 1200 kilometers,* Science **356**, 1140 (2017).

[66] B. Hensen *et al.*, *Loophole-free Bell inequality violation using electron spins separated by 1.3 kilometres,* Nature **526**, 682 (2015).

[67] S. Zaske *et al.*, *Visible-to-Telecom Quantum Frequency Conversion of Light from a Single Quantum Emitter,* Physical Review Letters **109**, 147404 (2012).

[68] T. Miya, Y. Terunuma, T. Hosaka and T. Miyashita, *Ultimate low-loss single-mode fibre at 1.55 μm,* Electronics Letters **15**, 106 (1979).

[69] E. Purcell, *Spontaneous emission probabilities at radio frequencies,* Physical Review **69**, 681 (1946).

[70] D. Englund *et al.*, *Deterministic Coupling of a Single Nitrogen Vacancy Center to a Photonic Crystal Cavity,* Nano Letters **10**, 3922 (2010).

[71] A. Faraon, P. E. Barclay, C. Santori, K.-M. C. Fu and R. G. Beausoleil, *Resonant enhancement of the zero-phonon emission from a colour centre in a diamond cavity,* Nature Photonics **5**, 301 (2011).

[72] E. Janitz *et al.*, *Fabry-Perot microcavity for diamond-based photonics,* Physical Review A **92**, 043844 (2015).

[73] S. Bogdanović *et al.*, *Design and low-temperature characterization of a tunable microcavity for diamond-based quantum networks,* Applied Physics Letters **110**, 171103 (2017).

[74] D. Riedel *et al.*, *Deterministic Enhancement of Coherent Photon Generation from a Nitrogen-Vacancy Center in Ultrapure Diamond,* Physical Review X **7**, 031040 (2017).

[75] J. Casanova, Z.-Y. Wang and M. B. Plenio, *Noise-Resilient Quantum Computing with a Nitrogen-Vacancy Center and Nuclear Spins,* Physical Review Letters **117**, 130502 (2016).

[76] J. Casanova, Z.-Y. Wang, J. F. Haase and M. B. Plenio, *Robust dynamical decoupling sequences for individual-nuclear-spin addressing,* Physical Review A **92**, 042304 (2015).

[77] V. V. Mkhitaryan, F. Jelezko and V. V. Dobrovitski, *Highly selective detection of individual nuclear spins with rotary echo on an electron spin probe,* Scientific Reports **5**, 15402 (2015).

[78] J. Zopes *et al.*, *High resolution quantum sensing with shaped control pulses,* arXiv:1705.07968 [quant-ph] (2017).

[79] F. Dolde *et al.*, *High-fidelity spin entanglement using optimal control,* Nature Communications **5**, 3371 (2014).

[80] R. Blume-Kohout *et al.*, *Demonstration of qubit operations below a rigorous fault tolerance threshold with gate set tomography,* Nature Communications **8**, 14485 (2017).

[81] J. P. Gaebler *et al.*, *High-Fidelity Universal Gate Set for ${{{̂9}\mathrm{Be}}}{̂+}$ Ion Qubits,* Physical Review Letters **117**, 060505 (2016).

[82] C. J. Ballance, T. P. Harty, N. M. Linke, M. A. Sepiol and D. M. Lucas, *High-Fidelity Quantum Logic Gates Using Trapped-Ion Hyperfine Qubits,* Physical Review Letters **117**, 060504 (2016).

[83] T. Yamamoto *et al.*, *Strongly coupled diamond spin qubits by molecular nitrogen implantation,* Physical Review B **88**, 201201 (2013).

[84] C. Cabrillo, J. I. Cirac, P. García-Fernández and P. Zoller, *Creation of entangled states of distant atoms by interference,* Physical Review A **59**, 1025 (1999).

[85] S. D. Barrett and P. Kok, *Efficient high-fidelity quantum computation using matter qubits and linear optics,* Physical Review A **71**, 060310 (2005).

[86] E. T. Campbell and S. C. Benjamin, *Measurement-Based Entanglement under Conditions of Extreme Photon Loss,* Physical Review Letters **101**, 130502 (2008).

[87] T. Legero, T. Wilk, M. Hennrich, G. Rempe and A. Kuhn, *Quantum Beat of Two Single Photons,* Physical Review Letters **93**, 070503 (2004).

ACKNOWLEDGEMENTS

Q(u)T(ech) is a very special place. I realized this right from the start when I applied and was told to bring my football gear because we were going to play that afternoon. The vibrant scientific atmosphere but also QT's nonchalance – best exemplified by anecdotal evidence of football matches with applicants – are what dragged me into this place. Not only did this unregrettable decision allow me to work with inspiring colleagues but also to make lasting friendships. In the following I will try my best to express my gratitude towards the people who supported me over past years.

Ronald, I am very grateful that you have provided me with the opportunity to become part of your team. During my time here you achieved whatever you set out to do and I am convinced that this trend will continue in the future. I admire your broad set of skills that allows you to not only stay up-to-date with the efforts in your team but also to immediately grasp underlying concepts and to always ask the right questions that guide the team towards new results.

Tim, thank you for taking me under your wing during my first year and for all the insightful discussions thereafter. I can proudly say that Zeno was my first leading project in Delft and that it was a formative experience for me and yielded one of the most entertaining referee reports of all time. Now that you are leading your own group I am sure that many more people will benefit from — and enjoy — your thoughtful insights and support.

My colleagues within Team Diamond form a special research group whom I would like to thank for the past years which yielded great experiences both in the lab and elsewhere. The current research conducted within Team Diamond rests on a foundation of previous efforts and as a result a plethora of useful tools, methods and insights. I would therefore like to thank the former members of Team Diamond – Toeno, Gijs, Wolfgang, Cristian, Lucio and Lilian – for all their invaluable contributions that make this foundation rock solid. These tools can however only unfold their potential if the compounded knowledge is actively transferred. Therefore, I would like to thank all senior PhDs I had the chance to work with shortly after my arrival Julia, Machiel and Bas. Julia, thank you for showing me everything about carbon spins, the little tricks needed to fill LT2 without disturbing the magnet and all the support you provided for our press releases. Machiel, you were a great cleanroom mentor/buddy. I believe that no other paper was written as swiftly as the memory paper! I wish you all the best in academia. This wish extends itself to you, Bas. Joining the Bell project and working with you taught me the ways of remote entanglement but you were also a role model in terms of organization, thoroughness and scientific rigour. Even though I have to admit that I am not missing those night shifts.

This thesis would not have been possible without my partners in crime. Whether we

were a scientific tandem or tricycle depends on the project but it is clear that you both had a great impact on my time here: Thank you Peter and Andreas. Andreas, we go way back; I won't reiterate the acknowledgements of my master's thesis here (mainly because there is no proper table football in Delft!). Instead, let me say that I admire your quick-and-dirty way of hypothesis testing, organizational foresight and unorthodox ideas. You have saved countless hours of my time by counterbalancing my idealistic view on for instance beautiful (i.e. overthought) measurement code with your goal-oriented drive. You combine the virtues of a group leader and I know that rare-earth ions are the next big thing.
Peter, I cannot overstate how much fun it was to have you around but let me try anyways. I learned tremendously from your analytic problem-solving skills and enjoyed your energetic and cheerful presence. Not only do I consider us a great team but we shared so many diverse conversations and activities outside of work that I would run out of space listing them here. I am looking forward to more climbing trips and am sure that your path outside of academia will be a continuation of your success.

To all diamond members with whom I did not work as closely but whose presence was nevertheless just as inspiring and enjoyable. Stefan, having you in my office for the last years has forged a great friendship. You are a very humble buddy that never loses his cool (and will continue to do so in the US and Spain). Suzanne, we started around the same time and ended up taking different paths that intersected occasionally. Whenever these paths crossed I got to work with an empathic, ambitious and organized person. All the best for your final year! Hannes, our overlap in Delft was only brief yet getting the chance to work with you allowed me to learn a lot. Anaïs, your vivid presence lifted our spirits throughout Bell and beyond! Max, our lunch-break conversations about crypto and general investing are a hallmark of your structured mind and organizational approach to science. I am really impressed with the speed at which you picked up on GST! Valeria and Wouter, even though your time in Delft got cut short, I got to meet two genuine and friendly people whose company I did enjoy very much. I'll certainly appreciate hearing about your new adventures. Mohamed, our conversations dug deep into NV-nuclear and even NV-nuclear-nuclear interactions; your PhD is off to a great start and I know that you will continue in the same fashion. Maarten, I am happy that you were the latest addition to the office as you are continuously oozing a chill vibe. I am looking forward to record-long Nitrogen coherence times! Michiel, I still owe you a gold fish and I will certainly deliver! Jaco, from two meters to tens of kilometres: NV-NV entanglement is about to be pushed to the limit! Madelaine, another officemate of mine! Your enthusiasm and commitment are going to carry you far. Adriaan, you were my first bouldering buddy here in Delft (and another short-term officemate)! I really appreciate our hallway chats full of slightly-sarcastic complaints; those were always fun AND relieving.
Looking at all the talent that joined Team Diamond recently, I know that the future for NV-based quantum networks with error-corrected nodes is bright! Cheers to you and lots of success in your pursuits, Sophie, Matteo, Conor, Joe and Airat!

During my time here I also had the privilege to try myself as supervisor; I am grateful that Sten, Jacob and Jesse chose to embark onto their journey into academia together with me. I hope you learned as much from our time together as I did. Sten, while I always appreciated your uplifting spirit, you also put in the work to take more (carbon-)fingerprints than a criminal investigator during your time here. In the end this laid the foundation for the distillation experiment! Jacob, your optimizer saved us from countless hours of set-up babysitting I was really impressed with the speed at which you could tackle new obstacles. Jesse, your programming prowess in combination with your logical approach to our nuclear-spin feedback sparked many ideas for parts of this thesis; all the best for your PhD... auf Wiederschnitzel!

As QuTech continues to grow it becomes an increasingly intertwined entity of scientific collaboration. Thank you Martin, Anna, Dirk, Sander and Erwin for many enlightening discussions on the engineering side of NV centres and your significant contribution to Team Diamond! I further want to express my gratitude towards everyone within the Quantum Software group. One of the reasons that our QINC days resulted in several publications and many fruitful ideas is in large parts due to you, Stephanie. Your drive and curiosity imprint themselves onto our daily interactions within the QINC roadmap. Filip, thank you for a great time in Cambridge. We should go punting again! Together with you and Kenneth I had many interesting repeater discussions and I am grateful that I could make a humble contribution to your theoretical endeavour! I would also like to thank Simon and Naomi for several skype calls, their instrumental theory support that got me excited about the distillation project and for the invitation to Oxford.

This work would not have been possible without tapping into the vast expertise of the people that constitute the backbone of QuTech. Raymond, Raymond and Marijn, thank you for many discussions on the ADwin, microwave switches and all kinds of electronic gadgets whose function I could only envision and you already happened to have developed. All lab related issues find a solution due to your help; thank you Mark, Jelle, Remco, Olaf, Jason and Siebe. Thank you Marja, Yuki, Chantal and Joanna for keeping the show up and running.

QuTech is a cordial environment that guarantees good times through all the uitjes, friday-afternoon TPKV, sports days, summer bbq sessions and christmas parties etc. I believe that the friendships I have made will transcend my time here at QuTech and remain with me. Alex, your engaging spirit (and potentially your caffeine addiction) has granted me many good mornings that were filled with deep conversations or the most recent gossip. James, getting to know you and having lived with you has enriched my life. Thank you for the countless experiences (house parties) and your support that endured my late-night rants. Florian, while your first creation found a (forcibly) large costumer base... please do not invent another drink. Thank you for all your organizational efforts; without you the Aachen connection would not have been the same. Michiel, you chess-playing pub-quizzing trivia archive. Being around you always results in thoughtful insights that are seasoned with your wits; side effects of these meet-ups may include sleep deficits though. Toivo, my bouldering buddy! Don't worry, I think Peter, you and me had equally unsavoury shoes during our sessions such that the source of that specific aroma was indistinct! Your smarts and broad interests guarantee that anything you will end up doing will be impactful (but don't try to bring your old climbing shoes to those gigs!). All the best to you and Heleen on your upcoming adventures. There are many more people

within QuTech that have brightened my day regularly and I would run out of space listing all of them individually: I would like to thank everyone within QuTech for creating this cordial spirit.
Mastering your PhD can only become better if you have peers beyond your faculty to exchange your worries and to plot the coming years! Thank you Jasmine, Fardin and Nikos for sticking around since the PhD start-up and for all those happy meet-ups!

Wenn ich am Rad der Zeit drehe und nach Deutschland zurück blicke, sehe ich viele Menschen denen ich sehr dankbar bin. Ein großes Dankeschön an all meine ehemaligen Kollegen, im Besonderen Gerhard, Stephan, Rudolf, Frank und Max für die Möglichkeit in ihren Gruppen meine jeweilige Abschlussarbeit zu verrichten und von ihnen das wissenschaftliche Handwerkszeug zu lernen. Ich hoffe, dass eure hohen Standards sich in dieser Arbeit wiederfinden lassen. Dieser Wunsch richtet sich auch an dich, Roland. Durch dich bin ich zuerst mit wissenschaftlicher Methodik in Berührung gekommen und konnte mich dem entsprechend auf die bevorstehenden Herausforderungen vorbereiten. In einer Reihe von Mentoren sind die grundsteinlegenden besonders bedeutend. Deshalb, vielen Dank an meine Lehrer die meine pubertäre Präsenz ertragen konnten und zur Sättigung meiner Neugier beigetragen haben. Meinen ehemaligen Kommilitonen vom Garchinger Stammtisch habe ich viele großartige Erinnerungen zu verdanken. Auf dass wir noch mehr Erlebnisse auf unseren zukünftigen Trips teilen! Das Gleiche gilt natürlich auch für all meine “Freggerla" aus der Heimat; obwohl uns doch große Entfernungen trennen fühlt es sich jedes mal so an als wäre ich nie weg gewesen falls ich dann doch mal vorbei schneie!

Meiner Familie gebührt besonderer Dank. Eure Geduld, stete Unterstützung und das Wissen mich jeder Zeit auf euch verlassen zu können bedeuten mir viel. Ich werde auch weiterhin mein Bestes geben damit dies auf Gegenseitigkeit beruht.

Sabine, jij bent mijn bron van liefde. Samen met jou, en vooral door jou, is het voor mij mogelijk vreugde in alledaagse dingen te vinden. Ik kijk vooruit naar onze toekomst.

Norbert Kalb
Delft, January 2018

LIST OF PUBLICATIONS

13. *Dephasing mechanisms of diamond-based nuclear-spin memories for quantum communication.*
N. Kalb, P.C. Humphreys, J.J. Slim, and R. Hanson.
arXiv:1802.05996

12. *One-second coherence for a single electron spin coupled to a multi-qubit nuclear-spin environment.*
M.H. Abobeih, J. Cramer, M. Bakker, **N. Kalb**, M. Markham, D.J. Twitchen, and T.H. Taminiau.
arXiv:1801.01196

11. *Deterministic entanglement generation between remote solid-state qubits.*
P.C. Humphreys*, **N. Kalb***, J.P.J. Morits, R.N. Schouten, R.F.L. Vermeulen, D.J. Twitchen, M. Markham, and R. Hanson.
arXiv:1712.07567

10. *Realistic parameter regimes for a single sequential quantum repeater.*
F. Rozpędek*, K. Goodenough*, J. Ribeiro, **N. Kalb**, V.C. Vivoli, A. Reiserer, R. Hanson, S. Wehner, and D. Elkouss.
arXiv:1705.00043

9. *Entanglement distillation between solid-state quantum network nodes.*
N. Kalb*, A.A. Reiserer*, P.C. Humphreys*, J.J.W. Bakermans, S.J. Kamerling, N.H. Nickerson, S.C. Benjamin, D.J. Twitchen, M. Markham, and R. Hanson.
Science **356**, 928 (2017).

8. *Loophole-free Bell test using electron spins in diamond: second experiment and additional analysis.*
B. Hensen, **N. Kalb**, M.S. Blok, A.E. Dréau, A. Reiserer, R.F.L. Vermeulen, R.N. Schouten, M. Markham, D.J. Twitchen, D. Elkouss, K. Goodenough, S. Wehner, T.H. Taminiau, and R. Hanson.
Scientific Reports **6**, 30289 (2016).

7. *Robust Quantum-Network Memory Using Decoherence-Protected Subspaces of Nuclear Spins.*
A. Reiserer*, **N. Kalb***, M.S. Blok, K.J.M. van Bemmelen, T.H. Taminiau, R. Hanson, M. Markham, and D.J. Twitchen.
Physical Review X **6**, 021040 (2016).

6. *Experimental creation of quantum Zeno subspaces by repeated multi-spin projections in diamond.*
N. Kalb, J. Cramer, M. Markham, D.J. Twitchen, R. Hanson, and T.H. Taminiau.
Nature Communications **7**, 13111 (2016).

5. *Repeated quantum error correction on a continuously encoded qubit by real-time feedback.*
J. Cramer, **N. Kalb**, M.A. Rol, B. Hensen, M.S. Blok, M. Markham, D.J. Twitchen, R. Hanson, and T.H. Taminiau.
Nature Communications **7**, 11526 (2016).

---

*Equally contributing authors

4. *Towards quantum networks of single spins: analysis of a quantum memory with an optical interface in diamond.*
   M.S. Blok[*], **N. Kalb**[*], A. Reiserer, T.H. Taminiau, and R. Hanson.
   Faraday discussions **184**, 173 (2015).

3. *Loophole-free Bell inequality violation using electron spins separated by 1.3 kilometres.*
   B. Hensen, H. Bernien, A.E. Dréau, A. Reiserer, **N. Kalb**, M.S. Blok, J. Ruitenberg, R.F.L. Vermeulen, R.N. Schouten, C. Abellán, W. Amaya, V. Pruneri, M.W. Mitchell, M. Markham, D.J. Twitchen, D. Elkouss, S. Wehner, T.H. Taminiau, and R. Hanson.
   Nature **526**, 682 (2015).

2. *Heralded Storage of a Photonic Quantum Bit in a Single Atom.*
   N. Kalb, A. Reiserer, S. Ritter, and G. Rempe.
   Physical Review Letters **114**, 220501 (2015).

1. *A quantum gate between a flying optical photon and a single trapped atom.*
   A. Reiserer, **N. Kalb**, S. Ritter, and G. Rempe.
   Nature **508**, 237 (2014).

---

[*] Equally contributing authors

NORBERT KALB

09. 04. 1988, Nuremberg, Germany

1998 - 2007	Secondary school, *Christoph-Jacob-Treu Gymnasium*, Lauf an der Pegnitz, Germany.
2008 - 2011	B. Sc. in Physics, *Technische Universität München.* Graduation research in the superconducting quantum circuits group at the Walther-Meissner Institute for Low Temp. Research. Advisor: Prof. dr. R. Gross.
2011 - 2014	M. Sc. in Physics, *Technische Universität München.* Graduation research in the Quantum Dynamics Group at the Max-Planck Institute of Quantum Optics. Advisor: Prof. dr. G. Rempe.
2012	Study abroad semester, *University of Queensland.* Brisbane, Australia
2014 - 2018	Ph.D. in experimental Physics, *Delft University of Technology.* Thesis: Diamond-based quantum networks with multi-qubit nodes Group: QuTech and Kavli Institute of Nanoscience. Advisor: Prof. dr. ir. R. Hanson.